

https://dspace.org/

Developing electrical tree resistant epoxy nanodielectrics with improved thermal properties

Hank, Andrew Marvin

2017

http://hdl.handle.net/10539/23454

Hank, Andrew Marvin (2017) Developing electrical tree resistant epoxy nanodielectrics with improved thermal properties, University of the Witwatersrand, <http://hdl.handle.net/10539/23454>

Downloaded from a DSpace repository. https://dspace.org/





UNIVERSITY OF THE WITWATERSRAND
JOHANNESBURG, SOUTH AFRICA

Developing electrical tree resistant epoxy nanodielectrics with improved thermal properties

Mr. Andrew Marvin Hank

A dissertation submitted to the Faculty of Engineering and the Built Environment, University of the Witwatersrand, in fulfilment of the requirements for the degree of Master of Science in Engineering

25 May 2017

Declaration

I, Andrew Marvin Hank, am registered for Master of Science in the School of Electrical and Information Engineering, I herewith submit this dissertation *"Developing electrical tree resistant epoxy nanodielectrics with improved thermal properties,"* for the fulfilment of the requirements for the degree of Master of Science in Engineering.

I hereby declare the following:

- I am aware that plagiarism (the use of someone else's work without their permission and/or without acknowledging the original source is wrong;
- I confirm that the work submitted herewith for assessment is my own unaided work except where I have explicitly indicated otherwise;
- This task has not been submitted before, either individually or jointly, for any course requirement, examination or degree at this or any other tertiary educational institution;
- I have followed the required conventions in referencing the thoughts and ideas of others;
- I understand that the University of the Witwatersrand may take disciplinary action against me if it can be shown that any part of this work is not my own unaided work or that I have failed to acknowledge the sources of the ideas or words in this dissertation.

Signature: _____

Date: _____

Abstract:

Two of the main contributors to high voltage insulation failure are thermal and electrical stresses. The failures may be mitigated by using nanodielectrics. The enhanced effect of nanoparticles in nanodielectrics is attributed to an interaction zone/interphase around each individual nanoparticle between the nanoparticle and host polymer. However, particle clumping or agglomerates are a major challenge in nanodielectric technology. In this work mitigation of the clumping challenges was explored through Rheology in determining optimal particle loading levels. The nanodielectrics studies were Boron Nitride and Carbon Nanospheres in Araldite Epoxy. The rheology results indicated an optimal loading level of 1.09 vol % to 1.35 vol% for Boron Nitride in Epoxy and 0.33 vol% for Carbon Nanospheres in Epoxy. Microscopy, dielectric spectroscopy, electrical tree characterisation, thermal expansion and laser flash analysis were used to validate the efficacy of the rheology results. The results indicated improved properties of the resultant dielectric such as; increased mechanical stiffness, increased electrical resistance and the percolation threshold, partial discharge suppression and increased thermal conductivity at the glass transition temperature. This study has established a rheology-based technique incorporated in the manufacturing process to determine the optimal filler loading of C/Epoxy and BN/Epoxy nanodielectrics. Future work is recommended as investigating either new particle types such as Sulphur hexafluoride in Carbon Nanospheres or mixtures of Carbon Nanospheres and Boron Nitiride.

Executive Summary:

Two of the main contributors to high voltage insulation failure are thermal and electrical stresses. The failures may be mitigated by using nanodielectrics. The enhanced effect of nanoparticles in nanodielectrics is attributed to an interaction zone/interphase around each individual nanoparticle between the nanoparticle and host polymer. However, particle clumping or agglomerates are a major challenge in nanodielectric technology.

There is therefore a need for non-intrusive methods of evaluating dispersion or distribution of particles to evaluate the quality of the nanodielectrics during synthesis. In this study, rheology was used to determine optimal filler loading level in the nanodielectrics investigated. This study attempts to add knowledge for transferring nanodielectric technology from the lab environment to bulk manufacturing.

The nanodielectrics in the study were developed using hexagonal Boron Nitride (BN) with a characteristic diameter of 80-90 nm and Carbon Nanospheres (CNS) with characteristic diameter of 80-180 nm in an epoxy (Araldite Cy 231-1 and Aradur Hy 931) polymer matrix.

A key conclusion from the rheology analysis was the postulation that the samples with optimal particle distributions (optimal level/optimal filler loading level) were concentrations within the hydrodynamic/colloidal interaction regions which were minimal in viscosity.

Below the optimal level, it is suggested that agglomerates were too far apart to make contact during mixing which prevented them from breaking into the nanoparticles. Above the optimal level, the agglomerated particles were not broken due to agglomerates already being in contact. In the present case, the optimal loading level would be 2.08/1.09 vol% to 2.59/1.35 vol% for BN particles in Araldite(resin)/epoxy (solid), and 0.7/0.33 vol% for CNS in Araldite/epoxy.

Various tests (microscopy, dielectric spectroscopy, electrical tree characterisation,

thermal expansion and laser flash analysis) were conducted to validate the rheological optimal filler loading levels of C/Epoxy and BN/Epoxy nanodielectrics developed in this study.

Atomic Force Microscopy (AFM) was used to investigate the properties of the interphase for the BN and CNS particles. By using AFM, the interphase around each nanoparticle was measured to be ~10-90 nm for CNS and ~130 nm for BN particles. The bulk DMT Young's moduli of the nanodielectrics approached that of the interphase. In the optimal region, the Boron Nitride particles provide a dramatic increase in mechanical stiffness by improving the Young's modulus from 1.7 GPa to ~55 GPa. The CNS particles provide slightly increased mechanical stiffness with Young's modulus of 4 GPa.

Dielectric spectroscopy was used to investigate the permittivity and conductivity from 40 Hz to 10 MHz at ~25 ^{o}C. The percolation threshold for CNS particles in Epoxy was established as 0.89 vol%. From the results, the optimal loading levels had an increase in permittivity at 50 Hz by 8 % and 5 % for BN/Epoxy and C/Epoxy respectively when compared to pure epoxy. Additionally, there was an increase in electrical resistance at 50 Hz by six times and 18 times for BN/Epoxy and C/Epoxy respectively.

Electrical tree tests were used to characterise the nanodielectrics and correlate the rheology results. The electrical trees grown in the nanodielectrics were analysed using AFM, X-ray computer tomography, partial discharges (PDs) and statistical analysis of the mean, variance, skewness and kurtosis of the PD data.

It is concluded that the extent of effectiveness of nanoparticles in suppressing the rate of electrical tree induced degradation is on the behaviour of the PD activity in the tree channels. And the physical characteristics of the channels in the nanodielectrics in comparison to that in unfilled epoxy. In that regard, for BN/Epoxy, 1.09 vol% to 1.35 vol% represent the optimal loading level region where PD activity is restricted to relatively short bursts that are interspaced by relatively long periods of no PD activity. Similarly, for C/Epoxy, the periodical PD bursts events occur only in 0.33 vol%

samples that also survived for relatively much longer periods compared to the higher loadings. It is remarkable that the optimal performance of 1.09 vol % to 1.35 vol% for BN/Epoxy and 0.33 vol% for C/Epoxy in electrical tree tests confirm the efficacy of the rheology tests. In the optimal samples, electrical tree channels characterised using X-ray computer tomography and AFM are shown to be larger for the nanodielectrics ~20 µm compared to pure epoxy ~6 µm.

From the electrical tree results, it is speculated that the CNS particles act as electron scavengers which remove electrons from the electrical degradation mechanism. By removing electrons and performing as capacitors, electrical trees are forced to go around the particles causing the path across to be increased and thereby retarding the tree process. With the Carbon Nanospheres, low concentrations are required to avoid the percolation threshold at 0.89 vol% and hence preventing the material from becoming a conductor.

In BN/Epoxy, the BN particles provide a significant increase in mechanical stiffness which raises the elastic moduli of the material. Hence it is difficult for electrical trees to propagate. It is postulated that when an electrical tree encounters a nanoparticle, the tree channel erodes the walls of the existing tree until there is sufficient energy before the channels continue. Therefore, there is an increase in the required energy for trees to propagate in both nanodielectric.

The epoxy used in this work is commonly used in high voltage applications such as cable joints. The thermal expansion of the optimally loaded nanodielectrics and pure epoxy was therefore analysed using cable joint temperatures of 25 ^{o}C to 250 ^{o}C. The results show that the rate of expansion for the optimally loaded C/Epoxy is higher than BN/Epoxy and pure epoxy for the entire temperature range. For C/Epoxy, the rate of thermal expansion is 146 %, 30 %, 8.2 %, 2.9 %, and 2.5 % higher than pure epoxy at 50 ^{o}C, 100 ^{o}C, 150 ^{o}C, 200 ^{o}C, and 250 ^{o}C respectively. For the BN/Epoxy, the rate of thermal expansion is 146 % and 13.3 % higher than pure epoxy at 50 ^{o}C and 100 ^{o}C

respectively. The BN/Epoxy rate of thermal expansion is then 1.13 %, 0.73 % and 0.9 % lower than pure epoxy for the remaining temperatures.

Laser flash analysis provided interesting results of the thermal conductivity for pure epoxy and the nanodielectrics. The epoxy is in crystalline and amorphous states at 100 ^{o}C and 200 ^{o}C respectively. The results show an increase in thermal conductivity at the glass transition temperature of 150 ^{o}C. At this temperature, the thermal conductivity was increased by from 0.17 W/(mK) to 0.48 W/(mK) for BN/Epoxy and 0.35 W/(mK) for C/Epoxy indicating an increase of ~180 % and ~105 % respectively.

This study has established a way to reproduce nanodielectric samples which will allow for quality assurance techniques to be established for nanodielectric manufacturing. One contribution is a rheology-based technique incorporated in the manufacturing process to determine the optimal filler loading of C/Epoxy and BN/Epoxy nanodielectrics. The efficacy of this method was validated using various microscopy analyses as well as electrical tree PD and dielectric spectroscopy analyses.

Dedication

To my family for all the love and support.

Acknowledgements

The first entity I would like to acknowledge is God for gifting me with immeasurable opportunities to fail and succeed. I certainly have learned that success and greatness cannot be achieved or appreciated without suffering. I would then like to acknowledge the first most important human, my mother Prof Laetitia Rispel, for unconditional love, support, and believing in me, and for trying to provide the things she never had as a poor coloured child in a backwater town in the middle of nowhere. Especially for teaching me the values of trying to make the world a better place in whatever small way you can.

I would then like to acknowledge my father, Dr. Edward Hank, for teaching me that sometimes words cannot be used to articulate or describe feelings, and secondly about the importance of forgiveness. I would then like to thank my baby sister, Ms. Nadine Hank, for looking up to me and being my partner in crime.

I wish to extend extensive thanks to my electrical engineering supervisor Prof. Cuthbert Nyamupangedengu, I still cannot write or say your surname without making a mistake. But thanks for entertaining my nonsense, calling me your enemy, talks about politics, philosophy but especially telling me to apply for the many bursary opportunities.

To my metallurgical supervisor Prof. Iakovos Sigalas, special thanks for allowing me to pick your brain for the chemical and metallurgical engineering knowledge and expertise and the invaluable feedback and comments on the various aspects of the work. Mr. Kerren Ortlepp thanks for being around to bounce ideas off and the general humour. You certainly are a special kind of friend. Special thanks to the Leeburn family, especially Dominic, for showing me the real-life applications of engineering, and the many pleasant memories. Thanks to Prof Ivan Hofsajer for the philosophy and social lessons, as well as being a cool first and fourth-year supervisor. To Dr. Richard

Candy for the many lessons, and being a role model. Finally, my Karate Sensei Jp Rodrigues for showing me the value of perseverance.

There are many other people who I would like to thank who have helped me get to this point, but special thanks to the financial institutions, the South African National Research Foundation (NRF) and Eskom for the Undergraduate and postgraduate studies. The INternational Science Promoting Innovation and entREpreneurship (INSPIRE) scholarship for the opportunity to go live and study nanotechnology in Sweden.

Table of Contents

Chapter 1 : Introduction 1

1.1 Introduction 1

1.2 Glossary 1

1.3 Background 2

1.4 Problem Statement 7

1.5 Research Questions 7

1.6 The Dissertation Structure 10

1.7 Conclusion 11

Chapter 2 : Insulation and High Voltage Engineering 13

2.1 Introduction 13

2.2 Glossary 13

2.3 Self-Healing Insulation Material 13

2.3.1 Air as an Insulation Material 14

2.3.2 Sulphur Hexafluoride as an Insulation Material 15

2.3.3 Mineral oil as an Insulation Material 15

2.4 Solid Insulation Materials 16

2.5 Solid Insulation Failure Mechanisms 18

2.6 Conclusion 22

Chapter 3 : Nanotechnology, History, Nature and The World 24

3.1 Introduction 24

3.2 Glossary 24

3.3 Background to Nanotechnology 25

3.4 Nanocomposites and Nanodielectrics 28

3.5 Nanodielectric Material Synthesis 31

3.6 Models used for explaining Nanodielectric Phenomena 33

3.6.1 The Intensity and Double Layer Model 34

3.6.2 The Multicore Model 36
3.6.3 Interphase Volume Model 37
3.6.4 Polymer Chain Alignment Model 40
3.6.5 New Barrier Model 42
3.6.6 Unified Permittivity and Thermal Conductivity Model 42
3.6.7 The Considerations when manufacturing a nanodielectric. 43
3.7 Conclusion 44
Chapter 4 : Rheology Incorporated Nanodielectric Synthesis 46
4.1 Introduction 46
4.2 Background 46
4.3 Choice of filler particle types 47
4.3.1 The Electron Microscope principle of operation 48
4.3.2 Identifying Boron Nitride 49
4.3.3 Identifying Carbon Nanospheres 50
4.3.4 Carbon nanosphere synthesis. 51
4.4 Tools for evaluating particle concentrations. 52
4.4.1 The principle operation of a Zetasizer 53
4.4.2 The principle operation of Rheology 53
4.5 Nanodielectric synthesis procedure 55
4.6 Verification of optimal filler loading using Scanning Electron Microscopy. 69
4.6.1 Sample preparation methodology 69
4.6.2 C/Epoxy SEM analysis 72
4.7 Conclusion 73
Chapter 5 : The AFM and Dielectric Spectroscopy characterisation of the C/Epoxy and BN/Epoxy Nanodielectrics 75
5.1 Introduction 75
5.2 Background 75
5.2.1 The principle of AFM 77
5.3 Atomic Force Microscopy characterisation of the interphase region of the nanodielectrics 78

5.3.1 AFM experimental methodology. 78
5.3.2 PF-QNM results and discussion..... 80
5.4 Dielectric Spectroscopy characterisation of the nanodielectrics. 88
5.4.1 The principle of dielectric spectroscopy..... 88
5.4.2 Dielectric spectroscopy sample preparation methodology 90
5.4.3 Dielectric spectroscopy measurement results and analysis 92
5.5 Conclusion 98
Chapter 6 : Electrical tree Behaviour in the C/Epoxy and BN/Epoxy nanodielectrics ..100
6.1 Introduction 100
6.2 Background 100
6.3 Electrical tree PD characterisation.....103
6.3.1 The electrical tree sample preparation.....103
6.3.2 Electrical tree Partial Discharge Time Evolution Analysis 106
6.4 PD phase-resolved-patterns and quantitative statistical analysis.....122
6.4.1 PDPRP experimental results and discussion 123
6.4.2 PD magnitude distribution statistical parameters (mean, variance, skew, and kurtosis) of the electrical tree PD in the nanodielectrics 133
6.5 Characterising electrical tree micro-tunnels in the nanodielectrics using XCT and AFM 137
6.5.1 X-ray Computer Tomography image analysis of the electrical trees. 138
6.5.2 Atomic Force Microscopy profiling of the electrical tree tunnels 143
6.6 Further Discussions 149
6.6.1 Carbon nanosphere retardation mechanisms. 149
6.6.2 Hexagonal Boron Nitride retardation mechanisms. 151
6.7 Conclusion 153
Chapter 7 Thermal Properties.....155
7.1 Introduction 155
7.2 Background 155
7.3 The Thermal Measurement Experimental Methodology 157

7.4 Thermal expansion and conductivity results and discussion.....161
7.5 Conclusion 166
Chapter 8 : Consolidation of results and future work. 168
8.1 Introduction 168
8.2 Interphase models discussions and possible enlightenments based on the findings of the present research work.....168
8.3 The effect of nanoparticles on electrical treeing.....174
8.4 Impact of this research.....176
8.4.1 The nanodielectric recipe using direct dispersion.....177
8.5 Recommendations for future work 178
8.5.1 Dispersion, Distribution and agglomeration necessities.....179
8.5.2 New particle types.....180
8.5.3 Continued work.....180
8.6 Conclusion 181
Chapter 9 Conclusion.....182
References 186

Appendix A Quantifying nanoparticle dispersion using rheological techniques in epoxy resin.
Appendix B Investigating the percolation threshold of Carbon/Epoxy Nanodielectrics using Dielectric Spectroscopy
Appendix C Partial Discharge grouping implementation.
Appendix D Statistical table of mean, variance, skewness and kurtosis of PD data.
Appendix E Electrical tree profiling in nanodielectrics using Atomic Force Microscopy.
Appendix F The criticality of filler loading in C/Epoxy and BN/Epoxy nanodielectrics.

List of Figures

Figure 1-1: Pie Chart of Cigré results for the main causes of generator failure [10].... 3
Figure 1-2: The relative interphase/interaction zone (10-25 nm) to sphere particle relationship shown for micro (1 µm-500 nm), submicro (500 nm-100 nm) and nano (100 nm-1 nm) spherical particles [19]. 5
Figure 1-3: Differences between particle distribution and dispersion in a matrix. (A) Shows poor dispersion and distribution, (B) shows good distribution but poor dispersion, (C) shows poor distribution but good dispersion and (D) shows good dispersion and good distribution [29]. 6
Figure 1-4: Flow diagram illustrating methodology applied in how optimally loaded thermally conductive nanoparticles in epoxy improve the electrical and thermal performance of epoxy. 9
Figure 2-1: Flow diagram showing basic epoxy manufacturing procedure [39]. 17
Figure 2-2: Chemical structure of complete polymer chain of Bisephenol-A epoxy adapted from [39]. The unimportant indicates repeats in the polymer chain..... 17
Figure 2-3: Flow diagram of postulated stages of solid insulation failure [1]–[3]. ... 20
Figure 2-4: Proposed by the author, a flow diagram illustrating a consolidated process of the start and end of the partial discharge and electrical tree process resulting in electrical insulation failure [1] – [3]. Note each stage will have increasing probabilities as electrons, ions and photon feedback occurs..... 21
Figure 2-5: Trapped electron gap theory indicating that electrons in the trapped sites of insulators have lower band gap energy requirements to get to the conduction band.. 22
Figure 3-1: Nelumbo Nucifera showing hydrophobicity properties, the full image of the flower on (left). Image of water droplets flowing on the surface of the leaf (right). Permission of use by T. Voekler under the Creative Commons License [51]–[53]. .. 26
Figure 3-2: Lycurgus cup showing reflected light effect (left) and transmitted light from inside/above the cup (right). The image is taken from British museum collection under the Creative Commons License [51]–[53]. 26

Figure 3-3: Images were taken by the author of the Nano-cathedral project in Pisa Italy as part of the Horizon 2020 project. Text left: “Nanomaterials for the conservation of European architectural heritage developed by research on characteristic lithotypes.” Image of author in Nano-cathedral (right) 27
Figure 3-4: Nucleation for solid and liquid phase transformations. The rate of nucleation is faster in heterogeneous systems compared to homogenous systems..... 28
Figure 3-5: Different Nano-filler shapes, the arrows indicate the possible directions for electron movement, 0D or particle (left); 1D, tube or wire (centre); 2D, flake or plane (right). Adapted from [9]..... 29
Figure 3-6: Illustration of the differences between exfoliated and intercalated particles in an insulation matrix (Adapted from [65]). 32
Figure 3-7: DLVO Theory which describes the force interactions of molecules and small particles, the double layer model (A) and DLVO model (B) [59], [67]..... 35
Figure 3-8: Intensity model by Lewis which describe how the interphase is a function of particle concentration or physical intensities [59]. 35
Figure 3-9: Multi-core model proposed by Tanaka et. al. showing the three different layers which represent the interphase on the left, the assumed face centred cubic crystal structure in the centre, Particle radius (a) and particle distance (D) on the right [60].36
Figure 3-10: Interphase volume model by Raetzke and Kindersberger showing homogeneously dispersed nanoparticles with the different interphases (A) shows the face centred cubic crystal structure, (B) shows the diagonal with particles sufficiently far away that they do not interact, (C) Shows the particles close enough that the interphases touch, (D) the interphases overlap, (E) the particles are in contact [61]..40
Figure 3-11: Polymer chain alignment model by Andritsch et. al. showing unorganised polymer chains on the left and organised polymer chains on the right [64]. 41
Figure 4-1: The generalised model used for TEM, FIB and SEM microscopes, note, a FIB has a SEM placed 45° to the sample stage [9]. 48
Figure 4-2: Image of received h-BN particle agglomerates showing a collection of rough h-BN particles with varying particle sizes confirming 80-90 nm, SEM on the left, TEM on the right..... 50

Figure 4-3: TEM image (A), particle size distribution (B), SEM image (C) of the synthesised CNSs. 52
Figure 4-4: Block diagram describing rheological analysis applications [76]..... 55
Figure 4-5: Typical flow characteristics of a material determined using rheology [38]. 55
Figure 4-6: Flow diagram showing an adapted form of the generic manufacturing procedure of Epoxy Nanocomposites. The open circle indicates the start and closed circle indicates the end of the process. 57
Figure 4-7: Nanoparticles in Araldite mixture before shearing of final sample batch, Carbon Nanospheres left and Boron Nitride right. 59
Figure 4-8: Dispermat AE high shear mixing device and Vacuum chamber used in nanodielectric synthesis. 59
Figure 4-9: Rheolab QC (A), Din Coaxial Cylinder (Bob CC27/p4478 and cup C-CC27) (B) and A schematic diagram of a Din Coaxial Cylinder measurement device with grooves used to measure rheological characteristics [38]. 59
Figure 4-10: Raw rheology results for the different volume fractions for BN/Araldite in (A) and with Viscosity in (B), the C/Araldite in (C) with the C/Araldite Viscosity in (D). 63
Figure 4-11: Rheology results showing the normalised rheology results at a shear rate of 100/s and different rheology regions with the C/Araldite results in (A) and the BN/Araldite results in (B). 64
Figure 4-12: Image of Araldite with hardener added showing discolouring for pure and BN/Epoxy before shearing. Note the hardener is denser than the Araldite and the crosslinking process has begun as seen by the small channels in the pure epoxy. 67
Figure 4-13: Image of C/Epoxy and BN/Epoxy during the shearing process..... 67
Figure 4-14: Images of bubbles being extracted in the samples after shearing, pure epoxy (left) BN/Epoxy (middle), C/Epoxy (right). 67
Figure 4-15: Aluminium moulds used for the manufacture of different epoxy samples with copper holders fitted with grub screws to hold needles for electrical tree experiments. 68

Figure 4-16: Aluminium moulds used to remove gas bubbles introduced from pouring the samples. 68
Figure 4-17: Image showing an example of final manufactured sample batch of pure Epoxy. 68
Figure 4-18: Image showing EDS investigation results of as received BN particles. 70
Figure 4-19: Backscatter SEM image of received Boron Nitride submicron particles. 70
Figure 4-20: SEM image of the pure epoxy after surface polishing showing solid sample surface with good surface binding. 71
Figure 4-21: Clean epoxy sample showing crater marks after 200 nm observations, spots of dust on the surface. 71
Figure 4-22: Sample surface comparison of different BN/Epoxy loading levels using SEM. 72
Figure 4-23: SEM image showing surface of 1.09 vol% BN/Epoxy nanodielectric (left) with individual and large clusters of particles well distributed and 0.55 vol% (right) BN/Epoxy nanodielectric with larger clumps of particles poorly distributed..... 72
Figure 4-24: SEM images of CNS particles (left) C/Epoxy with 2.78 % (middle) and 0.33 % (right). 73
Figure 5-1: The generalised principle operation of an Atomic Force Microscopy showing the cantilever interacting with sample force fields and sample surface[9]... 76
Figure 5-2: Top down view of AFM measurement operation details for Tapping mode, PF-QNM, and SVM. Å or Ångstrom is a unit of measure defined in Section 3.2. In tapping mode, the cantilever does not touch the sample surface. While in PF-QNM and SVM modes the cantilever is in direct contact. 76
Figure 5-3: Side view showing custom designed surface evolution using PF-QNM AFM on optimally loaded BN/Epoxy and C/Epoxy to establish particles, epoxy, and interphase. 80
Figure 5-4: PF-QNM Analysis at 600 nN on pure epoxy, surface height (left) and mechanical properties (right). 81

Figure 5-5: PF-QNM Analysis at 600 nN on C/Epoxy, surface height (1) and Young's modulus image (2), the lines of interest for section AB (3) showing mechanical properties, section BC (4) showing mechanical properties and section EF in (5) showing mechanical properties. 81
Figure 5-6: PF-QNM Analysis at 600 nN on BN/Epoxy, surface height (1) and Young's modulus image (2), the lines of interest for section AB (3) showing mechanical properties, and section BC (4) showing mechanical properties. 82
Figure 5-7: Surface Young's modulus evolution profile of C/Epoxy with the set points at 600 nN (A), 700 nN (B), 800 nN (C), 900 nN (D) and 1 000 nN (E), respectively. 83
Figure 5-8: Surface Young's modulus evolution profile of BN/Epoxy with the set points at 600 nN (left) and 700 nN (right). 83
Figure 5-9: Frequency response of permittivity mechanisms for different regions (adapted from [88]). 88
Figure 5-10: Agilent impedance analyser 4249A with the 16451B test fixture on left and on right the parallel plate capacitor model of the DS measurement method adapted from [93]. 90
Figure 5-11: BN/Epoxy and C/Epoxy samples prepared for DS before painting(left), painting technique of centre to the outside (middle), final sample (right). 91
Figure 5-12: Frequency spectrum of the real part of the complex permittivity in C/Epoxy nanodielectrics. The Solid vertical line indicates the Beta Relaxation Peak. 92
Figure 5-13: Frequency spectrum of the imaginary part of complex permittivity in C/Epoxy nanodielectrics. The Solid vertical line indicates the Beta Relaxation Peak. 93
Figure 5-14: Frequency spectrum of the electrical conductivity in C/Epoxy nanodielectrics. The Solid vertical line indicates the Beta Relaxation Peak. 95
Figure 5-15: Real permittivity showing the addition of BN/Epoxy and reproduced C/Epoxy optimally loaded sample. 96

Figure 5-16: Imaginary permittivity showing the addition of BN/Epoxy and reproduced C/Epoxy optimally loaded sample. The Solid vertical line indicates the Beta Relaxation Peak 96
Figure 5-17: Conductivity showing the addition of BN/Epoxy and reproduced C/Epoxy optimally loaded sample. The Solid vertical line indicates the Beta Relaxation Peak. 97
Figure 5-18: Sample resistance at power frequencies for the optimally loaded nanodielectrics and pure epoxy. 97
Figure 5-19: Sample permittivity at power frequencies for the optimally loaded C/Epoxy and BN/Epoxy nanodielectrics and pure epoxy. 98
Figure 6-1: Principle concept of how PD is generated, a threshold voltage in a cavity is exceeded, which causes ionisation in the cavity detected as current pulses [1] – [3]. 101
Figure 6-2: Sample configuration on left and test specimens for electrical tree experiments. 104
Figure 6-3: Test setup according to IEC 60270 on left and schematic circuit diagram on right used for Partial discharge analysis..... 104
Figure 6-4: Needle coupling facility to the high voltage source test rig showing failed epoxy and BN/Epoxy samples. 105
Figure 6-5: Image of needle coupling facility on left and on right the schematic diagram of the needle coupling facility to the high voltage source with edges spherically shaped to avoid corona. 105
Figure 6-6: Complete partial discharge magnitude time evolution of pure epoxy showing bush- branch characteristics in pure epoxy, sample 1 is bush-branch sample 2 is branch while sample 3 is bush. 107
Figure 6-7: Log-log graph showing the distribution of PD in pure epoxy sample 1 and 2 show branch-characteristics while sample 3 shows bush characteristics..... 107
Figure 6-8: Complete partial discharge magnitude time evolution of C/Epoxy showing bush- branch characteristics. 108
Figure 6-9: Log-log graph showing the distribution of PD in 0.33 vol% C/Epoxy.. 109

Figure 6-10: Complete partial discharge magnitude time evolution of 0.33 vol% C/Epoxy showing significantly suppressed discharges and repeatability of samples. 109
Figure 6-11: Log-log graph showing the distribution of PD in 0.33 vol% C/Epoxy and repeatability of samples..... 110
Figure 6-12: PDPRPs recorded every 20 minutes for the first four hours of the 0.33 vol% C/Epoxy. 110
Figure 6-13: Partial discharge magnitude time evolution of 0.89 vol% C/Epoxy showing semiconductor characteristics. 111
Figure 6-14: Log-log graph showing the magnitude distribution of PD in 0.89 vol% C/Epoxy. 111
Figure 6-15: Complete partial discharge magnitude time evolution of 0.26 vol% BN/Epoxy..... 112
Figure 6-16: Log-log graph showing the magnitude distribution of PD in 0.26 vol% BN/Epoxy..... 113
Figure 6-17: Partial discharge magnitude time evolution of 0.55 vol % BN/Epoxy. 113
Figure 6-18: Log-log graph showing the magnitude distribution of PD in 0.55 vol % BN/Epoxy..... 114
Figure 6-19: Partial discharge magnitude time evolution of 0.89 vol % BN/Epoxy. 114
Figure 6-20: Log-log graph showing the magnitude distribution of PD in 0.89 vol % BN/Epoxy..... 115
Figure 6-21: Partial discharge magnitude time evolution of 1.09 vol % BN/Epoxy. 115
Figure 6-22: Log-log graph showing the magnitude distribution of PD in 1.09 vol % BN/Epoxy..... 116
Figure 6-23: Partial discharge magnitude time evolution of 1.25 vol % BN/Epoxy verification sample. 116
Figure 6-24: Log-log graph showing the magnitude distribution of PD in 1.25 vol % BN/Epoxy verification sample. 117
Figure 6-25: Partial discharge magnitude time evolution of 1.35 vol % BN/Epoxy. 117

Figure 6-26: Log-log graph showing the magnitude distribution of PD in 1.35 vol % BN/Epoxy.....118
Figure 6-27: Complete partial discharge magnitude time evolution of 1.65 vol % BN/Epoxy.....118
Figure 6-28: Log-log graph showing the magnitude distribution of PD in 1.65 vol % BN/Epoxy.....119
Figure 6-29: Complete partial discharge magnitude time evolution of 1.96 vol % BN/Epoxy.....119
Figure 6-30: Log-log graph showing the magnitude distribution of PD in 1.96 vol % BN/Epoxy.....120
Figure 6-31: Complete partial discharge magnitude time evolution of 2.77 vol % BN/Epoxy.....120
Figure 6-32: Log-log graph showing the magnitude distribution of PD in 2.77 vol % BN/Epoxy.....121
Figure 6-33: Clean epoxy PDPRP evolution showing single erratic pulses with increasing partial discharge magnitudes for the first four hours. The numbering convention is also shown. 124
Figure 6-34: C/Epoxy 0.33 vol% showing predominantly small and quasi-uniform PD pulses a characteristic of bush tree types. 124
Figure 6-35: 0.89 % C/Epoxy sample 3 showing large tree channel magnitudes. These are characteristic of branch type trees. Images were taken every 30 seconds. 125
Figure 6-36: PDPRPs 0.25 vol% BN/Epoxy showing branch characteristics taken every 5 minutes. 125
Figure 6-37: PDPRPs for 0.55 vol% BN/Epoxy sample showing both branch and bush characteristics. 126
Figure 6-38: PDPRPs for 0.89 vol% BN/Epoxy showing region between bush and branch characteristics. 126
Figure 6-39: PDPRPs of 1.09 vol% BN/Epoxy showing bush-branch, mainly branch type characteristics and suppressed PD magnitudes. 127

Figure 6-40: PDPRPs for BN/Epoxy 1.25 vol% for first four hours showing suppressed PD magnitudes with branch like characteristics. 127
Figure 6-41: PDPRPs for BN/Epoxy 1.35 vol% for first four hours showing decreased PD magnitudes with bush characteristics. 128
Figure 6-42: PDPRPs of 1.65 vol% BN/Epoxy showing bush characteristics irrespective of magnitude. 128
Figure 6-43: PDPRPs of 1.96 vol% BN/Epoxy showing mainly branch type characteristics. 129
Figure 6-44: PDPRPs of 2.77 vol% BN/Epoxy showing continuously large PD magnitudes with mainly bush characteristics. 130
Figure 6-45: Different types of PDPRP corresponding to different types of electrical trees in pure epoxy. 130
Figure 6-46: Flow diagram showing a possible way of grouping the PD activity. Note, the data was filtered assuming according to the assumed average noise level of 0.5 pC. 132
Figure 6-47: PDPRP type variation predominance in BN/Epoxy as a function of particle filler loading level indicating an emphasis on the particular type of tree growth. 132
Figure 6-48: PDPRP type variation in C/Epoxy as a function of 0.33 vol% and 0.89 vol% against pure epoxy. 133
Figure 6-49: How mean, variance, skewness, and kurtosis inform changes to a Gaussian distribution. 134
Figure 6-50: Principle operation of X-ray computer tomography. 138
Figure 6-51: 3D rendered XCT image showing the gap between needle and plane of un-failed clean epoxy samples stressed for four hours. 139
Figure 6-52: 3D rendered image close to the needle tip showing small tubules vs large channels as characteristic of bush-branch trees. 140
Figure 6-53: 0.33 vol% C/Epoxy after 194 hours showing a void which is different to what has been expected from PD analysis. 140
Figure 6-54: 2D side view of void around needle tip in 0.33 vol% C/Epoxy. 141

Figure 6-55: Top down view of void around needle tip in 0.33 vol% C/Epoxy..... 141
Figure 6-56: Top down view of the void at needle tip in 0.33 vol% in C/Epoxy. 142
Figure 6-57: FEMM simulation of axis-symmetric results of the needle in pure epoxy. 142
Figure 6-58: FEMM axis-symmetric simulation of reconstructed void showing electric field distribution. 143
Figure 6-59: Sample preparation methodology to prepare samples after ageing, red/dashed line 2 mm from the base (a) expected sample surface from a bottom-up view (b), and side view of tree channel with possible slicing locations (c)..... 143
Figure 6-60: Micro-photography images of samples prepared for AFM analysis after electrical tree experiments showing discharge paths 0 % (A), BN/Epoxy samples (B) to (H) sequentially as 0.26 %, 0.55 %, 0.81 %, 1.09 %, 1.35 %, 1.65 %, 1.96 %, and 2.27%. The C/Epoxy samples (I) to (L) as 0.33 %, 0.84 %, 1.57 % and 2.78 %. 145
Figure 6-61: Polished sample surface of samples after polishing for AFM with Epoxy (left), 1.09 % BN/Epoxy (middle) and 0.33 % C/Epoxy (right). 145
Figure 6-62: Light microscope details of one of the sites investigated on the sample surface of Clean Epoxy (A), BN/Epoxy (B) and C/Epoxy (C) with a 100 µm length scale showing possible areas just before the needle tip. 146
Figure 6-63: AFM results showing tapping mode results (left), SVM results (middle) and 3D rendered image of an electrical tree channel and tubules in pure epoxy (right). 146
Figure 6-64: AFM results showing tapping mode results (left), SVM results (middle) and 3D rendered image of an electrical tree channel and tubules in BN/ epoxy (right). 146
Figure 6-65: AFM results showing tapping mode results (left), SVM results (middle) and 3D rendered image of an electrical tree channel and tubules in C/Epoxy (right). 147
Figure 6-66: Channel and tubule average measurement results of epoxy samples after electrical tree ageing. 148

Figure 6-67: Illustration of a possible explanation of electrical tree breakdown within BN/Epoxy for increasing loading levels from left to right, top to bottom. 152
Figure 7-1: Principle operation of dilatometer, a sample is placed between two clamps in a furnace and as the sample expands, the displacements on the clamps are measured. 159
Figure 7-2: Image of Orton dilatometer used to obtain thermal expansion measurements. 159
Figure 7-3: Laser flash analysis principle operation according to ASTM E 1461 160
Figure 7-4: Image of Flashline 3000 used to obtain thermal conductivity measurements. 160
Figure 7-5: Thermal expansion results for epoxy, 0.33 vol% C/Epoxy and 1.09 vol% BN/Epoxy. 162
Figure 7-6: Thermal conductivity results of epoxy and the nanodielectrics. 163
Figure 7-7: Specific heat results of epoxy and the nanodielectrics. 163
Figure 8-1: An adaption to the interphase volume model, agglomerates form before particles are in continuous contact. 172
Figure 8-2: An illustration of the different forces on an individual particle as particles concentration increases. Note the forces are labelled as $Fm, FDLVO, Fs$ for movement, DLVO and stokes respectively. 173
Figure 8-3: Proposed tree channel path model with pure polymer showing various channels paths for varying particle concentrations. 176
Figure 8-4: Flow diagram showing the nanodielectric recipe using direct dispersion. 178

List of Tables

Table 2-1: Chemical bond energies associated with epoxy resin [2]. 17
Table 3-1: Nanoparticles investigated thus far for nanodielectrics and nanocomposites [23], [59]–[64] 30
Table 4-1: Viscosity Shear time for 8 Wt % samples normalised to a shear rate of 100 $s-1$ 60
Table 4-2: Sample Details of Epoxy and Nanocomposites. Note 0 % is pure epoxy. 61
Table 4-3: BN/Araldite normalised Viscosity results at a shear rate of 100/s. 64
Table 4-4: C/Araldite normalised Viscosity results at a shear rate of 100/s. 65
Table 5-1: AFM properties of Epoxy and Nanodielectrics. 80
Table 5-2: Optimally loaded C/Epoxy and BN/Epoxy particle and interphase dimensions. 84
Table 5-3: Average Young's modulus results of C/Epoxy and BN/Epoxy for different applied forces. 84
Table 5-4: Average real part of complex permittivity values at different frequencies for C/Epoxy. 93
Table 5-5: Average imaginary part of complex permittivity values at different frequencies for C/Epoxy. 93
Table 6-1: Statistical summary of the Partial Discharge results for the different electrical tree samples when compared to pure epoxy. 136
Table 7-1: Thermal expansion dilation results at select temperatures. 163
Table 7-2: Laser Flash Analysis measurement results for the epoxy and nanodielectric samples. 164

List of Symbols

E_{max}	[kV/mm]	Maximum Electric Field
V	V	Voltage
r	[mm]	Needle tip Radius
d	[mm]	Gap distance
ΔG	[J]	Free energy
a	[m]	Particle Radius
ΔG_v	[J/m^3]	Free energy per unit volume
σ_{sl}	[J/m^2]	Particle Surface Free Energy
ε'	[F/m]	Real Permittivity
ε''	[F/m]	Imaginary Permittivity
ε_o	8.85×10^{-12} [F/m]	Permittivity of free space
t	[mm]	Thickness
A	[mm²]	Area
f	[Hz]	Frequency
ω	[rad/s]	Angular Frequency
σ	[S/cm]	Electrical Conductivity
P	[W]	Power
k	$[W/(mK)]$	Thermal Conductivity
dT	$[^oC]$	Change in Temperature
dx	[m]	Change in length
α	$5.6696\times10^{-8}[W/m^2K^4]$	Black body radiation constant
K	[K]	Absolute temperature
e	[dimensionless]	Emissivity
F	[N]	Force
$wt\%$	[wt%]	Weight percentage
ϕ	[vol%]	Volume fraction/percent
V_s	[m/s]	Particle settling velocity
η	[Pa.s]	Viscosity of a fluid
ρ	$[g/cm^3]$	Particle density
g	9.81 [m/s/s]	Gravitational constant
k_B	$1.38\times10^{-23}[m^2kg\ s^{-2}K^{-1}]$	Boltzmann constant
c	[J/(kg T)]	Specific heat
m	kg	Mass
Q	[J]	Energy

CHAPTER 1 : INTRODUCTION

"I am just a child who has never grown up. I still keep asking these 'how' and 'why' questions. Occasionally, I find an answer." – Stephen Hawking

1.1 Introduction

This chapter begins with a glossary of terms. The glossary is followed by a background of the relevant literature. The background in this chapter specifically focusses on contextualising the motivation and rationale behind this study. The background is followed by the problem statement and formulated research questions. A guide or 'road map' of the different chapters is then provided.

1.2 Glossary

1. *Insulation:* The function of insulation is to separate two points. In electrical systems, insulation is used to electrically separate points that are at different electric potentials and sometimes to provide mechanical separation. Insulation specifically for electrical applications is sometimes referred to as dielectrics. Dielectrics and insulation will be used synonymously throughout this document [1] – [3].
2. *Power System*: A power system is an interconnected electrical system comprised of generation, transport and the monitoring of supply and demand of electrical energy using the transmission and distribution systems. Power systems are required to maintain a stable supply of electricity from supplier to customers [4], [5].
3. *Power System Stability*: Power system stability is the ability of a power system to regain operating equilibrium after being subjected to a disturbance such that the power system remains intact [6]. For a power system to be stable it must have generators in synchronism and voltages at rated values with a good balance between supply and demand [7].
4. *High voltage:* High voltage (HV) refers to voltage levels at least greater than 1 kV and is subject to the environment [1]–[3]. Some definitions break high voltage into 600 V- 69 kV, 69 kV – 230 kV, 230 kV – 1 100 kV and >1 100 kV as Low Voltage, Medium Voltage, High Voltage, Extra High Voltage, and Ultra High Voltage.

5. *Discharge*: A point at which electrical stress causes damage to any type of insulation material that may ultimately compromise power system stability [1], [2]. This may be partial as seen with corona or complete with electrical arcing such as lightning.
6. *Ionisation*: A path created by a discharge which allows for continuous discharges to take place [1]–[3].
7. *Electrical tree:* An electrical tree is a form of solid insulation degradation which ensues under high electric fields. It is made of occurs as a cumulative process of small discharges which cause a tree shape to form [1]–[3].
8. *Composite*: Mixture or combination of at least two nano – or macro-constituents which differ in form and chemical composition, and which are essentially insoluble in each other [8]. A basic example of a composite would be a cappuccino which is made of milk, sugar, coffee and water.
9. *Filler/additive:* A filler or additive refers to a type of particle added to insulation to create a composite.
10. *Agglomerate:* A collection of particles held together by van der Waals forces[9].
11. *Surface conditioning/functionalisation:* Chemically changing the surface properties of particles to facilitate agglomeration or separation of particles [9].

1.3 Background

ESKOM in South Africa along with power system utilities globally require lower operational costs to maintain power system stability. One of the major contributors to increased operational cost is insulation failure [10]–[12]. In 2003 the Council on Large Electric Systems (Cigré) published a study on the causes of failure in 76 hydro generators, and this is summarised in Figure 1-1 [10]. While insulation has been engineered to last for decades, the statistics highlight that failure of insulation (dielectrics specifically for electrical applications) plays a major role in the failure of generators, motors, transformers, cables and other electrical equipment [13], [14]. When electrical equipment fails, the power system stability is compromised which may in certain situations result in loss of electrical supply and a worst case scenario may be a potential countrywide blackout.

There have been previously two generations of insulation material [15]. The first generation, based on natural materials like wood and marble, was in the early 20th

century [15]. The second generation, based on polymer materials, was introduced in the 1950s and still widely used in modern insulation [15].

Two of the insulation failure modes in Figure 1-1 are attributed to poor heat transfer and electrical degradation [11], [12]. In solid insulation, inefficient heat transfer in certain areas of insulation results in hot spots which cause deformation of the insulation [11]. One possible result of insulation deformation is the creation of gas cavities within the insulation [12], [16]. These deformations coupled with high voltage cause electrical stress resulting in either gas discharges and/or cause electric field enhancement. The discharge process will be explained in detail in the next chapter.

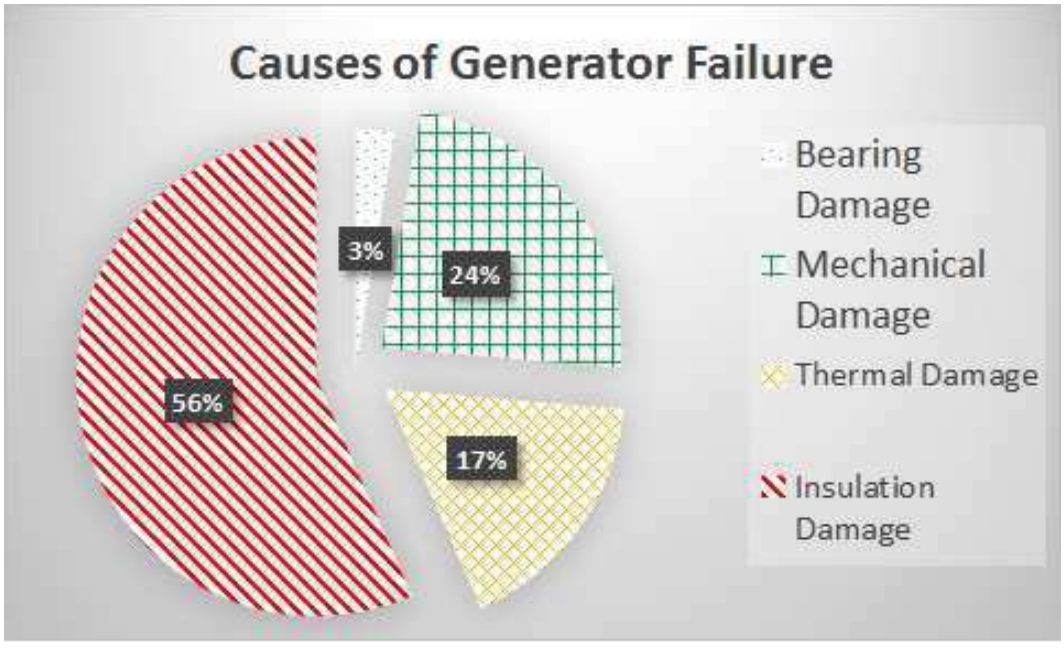

Figure 1-1: Pie Chart of Cigré results for the main causes of generator failure [10].

Gas discharges in cavities lead to the formation of ions, high energy electrons, and radicals which barrage the insulation walls of the cavity and eventually forms pits [12], [16]. The pit further enhances the electric field which grows an electrical tree. Once the electrical tree has grown a sufficient length it forms a bridge through the insulation between points of high voltage and ground potential [12], [16]. This bridge leads to complete insulation failure in the form of catastrophic destruction of the associated electrical equipment [16]. A common occurrence of this is found

in transformer windings and is usually caused by water getting into the insulation oil. When mixed with carbon in the oil the breakdown of the insulation is exacerbated [16]. Electrical trees are evidence of a cumulative and irreversible process which leads to failure in solid insulation [12]. **It is therefore required to improve the performance of electrical insulation which may possibly be achieved through nanocomposite polymer materials.**

Lewis [17] suggested in 1994 that for insulation to be significantly improved, the size of particle additives needed to decrease to the nanoscale and then added to insulation material. Micro, submicro and nano-spherical particles are illustrated in Figure 1-2 which in certain situations allow for electrical, chemical, thermal and mechanical properties of insulation to be strengthened [18]. Microparticles have already been widely used in silicon rubber based insulation, but in certain polymers, microparticles performed as defects and did not find many new applications [1]–[3].

There are three kinds of fillers/particles/additives, "particles, plates, and fibres," which will be discussed in detail in Chapter 3 [19]. The characteristic particle size (explained in detail in Chapter 3) are 1 μm to 500 nm, 500 nm to 100 nm, and 100 nm to 1 nm for micro, submicro, and nanoparticles respectively [19].

The benefits by the addition of nanofillers are firstly attributed to the high surface area to volume ratio (small amounts have large effects), and secondly to an interaction zone/interphase which has been assumed to be between 10-25 nm [19], [20]. While the mechanical and civil properties of composite materials have been relatively well investigated, the electrical and thermal improvements have not been researched extensively [18].

In the late 20th century, ASEA Brown Boveri (ABB) was the first to demonstrate that the thermal conductivity of machine winding insulation could be doubled by the use of aluminium oxide powder [21]. In light of these developments, as the particle size decreased, the overall improvement to the insulation increased because of the interphase changing the properties of the insulation around the particles [16], [22].

Submicro and nanoparticles have given significant improvement effects due to the

large ratio of the interphase to particle size; provided there is a good distribution and dispersion of the submicro/nanoparticles when compared to microparticles [19], [23]–[28].

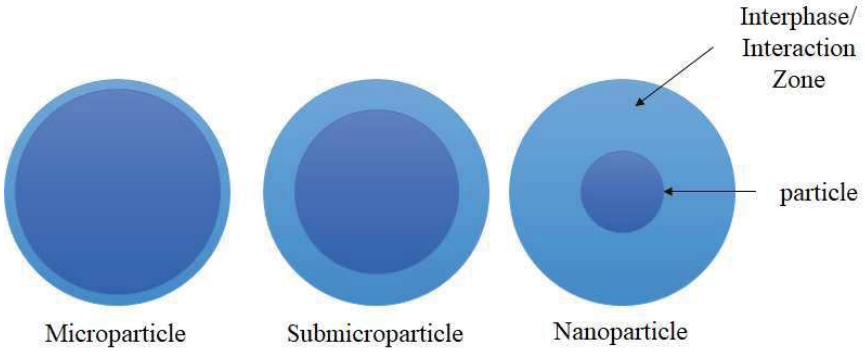

Figure 1-2: The relative interphase/interaction zone (10-25 nm) to sphere particle relationship shown for micro (1 µm-500 nm), submicro (500 nm-100 nm) and nano (100 nm-1 nm) spherical particles [19].

Dispersion refers to the extent to which individual particles are separated from each other, and distribution refers to the spreading of particles/groups of particles inside the insulation [26], [29]. The differences between dispersion and distribution are shown in Figure 1-3 [29]. At the submicro/nanoscale, the intermolecular van der Waals forces are relatively strong which may cause the particles to form particle clumps or "agglomerations" [23], [30]. Currently, it is believed that agglomerations of submicro/nanoparticles compromise the insulation performance because they create deformations [17], [21], [28], [29]. Alternatively, the overall insulation behaves at best like a system filled with microparticles when using non-conductive particles [19], [23], [30], [31].

When the particle – insulation interaction is relatively weak, it is significantly easier for agglomerates to form [24]. The agglomerates present in the insulation create poor interfaces between the insulation and the filler particles [32]. There is currently no comprehensive method of preventing agglomerations, however, homogenous dispersion (possibly achieved by chemically modifying the particle surface) of filler particles in the insulation is the current suggested approach (Figure 1-3 (D)) [24].

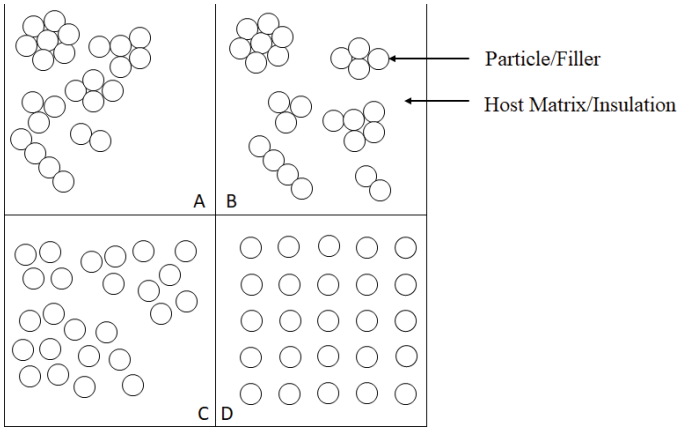

Figure 1-3: Differences between particle distribution and dispersion in a matrix. (A) Shows poor dispersion and distribution, (B) shows good distribution but poor dispersion, (C) shows poor distribution but good dispersion and (D) shows good dispersion and good distribution [29].

Research has however shown that by chemically modifying the surface of the particles the dispersion can be improved because a layer of the interphase is filled and the strength of the intermolecular forces among the submicro and nanoparticles decreases [23], [25], [33]. Without regard to the long-term effects of surface modification/conditioning; surface modification is being used extensively in nanodielectric manufacturing [34], [35]. If the layer of surface modification is too thick it may become an area where hot spots develop which contribute to thermal deformation [34], [35]; a decrease in the permittivity of the insulation has been attributed to the surface modification of the particles and immobilisation at the interface between particle and insulation [26], [30], [36].

Currently, electron microscopy techniques are used to evaluate dispersion and distribution of particles in different kinds of polymers (matrices), but these methods rely on the sample being manufactured first and can only provide information on the sample surface [12], [19], [24], [37]. There are indirect techniques for characterising the composite dispersion such as using visible light, depth mapping, X-ray diffraction, Fourier transform infrared spectroscopy, and the rheology characteristics to observe liquid flow behaviour [12], [19], [24], [37]. The alternatives to microscopy have been rarely used with regard to composite

insulation systems which therefore would be worth investigating.

1.4 Problem Statement

Two of the main contributors to high voltage insulation failure are thermal and electrical stresses. This failure may be avoided by improving the insulation quality through the addition of nanoparticles during the manufacturing process. The nanoparticles selected would need to improve the electrical and thermal properties. However, due to strong intermolecular forces on the nanometre scale, the particles clump together or agglomerate and cause defects to form. The problem is that there is not a comprehensive non-intrusive method of evaluating dispersion/distribution of particles in evaluating the quality of the nanodielectrics as in situ quality of control of the manufacturing process. Although rheology has been used extensively for polymer research and nanocomposites, there is little evidence of application in the development of nanodielectrics. Secondly, in search of thermally conductive insulation, the focus has been on the use of ceramic/electrically inert particles other than electrically conductive particles such as carbon variants. In order to address these problems, research questions were formulated as presented in the next section.

1.5 Research Questions

The focus of this dissertation is on the use of nanosized-fillers for the improvement of electrical insulation systems. The nanoparticles selected were based on high thermal conductivity properties. There was an attempt to not compromise the electrical insulation properties. The developed insulation was intended to use known good thermally conductive particles to provide good thermal conductivity properties while maintaining or improving the electrical properties. The key electrical property investigated is the ability to retard or inhibit electrical tree growth. This research was broken up into many areas in order to determine how thermally conductive nanoparticles can be used to improve electrical insulation. This research was guided by the desire to address the following research questions:

1. How can rheology be used as an alternative to microscopy techniques in evaluating the distribution and/or dispersion of particles in a matrix?
2. How do different concentrations of two different types of thermally

conductive nanoparticles [Carbon Nanospheres (C) and Boron Nitride (BN)] affect the electrical and thermal properties of the resultant nanodielectric?

3. What are the optimal loading levels of particles for C/Epoxy and BN/Epoxy that give optimal electrical and thermal performance if they can be determined?

The experimental investigation methodology used to address the research questions is illustrated graphically in Figure 1-4. These are summarised as developing a hypothesis that an optimal loading level exists for particle concentration. This may be determined through rheology and validated with microscopy and electrical characterisation techniques. Upon establishing the optimal loading level, further analyses on the synthesised nanodielectrics provided further insight into other nanodielectric parameters. After consolidating the various results, the conclusions drawn. A correlation between nanoparticle performance and concentration was also determined.

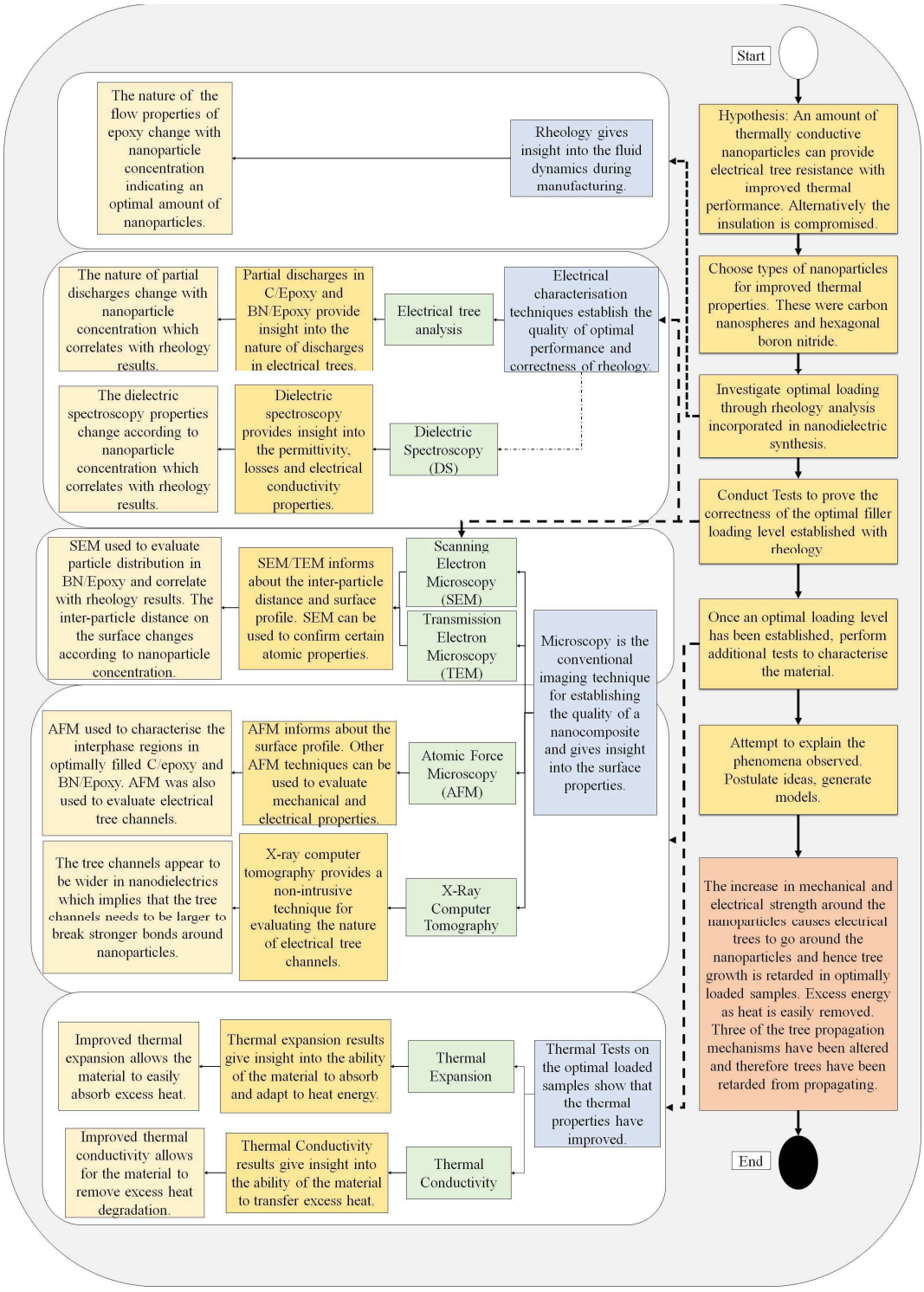

Figure 1-4: Flow diagram illustrating methodology applied in how optimally loaded thermally conductive nanoparticles in epoxy improve the electrical and thermal performance of epoxy.

1.6 The Dissertation Structure

In Chapter 2 different types of high voltage, insulation is discussed. The conventional understanding of the dielectric problems is highlighted. Special focus on partial discharges and electrical trees are introduced and are followed by a proposal of an "electrical tree process," model based on literature. Chapter 3 discusses nanotechnology broadly; with examples from history, nature, and applications in modern society. The different methods of manufacturing nanodielectrics are discussed in line with the conventional theory of modelling required for these new insulation materials.

Chapter 4 presents the nanodielectric synthesis process. It starts with a discussion on the particle choices and considerations. This is followed by an introduction to rheology as a possible alternate technique to understanding nanodielectrics. A general understanding of microscopy with the operation, understanding, and limitations of the various microscopy techniques is then provided. Particular focus is given to Scanning and Transmission Electron Microscopy (SEM/TEM). The nanodielectric manufacturing process is then described in detail. Some of the microscopy and rheology analyses results of the materials are then provided. The rheology results firstly showed a possible optimal loading level based on particle concentration. The first part of correlation was established using SEM and was published in the International Symposium of High Voltage Engineering in 2015 and is included in Appendix A.

Chapter 5 highlights the nanodielectric characterisation techniques. Particular focus is given to two characterisation techniques. The first, Atomic Force Microscopy (AFM) was used to characterise the interphase in optimally filled nanodielectrics. The second, dielectric spectroscopy was used to evaluate the permittivity and conductivity of the C/Epoxy and optimally filled BN/Epoxy. Part of the dielectric spectroscopy was published in the South African Universities Power Engineering Conference (SAUPEC) 2017 and is included in Appendix B.

Chapter 6 reviews electrical tree degradation in solid insulation. Electrical tree partial discharges (PD) were used to evaluate the electrical trees. The PD analyses

provided the second validation of the optimal loading levels. The PD data was also analysed using statistical techniques and the implementation of the code can be found in Appendix C with the corresponding statistical tables in Appendix D. The electrical trees were imaged using X-ray computer tomography (XCT) and AFM of the optimally developed nanodielectrics. The AFM analysis of electrical trees was accepted for publication in SAUPEC 2017. This is included in Appendix E. The unpublished parts of Chapter 4, 5 and 6 are under review by IEEE and are included in Appendix F.

Chapter 7 introduces the different methods of heat transfer and discusses the heat characterisation of optimally filled nanodielectrics based on thermal expansion and thermal conductivity. The thermal expansion and thermal conductivity of the synthesised nanodielectrics are then provided.

Chapter 8 consolidates the results and discusses the evidence generated in the study in line with the methodology (Figure 1-4). Two models which attempt to explain the nanodielectric phenomena observed are proposed, the first model is a force model which builds on an existing nanodielectric model to describe some of the dynamics of the nanoparticles during manufacturing, the second is a model to describe the effect of nanoparticles on the electrical tree process. The future work and recommendations are also presented. Chapter 9 presents the conclusion to the dissertation.

1.7 Conclusion

In this chapter, a brief contextualisation of some challenges faced by power utilities such as lower operational costs and hydro generator insulation problems was provided. Some nanoparticle characteristics were presented and the corresponding challenges of dispersion and distribution. The problem statement and corresponding research questions were then presented. In summary, firstly, using rheology as a non-intrusive method of evaluating nanoparticle dispersion/distribution may be an alternative to microscopy. Secondly, by investigating nanoparticle concentration for Carbon and Boron Nitride variants, how are the electrical and thermal properties affected and does an optimal concentration exist? The experimental methodology

and a guide for the following chapters were then presented. Chapter 2 gives a review of different types of insulation systems in high voltage applications.

CHAPTER 2 : INSULATION AND HIGH VOLTAGE ENGINEERING

"Right, and wrong are not what separate us and our enemies. It's our different standpoints, our perspectives that separate us. Both sides blame one another. There's no good or bad side. Just two sides holding different views." – Squall Leonhart

2.1 Introduction

Insulation materials are the backbone of electrical equipment and power systems as they allow for safe electrical energy transmission [15]. As established in the previous chapter, while insulation is the backbone of a power system, it is also the fundamental weak point. Therefore, this work aims to address some of the shortfalls in electrical insulation. This chapter review's insulation material in a broad sense of high voltage engineering applications. "Self-healing," and solid insulation will be discussed [1]–[3]. The discussions include the modern use, manufacturing, and some failure mechanisms in the different insulation materials, highlighting the entry of nanodielectrics in insulation technology.

2.2 Glossary

1. *Self-healing insulation*: A material, mainly liquid or gas, that may chemically recover to an initial state after an electrical discharge/breakdown event [1], [2].

2.3 Self-Healing Insulation Material

In order to address some of the societal needs such as electricity delivery which enables cooking, and manufacturing, insulation has gone through three main development evolutions [15]. The first insulation materials such as wood and rubber were used but could not meet growing electrical demands. The second generation of insulation based on polymers allowed for increased electrical supply demands.

Modern society has new challenges in various technology industries which have been discussed briefly by Li *et. al.* [15].

For the modern and future electrical industry, Li *et. al.* [15] highlighted electrical insulation problems which are categorised into five main areas. *High specific energy* materials for capacitors and batteries to be used in renewable energy applications. *Higher electric field sustainability* for space charge accumulation and faster polarity reversal applications. *Reusable, sustainable and environmentally friendly* technology which can replace second generation polymer insulation. *Improved thermal* insulation which enables improved motor, generator and breaking capacities; this insulation may also be useful for high-speed trains and electric cars. Lastly, advancements in spacecraft technology call for the development of insulating materials with *greater radiation resistance and better space charge dispersion*. Hence there has been working interest into the development of the third generation of insulation materials termed nanodielectrics.

In developed economies, the challenges for electrical industries currently relate to the desire or use of renewable energy, while in developing economies the challenges are based on the lack of access [2], [15]. In South Africa, both challenges are faced. With increasing population sizes, an increasing demand for electricity, and a need to transport electricity effectively and efficiently over long distances; it has become necessary to utilise HVAC and HVDC transmission technologies [1]–[3]. Within the HVAC transmission system, the two examples of gaseous self-healing (explained in the glossary) electrical insulation are air and sulphur hexafluoride (SF_6).

2.3.1 Air as an Insulation Material

The main insulation used in overhead HV transmission lines is air, as a type of self-healing insulation. However, in the future, given the lack of the aesthetic appeal of overhead HV transmission lines as dictated by society [1]–[3], increased electrical supply will likely be provided through the use of underground HV cables. Regardless, the benefit of air is the relatively abundant supply despite the breakdown dependence on humidity, pressure, and temperature.

Specifically with transmission line applications, when the air around a conductor is compromised, faults may occur which interrupt the supply of electricity and hence power system stability [1]–[3]. This insulation failure, apart from changes in air conditions, may be a result of contaminants such as smoke from the fire, rain, or bird excrement [1]–[3]. The contaminants either change the electric field around the conductor and/or create short circuit paths.

2.3.2 Sulphur Hexafluoride as an Insulation Material

The SF_6 gas is electronegative, and mainly used in gas insulated switch gear (GIS) systems [1]–[3]. The main benefit of SF_6 is when a free electron collides with an SF_6 molecule, two reactions may take place as shown in Equation (2-1) [1]–[3]. The negative ions generated under GIS electric field conditions do not allow for a continuous ionisation process to occur and provide a means to remove free electrons [1]–[3].

$$SF_{6(g)} + e^- \rightarrow SF^-_{6(g)}$$
$$SF_{6(g)} + e^- \rightarrow SF^-_{5(g)} + F^-_{(g)} \quad (2\text{-}1)$$

Compared to air, SF_6 has a dielectric strength 2-3 times greater, and better heat dissipation properties [1]–[3]. There are several downfalls to SF_6. The first is if concentration levels are compromised, beyond a particular level it may become a liquid, which may be undesirable [1]–[3]. Secondly, SF_6 is a greenhouse gas and hence an environmental concern. Cigré is currently pursuing alternatives to SF_6. However, for most conditions SF_6 performs comparably with transformer oil [1]– [3].

2.3.3 Mineral oil as an Insulation Material

Mineral oil is an example of a liquid insulation system obtained by fracturing crude oil. It has been widely used in transformers due to its heat dissipation and high dielectric strength properties [1]–[3]. In the event of a transformer exploding, apart from compromising power system stability, mineral oil impacts negatively on the environment [1]–[3]. Some problems with mineral oil include that they are non-

renewable, non-biodegradable, and flammable. There are now efforts to pursue insulation oil (Ester oil) developed out of plant based products which may replace mineral oil [15]. The current downfall with Ester oils is the very small voltage threshold between partial discharge inception and streamer breakdown.

In certain situations, such as with underground or undersea cables, generator winding insulation, and motors, it is not possible to use self-healing insulation. Therefore, there is a need for solid insulation materials.

2.4 Solid Insulation Materials

There are various types of solid insulation systems such as wood, ceramics, plastics, and glass [1] – [3]. In order to address higher voltage requirements and improved thermal conductivity as highlighted by Li and Cigré, epoxy is a common solid insulation material. Epoxy, a type of plastic, finds uses in generators, switchgear, and bushings, it has high malleability and relative ease of manufacturing compared to other types of insulation systems.

Epoxy is a versatile solid insulation material which finds many applications from low voltage electronic applications up to high voltage applications in the region of ~100 kV. In general, epoxy is obtained by combining two parts, a resin, and a hardener. A basic epoxy manufacturing process is shown in Figure 2-1. Bisephenol-A epoxy is medium-high-voltage (MV) type of epoxy mainly used in 10-50 kV applications [38], [39].

Bisephenol-A epoxy is made from Araldite (resin) and Aradur (hardener). The complete chemical structure of Bisephenol-A epoxy, once the resin and hardener have crosslinked, is shown in Figure 2-2 [39]. The associated chemical bond energies of epoxy are provided in Table 2-1 [39]. Note that while in Figure 2-2 dashed lines are used, they do not indicate changes in bond type, they are assigned based on the bond energies and breakdown order shown in Table 2-1.

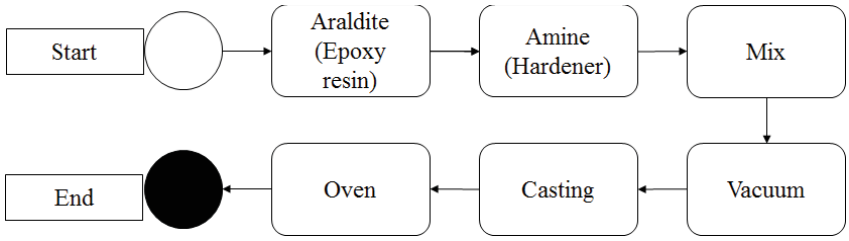

Figure 2-1: Flow diagram showing basic epoxy manufacturing procedure [39].

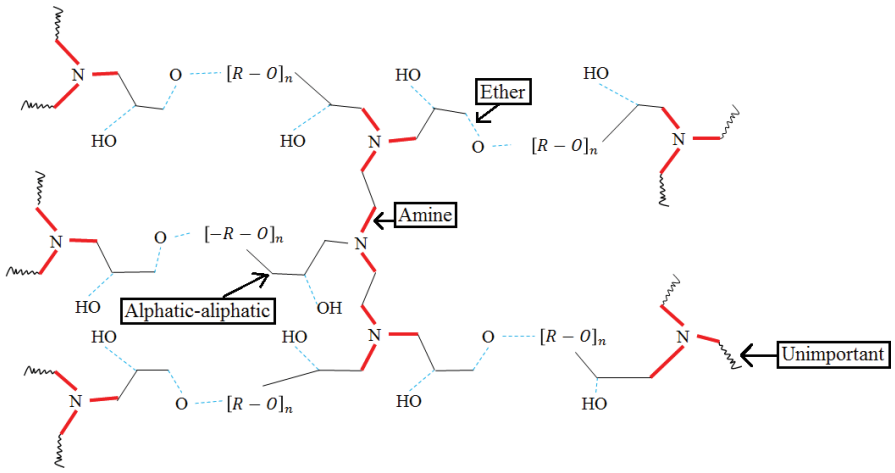

Figure 2-2: Chemical structure of complete polymer chain of Bisephenol-A epoxy adapted from [39]. The unimportant indicates repeats in the polymer chain.

Table 2-1: Chemical bond energies associated with epoxy resin [2].

Bond Type	Group structure	Energy (kJ/mol)	Probable bond Scission Order
C-H	aromatic	435	Resin only
C-H	**methyl**	**410**	**5**
C-H	**methylene**	**400**	**4**
C-O	**Ether**	**331**	**2**
C=O	Ketone	729	N/A
C-C	**Aliphatic-aliphatic**	**335**	**3**
C-C (aromatic chain)	Aromatic-aliphatic	347	Resin only
C-N	**Amine**	**305**	**1**
O-H	**Hydroxyl**	**424.4**	**6**

As with self-healing insulation, there are also challenges with solid electrical insulation systems. These may be poor heat transfer, imperfect manufacturing, or various degradation mechanisms. The following section discusses some of the electrical degradation mechanisms.

2.5 Solid Insulation Failure Mechanisms

Assuming there are no contaminants or air cavities trapped in the solid insulation, the failure of solid insulation under electric stress is characterised by molecular bond scission under the influence of high energy electrons, ions and photons [1]–[3]. This process of bond scission has several stages illustrated in Figure 2-3. A seed electron under high electric field conditions causes bombardment and destroys the insulation. The form the destroyed region takes is that of a tree and hence has been termed "electrical tree." The electrical tree grows and bridges points between a high voltage and ground potential and therefore causes complete insulation destruction [1]–[3].

Electrical trees which are currently postulated as the processes followed in solid insulation is illustrated in Figure 2-3 and Figure 2-4 [2], [33], [40]. Currently, there are two theories [1]–[3], based on quantum mechanics, which attempt to explain how electron initiation takes place [1]–[3]. These theories are "cathode/anode (metallic) emission," or "shallow trapped electrons [1]–[3]." These theories also assume that an insulator was manufactured perfectly [1]–[3].

The first theory claims that under high electric field conditions (common with high voltage), electrons are ejected from a metallic surface, purely based on the electron cloud surrounding metals, and the process of Figure 2-3 follows. The second theory, shown in Figure 2-5, claims that during the polymer insulation manufacturing process while cross-linking takes place, electrons are trapped between the conduction and valence bands in an insulator in trap wells (see Figure 2-5). Under a high electric field, any electrons in the trapped sites enter the conduction band, and the process of Figure 2-3 follows.

Once electron initiation has occurred, photons have been detected as

electroluminescence which has preceded any type of partial discharge activity [41]. Champion *et al.* [42] showed that for a needle-plane setup in an epoxy matrix, different trees would grow in epoxy samples that depended on the voltage applied. Dissado consolidated the results of understanding electrical trees in polymeric insulation [43]. Equation (2-2) allows for the voltages determined from Champion *et al.* [42] to be compared to changing experimental setups. There are three main categories of electrical trees termed: branch, bush-branch and bush type trees with corresponding RMS electric fields of ~0.9 MV/mm, ~1.1 MV/mm and 1.3 MV/mm respectively.

Once partial discharges are detected, several processes take place which is assumed to correlate with the partial discharge activity and are indicated in the flow diagram in Figure 2-4 [1] – [3]. The main processes which take place are mechanical crack formation as results of chemical bond scission, electron, and ion bombardment, gaseous pressure builds up, and photon emission detected through electroluminescence as the solid insulation is broken down into its principal gaseous components.

Given literature in [1] – [3], electrical tree types by Champion *et al.* [42], and bond energies are given in Table 2-1 there is a possible explanation for the electrical tree shapes produced. If the growth of an electrical tree was only a function of the electric field in a needle-plane setup, at lower electric field strengths, certain bonds do not experience scission, which gives the appearance of a branch type tree. As the electric field increases, locally around the needle tip, more bonds experience scission because the electrons in the system have more energy, and hence a bush-branch tree grows. Further increase in the electric field, has a larger localised electric field which causes a larger full bush than bush-branch. Beyond the bush-tree electric field level, the insulation cannot withstand the electric field stress and hence there is complete insulation breakdown. This insulation breakdown point has been termed dielectric breakdown and the ability to withstand dielectric breakdown is the dielectric strength.

$$E_{max} = \frac{2V}{r \ln\left(1 + \frac{4d}{r}\right)} \quad (2\text{-}2)$$

Where:

- E_{max} is the maximum applied electric field (kV/mm).
- V is the applied RMS voltage (kV).
- r is the needle tip radius (mm).
- d is the gap distance (mm).

With particular reference to epoxy, once the discharges cause epoxy bond scission and the possible gaseous formation of principle atom components, it is assumed that the discharge mechanisms in the resultant gaseous environment take place shown in equation (2-3) [2]. The significance of process (2-3) is the formation of ozone, nitrous gas, and nitric acid. If this is the case, there would be assisted acidic degradation in the tree channels. Other reactions which may take place are the formation of carbon monoxide, carbon dioxide, water vapour as with any combustion reaction. Additionally, tracking experiments have found evidence of the carboxylic acid formation with a type of epoxy [44]. Research within Cigré to further understand the products generated during the electrical treeing process is ongoing.

Electrical treeing (the growth of electrical trees) is the ultimate failure mode of solid polymer insulation. Therefore, the resistance to electrical treeing inherently becomes a key performance parameter for solid polymer insulation. The resistance to electrical trees may be achieved by increased mechanical stiffness which would prevent crack formation. Alternatively, electrical trees are essentially driven by stray electrons, ions, and photons. Hence, if nanoparticles which are considered electron scavengers are used, the electrical treeing process may be retarded. A choice of nanofiller in developing a nanodielectric, therefore, relies on the ability to provide additional mechanical support and the ability to remove additional electrons.

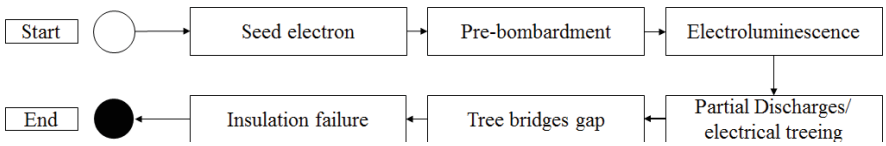

Figure 2-3: Flow diagram of postulated stages of solid insulation failure [1]–[3].

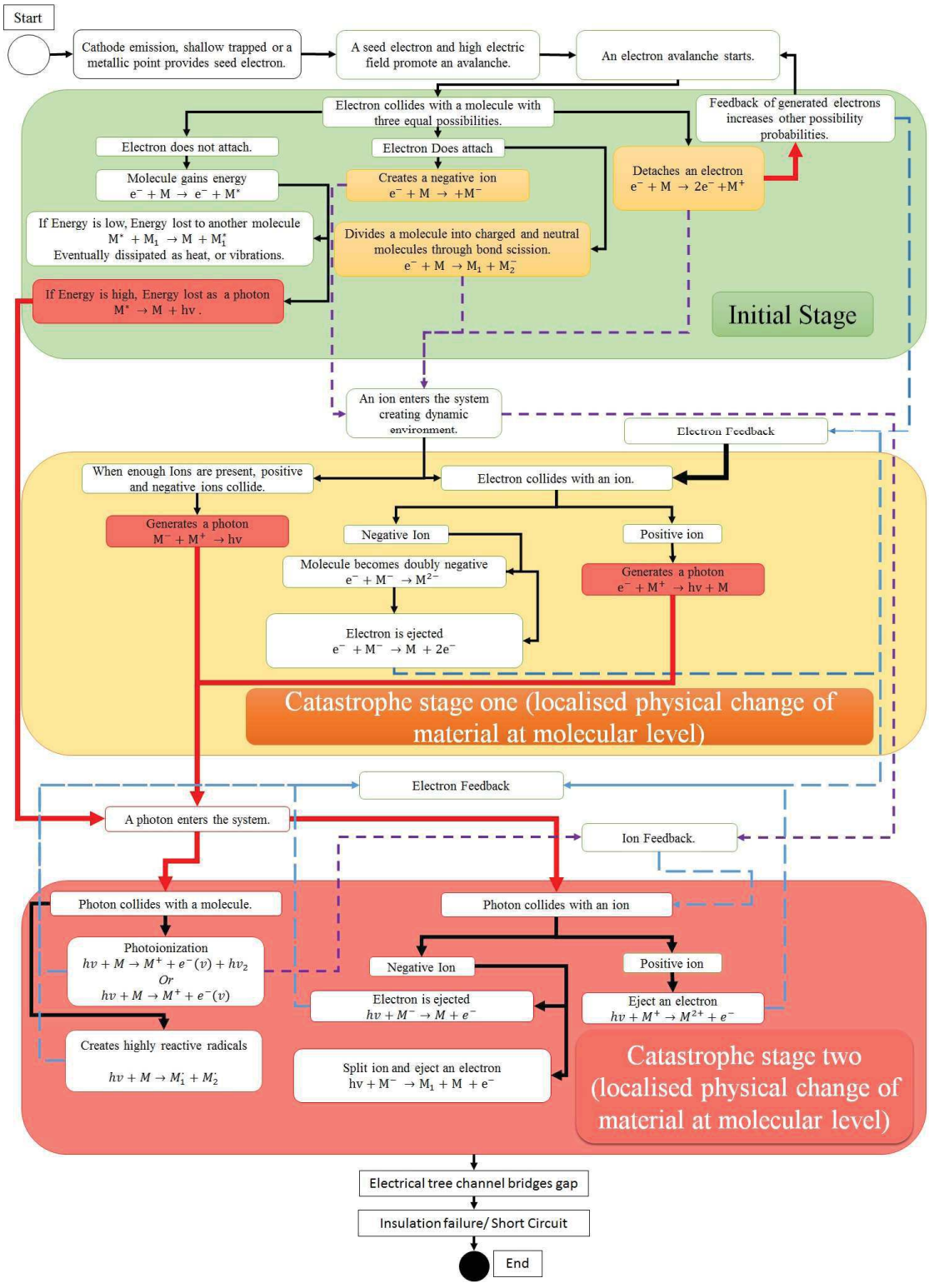

Figure 2-4: Proposed by the author, a flow diagram illustrating a consolidated process of the start and end of the partial discharge and electrical tree process resulting in electrical insulation failure [1] – [3]. Note each stage will have increasing probabilities as electrons, ions and photon feedback occurs.

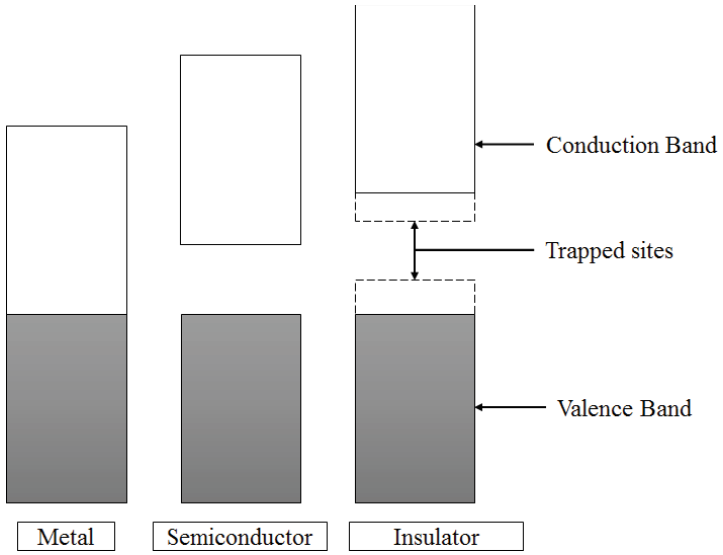

Figure 2-5: Trapped electron gap theory indicating that electrons in the trapped sites of insulators have lower band gap energy requirements to get to the conduction band.

$$3O_{2(g)} + hv \Rightarrow 2O_{3(g)}$$

$$N_{2(g)} + O_{2(g)} + hv \Rightarrow 2NO_{(g)}$$

$$NO_{(g)} + 0.5 \times O_{2(g)} \Rightarrow NO_2 \quad (1)$$

$$2NO_{2(g)} + H_2O_{(g)} \Rightarrow HNO_{3(g)} + HNO_2$$

2.6 Conclusion

In order to maintain good electrical supply in a power system, there is a requirement on the strength of electrical insulation. This chapter reviewed insulation material in a broad sense for high voltage engineering applications. Some of the challenges with modern insulation systems were presented. Self-healing insulation such as air, SF_6 and transformer oil were discussed. These self-healing insulation materials do have their challenges and cannot be used in all applications hence the need for solid insulation.

Certain applications require solid insulation materials such as cables and generators.

Solid insulation material was discussed with particular reference to epoxy. The major electrical challenge with regard to solid insulation is electrical tree degradation. A flow diagram model based on literature was proposed to explain the process of electrical trees. This model will be used as the foundation of understanding the effect that nanoparticles have on electrical trees. Solutions to solid insulation problems lie in nanodielectric technology.

The next chapter discusses nanotechnology in history, nature and some modern applications. Within the umbrella of nanotechnology, nanocomposites and nanodielectrics have found wide use. Some discussions on nanocomposites are presented. Nanodielectrics and the nanodielectric models developed is then highlighted with a critical analysis.

CHAPTER 3 : NANOTECHNOLOGY, HISTORY, NATURE AND THE WORLD

"If you believe in your dreams, I will prove to you, that you can achieve your dreams just by working hard." – Rock Lee

3.1 Introduction

Nanotechnology is an enabling technology which allows for a new understanding of the world. By understanding the effects in the nano-world, new technology may be developed to address modern problems such as electrical trees in solid insulation. This chapter review's nanotechnology by briefly highlighting observed nanotechnology applications in history, nature, and modern society. Different nanoparticle types are discussed with some of their applications. This is followed by the manufacturing techniques used in the formation of nanocomposites and nanodielectrics. A brief summary of different nanoparticles for nanodielectric applications is presented along with discussions on the models which have been generated for nanodielectrics.

3.2 Glossary

- "*Nanoscience and nanotechnology* refer to the science and technology of matter, manipulated at the nanolevel. It is an area in which traditional disciplines converge," [9]. The significance of nanotechnology is that traditional physics understanding for bulk materials in some cases is no longer applicable to the nano-world. Nanotechnology also allows for bottom-up approaches to applications.
- *Nano*: A unit of measure which refers to 10^{-9} m.
- *Ångstrom*: A unit of measure which refers to 10^{-10} m and unit used to measure the distance between atoms.
- *Hydrophobicity:* The property of repelling water [45].
- *Suspensions:* liquid systems which have particles present which may or may not sit independently separated within the liquid matrix.

- *Nanocomposite*: Within the umbrella of nanotechnology refers to a composite material which has some type of nanoparticle/s-infused in the product.
- *Nanodielectric*: A nanocomposite previously termed "Nanometric dielectric, [17]" used specifically for dielectric functions.

3.3 Background to Nanotechnology

This section discusses nanotechnology applications in nature, history, and some modern applications with particular consideration to society. By understanding nanotechnology found in history and nature, it may be possible to exploit the nano-effects for modern technological applications.

In nature, the Nelumbo nucifera or Indian lotus, the national flower of India, has super-hydrophobicity properties which allow it to be self-cleaning, see Figure 3-1. A water drop attempts to minimise surface tension, thus forming a sphere [9].

The cells on the leaf have high roughness on a 100 nm scale which lowers adhesion on the surface of the leaf [9]. This allows for water droplets to attain an almost spherical form and the droplets just roll off. The property of super-hydrophobicity has seen commercial applications in the development of hydrophobic coating to prevent clothes from being stained [46]. For electrical applications, silicon rubber particles, which also have hydrophobic properties, could be applied to transmission line insulators which would prevent the formation of dust and water pollution on the insulator surface [9].

Apart from nature and commercial applications, nanotechnology has been found in history [47]–[50]. An example of nanotechnology in history is the Lycurgus cup. The Lycurgus cup was developed in the fourth century AD and is shown in Figure 3-2 [9], [51]–[53]. The cup was fascinating because it would change colour depending on the nature of light (transmitted through or reflected from) applied to the cup [47]. Studies performed showed that gold and silver nanoparticles contributed to this observational effect [47]. With reference to the cup, as the gold and silver particle sizes decreased, the amount of light absorbed in the visible

spectrum increased. Gold particles reflected the higher wavelengths, which resulted in a red colour in transmitted light from within or above the cup [47]. Similarly, the silver particles resulted in a green colour in reflected light from the sides of the cup [47]. These colour changes have also been shown when analysing the colours obtained in the 1000-year-old church stained glass windows, see Figure 3-3 [49], [50].

Part of Horizon 2020, an initiative to develop nanotechnology in Europe with € 80 billion funding, looks at using optical properties of Zinc Oxide (ZnO) quantum dots (1-10 nm) for photocatalysis [54], [55]. The quantum dots absorb UV light which makes it easier to split water. Currently, still in development, the use may find applications in the development of hydrogen fuel cells for large scale energy generation.



Figure 3-1: Nelumbo Nucifera showing hydrophobicity properties, the full image of the flower on (left). Image of water droplets flowing on the surface of the leaf (right). Permission of use by T. Voekler under the Creative Commons License [51]–[53].



Figure 3-2: Lycurgus cup showing reflected light effect (left) and transmitted light from inside/above the cup (right). The image is taken from British museum collection under the Creative Commons License [51]–[53].



Figure 3-3: Images were taken by the author of the Nano-cathedral project in Pisa Italy as part of the Horizon 2020 project. Text left: “Nanomaterials for the conservation of European architectural heritage developed by research on characteristic lithotypes.” Image of author in Nano-cathedral (right)

Elsewhere in history, increased durability and strength attributed to the Damascus blades used in the 16th and 17th centuries were found to be due to a combination of carbon nanotubes and iron carbide found in the steel [9], [48], [56]. This has been explained based on Nucleation [57], [58]. Nucleation is associated with phase transformations (gas-liquid-solid) and refers to the formation of nanocrystallites during phase transformations [58]. The nanocrystallites are referred to as nuclei. The force which causes the formation of nuclei is given by the free energy shown in equation (3-1) and the rate of nucleation shown in equation (3-2). When the rate of nucleation is equated to zero, the critical radius of a particle can be derived and is also shown in equation (3-2). While the surface free energy is greater than the volume free energy, nucleation will occur. As the overall particle grows in size, once the critical radius has been met, the volume free energy will be greater than the surface free energy. When the volume free energy is greater than the surface free energy nucleation will no longer occur. The rate of nucleation obtained from equations (3-1) and (3-2) is illustrated graphically in Figure 3-4. In general, nucleation and growth of the nuclei has been used when designing materials with increased mechanical strength especially with metal alloys.

The wide use of nanotechnology applications from history to modern day has prompted various fields of research into understanding the different realms of nanotechnology. The use of nanotechnology, although unknowingly in certain

instances at the time, has allowed for interesting artistic and utility applications of nanocomposites in history. **Therefore, there has been a drive to develop nanocomposites to address some of the electrical insulation challenges by using nanotechnology through nanocomposites.**

$$\Delta G = \frac{4}{3}\pi a^3 \Delta G_v - 4\pi a^2 \sigma_{sl} \tag{3-1}$$

$$\frac{dG}{da} = 4\pi a^2 \Delta G_v - 8\pi a \sigma_{sl} = 0 \Rightarrow a^* = \frac{-2\sigma_{sl}}{\Delta G_v} \tag{3-2}$$

Where:

- ΔG is the free energy (J).
- a is the radius or apparent radius of a solid particle (m).
- a^* is the critical radius. Beyond that the nucleus/size of the particle increases.
- ΔG_v is the free energy change per unit volume (J/ m^3).
- σ_{sl} is the free energy per surface energy (J/ m^2).

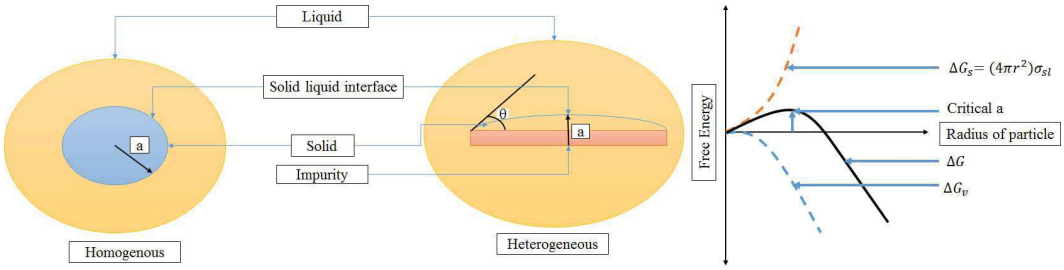

Figure 3-4: Nucleation for solid and liquid phase transformations. The rate of nucleation is faster in heterogeneous systems compared to homogenous systems.

3.4 Nanocomposites and Nanodielectrics

A nanometric dielectric or nanodielectric is a sub-division of nanocomposites which is used primarily for its dielectric properties in high voltage applications [31]. When Lewis defined Nano-metric dielectrics, the conditions for the characteristic dimension for nanometre particles were <200 nm [17]. In the last twenty years, it has been established that a nanoparticle is considered nano if the characteristic property of the particle is from 1 nm to 100 nm [19].

There are three broad types of nanoparticles/nano-fillers shown in Figure 3-5 [9]. There are 0D or ~spherical particles; 1D, tubes, fibres or wires; 2D, flakes or planes. The dimension of the filler only defines the possible directions for electron movement through the particle [9]. Each type of particle has a characteristic which makes the particle nano, these are the particle diameter, tube/wire diameter, and flake thickness for 0D, 1D and 2D particles respectively. A tube like a carbon nanotube may have a length of 1 nm to 1 mm, but because the diameter of the tube is 1 nm, it is still considered a nanofiller [9].

Some of the nanoparticles investigated for nanodielectrics or nanocomposites are summarised in Table 3-1 [23], [59]–[64]. There is a brief list of the pros and cons of the investigated nanoparticles investigated thus far. Some of the particle types used in nanocomposites may not necessarily be beneficial for high voltage insulation but may be useful for electronic insulation materials.

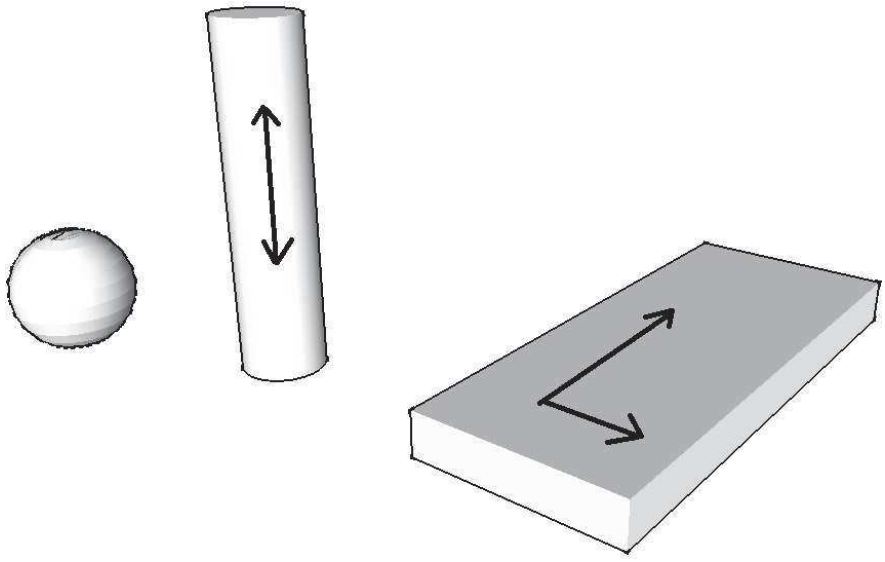

Figure 3-5: Different Nano-filler shapes, the arrows indicate the possible directions for electron movement, 0D or particle (left); 1D, tube or wire (centre); 2D, flake or plane (right). Adapted from [9].

Table 3-1: Nanoparticles investigated thus far for nanodielectrics and nanocomposites [23], [59]–[64]

Filler Material	Pros	Cons
Cellulose (plant) Nanofibers	Improve mechanical properties, biodegradable, makes a lot of paper.	Tubes/fibres are points of conduction under high voltage applications, flammable.
Silica (SiO)	High electrical resistivity, low dielectric constant.	Low thermal conductivity.
Alumina (AlO)	Low Cost, high electrical resistivity, good thermal conductivity.	High dielectric constant at frequencies >1 MHz resulting in conduction properties.
Carbon Nanotubes	Easy to manufacture, good mechanical strength and thermal conductivity.	Tubes/fibres are points of conduction under high voltage applications, electrical conductor.
Graphene	good mechanical strength and thermal conductivity.	Currently difficult to manufacture, conducts electricity.
Silicon Carbide (SiC)	High thermal conductivity.	High Dielectric Constant.
Magnesium Oxide (MgO)	Improves space charge and thermal conductivity.	Lengthy synthesis.
Zinc Oxide (ZnO)	Improves mechanical properties, Used for water catalysis, good optical properties.	Lengthy synthesis.
Titania (TiO_2)	Improves mechanical properties and breakdown strength.	Lengthy synthesis.
Boron Nitride (BN)	Second best thermal conductor high electrical resistivity, low dielectric constant, low density, thermal profile remains constant at nano and micro.	Properties dependent on hexagonal (platelet) or cubic (diamond) shape.

3.5 Nanodielectric Material Synthesis

Tanaka *et. al.* [65] gives an in-depth understanding of the different synthesis techniques for insulation filled with particles or nanodielectrics. Despite the well-established insulation manufacturing methodologies, the final nanodielectric is incredibly dependent on the material synthesis as the properties are not intuitive nor predictable. The methods described for insulation manufacturing are intercalation, molecular composite formulation, and direct dispersion. The first decision to be considered for nanodielectric manufacturing is whether or not to surface condition the nanoparticles. Surface conditioning involves coating the nanoparticle with a layer which changes the zeta potential of the particle (discussed later in Section 3.6) and makes the probability of particle-insulation bonding possible.

The differences between intercalated and exfoliated particles are shown in Figure 3-6 [65]. Conceptually, intercalation can be described as having different layers (mostly platelet nanoparticles) packed like a sandwich in a box (interspaced with insulation), exfoliate refers to having the parts of a sandwich (the nanoparticles) drifting independently in the box (in the insulation) [66].

Depending on the intended application, there are positives and negatives to the use of intercalation [65], [66]. Intercalated particles are desired for increased mechanical strengths in some mechanical applications. Exfoliated particles are desired more for electrical applications to prevent continuous conductive parts. The challenges with intercalated particles are ensuring the particles are aligned in a particular direction. While the exfoliated particles have a complicated particle separation process and cannot be surface conditioned.

There are three types of intercalation processes, namely: intercalation by solution, in-situ intercalation and melt intercalation [65]. The first two methods of intercalation involve insulation which begins as liquids while the last intercalation method begins with solid insulation.

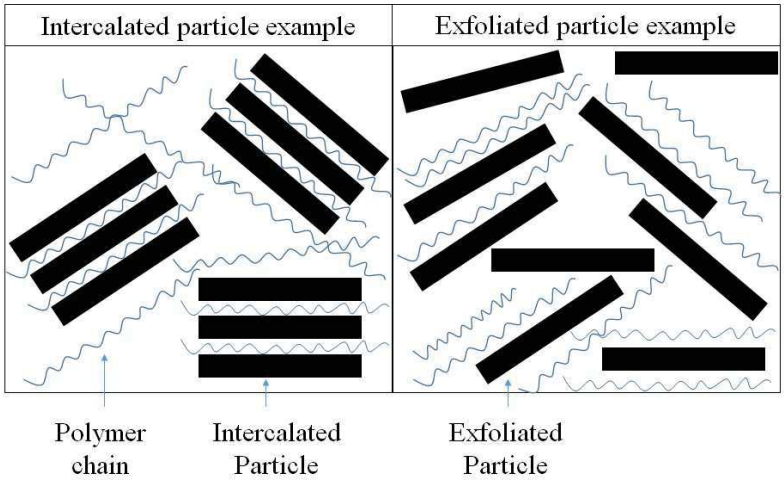

Figure 3-6: Illustration of the differences between exfoliated and intercalated particles in an insulation matrix (Adapted from [65]).

Intercalation by solution involves mixing particles (mainly silicate/layered particles) which swell (like clay) in a solvent (like water); the mixture of particles and solvent are then added to the insulation (the resin in the case of epoxy); the insulation then displaces the solvent by differences in chemical potential [65]. The solvent is then removed, possibly by an evaporation process [65]. Failure to remove the solvent has the risk of compromising the cross-linking of the insulation.

In-situ intercalation has the insulation with particles mixed. A catalyst or heat is applied to the mixture before swelling of the particles takes place [65]. If the initial state of the insulation is a solid, melt intercalation has the insulation heated until the insulation is soft or more fluid like, and particles are then added, and distributed appropriately, the mixture is then left to solidify. Molecular composite formulation involves adding molecular rods to insulation by melting two insulation materials which are immiscible (basic examples are water and oil) [65]. The melted materials are mixed together with a compatibilizer (a substance which makes immiscible materials mix) which promotes the formation of fibrils (long polymer chain structures) and dispersion [65]. This manufacturing technique is favoured for quantum dot (1-10 nm) particles as the particles grow within the insulation matrix which may not necessarily agglomerate. The major drawback is that if the particles do not bond with the insulation then the particles create poor interfaces which may promote crack formation.

Direct dispersion involves taking readily available nanoparticles and mixing with an insulator through various violent mixing techniques [65]. The particles may or may not be surface conditioned. The main benefit of direct dispersion is its simplicity similar to adding sugar to coffee and hence would facilitate nanodielectric technology transfer to industrial applications. The process requires that nanoparticle agglomerates are broken during the mixing process. Among the various methods of developing a nanodielectric, the easiest is the direct dispersion and hence was selected as the synthesis approach in this study.

Once a nanodielectric has been manufactured, although the system during manufacturing may have been binary as one type of nanoparticle mixed with one type of insulation material, the final nanodielectric is composed of three regions. The host insulation, the nanoparticles, and the interface region or interphase around the nanoparticle [59]–[64]. There is currently very little knowledge about the interphase, but what has been established is that the interphase is different to both the particle and host matrix. The differences are postulated as electrical, mechanical, or chemical. Since 2004, various models to explain the observed effects have been generated in an attempt to explain the nanodielectric phenomena [59]–[64] as reviewed in the next section.

3.6 Models used for explaining Nanodielectric Phenomena

The science of nanodielectrics is centred around how the nanoparticles interact with the host material matrix. Consequently, a number of researchers have developed models to explain and understand the phenomena. By understanding the interface region around the nanoparticle one can custom design/tailor make a nanodielectric for specific purposes with intended consequences. This section reviews the common models found in the literature. There are currently six models specifically used as an attempt to explain nanodielectric phenomena [59]–[64]. It should be stated that currently the interphase is still not understood, so each new model is progressively better. But not one model is absolutely correct.

Each model attempts to explain the observed nanodielectric effect by attributing the improved effect to the interphase. These models are the *Intensity* model, *Multi-core*

model, *Polymer chain alignment* model, *Potential new barrier* model, the *Interphase volume* model and the *Unified permittivity and temperature* model.

Currently, all experimental work used for the modelling has been based on nanoparticle types of ceramic, metal oxides, boron nitride and clay hosted in various insulation systems as shown in Table 3-1. The individual models are discussed in the following sub-sections based on the experimental evidence or literature used to generate each model. All the models attempt to answer the question; **"What is the interphase?"** All models start by assuming the following:

- All particles are homogeneously or uniformly dispersed/distributed in the host matrix.
- All particles are spherical and have the same diameter (simplify maths).
- The interphase between nanoparticle and host matrix exists and is of some fixed length or thickness.

3.6.1 The Intensity and Double Layer Model

The intensity model is based on colloidal chemistry using the Derjaguin-Landau-Verwey-Overbreek (DLVO) theory. An in-depth understanding of DLVO theory is provided in [59], [67] and illustrated in Figure 3-7. The DLVO theory attempts to explain the forces to be considered by looking at Coulombic electrostatic repulsion or attraction and Van der Waals attraction. The double layer electrostatic potential describes the electrostatic influence on ions around a particle.

The double layer theory claims that "at the surface of each molecule or particle, there is a difference in electrical and chemical potential which results in electrostatic force (generally assumed to be repulsive because of Coulombs Law)." There are limitations to DLVO theory because firstly it is not the only factor to be considered for suspension stability. Secondly, for most cases, it may only be valid in vacuums or when particle sizes don't exceed 10 nm. Thirdly, the net electric charge on a particle may be neutral, negative or positive which may in certain situations result in attractive forces due to Coulombs Law. **However, the intensity model claims that the interphase or interaction zone is a function of DLVO theory and does not exceed ~10 nm.** This assertion needs further validation and will be checked in this work.

The intensity model, first proposed in 2004 defines an intensity as some physical, chemical or electrical property which can change and is illustrated in Figure 3-8. Building on from DLVO theory, the intensity model, claims that the intensity of a material property "A" does not change abruptly at an interface change, but rather gradually changes over some small distance. The intensity is speculated on the particle type which is shown for A1 and A2 as two types of particle intensities. **The interphase is, therefore, the region in which the intensity of the material around the nanoparticle is different to particle and host matrix.** The drawback of this model is that it is based on theory with very limited experimental work done. The multi-core model attempted to address some of the missing experimental work.

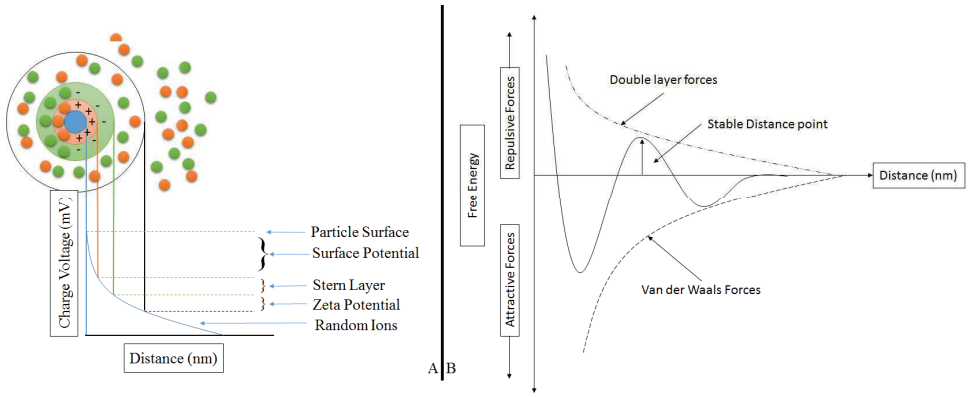

Figure 3-7: DLVO Theory which describes the force interactions of molecules and small particles, the double layer model based on the surface potential, Stern Layer and Zeta potential (A) and DLVO model based on the double layer forces and Van der Waals forces(B) [59], [67].

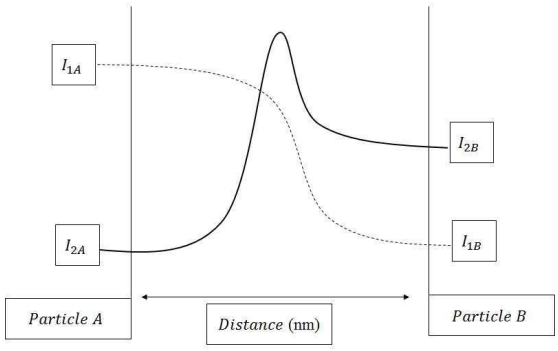

Figure 3-8: Intensity model by Lewis which describe how the interphase is a function of particle concentration or physical intensities [59].

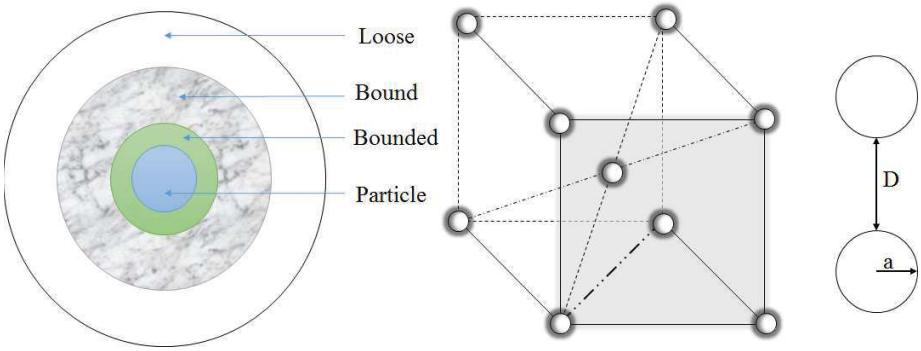

Figure 3-9: Multi-core model proposed by Tanaka *et. al.* showing the three different layers which represent the interphase on the left, the assumed face centred cubic crystal structure in the centre, Particle radius (a) and particle distance (D) on the right [60].

3.6.2 The Multicore Model

The multi-core model was proposed by Tanaka in 2005 and shown in Figure 3-9 [60]. It has been the model which has received the most popularity within the nanodielectric research fraternity because of its versatility, and the experimental evidence. The model was generated by investigating Silica (SiO) particles in polyamide (EPPS) insulation on Partial Discharge (PD) resistance and using X-ray diffraction spectra (XRD). It has since been used to speculate on various materials using spherical inorganic nanoparticles.

The model is based on the premise that there are three regions around the nanoparticle termed the bounded, bound and loose layer. The model firstly assumes that the nanoparticles (uniform size, dispersion, and distribution) have been surface conditioned, and hence the bounded layer represents the region of surface conditioner around the nanoparticle. Beyond the bounded layer, the bound layer represents the same double layer electrostatic potentials used for the intensity model. The third layer, termed the loose layer, represents a region that is influenced by the nanoparticle, as a pure polymer, but would still be different in function and property to the pure polymer. The mathematics to describe the multi-core model are described in equations (3-3) to (3-6). From Figure 3-9 (right), (3-3) describes the distance between particles, and (3-4) gives the surface area of particles. By

assuming a face centred cubic crystal structure (Figure 3-9 (centre)) yields (3-5) and (3-6) which considers particle concentration.

$$D = \left[\left(\frac{\pi\sqrt{2}}{6}\phi\right)^{\frac{1}{3}}\right]a \tag{3-3}$$

$$S = \frac{6\phi}{a} \tag{3-4}$$

$$D = \langle\left\{\frac{\pi}{6}\left(\frac{\rho_n}{\rho_m}\right)\frac{100}{wt\%}\left[1 - \frac{wt\%}{100}\left(1 - \frac{\rho_m}{\rho_n}\right)\right]\right\}^{\frac{1}{3}} - 1\rangle\, a \tag{3-5}$$

$$S = \frac{\pi a^2}{(D+a)^3} \tag{3-6}$$

Where the symbols are shown in Figure 3-9:

- D is the inter-particle distance (nm).
- ϕ is the particle volume fraction (vol%) and wt% is the particle weight percentage.
- S is the surface area per unit volume (/m).
- ρ_n and ρ_m are the nanoparticle and matrix densities respectively (g/cm^3).

Based on this model, **the interphase is made of three distinct regions around the nanoparticle which may also be a result of surface conditioning.** The model is limited to a spherical particle of a fixed size and an **interphase of a fixed length not exceeding 25 nm** and relies on the particles always being equidistant. The main challenge to this model is there are no considerations for increasing particle concentration and the attempt to address this was made by the interphase volume model.

3.6.3 Interphase Volume Model

The interphase volume model was proposed by Raetzke and Kindersberger in 2010 and shown in Figure 3-10 [61]. It was generated by looking at two different types of Silica particles in silicon rubber for high voltage arcing and resistance to tracking and erosion. It was the first model to build on the multi-core model by introducing additional mathematics to explain how the increase in particle concentration may affect the bulk material and the interphase. An additional add-on was the particle

size as an independent changing variable. The model assumes that particles are homogeneously dispersed and distributed in order to simplify the maths. The mathematics describes how there are four categories based on particle concentration. The first region is as shown in Figure 3-10 (A) and (B), the particles are sufficiency far away so there is no contact and the volume of the matrix is larger. As the concentration of particles increase, the second region is reached, Figure 3-10 (C), where the particles move closer together until the interphases touch. The third region, Figure 3-10 (D), describes how the interphases overlap with increased concentrations and there is little insulation remaining. The final region, Figure 3-10 (E), describes how the particles are in contact and the region of interphase and insulation is less than filler content.

The corresponding mathematics to describe the model is given in as equations (3 - 7) to (3-15), where symbols have been defined previously or defined in Figure 3-10 (C). The volume of the interphase is the volume of the apparent particle minus the particle radius in (3-7) and illustrated in Figure 3-10. The regions of validity in Figure 3-10 (B)-(E) are: the particles are far apart (3-8), the particles are far close and the interphases are touching (3-10), the interphases are overlapping (3-12), and there is no matrix as the particles are in contact (3-14) respectively. The volume of the interphase is therefore described by equations (3-9), (3-11), (3-13) and (3-15) respectively.

$$\frac{2}{\sqrt{3}}(a+2t) \leq D \tag{3-7}$$

$$V_i = V_{2a+2t} - V_p = \frac{1}{6}\pi[(d+2t)^3 - a^3] \tag{3-8}$$

$$p_{i-1} = \left[\left(1+\frac{2t}{a}\right) - 1\right] \tag{3-9}$$

$$(a+2t) \leq D \leq \frac{2}{\sqrt{3}}(a+2t) \tag{3-10}$$

$$p_{i-2} = p\left[\left(1+\frac{2t}{a}\right) - 1 - 8\left(\frac{1}{2}+\frac{t}{a}-\frac{\sqrt{3}D}{4a}\right)^2\left(2+\frac{4t}{a}+\frac{\sqrt{3}D}{2a}\right)\right] \tag{3-11}$$

$$\frac{2\sqrt{2}}{3}(a+2t) \leq D \leq (a+2t) \tag{3-12}$$

$$p_{i-3} = p\left[\left(1+\frac{2t}{a}\right) - 1 - 8\left(\frac{1}{2}+\frac{t}{a}-\frac{\sqrt{3}D}{4a}\right)^2\left(2+\frac{4t}{d}+\frac{\sqrt{3}D}{2a}\right) - 6\left(\frac{1}{2}+\frac{t}{a}-\frac{D}{2a}\right)^2\left(2+\frac{4t}{a}+\frac{D}{a}\right)\right] \tag{3-13}$$

$$D \leq \frac{2\sqrt{2}}{3}(a+2t) \tag{3-14}$$

$$p_{i-4} = 1 - p \tag{3-15}$$

Where:

- V_i, V_{2a+2t} and V_p are the interphase, apparent particle, and actual particle volumes respectively.
- t is the interphase thickness.
- $p_{i-1}, p_{i-2}, p_{i-3}$, and p_{i-4} are the interphase content in each region of Figure 3-10 (B) – (E).

The significant contribution of this model was that **the volume of the interphase was not as homogenous as previously assumed based on particle concentration.** Additionally, the indication that **there is a saturation point where additional nanoparticles may be added but will not contribute to the bulk properties of the material** was indicated. The major problem with this model is that it does not interrogate the interphase properties and does not take into account the DLVO properties indicated by Lewis and Tanaka *et. al.* Given the first three models, no attempt has been made to understand the nanodielectric synthesis properties. Additionally, there is a lack of understanding on the effect that different particle types would have on the nanodielectric. The Polymer chain alignment model, therefore, attempted to address some of these challenges.

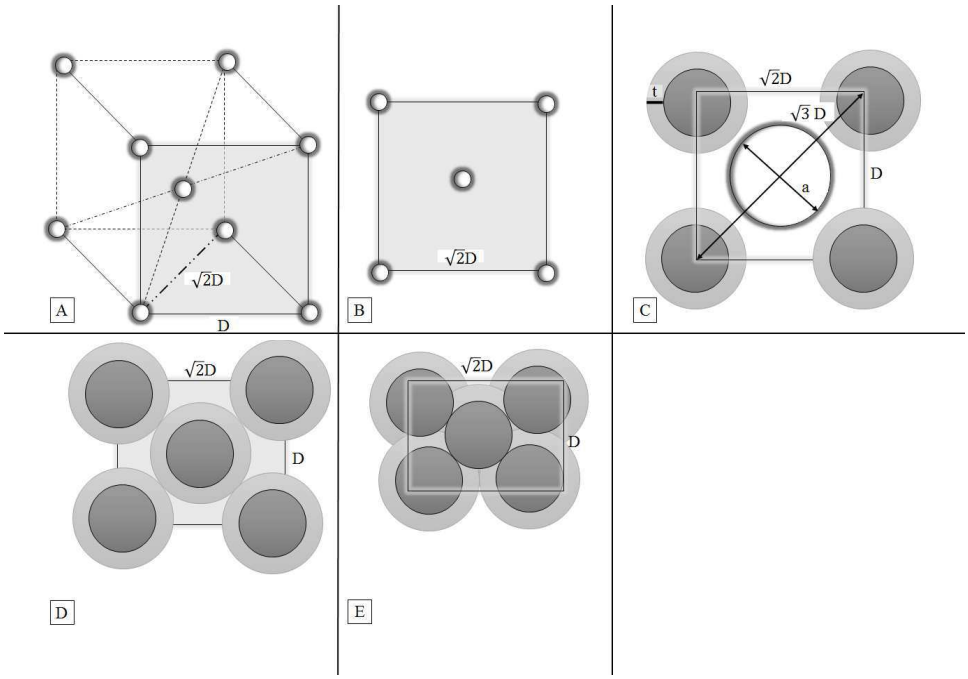

Figure 3-10: Interphase volume model by Raetzke and Kindersberger showing homogeneously dispersed nanoparticles with the different interphases (A) shows the face centred cubic crystal structure, (B) shows the diagonal with particles sufficiently far away that they do not interact, (C) Shows the particles close enough that the interphases touch, (D) the interphases overlap, (E) the particles are in contact [61].

3.6.4 Polymer Chain Alignment Model

The polymer chain alignment model (PCAM) was first proposed by Andritsch *et. al.* in 2011 and shown in Figure 3-11 [64]. It was the first model to assume the particle may not necessarily be spherical. The particle shapes analysed were only platelet and spherical types and goes back to double layer electrostatic modelling. The particles investigated were magnesia (MgO), alumina (AlO), aluminium nitride (AlN) and hexagonal boron nitride (BN) in an epoxy matrix with various surface conditioners.

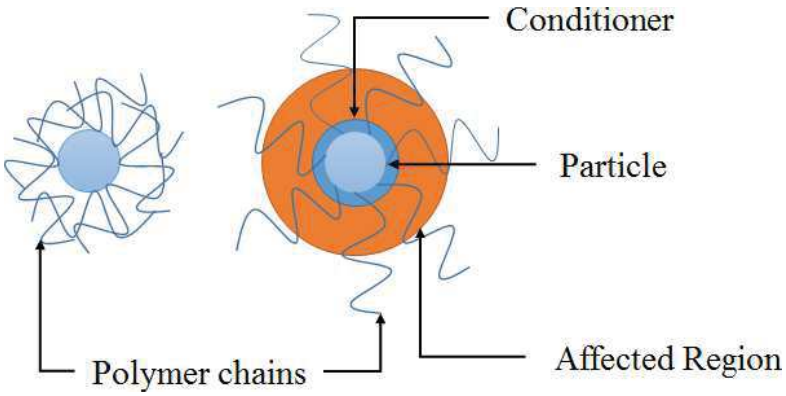

Figure 3-11: Polymer chain alignment model by Andritsch *et. al.* showing unorganised polymer chains on the left and organised polymer chains on the right [64].

The ultimate objective behind the PCAM model was that the properties of a nanocomposite are a result of the nature of the synthesis process. The model stresses the importance of surface conditioning of the particles before adding the particles to a matrix. The justification for surface conditioning was that it serves to ensure an increased zeta potential between nanoparticles causing the particles to repel each other. The second justification was that during the polymerization process, there is no guarantee that the particles will bond with the matrix, hence the surface conditioning ensures the particles bond with the host matrix.

The model claims that due to the surface conditioning, the polymer chains around the particle (provided the surface conditioner bonds firstly to the particle, and secondly to the matrix) orient to be more ordered labelling an affected region around the particle to be the interphase.

The main contribution of this model was **the interphase is a result of surface conditioning, particle size, particle shape and particle surface conditions/type. Additionally, the nanodielectric is a function of suspension dynamics during material synthesis and hence there is a need to understand the synthesis.** There was still a gap in experimental knowledge with regard to particle concentrations which the New barrier model attempted to address.

3.6.5 New Barrier Model

The new barrier model proposed in October 2011 by Li *et. al.* [63] builds on from the multi-core model. The model was generated by using results from dielectric spectroscopy, glass transition temperature, and breakdown voltage on alumina and titania (TiO) particles in epoxy. **They were the first to suggest a possible optimal loading of nanoparticles between 0.1 wt% and 10 wt%**. Like the polymer chain model, this model reduces the number of regions in the interphase. This model labels the bound and loose regions from Figure 3-9 as a transition region. The model focuses on quantum mechanics and electron tunnelling within and around the nanoparticles. The model also pulls on information from the interphase volume model and discusses how electron trapping or the inhibition of electron trapping occurs around the nanoparticles. The work energy function for an electron to transition from the valence or trapped band to the conduction band was used to explain the interphase.

At low filler concentration, the particles are independent in the insulation, at higher concentrations, if the interphases are in contact, the particle-interphase chains may result in conductive pathways. Hence, an investigation into optimal loading levels would be needed for nanodielectric manufacturing. There was some work on some of the thermal properties but there was still need for an attempt at understanding the relations between thermal and electrical degradation. The Unified permittivity and thermal conductivity model attempted to address these issues.

3.6.6 Unified Permittivity and Thermal Conductivity Model

Tsekmas *el. al.* [68] proposed the unified permittivity and thermal conductivity model in 2014. They assumed the validity of the polymer chain model shown in Figure 3-11. By considering surface conditioner and surface water absorption of nanoparticle they produced a battery of permittivity and thermal conductivity tests for different nanoparticle types. They looked at Magnesia, Aluminium nitride, alumina, hBN, cubic-BN with particle sizes from 22-150 nm to develop a model which attempts to unify the electrical permittivity and thermal conductivity of these nanoparticles in an epoxy matrix.

They also compared simulations done in Comsol ™ to experimental results to obtain some good agreement with the model. **They established the interphase as two regions; the first region as a constant thickness based on surface conditioner and water uptake. The second region was a loose region which was variable and depended on inter-particle distance and hence particle concentration.**

3.6.7 The Considerations when manufacturing a nanodielectric.

Given the different models, there is still a lack of understanding in terms of "What is the interphase?" But the models have informed on the considerations needed when synthesising a nanodielectric. This section summarises what has been established as the considerations when producing a nanodielectric. The considerations from the literature are summarised as follows:

1. The interphase is the region around the nanoparticle which is different to particle and host matrix.
2. The interphase is made of two or three distinct regions around the nanoparticle which may be a result of surface conditioning.
3. The interphase is possibly a fixed length not exceeding ~10-25 nm.
4. The interphase is a result of particle size, particle shape, and particle surface conditions/type.
5. The interphase depends on inter-particle distance and hence particle concentration.
6. The volume of the interphase is not homogenous and depends on particle concentration.
7. There is a possible optimal loading of nanoparticles for titania and alumina between 0.1 wt% and 10 wt%; it may vary for different particle types.
8. There is a saturation point where additional nanoparticles may be added but will not contribute to the bulk properties of the nanodielectric.
9. The nanodielectric is a function of suspension dynamics during material synthesis and hence there is a need to understand the synthesis dynamics.
10. At low filler concentration, the particles are independent in the insulation, at higher concentrations, if the interphases are in contact, the particle-interphase chains may result in conductive pathways.

Given these considerations, by varying the particle concentration and analysing concentration effects during material synthesis, an optimal point may be achieved. There is also missing information on how to determine the properties of the interphase. The next chapter discusses the nanodielectric synthesis properties.

3.7 Conclusion

This chapter reviewed nanotechnology by briefly highlighting observed nanotechnology applications in history, nature and modern society. The Indian lotus flower, Lycurgus Cup, Cathedral windows and Damascus blades were discussed as examples of nanotechnology in nature and history. The particle, tube, and platelet particle types were illustrated and discussed. Additionally, a brief summary of different particles used for nanocomposite and nanodielectric applications was provided. The nanodielectric manufacturing methods were discussed and the six models developed to understand the science of the nanodielectrics was presented. The models presented were the Intensity model, Multi-core model, Interphase volume model, Polymer chain alignment model, Potential new barrier model, and unified permittivity and thermal conductivity model.

The considerations required for manufacturing a nanodielectric and establishing the interphase was summarised into ten points. The interphase is a region around the nanoparticle which is different to the host matrix based on electrical, chemical, and mechanical properties. Additionally, it has two or three distinct regions and a fixed length ~10-25 nm. The interphase is dependent on concentration, particle size, shape, and particle surface conditions. The volume of the interphase is not homogenous, there is a saturation point, and it depends on particle concentration and there may be an optimal concentration level between 0.1 wt% and 10 wt%. The nanodielectric is a function of suspension dynamics and material synthesis and by understanding these new insights may be obtained. At low filler concentration, the particles are independent in the insulation, at higher concentrations, if the interphases are in contact, the particle-interphase chains may result in conductive pathways.

The next chapter presents the nanodielectric synthesis and considerations for manufacturing a nanodielectrics. The principle techniques used to analyse the

stages of the nanodielectric are introduced. The principles of rheology, zeta-potentials, and some microscopy techniques are presented. In order to address the electrical tree problems introduced in Chapter 2 a discussion on the particle, choices are presented. This is followed by the synthesis procedure using rheology. The first sets of results to validate optimal loading levels using rheology and microscopy are then presented.

CHAPTER 4 : RHEOLOGY INCORPORATED NANODIELECTRIC SYNTHESIS

"An informed question. But difficult to answer. I am what you see." - Nanaki

4.1 Introduction

When synthesising and understanding nanodielectrics there are various tools available. Some of these tools will be introduced and discussed based on their operation mechanics and information provided. A brief discussion on particle choices is given. Rheology was selected as an analysis tool followed by Scanning Electron Microscopy (SEM), and Transmission Electron Microscopy (TEM). The nanodielectric synthesis procedure and rationale is presented. A discussion of the rheology and microscopy results is provided along with their relevance.

4.2 Background

In Chapter 2, electrical treeing was reviewed as the ultimate failure mode of solid polymer insulation. Hence there is a need to develop electrical tree resistant solid polymer insulation. The resistance to electrical trees may be achieved by using nanoparticles which provide additional mechanical strength which would prevent crack formation. Furthermore, since electrical trees are essentially driven by stray electrons, ions, and photons, nanoparticles which are electron scavengers may retard the electrical treeing process. The electrical tree process is a function of mechanical, electrical, thermal and chemical degradation. A choice of nanofiller, therefore, relies on the ability to provide additional mechanical support and the ability to remove additional electrons.

Once an appropriate nanoparticle is selected, there is a need to establish an optimal loading level of nanoparticles in the matrix. In the literature, it has been established that there is a possible optimal loading of nanoparticles between 0.1 wt% and 10 wt% but may vary for nanoparticle type. Alternatively, another consideration is a saturation point where additional nanoparticles may be added but will not contribute to the bulk properties of the nanodielectric. At low filler concentration, the particles

are independent in the insulation, at higher concentrations, if the interphases are in contact, the particle-interphase chains may result in conductive pathways. As the nanodielectric is a function of suspension dynamics during material synthesis there is a need to understand the synthesis dynamics.

In nanodielectric research, determination of the filler optimal loading levels has largely been done through the mix and test iterative processes and validated by post-manufacturing microscopic analyses. In that regard, Scanning Electron Microscopy (SEM) and Transmission Electron Microscopy (TEM) techniques have been commonly used to determine particle distribution and dispersion. Other tools such as X-ray diffraction (XRD) and Fourier transform infrared spectroscopy (FTIR) have also been used. SEM and TEM are also commonly used in the characterisation of nanoparticles.

The following sections discuss firstly the design choices with regard to the nanoparticle choice. The principle operation of some microscopes is then presented, followed by the characterisation of the nanoparticles using SEM and TEM. This is followed by a discussion on the available methods used to analyse the synthesis dynamics. A manufacturing process that incorporated rheology was used to establish reproducible results and is presented.

4.3 Choice of filler particle types

There has been a large selection of nanoparticles previously investigated and summarised in Table 3-1. Given the various possibilities, two particles were identified and determined appropriate for providing electrical tree resistance and increased thermal performance. These were hexagonal – boron nitride (BN) as well established, and Carbon nanospheres (CNS) as a pilot study. Microscopy as a tool could serve two purposes. The first was characterising particle dimensions, and secondly verifying particle distribution and dispersion. The principle operation of microscopy is presented in the next sub-section. The following sub-sections discuss the design choices for BN and CNS respectively.

4.3.1 The Electron Microscope principle of operation

An illustration of the principle operation of electron microscopes is shown in Figure 4-1 [9]. For TEM and SEM, there is some kind of electron gun source, while in Focused Ion Beam (FIB) the source uses ions. The gun source ejects particle beams and high voltage lenses are used to focus the beam into a fine line. The beam interacts with the surface and different interactions are observed for ions and electrons. When an electron hits the sample surface, different interactions such as backscattered electrons (electron collision removal) and X-rays are generated, or the electron travels through the sample. SEM is based on detection of different backscattered electrons. TEM is based on the electrons transmitted through the sample. Energy Dispersive X-ray spectroscopy (EDS) uses the X-rays emitted to characterise the chemical composition of the materials.

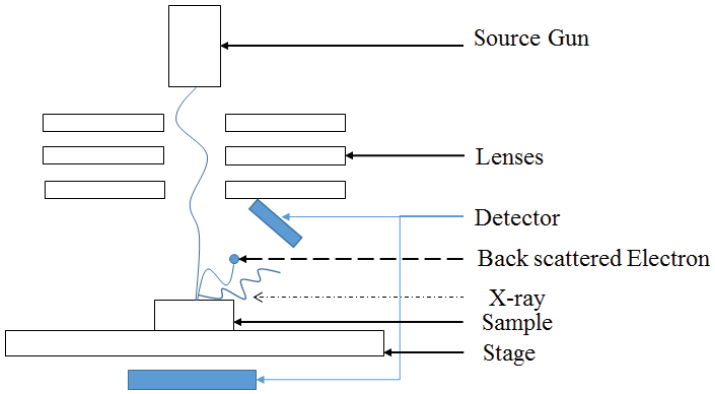

Figure 4-1: The generalised model used for TEM, FIB and SEM microscopes, note, a FIB has a SEM placed 45° to the sample stage [9].

With FIB, in addition to SEM, the ions are sufficiently larger than electrons, which allows for FIB to be used for cutting or digging on a sample surface using a wrecking ball effect. FIB has been used in nanocomposite and nanostructured manufacturing but not necessarily in nanodielectric analysis [9].

One of the fundamental reasons for the development of electron microscopes was the belief that the wavelength of light is the limiting factor on what could be observed. However, using a light microscope, the Nobel prize in chemistry was awarded in 2014 for showing that a light microscope could be used for analysing nanomaterials in a cell [69]. The principle was based on using multiple observation layers, and nanoparticles to illuminate different parts of a cell. It was thus shown

that the wavelength of light is no longer a limiting factor when analysing materials. Therefore, we may start seeing new results on observation of nanoparticles from SEM/TEM in the future.

While SEM/TEM are used as fundamental tools in nanodielectric analysis, there are limitations to consider. Firstly, SEM/TEM has to be operated with a complete vacuum to allow for electron or ion travel. Secondly, EDS cannot be used for elements below Boron and currently have 1-10 monolayer (1 nm) requirements. Although EDS is dependent on X-ray interaction, if after 10 monolayers there is a material change, the scattered X-rays may be of the surface material and not the intended observed material. Thirdly, there is a limitation on the ability to identify nanoparticles with the same atomic number as a host matrix. Lastly, non-metallic samples have to be coated with a few metallic or conductive monolayers in order for the electron interactions to be detected in SEM and to prevent the sample from burning. In this work, A Sigma HD SEM by Carl Zeiss was used for the SEM analysis with a 10 kV operating voltage and all samples were coated with three layers of palladium gold. For TEM an FEI Technai G2 spirit electron microscope operating at 120 kV was used.

For TEM, a sample specimen was prepared by dispersing a few particles in ethanol (1.0 mL) and the mixture sonicated to form a homogeneous solution. A few drops of the homogeneous solution were placed onto a carbon-coated copper grid and the grid dried in ambient air for 30 minutes before inserting it in the microscope. The following subsection discusses the design considerations for BN.

4.3.2 Identifying Boron Nitride

With regard to ceramic or electrically inert nanoparticles which may provide increased thermal particles, some of the considerations are Titania, Silica, Alumina, Aluminium Nitride, and Nano-diamonds Cubic-Boron-Nitride and Hexagonal-Boron-Nitride (BN). Diamond as a bulk material holds first place for being mechanically strong and a good thermal conductor and electrical insulator [45]. The second best material for the same properties is Boron Nitride variants [45]. However, recent studies for nano encapsulates indicate that nanodiamonds do not maintain the same thermal conductivity when downsized to nano levels while

Boron Nitride does [32].

In recent years BN has found increased popularity due to the ability to synthesise variants which are comparable to carbon variants [70]. The appeal of Boron Nitride is firstly it is the second highest thermal conductivity and mechanically strong material to diamond [11], [18], [26], [35], [70]. Hence BN should not adversely affect the electrical conductivity properties of insulation systems. On the one hand, for both cubic and hexagonal BN, it is difficult to create a model in software for simulation unless the particles are assumed spherical.

In this study, Hexagonal BN nanoparticles with an average particle size of 80-90 nm (Xuzhou Jiechuang New Material Technology Co. Ltd.) were purchased for the nanodielectrics and are shown in Figure 4-2 [38]. The following sub-section discusses the design choices for CNS particles.

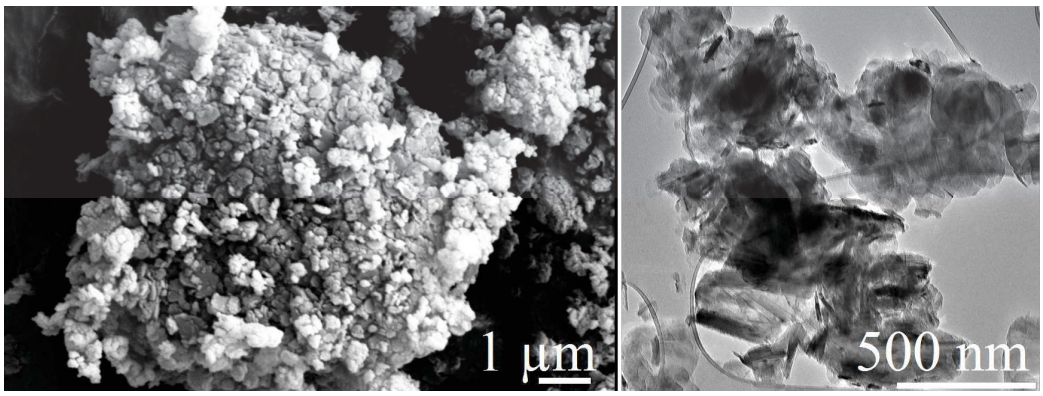

Figure 4-2: Image of received h-BN particle agglomerates showing a collection of rough h-BN particles with varying particle sizes confirming 80-90 nm, SEM on the left, TEM on the right.

4.3.3 Identifying Carbon Nanospheres

Bulk carbon is a better thermal conductor than Boron Nitride with $200-2000\ W/mK$ versus $3-740\ W/mK$ respectively. Apart from diamond, carbon is conventionally understood as an electrical conductor, and intuitively it is inappropriate for electrical insulation [45], [71].

However, recently, Jarvid *et al.* [72], reported encouraging findings on nanocarbon dielectrics specifically Fullerenes (carbon soccer/ Buckyballs) in Cross-linked

polyethylene (XLPE). The fact that carbon is also electrically conductive does not make it an obvious candidate nanofiller material for electrical insulation as highlighted by the nanoparticles evaluated for nanodielectrics in Table 3-1. From the study, Jarvid *et al.* found that the HVDC and space charge characteristics investigated for Fullerenes in XLPE were improved.

Initially the inclusion of carbon as a possible nanofiller material for investigation of HVAC applications was based on curiosity. The idea, however became realistic upon learning that the School of Chemistry at the University of the Witwatersrand could easily synthesise various carbon nanospheres which would be ideal for simulation purposes [73]. Therefore, with electrically conductive nanoparticles considered, CNS particles were selected as possible candidates for nanodielectrics to be investigated in this work. The following sub-section describes the CNS synthesis procedure.

4.3.4 Carbon nanosphere synthesis.

A comprehensive review of the different types of CNSs that have been made and the synthesis techniques that have been used to make CNSs have been described by Deshmukh *et al*. [73]. The manufacturing of the CNSs used in this work is a method described in [73]. [1]

A vertical chemical vapour deposition (CVD) reactor consisting of a hollow tubular quartz reactor (1.5 mm × 32 mm outer diameter) loaded in a furnace was used. A carbon source (acetylene, C_2H_2, from Afrox) and a carrier gas argon (Ar) were used in the CNS synthesis. The furnace was heated to 900 °C at a rate of 10 °C/min under Ar flow of (200 mL/min).

At 900°C, the Ar flow valve was closed and a C_2H_2 flow valve opened at a flow rate of 200 mL/min. Acetylene was pyrolyzed in the quartz reactor at 900 °C for 15 min and the CNS product collected in a round bottomed flask connected at the outlet of the reactor. The acetylene flow valve was closed and the quartz reactor cooled

[1] The synthesis of the CNS was completed and provided by Dr Bridget Mutuma. The author witnessed the synthesis and analysis process. Thanks is extended to Prof Neil Coville for entertaining the idea and Dr Bridget Mutuma for doing the CNS synthesis.

under a continuous flow of Ar gas to ambient temperature. After cooling, the Ar flow was stopped and the quartz reactor removed from the furnace. The products were then purified by soxhlet extraction using toluene in an oil bath heated to 150 °C for 16 hours. The purified product was then dried for 12 hours at 80 °C in a vacuum oven.

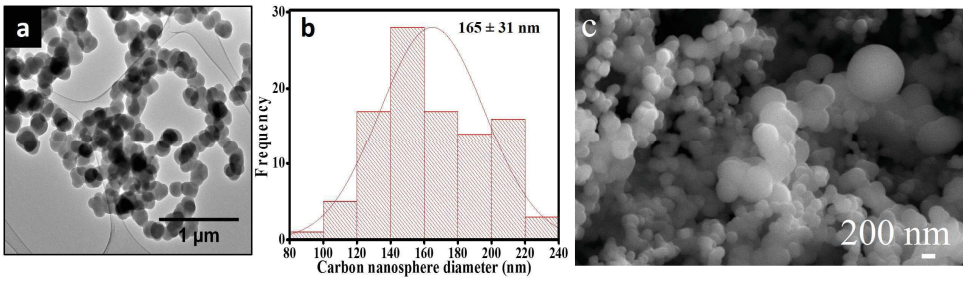

Figure 4-3: TEM image (A), particle size distribution (B), SEM image (C) of the synthesised CNSs.

The morphology of the synthesised CNSs was ascertained by SEM and TEM. The diameters of the CNS images obtained were measured by counting the individual particles. An example TEM and SEM image are shown in Figure 4-3.

As can be seen in Figure 4-3, the CNSs have spherical shapes and diameter sizes between 80 and 240 nm with an average size of 165±31 nm. The small CNS diameter results from the short residence time of the carbon source in the vertically oriented CVD reactor [74].

As can be seen in Figure 4-3, the CNSs form independent balls when the radii are above roughly 70 nm. Below 50 nm the CNSs form long chains of spheres. As the synthesis has not been optimised, there is no fixed size distribution. The CNSs for certain sizes were accreted (chained); however, the particles were deemed sufficiently small to be considered for nanodielectric studies. The CNSs were then used in the synthesis of the nanodielectric. The following section discusses the possible and chosen methods to analyse the material during the synthesis.

4.4 Tools for evaluating particle concentrations.

When analysing nanoparticle suspensions there are two possible tools namely ‘Zetasizer’ which analyses Zeta-potentials and ‘rheology’ which analyses flow

properties. The following sub-sections discuss the principle operation of a zetasizer and rheology.

4.4.1 The principle operation of a Zetasizer

Zetasizers use micro-electrophoresis/electrophoretic light scattering to measure the zeta-potential and average particle size for molecules and nanoparticles [9]. An electric field is applied to a liquid solution/suspension. Particle/molecules move with a velocity related to their zeta potential. Phase analysis light scattering is used to measure the average zeta potential distribution.

By analysing Zeta-potentials, one may obtain information confirming successful surface conditioning where agglomerates have broken down. Additionally, the information may indicate the average particle size of particles or agglomerates. The major limitation with using Zeta-potentials is the nanoparticle suspensions have to be in distilled water as a matrix and be dilute. Therefore, investigating a nanoparticle in a polymer matrix is not always possible, nor determining an optimal concentration. The alternative suspension evaluating medium is rheology. The following sub-section discusses rheology.

4.4.2 The principle operation of Rheology

Rheology is a liquid flow analysis technique. It allows for the ability to investigate particle concentration in a polymer matrix. However, rheology cannot inform on the degree of particle dispersion but only particle distribution in a matrix.

Rheology characterises the flow of matter particles in a system of liquids and has been reviewed in depth by Morrison, Schramm, and Ancey [75]–[77]. A simplified illustration of possible applications of rheological analyses is shown in Figure 4-4. Most liquid systems are either Newtonian or non-Newtonian [75], [76]. Ancey [77] provides a useful review of the non-Newtonian fluid characteristics in some media such as soil in water. Although the review by Ancey [77] only covers particle sizes from 1 µm (individual soil particles) to 1 m (rocks), the concepts and methodology may still be directly transferable to nanometre particles.

Figure 4-5 shows typical rheology parameters and how they are characterised [76]. Some relevant rheological definitions summarised from [38], [75]–[77] are given as follows:

1. The rheological equivalent of Ohm's law is viscosity which describes the resistance to the flow of a liquid. Viscosity is defined as the ratio of shear stress (applied force) to shear rate (rate of deformation measured in reciprocal seconds). The viscosity of a material is the most sought after result of rheology. The shear rate is the ratio of gap dimension to velocity. The shear stress is the ratio of force to area.
2. Liquid systems are either Newtonian or Non-Newtonian. Examples of the possible standard systems are shown in Figure 4-5. Some Non-Newtonian systems are described as thixotropic or rheopexy. In particular, when dealing with either epoxy or polyethylene, these materials are described as Non-Newtonian [25], [37].
3. Thixotropic (shear thinning/pseudoplastic) systems, in general, have decreasing viscosity with increasing shear rate. Rheopexy (shear thickening /dilatant) systems are the inverse of thixotropic systems where they increase in viscosity with increasing shear rate.
4. Non-Newtonian suspensions have seven states/effects, namely Brownian, hydrodynamic, colloidal, turbulence, friction, lubrication and collisions. Each state is dependent on the concentration and size of particles which can characterise the bulk material.

Kashiwagi *et al.* [25] analysed the effect of different shear times and shear speeds in PMMA nanocomposites and correlated rheology data with the critical time for obtaining good distribution in PMMA. Additionally, the work showed that utilising high shear rates allowed for a faster shear for a fixed particle concentration critical mixing time. Nevertheless, rheology has been underutilised as an analysis technique in the material characterisation of nanodielectrics [19], [37]. The following section provides an in-depth discussion of the nanodielectric synthesis process that incorporates rheology as employed in this work.

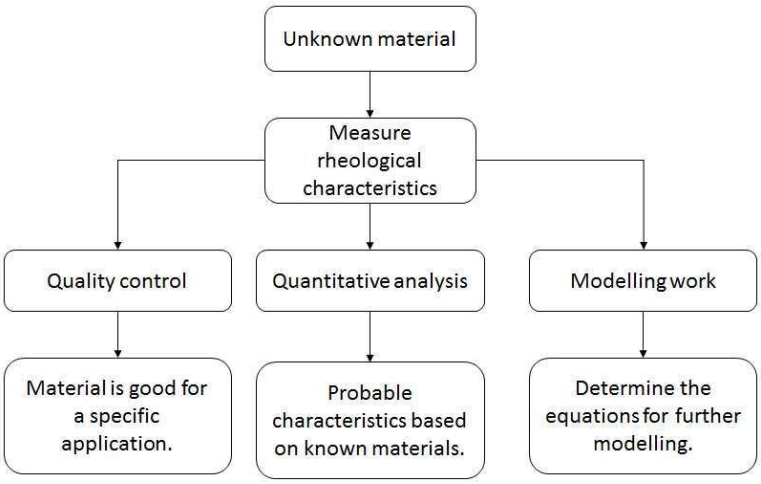

Figure 4-4: Block diagram describing rheological analysis applications [76].

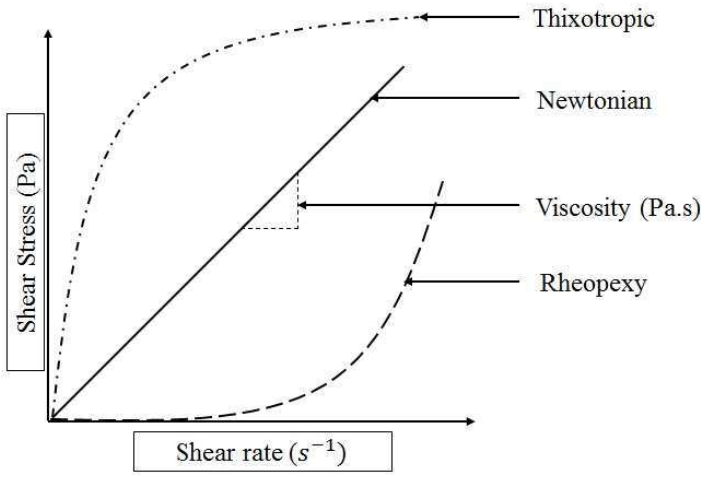

Figure 4-5: Typical flow characteristics of a material determined using rheology [38].

4.5 Nanodielectric synthesis procedure

The synthesis of CNSs and the CNS/filler nanodielectric, and BN/nanodielectric are described in this section. The fluid dynamic properties of the nanodielectric were analysed using rheology to determine the possibility of establishing optimal loading levels of the nanofiller. The rheology results for BN/Epoxy were correlated with SEM results to show a correlation between a minimum in particle concentration viscosities and inter-particle distance.

It is relatively easy to identify particles in SEM/TEM when the filler particles are

metal oxides and the host matrix is made of low atomic number elements which make the particles appear different to the host matrix. However, if the particles are of atomic numbers close to the host matrix, it becomes a challenge to evaluate dispersion or distribution of particles using SEM/TEM analyses. SEM and TEM tests are normally conducted on the end product which is a destructive test and limited in the ability to analyse the final nanodielectric [12].

Work by Tsekmes *et al.* [78] investigated the different effects of dispersion and distribution on the dielectric response of Boron Nitride (BN)-Epoxy nanocomposites. The results showed that samples that had surface modification enabled better dispersion of particles, and had superior thermal performance over unmodified particles.

On a particle, the surface properties as shown in Figure 3-7 (A) are based on the surface potential, Stern layer potential and the Zeta Potential. Fundamentally, surface conditioning changes the particle surface properties and has only been evaluated by investigating the Zeta potential [9]. By increasing or decreasing the zeta potential, the particles either agglomerate or repel each other if the Zeta potential is greater than ±30 mV. This assumes that the particles are in Brownian motion in a liquid, which may not necessarily be valid with nanodielectric manufacturing. Moreover, there needs to be an optimal amount of surface conditioner applied because excess or scarce amounts may result in compromised insulation performance [79].

Ideally, it appears that if good dispersion and distribution (Figure 1-3 D) can be achieved it may unlock the best performance in nanodielectrics. However, if good performance can be achieved with only good distribution and not necessarily good dispersion (Figure 1-3 B), then this may simplify the manufacturing process, and the quest for ideal characteristics may only be of academic importance.

In principle, the mix and test iterative processes and particle modifications are time-consuming, wasteful and may not be feasible if the bulk manufacturing of nanodielectrics is to be realised. Recently, however, attempts to predict optimal loading levels through modelling techniques have shown encouraging results by

Praeger *et. al.* [62]. It can be argued therefore that techniques to pre-determine the optimal loading either at the early stages of the manufacturing process or through modelling would be more efficient than the conventional iterative trial error methods. However, simulation work is dependent on a fundamental understanding of the material characteristics.

As established in the previous chapter, the nanodielectric synthesis approach uses a direct dispersion method. The nanodielectrics were fabricated using a direct dispersion technique with a modification to the epoxy manufacturing process shown in Figure 2-1 [18], [38] as illustrated in Figure 4-6.

Prior work is given in Appendix A [38] allowed for validation and refinement of the manufacturing process. As the purpose of the work was to achieve electrically tree resistant properties with improved thermal performance, as mentioned earlier, BN and CNS were selected as filler types. No surface conditioner was used because of the lack of knowledge on the long-term impact of surface conditioner on nanodielectrics performance. The additional concerns such as optimal surface conditioner amount make surface conditioner unattractive when considering the limited knowledge of the interphase without surface conditioner. As highlighted in Appendix A [38], Araldite CY 231-1 and Aradur HY 925 (obtained from Huntsman ™) is a type of epoxy that is commonly chosen for favourable insulation characteristics in high voltage applications [38], [80]. The following sub-sections detail the different stages in the nanodielectric manufacturing process shown in Figure 4-6.

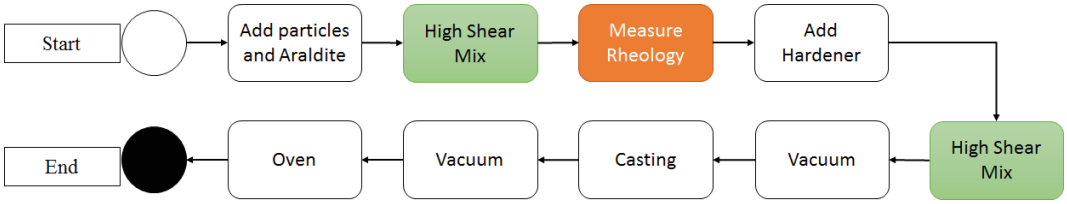

Figure 4-6: Flow diagram showing an adapted form of the generic manufacturing procedure of Epoxy Nanocomposites. The open circle indicates the start and closed circle indicates the end of the process.

One of the challenges when dealing with nanoparticles is the ability to measure amounts using a sensitive mass balance. In the case of CNS shown in Figure 4-3, the particles are conductive and hence electrostatic. Additionally, they have a low density (0.4 g/cm^3), so when attempting to place them in a beaker to determine particle amounts, the particles tend to "jump," out of the beaker. On the other hand, BN, shown in Figure 4-2, with a density of 2.25 g/cm^3, is electrically inert, which is easier to measure using a mass balance. Given these particle measuring challenges, one may be inclined to add the Araldite before the nanoparticles.

With reference to Figure 4-6 and Figure 4-7, **the nanoparticles were added first and then followed by Araldite**. It is also important to note that when doing the high shear mixing, if the sequence is altered the nanoparticles aren't already mixed with the Araldite, and therefore the nanoparticles become airborne and can have adverse health effects if inhaled. Three types of test specimens were manufactured; pure epoxy and BN/Epoxy as controls [38], and C/Epoxy for analysis. An image of the nanoparticles in Araldite before shear mixing are shown in Figure 4-7.

As established by Kashiwagi *et al.* [25], what was required for nanocomposite synthesis was to establish the critical mixing time. This could be achieved with high shear speeds. A Dispermat AE™ device, shown in Figure 4-8, which was available for the shear mixing had an operational maximum rotational velocity of 10 000 rpm. However, operating at that velocity for more than five minutes would result in the device overheating and causing the device protection systems to malfunction. Prior work by Kochetov had used a high shear mixer with 5000 rpm for five minutes with BN in the same epoxy system [79], [80]. However, there was no justification as to the choice of speed or time. It was therefore deemed necessary in the present work to investigate the critical speed and critical time for best results.

A pilot experiment was conducted to establish the critical mixing time by using 5000 rpm and varying the time with 8 wt% of BN in Araldite. The results were then analysed using rheology. The rheology was done using RheolabQC with a Din Coaxial Cylinder (Bob CC27/p4478 and cup C-CC27) see Figure 4-9. A schematic of the rheology measurement instrument is shown in Figure 4-9 with torque, gap distance, and area.

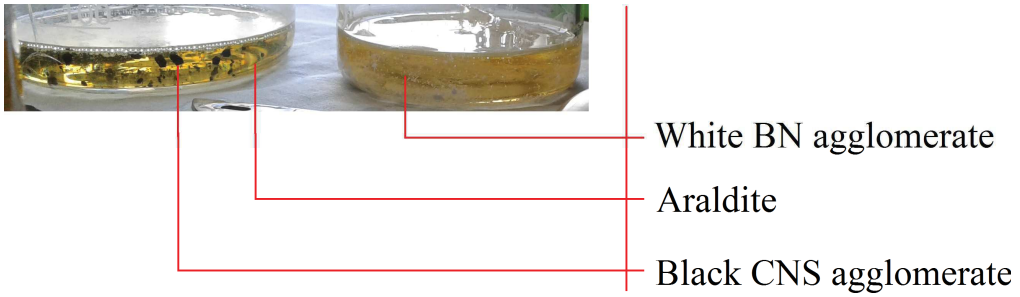

Figure 4-7: Nanoparticles in Araldite mixture before shearing of final sample batch, Carbon Nanospheres left and Boron Nitride right.

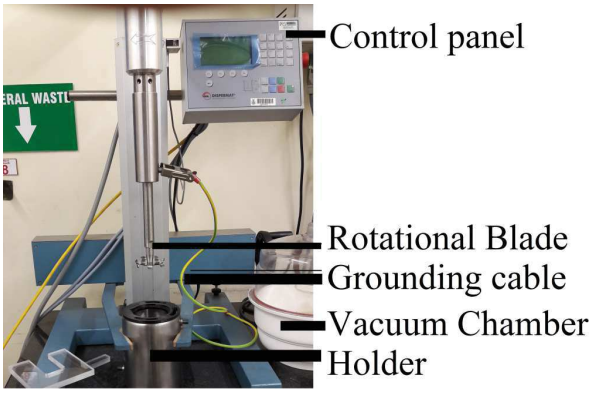

Figure 4-8: Dispermat AE high shear mixing device and Vacuum chamber used in nanodielectric synthesis.

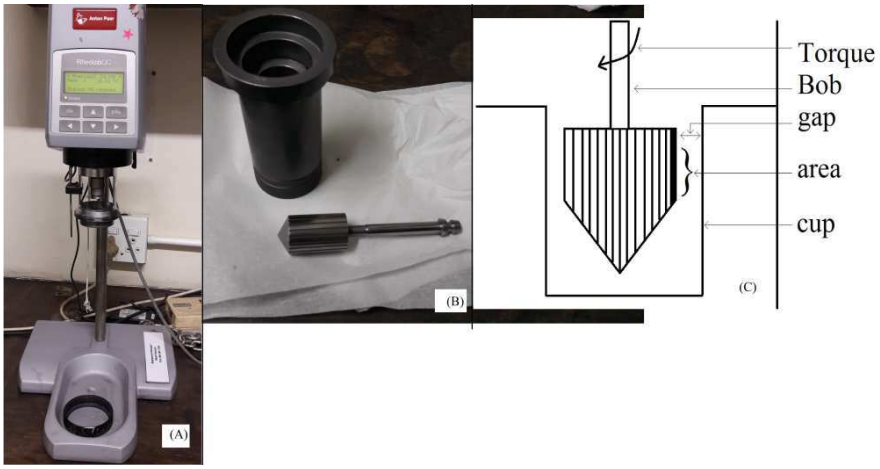

Figure 4-9: Rheolab QC (A), Din Coaxial Cylinder (Bob CC27/p4478 and cup C-CC27) (B) and A schematic diagram of a Din Coaxial Cylinder measurement device with grooves used to measure rheological characteristics [38].

The liquid under test (either Araldite or Araldite with nanoparticles) was added to the cup and the bob was rotated at varying speeds. The rheology analysis involved three shear stages. The first shear stage was a constant 500 s^{-1} for 30 seconds, followed by a rest state for 30 seconds. These initial stages were to remove any shear history still present from the shear mixing process. After the rest stage, a linear shear ramp from 0 s^{-1} to 1500 s^{-1} was applied.

Using the dimensions of the apparatus, the torque and speed were measured. These results were then used to determine the optimal shear rate and shear stress. Using a normalised shear stress and shear rate of 100 s^{-1} the viscosity was then determined and the initial results are provided in Table 4-1.

Table 4-1: Viscosity Shear time for 8 Wt % samples normalised to a shear rate of 100 s^{-1}

Shear time (min)	Wt%	Vol%	Viscosity (Pa.s)
5	7.54	4.18	5.1
10	7.54	4.18	4.1
15	7.6	4.22	4.13
20	7.52	4.17	4.09

Different samples of BN nanoparticles were added to Araldite (8 wt%) to characterise and assess the effect of shear time on the viscosity at 5 000 rpm after different mixing times (5, 10, 15 and 20 min). The results (Table 4-1) showed that the critical mixing time was achieved at 10 minutes. Beyond 10 minutes the viscosity does not change significantly. This confirms the work by Kashiwagi *et. al.* for Epoxy versus PMMA [25] and provided further insight into the fabrication of BN/Epoxy done by Tsekmas *et al.* [18], [38].

For a given wt% loading and shear rate, beyond the critical mixing time, the minimum viscosity achieved saturates and there is no indicated benefit from additional mixing apart from generating heat. It was therefore assumed that shearing at 5 000 rpm for 10 min would be sufficient time and speed/shearing rate for use at lower concentrations of both C/Araldite and BN/Araldite. As mentioned earlier, the densities of the h-BN and CNS was 2.25 g/cm^3 and 0.4 g/cm^3

respectively. Immediately after shearing the Araldite-nanoparticle mixture was analysed using rheology.

The rheology tests characterised the different Araldite-nanoparticle systems based on the various volume fractions indicated in Table 4-2. The results of the shear ramp are shown in Figure 4-10, Figure 4-11, Table 4-3 and Table 4-4. This analysis was repeated three times with three independent samples, one immediately after shearing, 1 hour after shearing, and 2 hours after shearing to observe settling time of agglomerates.

Table 4-2: Sample Details of Epoxy and Nanocomposites. Note 0 % is pure epoxy.

Weight Percentage of nanofiller (wt%)		Volume Fraction of nanofiller (%)		Araldite and nanofiller Viscosity (Pa. s)
Araldite and nanofiller	Araldite, nanofiller and hardener	Araldite and nanofiller	Araldite, nanofiller and hardener	
Hexagonal Boron Nitride				
0	0	0	0	7.08
0.98	0.5	0.51	0.26	5.15
2.02	1.03	1.05	0.55	4.84
2.98	**1.53**	**1.56**	**0.81**	**4.7**
3.96	**2.04**	**2.08**	**1.09**	**3.63**
4.9	**2.35**	**2.43**	**1.25**	**4.66**
4.58	2.53	2.59	1.35	5.14
5.92	3.08	3.14	1.65	6.35
6.96	3.64	3.72	1.96	5.69
8.02	4.22	4.3	2.27	6.28
Carbon nanospheres				
0.21	**0.11**	**0.694**	**0.325**	**2.9**
0.21	**0.11**	**0.696**	**0.328**	**4.01**
0.53	0.29	1.84	0.84	7.37
1	**0.53**	**3.34**	**1.57**	**2.74**
1.81	0.95	5.71	2.78	4.89

[a] Note 0 % refers to pure epoxy.

The optimal filler loading that gives optimal particle distribution has been postulated as that which gives a resultant mixture with a viscosity curve that matches that of the host material [37]. Hank *et al.* [38] showed, using rheology and SEM, that 4 wt% loading was better distributed compared to 2 wt% and 8 wt% BN in a BN/Epoxy nanocomposites.

From Figure 4-10, Figure 4-11, Table 4-3 and Table 4-4 and Appendix A [38], the first observation to note is that the Araldite is non-Newtonian in nature and the composite shows a slight rise in viscosity until a shear rate of ~100 s^{-1} followed by a slight decrease in viscosity until the yield point is met. After this yield point all materials show a decrease in viscosity.

Given that the Araldite general "shape" profile of viscosity versus shear rate does not change, but is shifted up/down the viscosity axis for different loading levels of BN/Araldite and C/Araldite, the viscosity was normalised to 100 s^{-1} indicated by the line in Figure 4-10 (A) - (D). The data is summarised in Figure 4-11 (A) for BN/Araldite and (B) for C/Araldite with the viscosity measurements given in Table 4-3 and Table 4-4. Figure 4-11 also shows the other normalised rheology results for the different times used for the Araldite-nanoparticle mixtures.

From Figure 4-11, the different possible suspension situations presented by Ancey [77] are evident. Generally, for both C/Araldite and BN/Araldite, initially, a steep decrease in viscosity is seen which indicates a Brownian motion region, which is then followed by a hydrodynamic/colloidal interaction region. For the h-BN, given that the density of the particles (2.25 g/cm^3) is double that of Araldite (1,18 g/cm^3), any agglomerates present appear to sediment and the viscosity within the hydrodynamic region (1-2%) appears to be faster (lower viscosity) for the rheology for BN/Araldite after one and two hours.

Increasing the concentration of the particles brings the Araldite-nanoparticle mixture into the colloidal interaction region which causes particles to be attracted to each other and overcome the viscous drag of the Araldite with their Van der Waals forces and agglomerate. The viscosity increases until the agglomerates are sufficiently large to begin turbulence effects. In the turbulent effect region, the

viscosity decreases until the point where particles are in contact that a slurry is formed and the bulk viscosity increases again. The general shape of the normalised rheology results shown in Figure 4-11 is similar to that of glass transition temperature variation with loading presented by Shengtao Li *et al.* [63] and is in agreement with the theory presented by Ancey [77]. The behaviour is also in agreement with the theoretical model for bulk properties of nanocomposite materials as presented by Praeger *et al.* in [62].

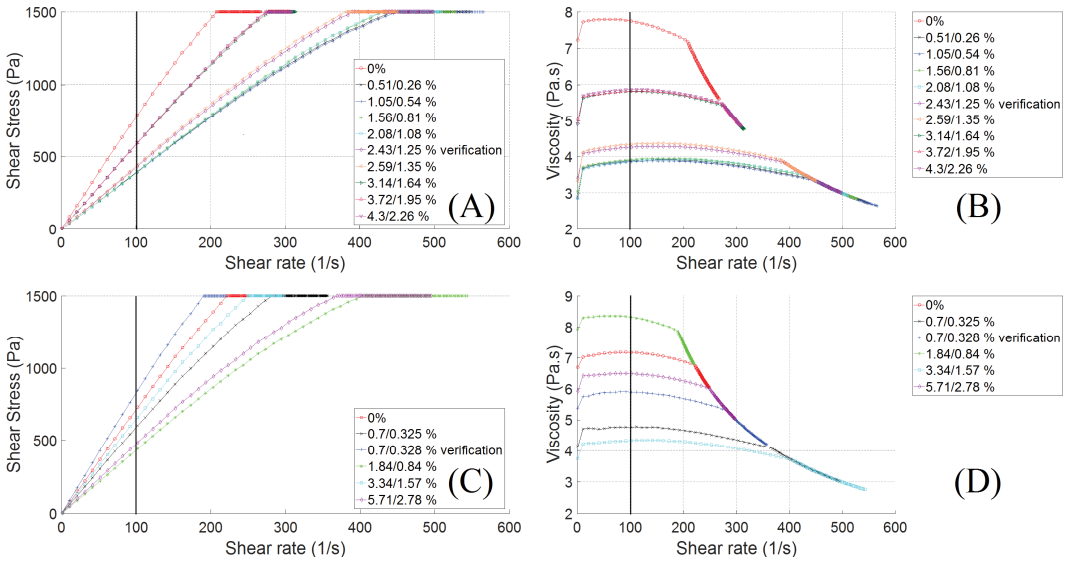

Figure 4-10: Raw rheology results for the different volume fractions for BN/Araldite in (A) and with Viscosity in (B), the C/Araldite in (C) with the C/Araldite Viscosity in (D).

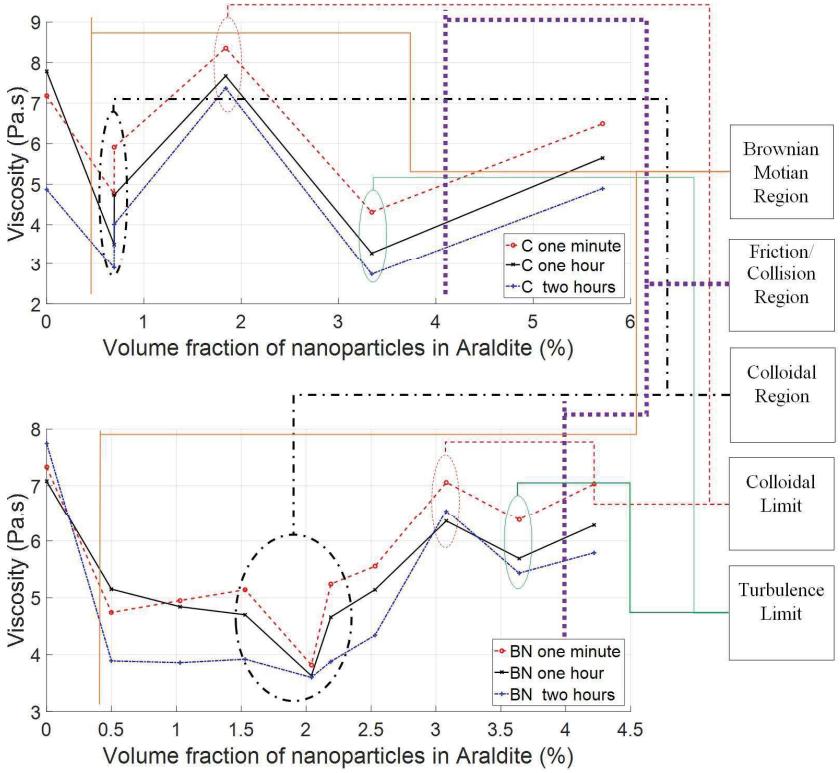

Figure 4-11: Rheology results showing the normalised rheology results at a shear rate of 100/s and different rheology regions with the C/Araldite results in (A) and the BN/Araldite results in (B).

Table 4-3: BN/Araldite normalised Viscosity results at a shear rate of 100/s.

Volume fraction of particles in Araldite (%)	Viscosity after 1 min (Pa. s)	Viscosity after 1 hour (Pa. s)	Viscosity after 2 hours (Pa. s)
0	7.33	7.08	7.75
0.98	4.74	5.15	3.89
2.02	4.95	4.84	3.86
2.98	**5.14**	**4.7**	**3.92**
3.96	**3.82**	**3.63**	**3.6**
4.9	**5.24**	**4.66**	**3.88**
4.58	5.55	5.14	4.34
5.92	7.06	6.35	6.54
6.96	6.38	5.69	5.43
8.02	7.03	6.28	5.79

Table 4-4: C/Araldite normalised Viscosity results at a shear rate of 100/s.

Volume fraction of particles in Araldite (%)	Viscosity after 1 min (Pa. s)	Viscosity after 1 hour (Pa. s)	Viscosity after 2 hours (Pa. s)
0	**7.18**	**7.79**	**4.87**
0.694	**4.76**	**3.51**	**2.9**
0.696	**5.91**	**4.74**	**4.01**
1.84	8.36	7.67	7.37
3.34	4.31	3.29	2.74
5.71	6.49	5.65	4.89

From Figure 4-10, Figure 4-11, Table 4-3 and Table 4-4, it was previously suggested that the viscosities which match the viscosity of the pure polymer may be optimally loaded [37]. The results show distinct minimum viscosities based on particle loading level. However, careful consideration must be taken with regard to the region the particles are in. BN/Araldite has one minima point within the colloidal region. Whereas C/Araldite has minimums in two regions.

However, because the second minimum occurs in the turbulent region, it cannot be considered as optimal. Therefore, a key conclusion from the rheology analysis is the postulation that the samples with optimal distribution are minimum points within the hydrodynamic/colloidal interaction regions. In the present case, it would be 2.08/1.09 vol% to 2.59/1.35 vol% in BN/Araldite, and 0.7/0.33 vol% in C/Araldite (viscosity results bold in Table 4-2). The notation (A/B vol%) is where A is the volume percentage of a particle in Araldite and B is volume percentage of particles in complete epoxy.

Once the rheology analysis was completed the hardener was added in a ratio of 100:92 for the Nanoparticle-Araldite mixture to hardener in accordance with the manufacturer data sheet. An image of the mixtures before shearing is shown in Figure 4-12. This final mixture was sheared again at 5000 rpm for 10 min, an image of the nanodielectric mixtures during shearing is shown in Figure 4-13. The shearing process creates a doughnut effect during the mixing which results in a chaotic environment. This process also generates nano and micro bubbles which

need to be removed. After shearing, the samples are placed in a vacuum chamber for 3 hours to extract air bubbles, this is shown in Figure 4-14.

Aluminium moulds shown in Figure 4-15 were coated with epoxy release agent (QZ 13 from Hi-Tech Polymers cc) and preheated to 140^oC (material data sheet curing temperature). If the liquid mixture was placed into the moulds before being placed in the vacuum chamber, the moulds became compromised. The degassing causes the bubbles and overall nanodielectric mixture to rise as nano bubbles are extracted. This results in either the holders in Figure 4-15 bonding to the mould in the case of moulds used for electrical tree samples, or the mixture overflowing out of the mould. If the moulds were not preheated, there is a temperature differential which causes the epoxy not to cure properly with undesired consequences such as trapped mechanical stresses.

The epoxy mixtures after degassing were then poured into the preheated moulds. However, the process of pouring the mixture into the moulds introduces bubbles again. The moulds were then placed back into the vacuum chamber to remove bubbles and left for 20 minutes, a reasonably short time that was to ensure that sufficient vacuum was achieved but also to prevent the moulds from cooling for too long. The moulds were then placed in an oven at $140\ ^oC$ to cure for 16 hours. The oven was then switched off and the samples were left to cool to room temperature for 5 hours before being removed from the oven and moulds.

An example of a sample batch is provided in Figure 4-17. The images presented in Figure 4-7 to Figure 4-17 are part of the final manufactured samples used to confirm repeatability of the experimental results. The samples were then analysed using SEM for surface characterisation.

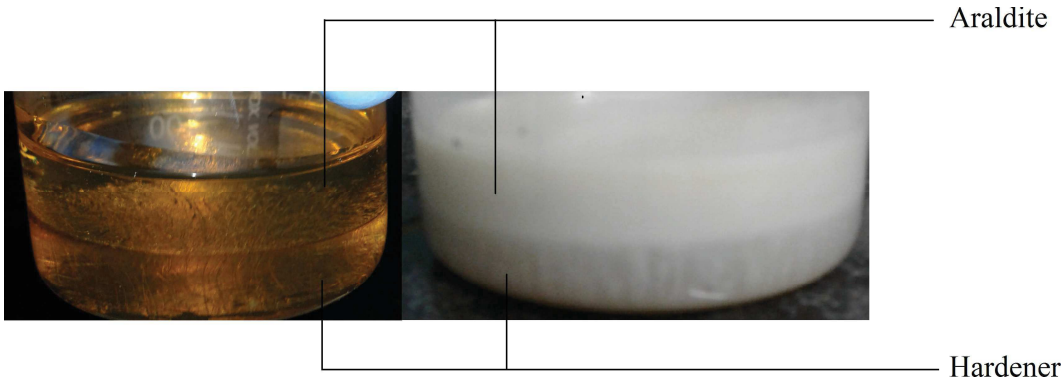

Figure 4-12: Image of Araldite with hardener added showing discolouring for pure and BN/Epoxy before shearing. Note the hardener is denser than the Araldite and the crosslinking process has begun as seen by the small channels in the pure epoxy.



Figure 4-13: Image of C/Epoxy and BN/Epoxy during the shearing process.



Figure 4-14: Images of bubbles being extracted in the samples after shearing, pure epoxy (left) BN/Epoxy (middle), C/Epoxy (right).

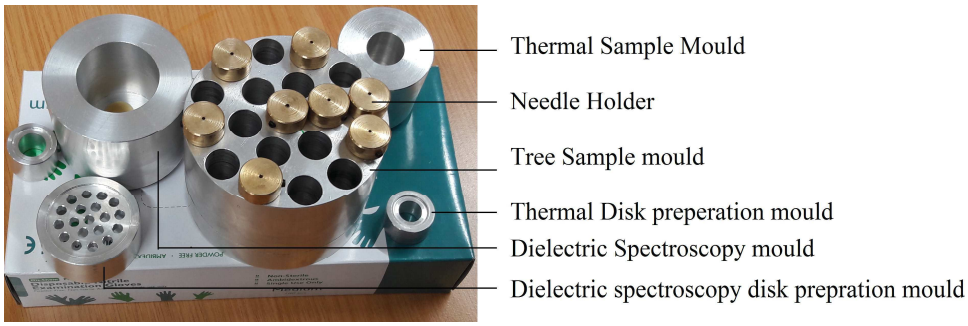

Figure 4-15: Aluminium moulds used for the manufacture of different epoxy samples with copper holders fitted with grub screws to hold needles for electrical tree experiments.

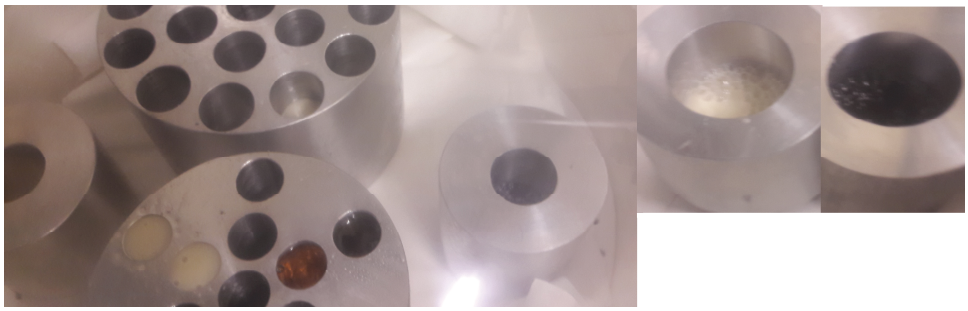

Figure 4-16: Aluminium moulds used to remove gas bubbles introduced from pouring the samples.

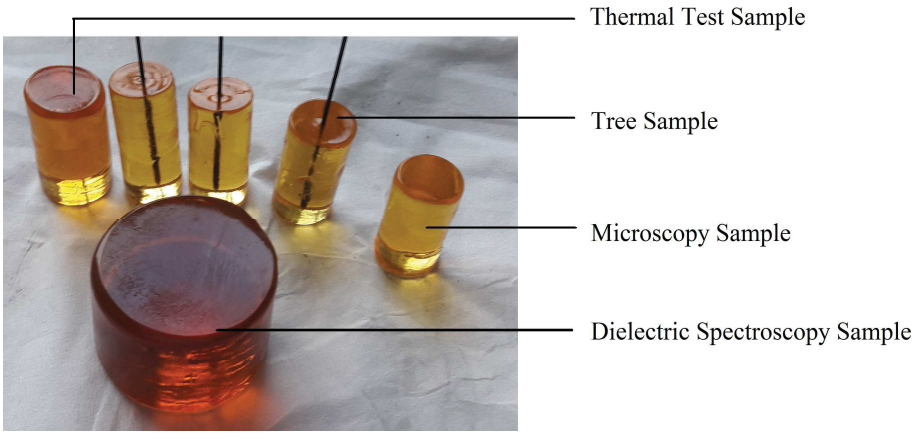

Figure 4-17: Image showing an example of final manufactured sample batch of pure Epoxy.

4.6 Verification of optimal filler loading using Scanning Electron Microscopy.

This section provides details on the first attempts to validate the rheology results. The following sub-sections discuss the SEM analysis for BN/Epoxy and the attempt at characterising the C/Epoxy using SEM.

4.6.1 Sample preparation methodology

The samples were analysed with SEM by preparing cylindrical disks. Cylinder samples were taken and sliced into disks. After slicing, the disk samples were surface conditioned (smoothed) using five stages of sandpaper polishing, sequentially starting at 220 mm, 1200 µm, 9 µm, 3 µm, and ending with 1 µm. The last two stages also required 1 µm diamond grinding paste. These disks were then cleaned with ethanol and distilled water to remove any residues and dust. The disk was then coated with three monolayers of palladium-gold to prevent melting of the sample. A Sigma HD SEM by Carl Zeiss was used for the SEM analysis with an operating voltage of 10 kV. Two images for SEM magnifications were investigated, 1 µm and 200 nm. The results presented here are on the 1 µm and 200 nm.

Figure 4-18 and Figure 4-19 give the Energy Dispersive Spectroscopy (EDS) results of the as received BN particles showing a contaminant and characterisation. Figure 4-20 and Figure 4-21 show the pure epoxy sample surface and the effect of high magnification on the image of epoxy. Figure 4-22 gives a sample surface comparison of the different BN loading levels from Table 4-2.

One of the significant results is the crack formation of the pure epoxy due to high electron bombardment on the surface. The next significant result is the change in sample surface texture as a result of the increased filler particle loading which allows for some correlation to be drawn from the rheology results.

Upon closer investigation, Figure 4-23 of the 1.09 vol% BN/Epoxy shows individual and relatively few small clumps of BN particles all fairly uniformly distributed. In contrast, a much lower loading of 0.55 vol% also Figure 4-23 has more and much bigger clumps with fewer individual particles and not as uniformly

distributed as 1.09 vol%. The final outcome of this SEM analysis on the BN/Epoxy samples indicates a strong correlation between the surface texture and rheology results notwithstanding the presence of agglomerates.

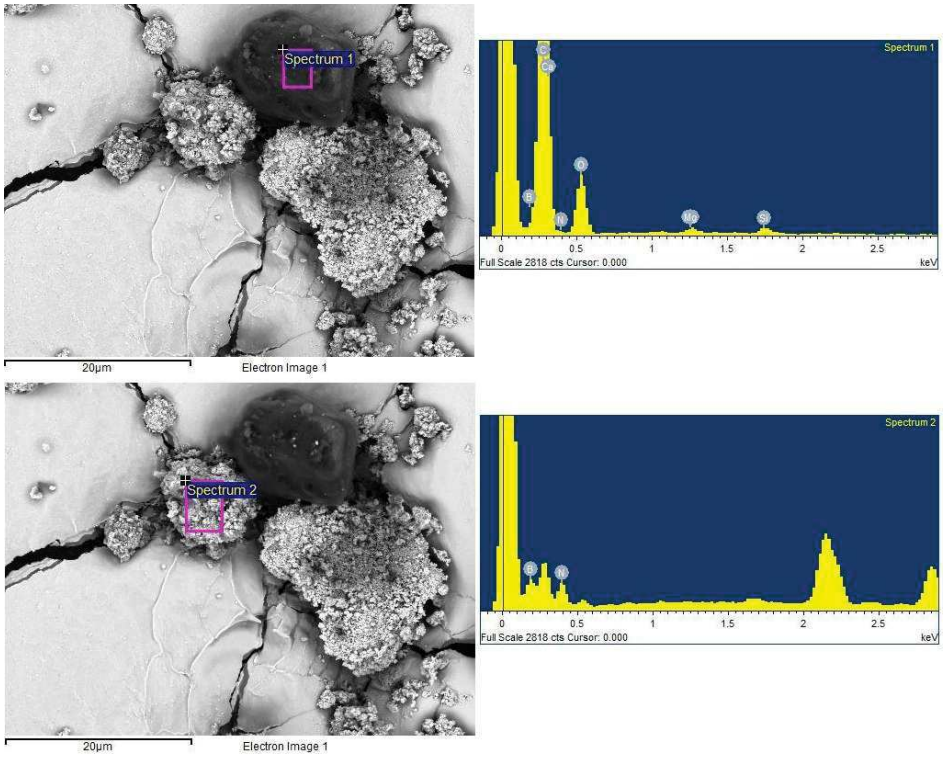

Figure 4-18: Image showing EDS investigation results of as received BN particles.

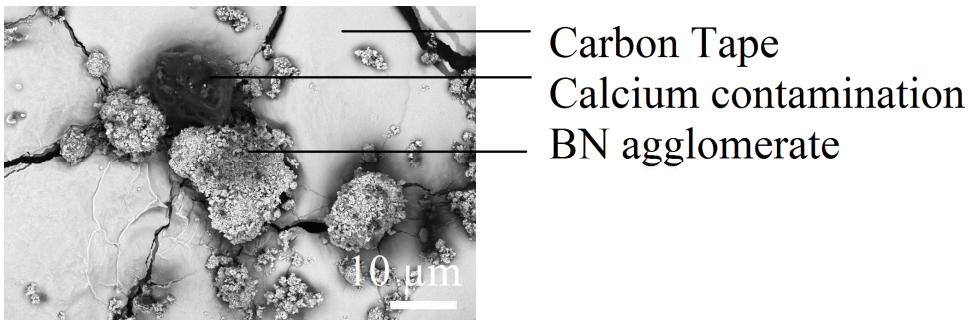

Figure 4-19: Backscatter SEM image of received Boron Nitride submicron particles.

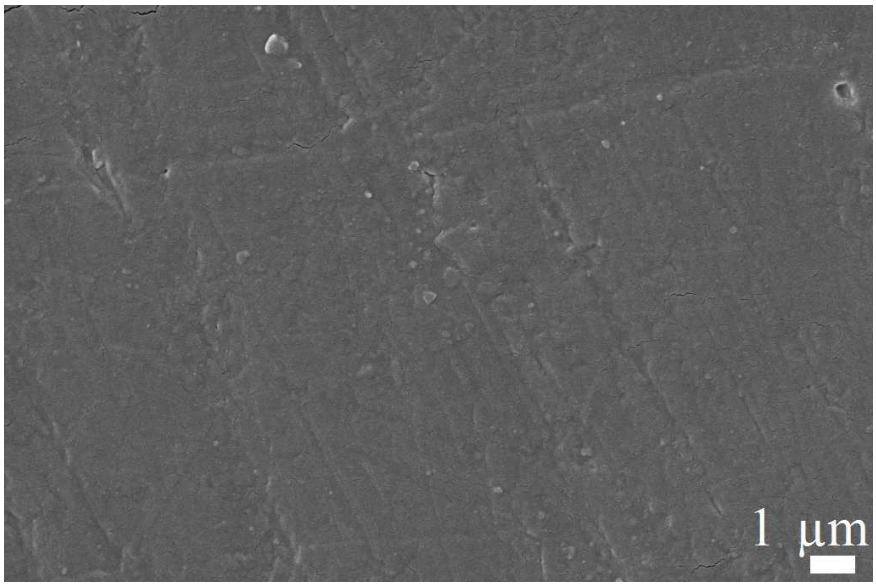

Figure 4-20: SEM image of the pure epoxy after surface polishing showing solid sample surface with good surface binding.

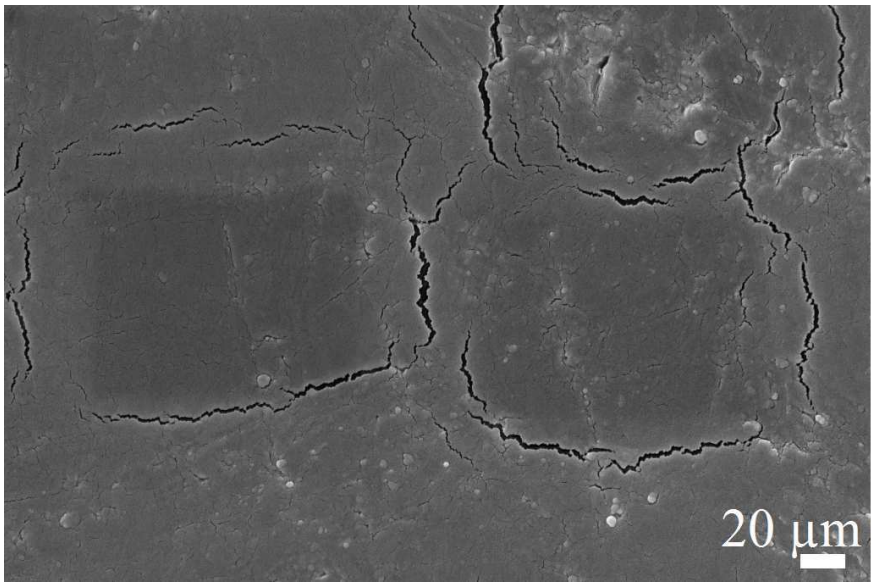

Figure 4-21: Clean epoxy sample showing crater marks after 200 nm observations, spots of dust on the surface.

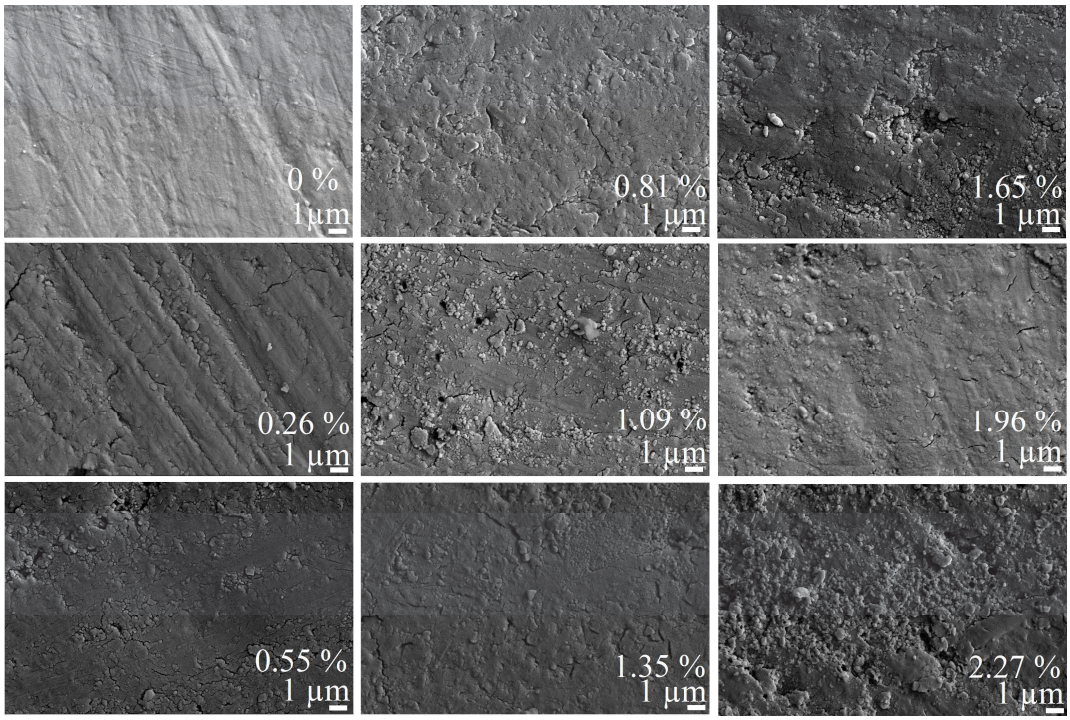

Figure 4-22: Sample surface comparison of different BN/Epoxy loading levels using SEM.

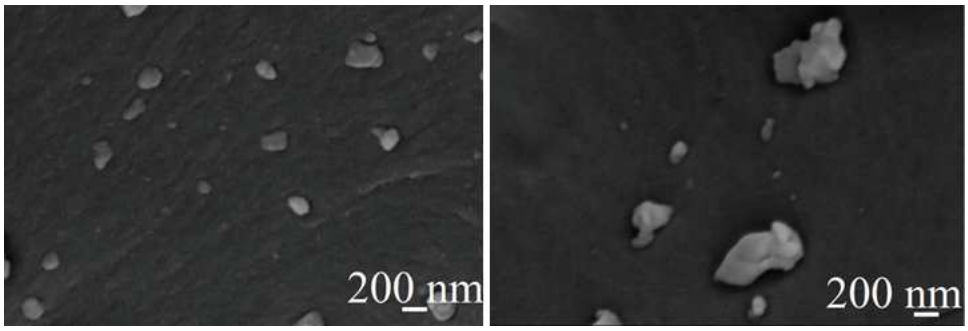

Figure 4-23: SEM image showing surface of 1.09 vol% BN/Epoxy nanodielectric (left) with individual and large clusters of particles well distributed and 0.55 vol% (right) BN/Epoxy nanodielectric with larger clumps of particles poorly distributed.

4.6.2 C/Epoxy SEM analysis

As for the BN/Epoxy a similar SEM analysis was applied to the C/Epoxy samples, examples are shown in Figure 4-24. There is clearly a distinction in surface texture difference between a heavily loaded and lightly loaded sample as shown. However, the particulates/textures on the surface could not be validated as CNS particles using

EDS. In the case of BN, EDS could be used, but since the epoxy matrix is a carbon based polymer it prevents CNS from being detected as individual particles.

The ability to detect the individual particles was significant because some dispersion and distribution level techniques based on SEM image processing software relies on the difference in surface contrast. Therefore, alternative methods were needed to quantify particle distribution in C/Epoxy. Given the inability to identify particle differences of CNS in Epoxy, there was a need for another surface characterisation technique. This technique is discussed in the next chapter.

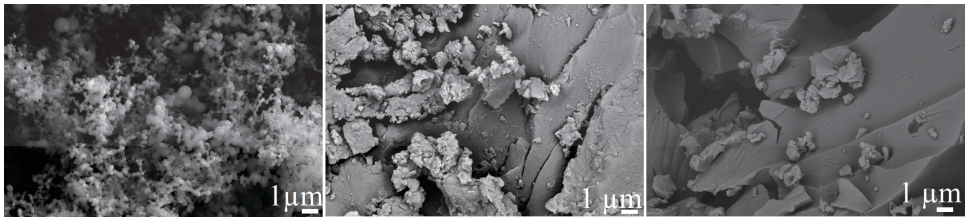

Figure 4-24: SEM images of CNS particles (left) C/Epoxy with 2.78 % (middle) and 0.33 % (right).

4.7 Conclusion

This chapter began by discussing the consideration for particle choice and operation of electron microscopes. The different particle choices of CNS and BN was highlighted for electric conducting and non-conducting particles. A discussion between the possible suspension analysis tools was provided between rheology and zetasizers.

Rheology was chosen and a comprehensive nanodielectric synthesis procedure was outlined. The rheology results indicated a possible optimal loading level based on the minima which occur in the hydrodynamic region in viscosity results.

A key conclusion from the rheology analysis is the postulation that the samples with optimal dispersion are points within the hydrodynamic/colloidal interaction regions. In the present case, it would be 2.08/1.09 vol% to 2.59/1.35 vol% in BN/Araldite, and 0.7/0.33 vol% in C/Araldite.

SEM results on the BN/Epoxy samples showed a change in surface texture between

the BN/Epoxy samples and a correlation could be drawn between the inter-particle distance of BN particles and the minima in rheology. The same SEM analysis could not yield useful results for C/Epoxy as the particles could not be confirmed in epoxy using EDS. Finally, it was concluded that a different technique would be required for C/Epoxy.

The following chapter discusses dielectric spectroscopy and Atomic Force Microscopy as alternatives for characterising the different nanodielectrics and further validation of the optimal loading values from the rheology based analysis. The dielectric spectroscopy results provide insight into the permittivity and conductivity of the nanodielectrics. Especially the 1.09 vol% BN epoxy and 0.33 vol% C/Epoxy samples. The Atomic Force Microscopy results provide insight into the interphase properties around the nanoparticles.

CHAPTER 5 : THE AFM AND DIELECTRIC SPECTROSCOPY CHARACTERISATION OF THE C/EPOXY AND BN/EPOXY NANODIELECTRICS

"My mission in life is not merely to survive, but to thrive; and to do so with some passion, some compassion, some humour, and some style." – Maya Angelou

5.1 Introduction

This chapter provides insights into the interphase and dielectric spectroscopy (DS) properties for the different nanodielectrics. In the previous chapter, optimally loaded nanodielectrics were identified using rheology. For Boron Nitride (BN)/Epoxy, the rheology results could be correlated with Scanning Electron Microscopy (SEM) analysis results. However, similar correlations could not be identified for Carbon Nanosphere (CNS) C/Epoxy due to Energy dispersive spectroscopy (EDS) constraints. Dielectric spectroscopy (DS) or Atomic Force Microscopy (AFM) may provide insights into the CNS distributions. The following chapter begins by providing a background into the principle operation of AFM, DS, and the interphase properties. The results and discussions are then presented.

5.2 Background

In Chapter 3 it was established that various interphase models have been developed to explain the science of nanodielectrics. Based on the models discussed there are several properties of the interaction zone or interphase which provide the nano-effect observed in the nanodielectric. Firstly, the interphase is the region around the nanoparticle which is different to the particle and host matrix. There are possibly several regions around the nanoparticle which may be a result of filler particle surface conditioning. As the nanodielectrics in this work were not surface conditioned there may only be one region around the particles. According to the literature, the interphase is possibly in the region of ~10-25 nm and depends on particle size, particle shape, and inter-particle relationships.

Previous work by Roy et. al.[81] in 2005 and Seiler and Kindersberger [20] in 2014 provided some investigations and evidence into the existence of the interphase. Using AFM analysis techniques, they showed that by considering the location of the particle the increased apparent particle size was due to the presence of the interphase. The following sub-section discusses the principle operation of AFM.

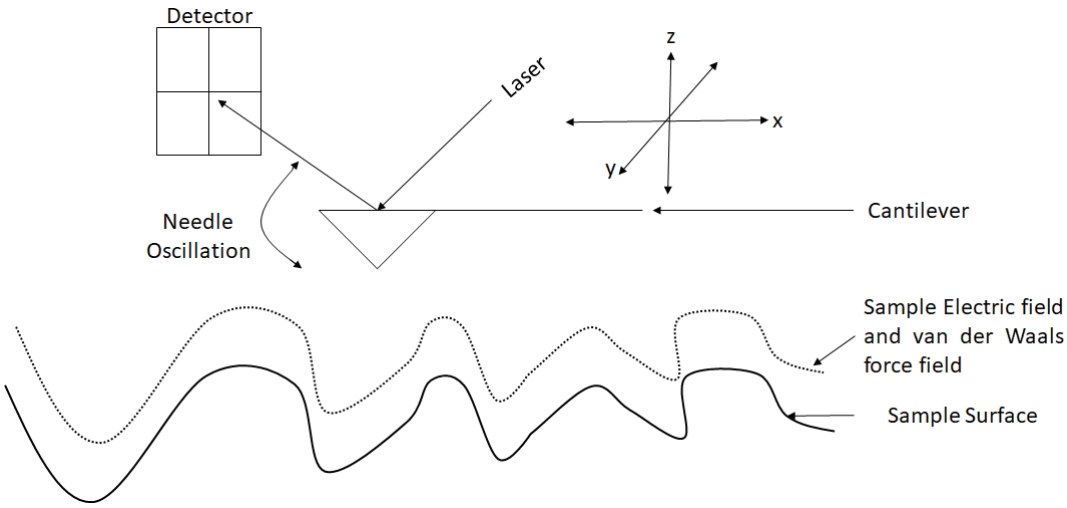

Figure 5-1: The generalised principle operation of an Atomic Force Microscopy showing the cantilever interacting with sample force fields and sample surface[9].

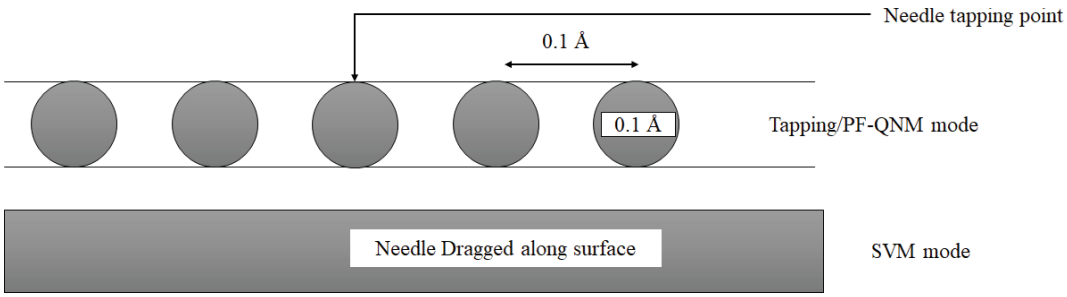

Figure 5-2: Top down view of AFM measurement operation details for Tapping mode, PF-QNM, and SVM. Å or Ångstrom is a unit of measure defined in Section 3.2. In tapping mode, the cantilever does not touch the sample surface. While in PF-QNM and SVM modes the cantilever is in direct contact.

5.2.1 The principle of AFM

AFM is a surface analysis technique like SEM or TEM, but the major benefit is that it does not require a vacuum chamber to perform the analysis. AFM may also be used to analyse liquid samples while both SEM and TEM require solid samples because of the vacuum conditions. A detailed explanation of the principle operation of any AFM is provided in these textbooks [9], [82]. One of the main forms of AFM analysis is tapping mode, with a schematic diagram explaining the operation shown in Figure 5-1 and Figure 5-2 [82].

A laser is shone on a cantilever and the cantilever is driven to resonant oscillation frequency using the piezo-electric material to oscillate at the cantilever resonant frequency. The cantilever tip radius and hence resolution is 0.1 Å. As the cantilever approaches the sample surface, the cantilever interacts with the van der Waals and electrostatic forces of the material.

There are several modes which can be employed by using an AFM such as tapping mode, scanning voltage mode (SVM) and Peak Force Quantitative Nanomechanical Mapping (PF-QNM). The different measurement techniques for tapping, SVM, and PF-QNM modes are illustrated in Figure 5-2 [9]. In tapping mode, as the tip approaches the surface, the cantilever experiences resistance to the oscillation, and a control system changes the height to maintain the oscillation. Changes in height are detected by the laser and recorded to obtain a height image [82]. It is important to note that while in tapping mode, the cantilever is not in direct contact with the sample surface.

While in SVM or PF-QNM mode, the cantilever is placed in direct contact with the sample surface. The difference between PF-QNM and SVM measurement techniques is illustrated in Figure 5-2. While in contact, with SVM an electric potential is measured and can be used to determine conductive pathways on a surface or residual charge [82]. PF-QNM is a relatively innovative technique in AFM analysis. PF-QNM is used to characterise the mechanical properties such as elastic modulus, surface adhesion, and dissipation energy of a material surface in the nanometre scale.

As illustrated in Figure 5-1, in the PF-QNM mode, the force as a function of tip-sample separation (force volume curve) is recorded and the Derjaguin, Muller and Toporov model (DMT) Young's modulus, adhesion force and dissipation energy can be extracted in real time [83], [84].

When Seiler and Kindersberger [20] presented evidence on the interphase for Silica particles in Epoxy, they used AFM in tapping mode. They attempted to account for differences in particle placement based on surface roughness (the average distance between low and high points on the surface).

The tapping mode methodology used indicated that the apparent particle sizes identified were larger compared to the pure particles. The differences were in the hypothesised region of 10-25 nm and hence an early conclusion was drawn to solidify the idea of the interphase being limited to 10-25 nm. The following section discusses how AFM was used in this work to characterise the pure epoxy, and subsequently the interphase in BN/Epoxy and C/Epoxy nanodielectrics.

5.3 Atomic Force Microscopy characterisation of the interphase region of the nanodielectrics

The rheology results presented earlier indicated that 1.09 vol% – 1.35 vol% BN/Epoxy and 0.33 % C/Epoxy were optimally loaded. Hence, PF-QNM analysis was done by the author while on a research stint at Uppsala University in Sweden[2]. An Auger Bruker Mode 8 AFM was used for the PF-QNM analysis.

5.3.1 AFM experimental methodology.

As with SEM, the samples were analysed by preparing cylindrical disks. After slicing, the disk samples were surface conditioned (smoothed) using seven stages of sandpaper polishing, sequentially starting at 220 mm, 1200 µm, 9 µm, 3 µm,

[2] The author wishes to extend gratitude to Hu Li and Klaus Leifer at Uppsala University for providing the training, fundamental understanding and use of the equipment to obtain the AFM results.

1 µm, 100 nm and ending with 50 nm. The samples were then cleaned with distilled water and ethanol to remove any residual dust and any other contaminants.

Note as mentioned earlier, PF-QNM analysis required the cantilever needle to make contact with the sample surface. Given PF-QNM analysis has a similar method of analysis to Tapping mode as indicated in Figure 5-2, the height details of a surface were also acquired. Two tests were performed, surface characterization and surface evolution.

As it is difficult to gauge the exact location of the particles since the particles are embedded inside the epoxy, a custom made PF-QNM analysis procedure was developed to both validate the particles and the interphase in the matrix shown in Figure 5-3. Below 600 nN, the cantilever did not penetrate the sample surface deep enough to interact with the particles in the matrix and hence the observed characteristics were just that of the epoxy.

The surface characterisation involved applying a force of 600 nN to characterise the sample surface. This allowed for areas of interest to be identified such as particles, cross-linked grain boundaries, and non-particle properties. It was then attempted to increase the applied force in increments of 100 nN until 1000 nN for C/Epoxy and 700 nN for BN/Epoxy. The BN/Epoxy could only be increased to 700 nN as the material was relatively hard and resulted in the needle tip breaking (200 € per needle tip)! The surface evolution allowed for confirmation of both the interphase and particles to be confirmed for the surface characterisation. The following section presents the results of the surface characterisation and surface evolution.

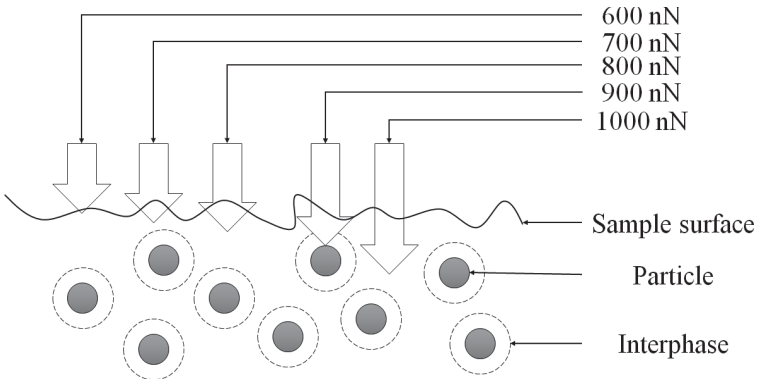

Figure 5-3: Side view showing custom designed surface evolution using PF-QNM AFM on optimally loaded BN/Epoxy and C/Epoxy to establish particles, epoxy, and interphase.

5.3.2 PF-QNM results and discussion.

The Young's modulus and height results of the base epoxy and the nanocomposites are summarised in Table 5-1 and the corresponding images presented in Figure 5-4 to Figure 5-8. The results of the surface characterisation are shown in Figure 5-4 to Figure 5-6. Note, surface roughness indicates the average height along the surface in Table 5-1.

Table 5-1: AFM properties of Epoxy and Nanodielectrics.

	Average surface Young's modulus (GPa)	Particle Young's modulus (GPa)	Surface Roughness (nm)
Epoxy	1.7	N/A	3.4
C/Epoxy	4.9	7-7.5	6.3
BN/Epoxy	34.9	55-56.8	3.24

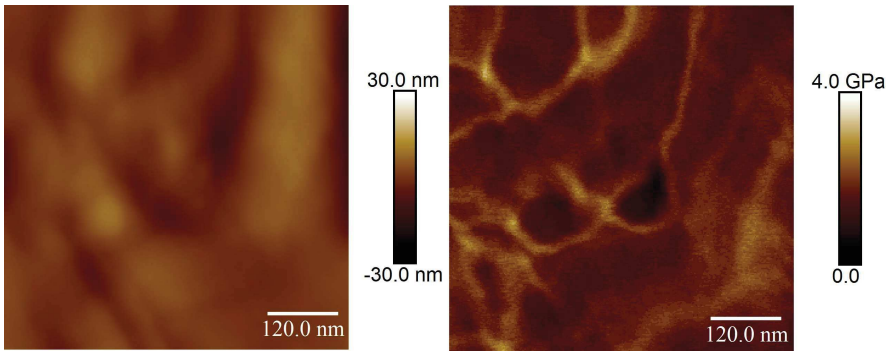

Figure 5-4: PF-QNM Analysis at 600 nN on pure epoxy, surface height (left) and mechanical properties (right).

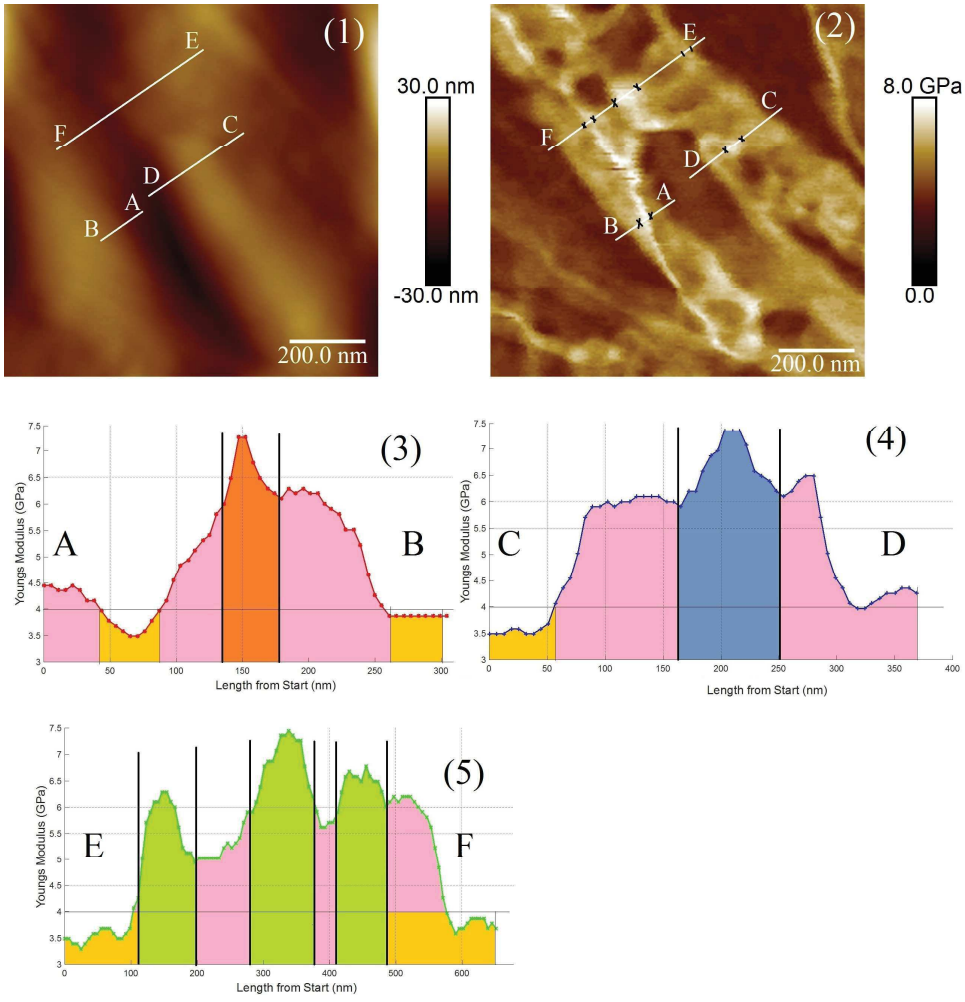

Figure 5-5: PF-QNM Analysis at 600 nN on C/Epoxy, surface height (1) and Young's modulus image (2), the lines of interest for section AB (3) showing mechanical properties, section BC (4) showing mechanical properties and section EF in (5) showing mechanical properties.

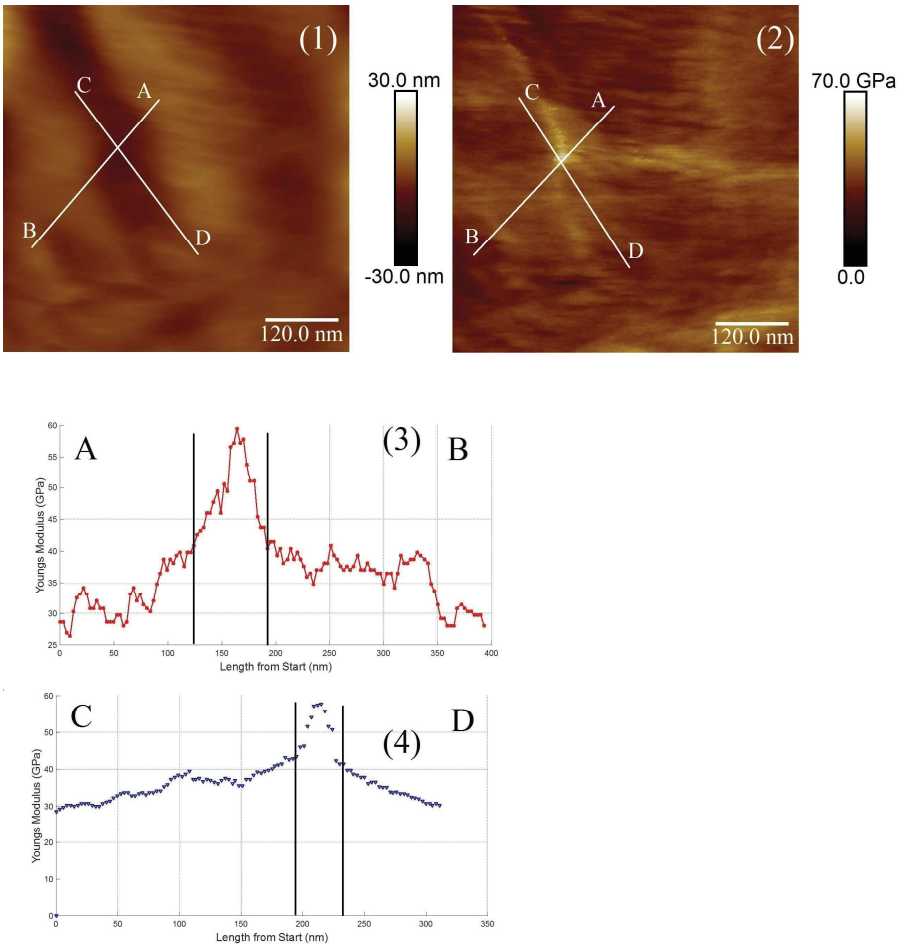

Figure 5-6: PF-QNM Analysis at 600 nN on BN/Epoxy, surface height (1) and Young's modulus image (2), the lines of interest for section AB (3) showing mechanical properties, and section BC (4) showing mechanical properties.

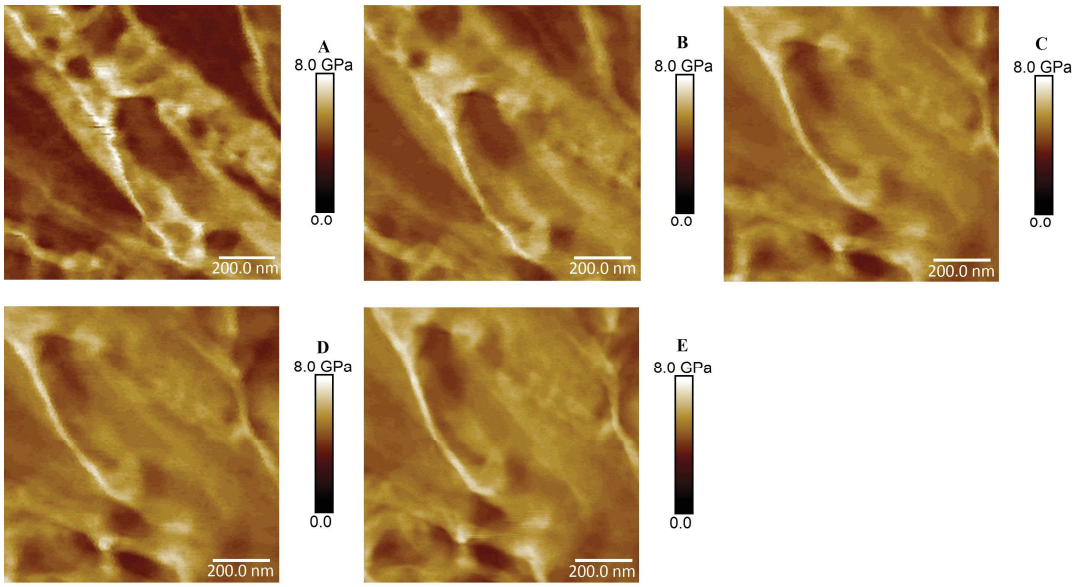

Figure 5-7: Surface Young's modulus evolution profile of C/Epoxy with the set points at 600 nN (A), 700 nN (B), 800 nN (C), 900 nN (D) and 1 000 nN (E), respectively.

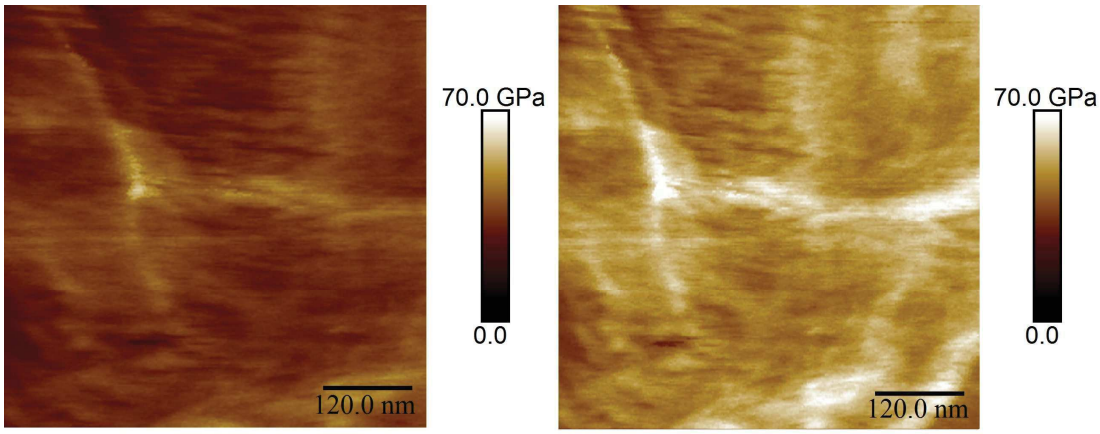

Figure 5-8: Surface Young's modulus evolution profile of BN/Epoxy with the set points at 600 nN (left) and 700 nN (right).

Table 5-2: Optimally loaded C/Epoxy and BN/Epoxy particle and interphase dimensions.

Section	Particle size (nm)	Interphase left (nm)	Interphase right (nm)	Section	Particle size (nm)	Interphase left (nm)	Interphase right (nm)
C/Epoxy AB	40	50	80	BN/Epoxy AB	70	124	153
C/Epoxy CD	80	114	64	BN/Epoxy CD	70	135	124
C/Epoxy EF	80	12.7	99	C/Epoxy EF	80	31	92
C/Epoxy EF	100	99	31				

Table 5-3: Average Young's modulus results of C/Epoxy and BN/Epoxy for different applied forces.

Force Applied (nN)	Average Surface Young's Modulus (GPa)
C/Epoxy	
600	4.905
700	5.034
800	5.712
900	5.905
1000	5.905
BN/Epoxy	
600	34.951
700	44.589

From the surface tests, areas of interest in the nanodielectric were identified such as individual particles and chains in the case of C/Epoxy and an individual particle in BN/Epoxy. These areas of interest were analysed for Young's modulus of the

surface and the results of the different sections are shown in Figure 5-5 and Figure 5-6 and summarised in Table 5-2.

The results of the force evolution are shown in Figure 5-7 and Figure 5-8 and the average Young's moduli from the force evolution are summarised in Table 5-3.

It is evident that small additions of nanoparticles enhance the average mechanical properties of Epoxy as shown in Table 5-1. Figure 5-4 shows that Young's modulus for epoxy ranges from 1 GPa to 3.5 GPa with an average Young's modulus of 1.7 GPa. This is in agreement with Young's modulus reported in the material data sheet [39]. It is also evident that epoxy has "grain boundaries" that could be oriented from the cross-linking process. Figure 5-4 also shows that between the grain boundaries, on the right, the black region appears to be either a region of un-cross-linked epoxy or possibly an air bubble, despite the rigorous attempt to remove air bubbles in the manufacturing.

From Figure 5-5 (1), in the height image, the surface does not show the presence of nanoparticles. The Young's modulus image in Figure 5-5 (2) shows Young's modulus of the C/Epoxy composite. The brightest areas show the presence of nanoparticles while the darkest areas are the pure epoxy.

By comparing the surface characterisation and surface evolution of Figure 5-5 and Figure 5-7, the individual particles could be confirmed. The Young's modulus of the CNS particles was identified as 7-7.5 GPa which did not change during the surface evolution. Similarly, Young's modulus of 55-56 GPa for the BN particle.

The BN particle present in Figure 5-6 (1) shows Young's modulus significantly higher than that of CNS with 56.8 GPa vs 7.5 GPa. By applying various set point forces, the evolution of Young's modulus mapping of the surface is shown in Figure 5-7, Figure 5-8 and Table 3.

These results demonstrate that the bulk Young's modulus approaches that of the interphase regions shown in Figure 5-5 (3) – (5) and Figure 5-6 (2) and (3). A summary of the particle and interphase dimensions obtained from Figure 5-5 (3) – (5) and Figure 5-6 (2) and (3) is provided in Table 5-2.

As mentioned earlier, Table 5-1 shows that the average epoxy Derjaguin, Muller, and Toporov model (DMT) Young's modulus is 1.7 GPa, however, there were regions shown in Figure 5-4 which reached 3.5 GPa. It was assumed that any material in the nanodielectrics which were above ~4 GPa would be either particle or interphase. It was further assumed that the nanofiller would be significantly different from the epoxy with regard to the particle measurements.

From Figure 5-5, C/Epoxy an 80 nm carbon nanosphere (indicated by the highest DMT Young's modulus ~7.5 GPa) shows an interphase (higher than 4 GPa and lower than 7 GPa) which can vary from ~10 nm (between two particles) to ~90 nm (outside of a particle) based on the influence of other particles (how close other particles are). This is in agreement with results reported by Tsekmas et. al. [68]. A 70 nm particle as part of an accreted nano line shows an interphase of 50 nm (left) and 80 nm right in Figure 5-6 (A). In Figure 5-6 (2) and (3) the BN nanoparticle of ~70 nm has an interphase of ~130 nm.

It is evident that the interphase is dependent on particle shape, particle size, and particle type. Figure 5-5 (5) shows that overlapping interphases between two particles and close together would be higher than that of particles further apart.

What has not been shown before in the literature is that the interphase which was previously assumed to be ~10 nm to ~25 nm, can be as large as double the characteristic diameter of the individual particle; one of the major contributions of this study. It is possible that due to the size of particles, the rate of nucleation (introduced in Section 3.3) around the particles has increased.

Assuming the theory of nucleation is still valid in nanodielectrics, the BN particles which are plate-like, facilitate heterogeneous nucleation resulting in an interphase which is almost double that of the particle size. The CNS particles have homogenous nucleation for the individual particles and heterogeneous nucleation in the case of the nano lines. This possibly contributes to the significant difference in Young's Moduli observed with the PF-QNM analysis between optimally loaded BN/Epoxy and C/Epoxy.

The current state of the knowledge in the literature about the interphase region is summarised as follows;

1. The interphase is the region around the nanoparticle which is different from the particle and host matrix.
2. The interphase is made of two or three distinct regions around the nanoparticle which may be a result of surface conditioning.
3. The interphase has a fixed length possibly not exceeding ~10-25 nm.
4. The interphase is a result of particle size, particle shape, and particle surface conditions/type.
5. The interphase depends on inter-particle distance and hence particle concentration.

The findings of the present work indicate the need to modify the knowledge as follows;

1. The interphase is indeed a region around the nanoparticle which is different to particle and host matrix according to the DMT Young's modulus results.
2. The interphase may be made of two distinct regions, not necessarily three as surface conditioning was not done on these particles.
3. The interphase is not a fixed length in the region of~10-25 nm but is variable based on particle size and can reach up to almost double the particle size.
4. The interphase is different for particle size, particle shape, and particle type.
5. The interphase does indeed depend on inter-particle distance and hence particle concentration.

Among properties of electrical insulation, permittivity is an important parameter especially as a function of frequency. Dielectric spectroscopy (DS) is the measurement of permittivity as a function of frequency. The following section discusses the use of DS as a method to establish the relationship between permittivity and particle concentration.

5.4 Dielectric Spectroscopy characterisation of the nanodielectrics.

In this section, the principle operation of dielectric spectroscopy (DS) is presented with permittivity and conductivity. The results show the effect of different levels of CNS in epoxy. A further comparison of dielectric characterisation of the optimally loaded 0.33 vol% C/Epoxy and 1.25 vol% BN/Epoxy samples is presented.

5.4.1 The principle of dielectric spectroscopy.

Relative permittivity is a measure of the polarizability of a material obtained by using frequency and/or temperature [79]. One method of obtaining permittivity is through dielectric spectroscopy (DS) [79]. Through DS, the dynamics of molecular motion of a complex material and the resultant characterisation of bulk material properties can be evaluated [85]. The generalised permittivity behaviour of a material as a function of frequency is shown in Figure 5-9.

Each frequency region reveals a different mechanism which influences the permittivity. Frequency ranges less than 100 MHz are some important regions for electrical insulation engineering [86]. Tsekmas *et. al.* established a good base for the permittivity considerations for hexagonal Boron Nitride in Araldite CY 231-1 and Aradur HY 925 (obtained from Huntsman ™) used in this work [68]. In this study, the 40 Hz – 10 MHz of the C/Epoxy samples were investigated and this region is dominated by dipolar polarisation mechanisms [79]. The dipolar polarisation mechanism describes how permanent and induced dipoles orient themselves in response to a changing electric field [87].

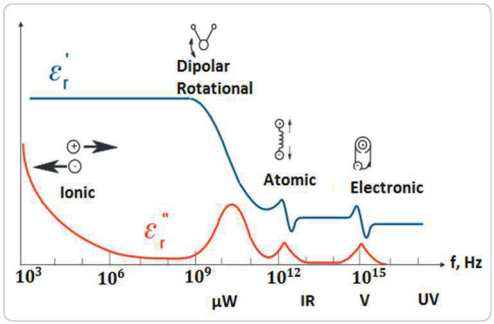

Figure 5-9: Frequency response of permittivity mechanisms for different regions (adapted from [88]).

The interphase is defined as a transitional layer that separates the host polymer and the added filler. It has been shown that the interphase has different crystallinity, glass transition temperature, permittivity and thermal conductivity from the host polymer and the nano-filler [1, 8]. In an optimally filled nanodielectric, the bulk properties are attributed to the interphase [17], [61], [62]. In the previous Section, the interphase was shown to vary in size to be at least double the size of the nanoparticle. Additionally, the bulk material Young's modulus property was found to approach that of the interphase.

In the literature, the lower relative permittivity of epoxy nanodielectrics at lower filler loadings has been reported; which is strongly associated with the presence of the interphase. The interaction of nanoparticles and polymer chains cause the interphase to be more pronounced at lower filler loadings [89], [90].

The nanoparticles cause a hindrance to polymer chain mobility and thus, less polarisation. Another possible reason for low relative permittivity at lower loading may be due to the hydroxyl groups (OH groups) present on the surface of nanoparticles, which can form a strong interaction with polymer chains [60]. Other work by Singha *et al* [91], claims that the epoxide groups may form strong hydrogen bonds with the free hydroxyl groups of nanoparticles. They also argue that this may be further enhanced by the amine groups from the hardener that are added during sample synthesis. However, the chemical validation has yet to be explored.

Percolation is defined as a point in which particles are in contact [92]. For conductive particles, it may be a point where a transition from an insulator nanodielectric to a conductor nanodielectric as a function of filler concentration and highly dependent on particle type (shape or conductive or non-conductive particle) [92]. The percolation effect may result in a pronounced increase of permittivity and conductivity. The critical value at which this transition occurs is known as the percolation threshold [92]. Above the percolation threshold, for this work, there is a continuous formation of conductive paths that further enhance the electrical conductivity of the nanodielectric [61]. Given that CNS particles are considered conductive, one of the objectives of this work is a C/Epoxy nanodielectric which inherently entails identifying the percolation threshold.

The following sub-sections describe the experimental methodology for the DS. The DS analysis was done on all C/Epoxy samples and the optimally loaded BN/Epoxy. A complete account of the test specimen's fabrication process is provided in Chapter 4.

5.4.2 Dielectric spectroscopy sample preparation methodology

For DS, samples were cut from a bulk material, shown in Figure 4-17. After slicing, the samples were surface conditioned (smoothed) using five stages of sandpaper polishing, sequentially the grain sizes started at 220 mm, 1200 µm, 9 µm, 3 µm, and ended with 1 µm. The last two stages also required 1 µm diamond grinding paste. The final fabricated samples for DS had a diameter of ~36 mm and thickness of ~1 mm suitable for use with an Agilent impedance analyser 4249A with the 16451B test fixture and a test voltage of 500 mV shown in Figure 5-10. As the sample preparation is quite a material expensive process, a total of three samples, per sample batch, were analysed using DS. A schematic diagram of the DS experimental setup is shown in Figure 5-10.

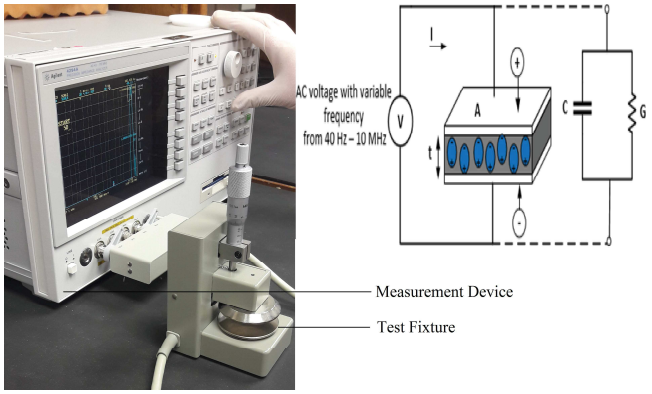

Figure 5-10: Agilent impedance analyser 4249A with the 16451B test fixture on left and on right the parallel plate capacitor model of the DS measurement method adapted from [93].

The samples were first cleaned with ethanol to remove any trapped residues and were kept under vacuum evacuation for 3 hours prior to the measurement. It was assumed that 3 hours was sufficient to remove any trapped air moisture.

The samples (Figure 5-11) were then coated with silver paint (colloidal silver from RS components). In order to ensure the samples did not develop conductive

pathways, the painting technique used was **edges first from centre to the outside** before completing the centre. The samples were coated on both sides to achieve good contact between the electrodes of the test fixture [87]. The silver paint also removed air gap errors introduced by micro-sized sample surface unevenness.

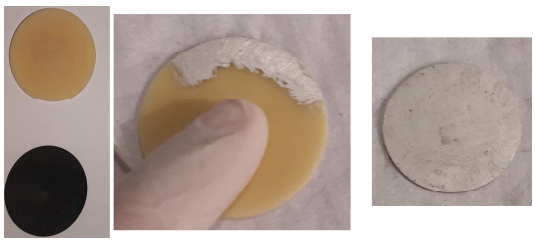

Figure 5-11: BN/Epoxy and C/Epoxy samples prepared for DS before painting(left), painting technique of centre to the outside (middle), final sample (right).

The measurements were done at ~25 ℃ ambient temperature. Each DS sample set was sandwiched between the electrodes of the test fixture, and connected to the impedance analyser. By measuring the complex impedance of the circuit (Figure 5-10), as a function of frequency, the real and imaginary parts of the complex permittivity were determined. These are shown in equation (5-1) (derived from equations (5-2) and (5-3)). The following sub-section presents the DS results.

$$\varepsilon^* = \varepsilon' - j\varepsilon'' \tag{5-1}$$

$$\varepsilon' = \frac{t \cdot \sin\theta}{\varepsilon_o \cdot A \cdot \omega |Z|} \tag{5-2}$$

$$\varepsilon'' = \frac{t \cdot \cos\theta}{\varepsilon_o \cdot A \cdot \omega |Z|} \tag{5-3}$$

Where:

- ε' is the complex permittivity.
- $\varepsilon'$is the real part of the complex permittivity, which represents the relative permittivity that measures the amount of polarisation [79].
- $\varepsilon''$is the imaginary part of the complex permittivity which represents the dielectric loss of a material, or the losses that are encountered during the polarisation processes [79].
- t is the thickness (mm).
- A is the area of the samples (mm²)
- ω = the angular frequency (rad/s).

5.4.3 Dielectric spectroscopy measurement results and analysis

Figure 5-12, Figure 5-13 and Figure 5-14, with Table 5-4 and Table 5-5 give the DS results[3] of the C/Epoxy samples for the different loading levels. The real and imaginary components of the complex permittivity and the conductivity were investigated in the frequency range of 40 Hz–10 MHz.

Figure 5-12 shows the real part of the permittivity which decreases with increasing frequency for all samples. Figure 5-13 shows the imaginary part of the corresponding permittivity. At low frequencies, the dipoles are able to keep up with the frequency and this results in higher polarisation. As the frequency increases polarisation then lags behind the electric field. This causes the reorientation of the dipoles to be opposed by internal friction, which generates heat and hence energy loss. The increase in loss is manifested as an increase in imaginary permittivity as a function of frequency as shown in Figure 5-13. A further increase in the applied electric field reaches a point where polarisation no longer occurs and this is termed the β-relaxation peak [88]. The β-relaxation peak is seen at around 5 MHz in both the real and imaginary parts of the complex permittivity (Figure 5-12 and Figure 5-13 solid black line).

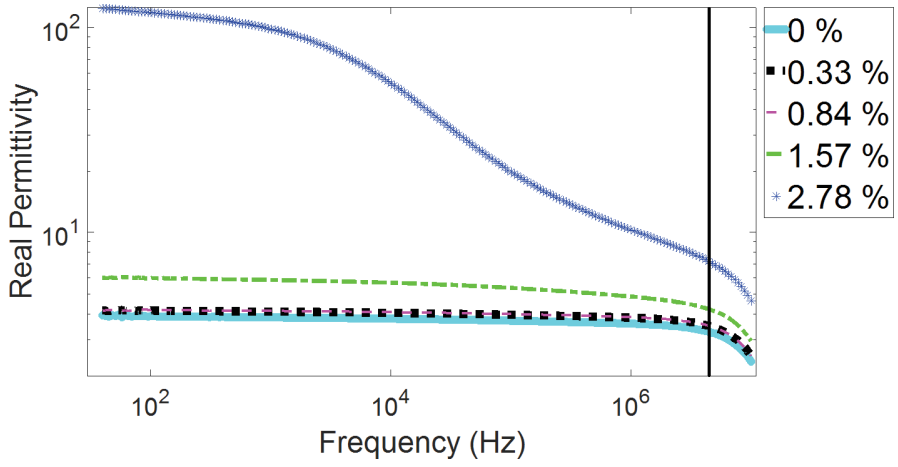

Figure 5-12: Frequency spectrum of the real part of the complex permittivity in C/Epoxy nanodielectrics. The Solid vertical line indicates the Beta Relaxation Peak.

[3] Acknowledgements are given to Prof Ivan Hofsajer at Wits University for doing the DS measurements and providing the results. The author was present for the experiments.

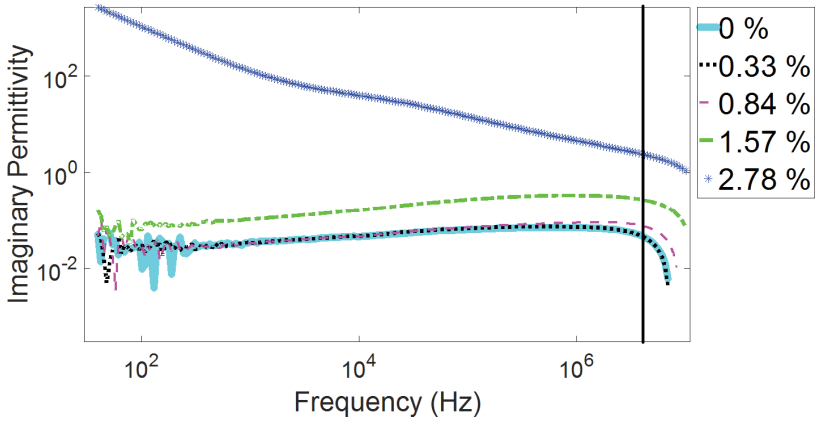

Figure 5-13: Frequency spectrum of the imaginary part of complex permittivity in C/Epoxy nanodielectrics. The Solid vertical line indicates the Beta Relaxation Peak.

Table 5-4: Average real part of complex permittivity values at different frequencies for C/Epoxy.

Vol%	50 Hz	1 kHz	0.1 MHz	1 MHz
0	**3.95**	**4.25**	**4.11**	**3.97**
0.33	**3.91**	**4.09**	**3.96**	**3.84**
0.84	4.14	4.14	4.03	3.90
1.57	5.98	6.17	5.50	4.90
2.78	88.4	98.39	19.89	10.35

Table 5-5: Average imaginary part of complex permittivity values at different frequencies for C/Epoxy.

Vol%	50 Hz	1 kHz	0.1 MHz	1 MHz
0	**0.05**	**0.04**	**0.07**	**0.07**
0.33	**0.011**	**0.03**	**0.07**	**0.09**
0.84	0.046	0.03	0.07	0.09
1.57	0.163	0.12	0.35	0.41
2.78	130.1	125.1	14.31	4.56

The unfilled epoxy sample results as shown in Table 5-4 and Table 5-5 are comparable to data observed previously by Tsekmas *et. al.* [68], [80] for the same epoxy. A key result in Table 5-4 is the pure epoxy having a relative permittivity of ~4 which provides good confidence in the manufacturing efforts. The complex permittivity values at low filler loadings highlighted in Table 5-4 and Table 5-5 are marginally lower than pure epoxy. The hindrance of polymer chains due to the presence of CNS results in lower permittivity as the degree of dipole orientation is reduced [94].

From Figure 5-12, Figure 5-13, Table 5-4 and Table 5-5; it is noted that permittivity of 0.84 vol% is slightly greater than that of pure epoxy. This can be explained by considering the percolation effects. The effects are noticeable in the 0.84, 1.57 and 2.78 vol% shown in Figure 5-12 and Figure 5-13, where values of real and imaginary permittivity are higher than that of pure epoxy. For higher filler loading samples, both the real and imaginary permittivity decrease with the increase in frequency.

According to Chung et. al. [95], the relative permittivity of carbon black at 100 kHz is ~100 which is significantly higher than epoxy ~4. As the particle concentration increases, the particles become closer together and consequently, the interphases get closer together and begin overlapping as mentioned by the Interphase volume model and the Potential barrier model [61], [79]. This is seen by permittivity values of heavily loaded the samples approaching that of carbon permittivity [8, 16]. The charge carriers, therefore, are able to move more freely between nanoparticles.

With reference to Figure 5-14, conductivity was plotted from equation (5-4). At low frequencies, the 2.78 vol% sample has conductivities (10^{-5}) which are five orders of magnitude greater than pure epoxy or 0.33 vol% (10^{-10}). As the frequency increases, the pure epoxy and lower filler loadings become increasingly conductive and approaches that of a heavily loaded sample.

$$\sigma = \varepsilon^{"} \cdot \omega \cdot \varepsilon_o \Rightarrow R = \frac{1}{\varepsilon^{"} \cdot \omega \cdot \varepsilon_o} \quad (5\text{-}4)$$

Where:

- σ is the bulk conductivity as a function of material losses (S/cm) and R is the resistance (Ω).

Figure 5-15 to Figure 5-17 show the DS results of the reproduced samples confirming that 0.33 % of C/Epoxy was reproduced and although was not the same as the first batch, was relatively close. The addition of the BN/Epoxy DS results provides further insight as to the placement of an optimally loaded BN sample permittivity and conductivity properties compared to pure epoxy and C/Epoxy. Both the reproduced samples have lower conductivity results than the pure and original C/Epoxy results. Hence for optimally filled samples, the electrical resistance has increased when compared to the pure virgin epoxy shown in Figure 5-18.

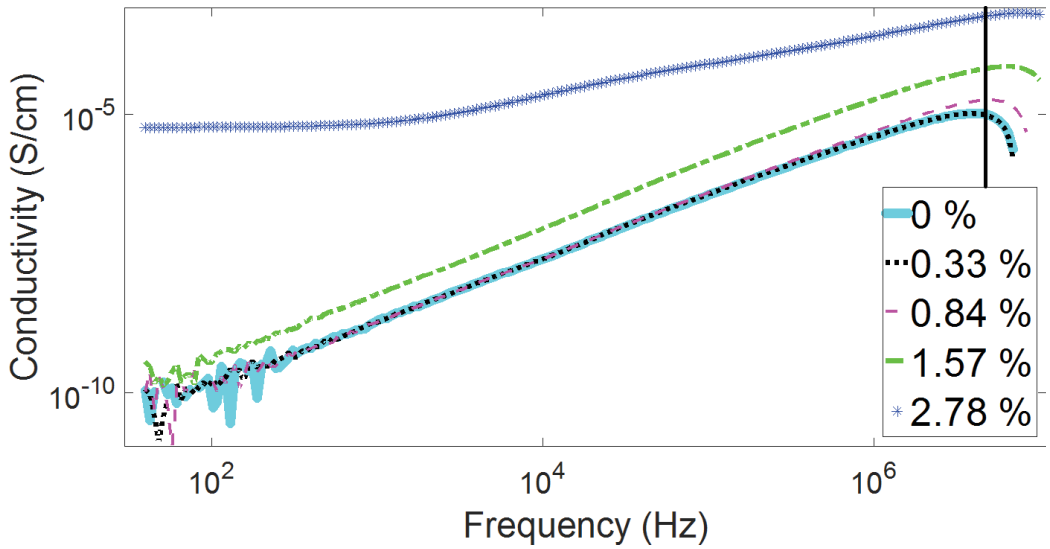

Figure 5-14: Frequency spectrum of the electrical conductivity in C/Epoxy nanodielectrics. The Solid vertical line indicates the Beta Relaxation Peak.

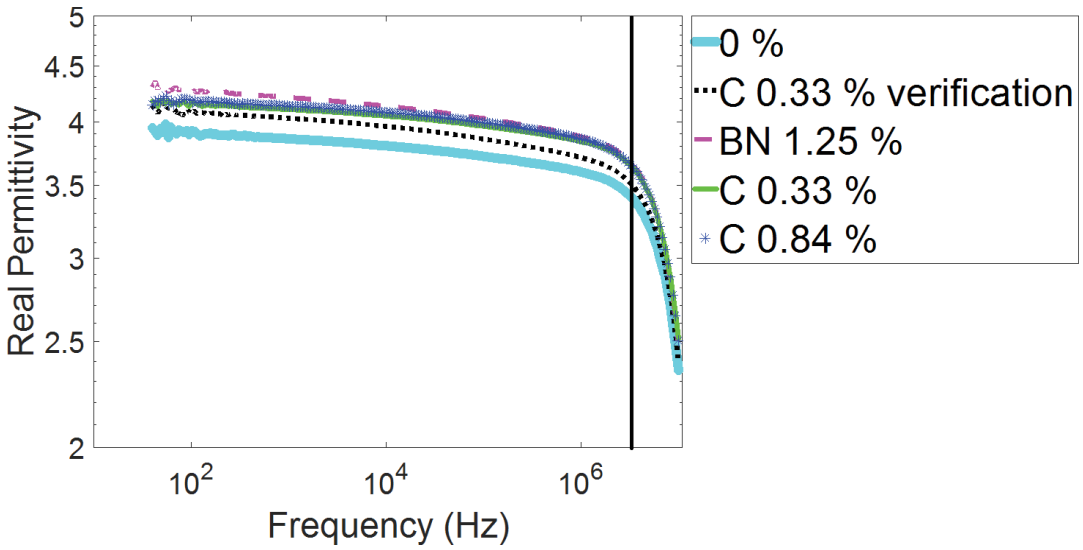

Figure 5-15: Real permittivity showing the addition of BN/Epoxy and reproduced C/Epoxy optimally loaded sample.

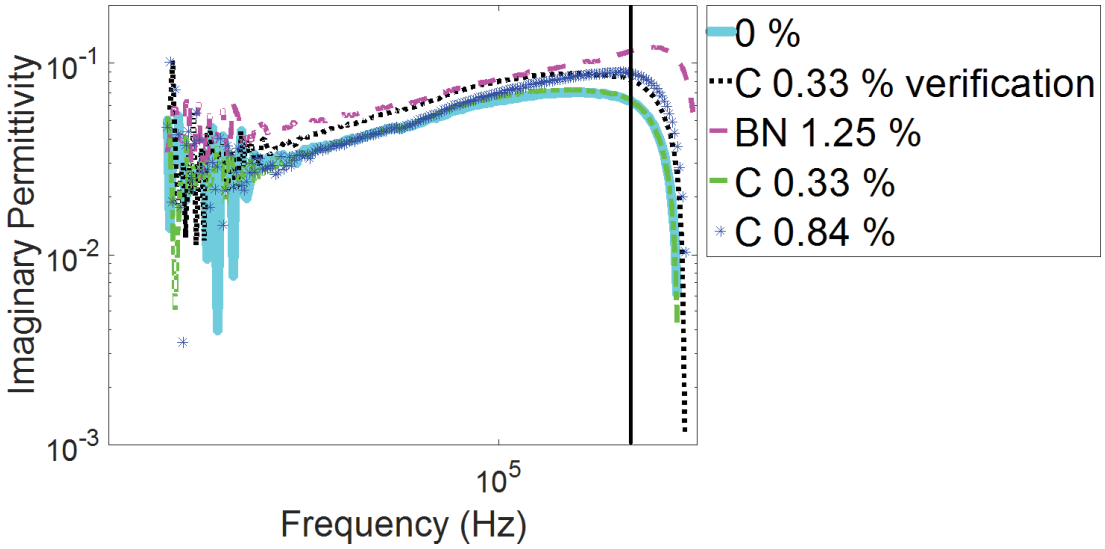

Figure 5-16: Imaginary permittivity showing the addition of BN/Epoxy and reproduced C/Epoxy optimally loaded sample. The Solid vertical line indicates the Beta Relaxation Peak

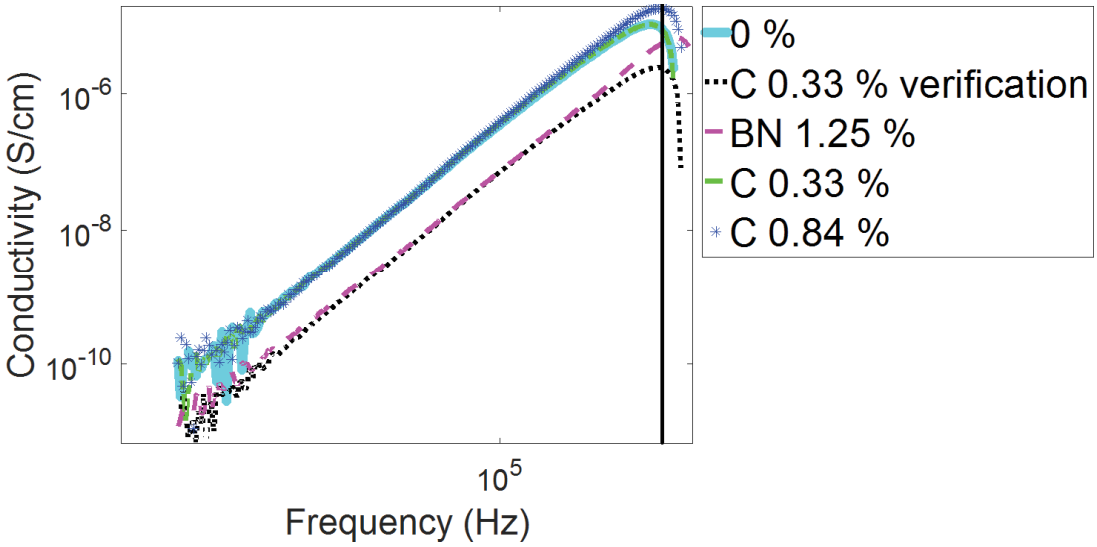

Figure 5-17: Conductivity showing the addition of BN/Epoxy and reproduced C/Epoxy optimally loaded sample. The Solid vertical line indicates the Beta Relaxation Peak.

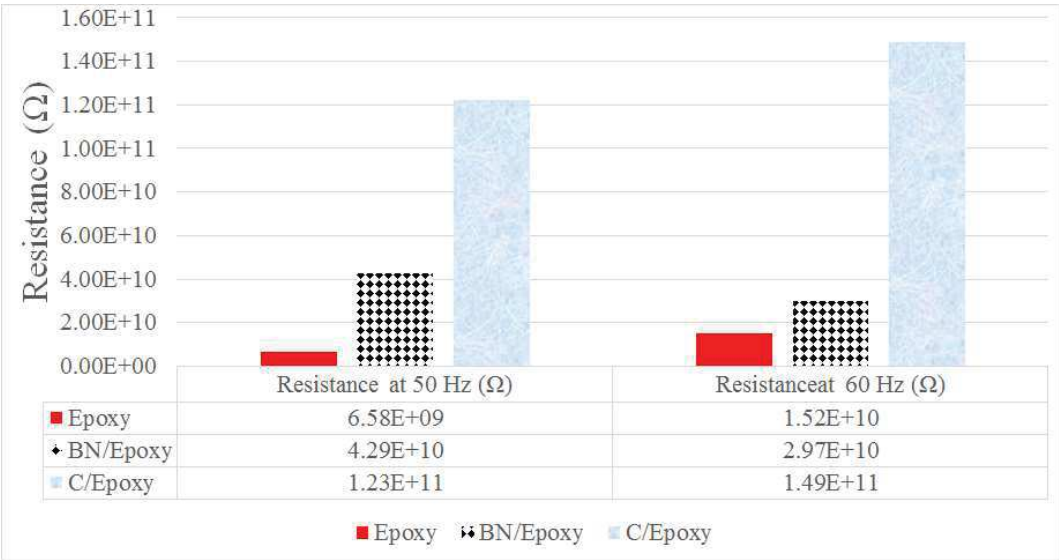

Figure 5-18: Sample resistance at power frequencies for the optimally loaded nanodielectrics and pure epoxy.

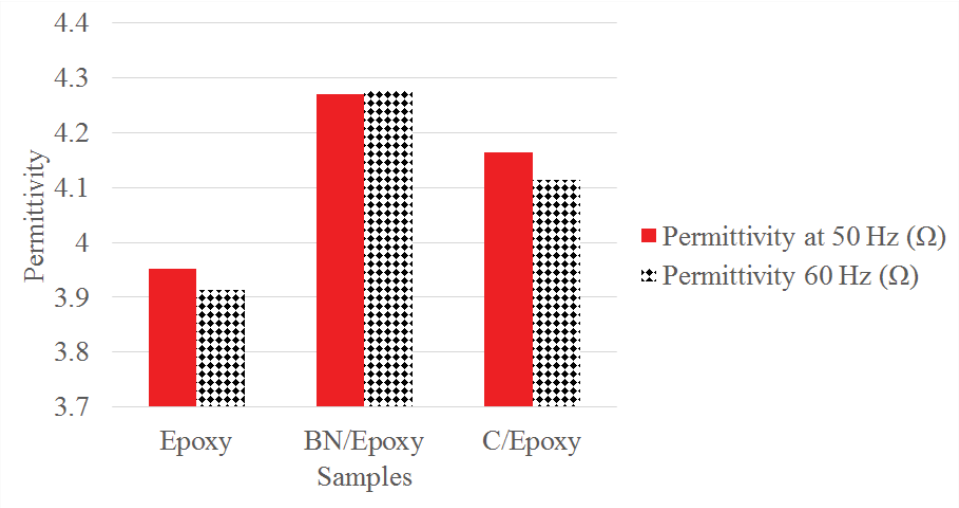

Figure 5-19: Sample permittivity at power frequencies for the optimally loaded C/Epoxy and BN/Epoxy nanodielectrics and pure epoxy.

From the results, the optimal loading levels had an increase in permittivity at 50 Hz by 8 % and 5 % for BN/Epoxy and C/Epoxy respectively when compared to the pure epoxy. Additionally, there was an increase in electrical resistance at 50 Hz by 6x and 18x for BN/Epoxy and C/Epoxy respectively.

The key results of this section can be summarised as follows:

- Increasing CNS particle concentration results in epoxy becoming increasingly conductive.
- The percolation threshold of C/Epoxy is 0.84 vol%.
- Optimally loaded BN epoxy and CNS epoxy have conductivities lower than pure epoxy indicating an increase in material resistance.
- The permittivity's and resistances at power frequencies for the optimally filled nanodielectrics are higher compared to pure epoxy.

5.5 Conclusion

In this chapter, the optimally loaded BN/Epoxy and C/Epoxy were characterised using AFM and DS. The principle operation of AFM and DS were presented. These were then followed by the results and discussions. The first key finding shown in this chapter was the interphase was mechanically different from the nanoparticle and host matrix according to the DMT Young's modulus results. The interphase

was found to not be a fixed length in the region of ~10-25 nm but a variable length based on particle size and can reach up to almost double the particle characteristic size. Increasing CNS particle concentration results in epoxy becoming increasingly conductive, and due to CNS particles being conductive the percolation threshold of CNS is 0.84 vol%. Optimally loaded BN/Epoxy and C/Epoxy have conductivities lower than pure epoxy indicating an increase in material resistance. However, there is also a slight decrease in permittivity due to restricted polar movement.

In the following Chapter, further insight into the electrical properties of the BN/Epoxy and C/Epoxy Nanodielectrics are presented. The samples were characterised using electrical trees by looking at the Partial Discharge phenomena, followed by X-ray Computer Tomography and Atomic Force Microscopy on the tree channels.

CHAPTER 6 : ELECTRICAL TREE BEHAVIOUR IN THE C/EPOXY AND BN/EPOXY NANODIELECTRICS

"When do you think people die? When they are shot through the heart by the bullet of a pistol? No. When they are ravaged by an incurable disease? No. When they drink a soup made from a poisonous mushroom!? No! It's when... they are forgotten." – Dr Hilukluk

6.1 Introduction

In this chapter, electrical tree phenomena are presented for the Carbon Nanosphere (CNS) and Boron Nitride (BN) particles in Epoxy (C/Epoxy and BN/Epoxy nanodielectrics). A comprehensive review of electrical trees is provided through partial discharges (PD) and imaging techniques. X-ray Computer Tomography (XCT), Finite element modelling (FEM) simulations, and Atomic Force Microscopy (AFM) were used to analyse the samples. Based on the PD investigations it can be shown that there is a correlation between PD and rheology for the optimally loaded 0.33 vol% C/Epoxy and 1.09-1.35% vol% BN/Epoxy. The following section provides the background to electrical trees. This will be followed by the analysis and discussion of the PD results.

6.2 Background

When characterising dielectric material there are several key parameters, namely dielectric spectroscopy, electrical trees, dielectric breakdown strength, partial discharges, and space charge analysis. The focus of this study is on electrical trees as this is the common ultimate failure mode of solid polymer insulation [1]. The performance of the optimally loaded C/Epoxy and BN/Epoxy as determined through rheology would be evaluated using electrical treeing tests.

Due to enhanced localised electric stress in the order of MV/mm, energy is transferred from the electric field into the molecular matrix and causes various

physiochemical changes. These changes may be scission of molecular bonds, heat, pressure builds up and various chemical processes.

As shown in Figure 2-3 and Figure 2-4, under high electric stress a seed electron either from trapped sites in the insulation or metallic surfaces enters the material matrix. While in a high electric field an electron avalanche is initiated. The electron avalanches cause molecular breakdown which is dissipated as excess heat, or the formation of ions, electrons, photons and radicals. The photons have been detected using electroluminescence as a stage before PD [41]. The charge movement results in insulation degradation as seen in Figure 4-21 which can be detected as PD [1] – [3]. The principle concept of PD is illustrated in Figure 6-1 [1] – [3]. A cavity in insulation causes electric field enhancement, once a threshold voltage in the insulation is exceeded, ionisation occurs causing a discharge. The discharges are detected as PD and can be viewed as partial discharge phase resolved patterns (PDPRPs) [1] – [3].

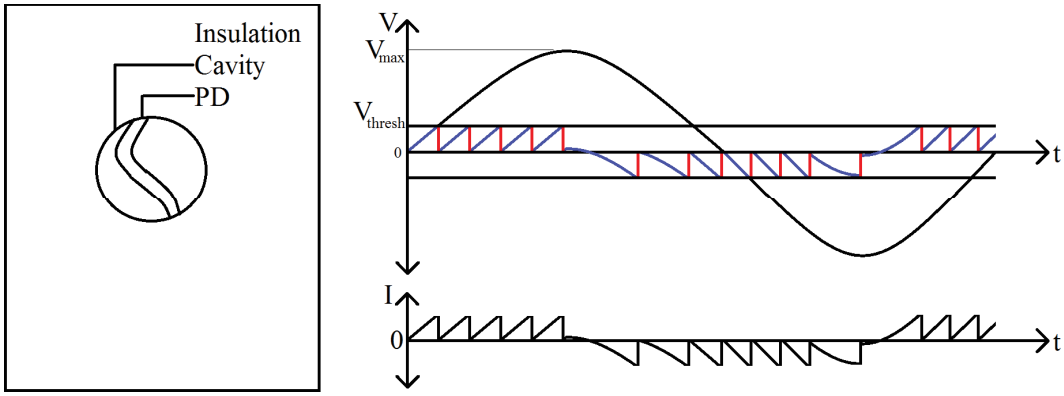

Figure 6-1: Principle concept of how PD is generated, a threshold voltage in a cavity is exceeded, which causes ionisation in the cavity detected as current pulses [1] – [3].

During continuous charge bombardment, degradation of the insulation ensues as tree shaped gas-filled nano and/or micro-tunnels propagate which have been termed "electrical trees," [1] – [3]. Electrical trees propagate through the insulation leading to complete insulation failure [1].

Applied electric field stress may be broken into three categories namely “safe operating conditions,” “Tree favourable conditions”, and “Dielectric breakdown limits [1] – [3].” Typically, insulation is designed to be within safe operating conditions. However, due to various parameters such as material defects, poor equipment handling, and non-designed operating conditions, electrical equipment moves very quickly into Tree favourable conditions [1] – [3]. Once in Tree favourable conditions insulation which may have been designed to last for decades would fail prematurely.

In the event where situations which cause Tree favourable conditions cannot be avoided, endurance to electrical tree degradation is therefore regarded as the ‘litmus test’ of solid polymer insulation quality. Moreover, electrical treeing tests are often used in evaluating the material engineering efforts [2]. Hence, evaluating electrical tree degradation when developing new solid polymer insulation such as nanodielectrics in the present study provides insights of quality assurance into the future of the material.

A common electrical tree experiment is a needle-plane electrode setup which is used to accelerate the treeing process. A material such as epoxy which may have a material lifetime of +60 years, which would fail in 15-20 years under tree favourable conditions. In the lab, a needle plane experiment is used to accelerate tree favourable conditions to failure within ~8 hours [1] – [3]. This enables rapid sample evaluation.

Champion *et al.* [42] went further and showed for a needle-plane setup, different trees would grow in epoxy samples that depended on the magnitude of the electric field applied. The three main categories of electrical trees, corresponding to electric field magnitude determined from equation (2-2), are a branch, bush-branch and branch types trees with corresponding RMS electric fields of ~0.9 MV/mm, ~1.1 MV/mm and 1.3 MV/mm respectively.

Champion *et al.* [42] also showed the correlation between PD activity and the tree shapes observed. The key findings were bush trees are characterised by small micro-tunnels and relatively small PD magnitudes ~50-200 pC. Branch trees are

characterised by a gradual build-up of PD activity from 10-50 pC to ~750 pC before ultimately failing. The following section provides the experimental methodology used to evaluate electrical trees in epoxy and the developed nanodielectrics.

6.3 Electrical tree PD characterisation.

Some of the common methods of investigating electrical trees are "time to failure", "inception stress," "rate of tree propagation," the "types of trees produced," or the "PD signatures" produced. By running electrical tree experiments with the nanodielectrics two objectives may be achieved. The first objective provides insight into the effect particle filler loading has on electrical trees. The second is a measure of the quality of the developed insulation.

Between the different electrical tree techniques, there are trade-offs. According to international standards such as ASTM Standard D3756-97, Time to failure, inception stress, the rate of tree propagation, and types of trees produced requires a minimum of ten samples and is not concerned with PD characteristics. PD analysis is a time-consuming process but provides a significant amount of insight into electrical tree nature and requires a minimum of three samples. Due to material and budget constraints, it was opted to go for PD analysis. The following sub-sections provide the experimental methodology and results of the electrical tree experiments using PD.

6.3.1 The electrical tree sample preparation

Test samples for electrical treeing were synthesised by casting X-253-1 Ogura needles (Ogura Industrial Jewel™) in the insulation which have a 5 µm tip radius with a 30° run off to a maximum needle radius of 1 mm. An image of these test samples is shown in Figure 6-2. In the casting mould, the needle was held in place by grub screws to ensure a needle tip to plane gap of 3 mm. The evolution of the electrical tree partial discharges was monitored according to international standard IEC 60270 using an ICMCompact™ PD measurement system [96]. An image of the test setup and a schematic diagram of the IEC 60270 setup is shown in Figure 6-3.

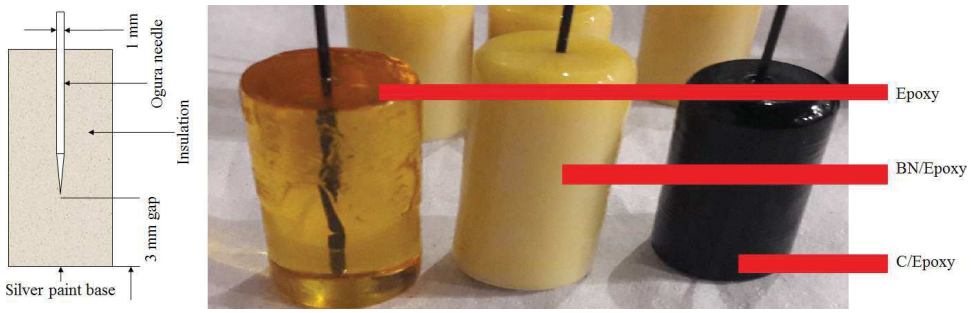

Figure 6-2: Sample configuration on left and test specimens for electrical tree experiments.

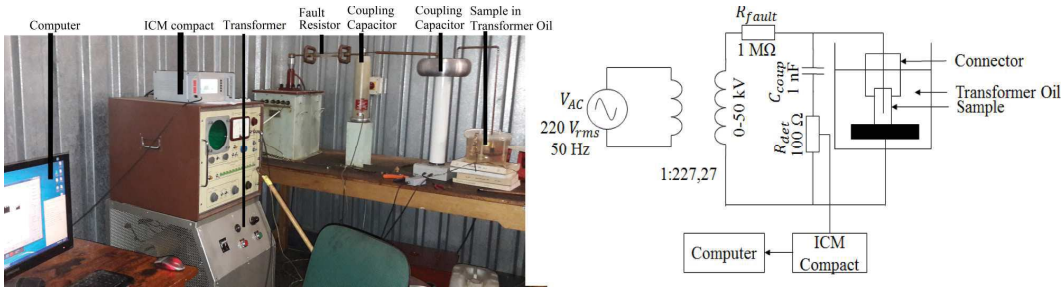

Figure 6-3: Test setup according to IEC 60270 on left and schematic circuit diagram on right used for Partial discharge analysis.

The experimental test rig is shown in Figure 6-4 and a schematic diagram of the needle coupling facility to the high voltage source is shown in Figure 6-5. As with the dielectric spectroscopy samples, silver paint base was applied to the bottom of the electrical tree sample to ensure the sample made good contact with the electrode.

The needle coupling facility to the high voltage source was specially made so as to be corona free. The entire test sample was immersed in insulating mineral oil to avoid spurious discharges and flashovers. The experiments were conducted in a double shielded high voltage laboratory with an average PD noise level of 0.2 pC.

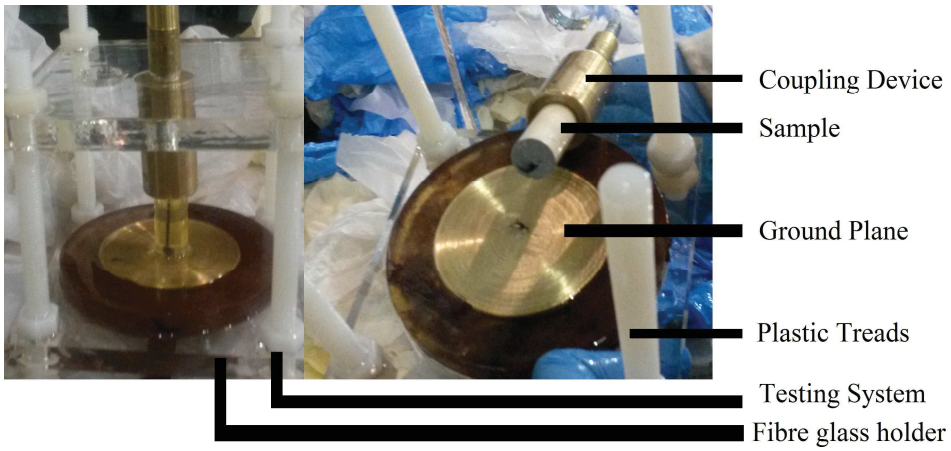

Figure 6-4: Needle coupling facility to the high voltage source test rig showing failed epoxy and BN/Epoxy samples.

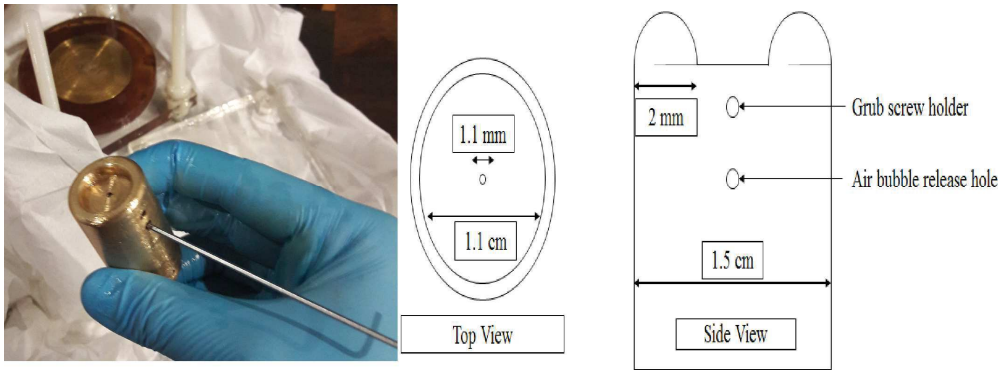

Figure 6-5: Image of needle coupling facility on left and on right the schematic diagram of the needle coupling facility to the high voltage source with edges spherically shaped to avoid corona.

Each sample was subjected to a 50 Hz sinusoidal linear ramp until ~20 kV RMS to establish an electric field of ~1 MV/mm on the needle tip. The voltage was then held constant until failure or long enough to capture required PD data. This electric field was specifically to grow bush-branch trees to easily see changes in tree nature based on PD activity. The maximum, minimum and average apparent PD magnitudes were recorded every second from the moment of tree inception until complete failure. In the event that a sample survived longer than 120 hours, the test was terminated.

Concurrently the corresponding partial discharge phase-resolved-patterns (PDPRP) were recorded. Screenshots were taken every 20 minutes of the PDPRPs which are

summarised for each sample set. The following sub-section provides the experimental results and discussion.

6.3.2 Electrical tree Partial Discharge Time Evolution Analysis

The PD time evolution from start to failure and the distribution of PD activity according to a number of discharges and magnitude of discharges for each sample set are shown in Figure 6-6 to Figure 6-32. Figure 6-6 shows electrical tree PD magnitudes of clean epoxy samples 1, 2 and 3. An important outcome is that Samples 1 and 2 show predominant branch like characteristics while sample 3 shows mainly bush characteristics, and this is in agreement with the results reported by Champion *et al.* specifically as having the same time scales and distributions [42].

Figure 6-7 shows that a concentration of large PD areas are characteristic of branch trees, while a ramp characteristic which is effectively a random magnitude probability of discharges is more bush like as established by Champion *et al.* [42]. In clean epoxy, as shown in Figure 6-6, generally the presence of PD activity is sustained from inception to the moment of complete failure with no interspaced periods of PD evanescence. The average time survival of these epoxy samples under these experimental conditions was ~2 hours.

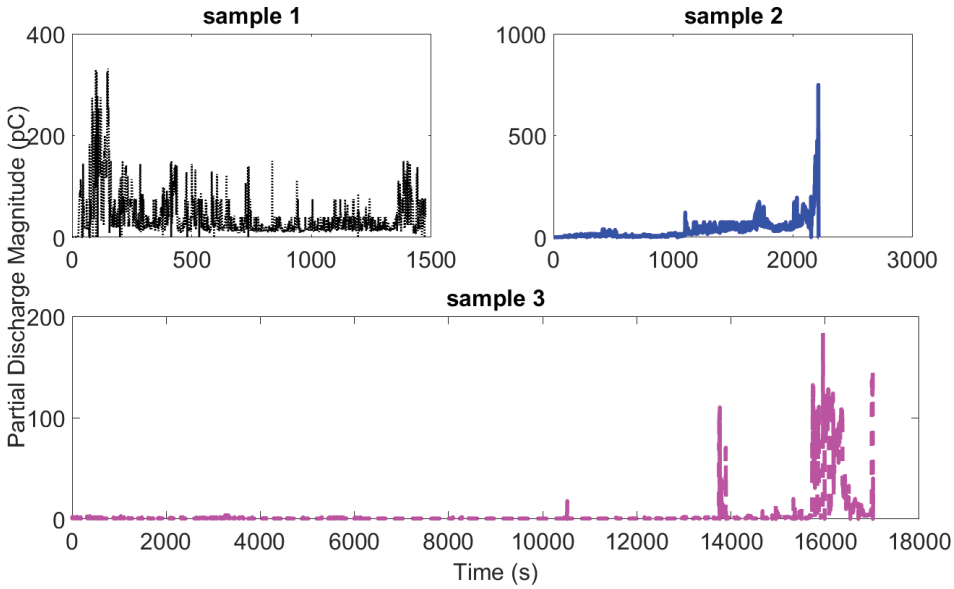

Figure 6-6: Complete partial discharge magnitude time evolution of pure epoxy showing bush- branch characteristics in pure epoxy, sample 1 is bush-branch sample 2 is branch while sample 3 is bush.

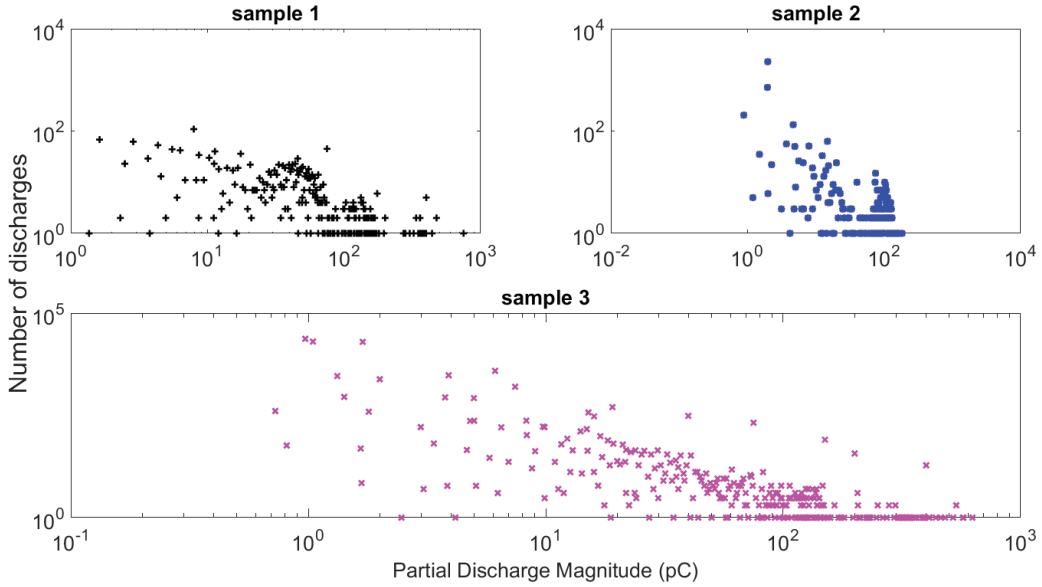

Figure 6-7: Log-log graph showing the distribution of PD in pure epoxy sample 1 and 2 show branch-characteristics while sample 3 shows bush characteristics.

The C/Epoxy samples showed remarkable behaviour; the ability to achieve samples which could hold the 20 kV voltage was limited to a maximum 0.89 vol%. As established using dielectric spectroscopy (DS), the samples above 0.89 vol% were increasingly conductive, hence they could not hold a voltage of 2 kV and would fail within seconds! Hence no further PD analysis was done on samples above 0.89 vol%.

In Figure 6-8 the 0.33 vol% C/Epoxy sample 3 maintained the voltage for 120 hours without failure, while sample 1 and sample 2 failed earlier. Compared to pure epoxy the overall magnitude of the PD is significantly suppressed where the maximum in pure epoxy being ~750 pC near failure, while the discharges in C/Epoxy do not exceed ~300 pC. Figure 6-9 shows ramp characteristics for all samples indicating very bushy type trees like pure epoxy. The average lifetime of these samples was remarkably longer, 120 hours compared to the 2 hours of pure epoxy!

Several batches of samples were reproduced to verify repeatability of the optimal

loading levels, Figure 6-10 and Figure 6-11 provide the verification of the 0.33 vol% samples. Once again sample 3 maintained the voltage for 120 hours without failure. However, there were a significant amount of PDs in the first few minutes and then the sample remained dormant. There were no recorded PD data in sample 2 as the data logger of the ICMCompact has a minimum magnitude resolution of 0.5 pC and sampling time of 1 second. However, the PDPRPs indicate that there was PD activity lower than 1 pC as shown in Figure 6-10. The results are remarkable and show good promise for further investigations of C/Epoxy nanodielectrics. Additionally, the average time for these samples was 44 hours compared to 2 hours of pure epoxy.

Figure 6-13 and Figure 6-14 give the results of 0.89 vol% C/Epoxy which effectively performed as a semiconductor. Sample 3 in Figure 6-13 failed at 17 kV. The average time of these samples was effectively 8 minutes. In 0.33 vol% samples (Figure 6-8) and 0.89 vol% (Figure 6-13) C/Epoxy the average PD magnitude is around ~50 pC which is relatively small compared to that in pure epoxy. This suggests that the type of electrical trees produced in C/Epoxy is of bush nature compared to the branch nature observed in clean epoxy.

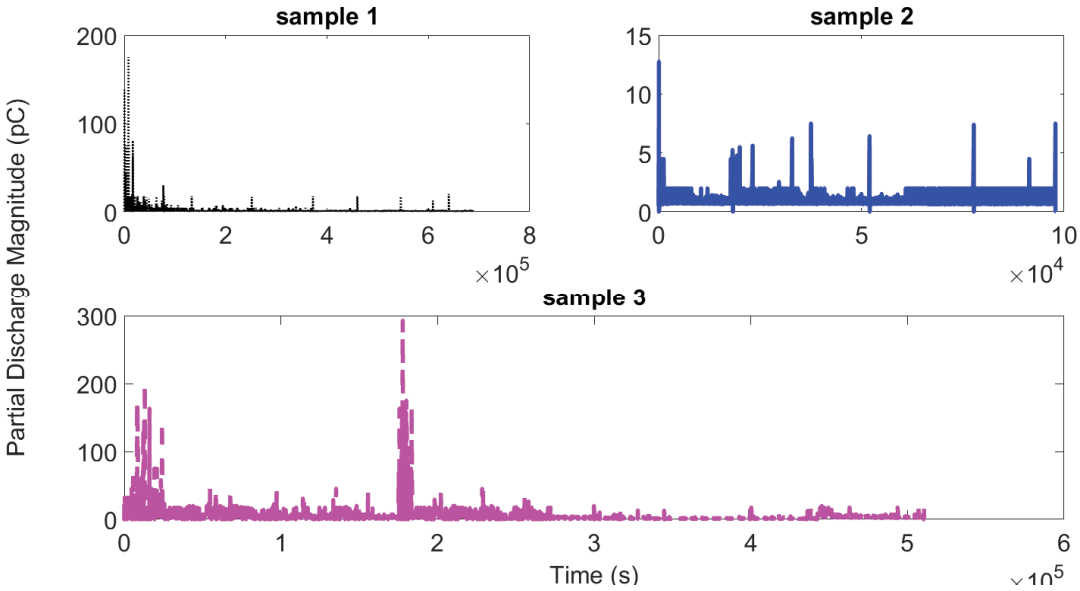

Figure 6-8: Complete partial discharge magnitude time evolution of C/Epoxy showing bush- branch characteristics.

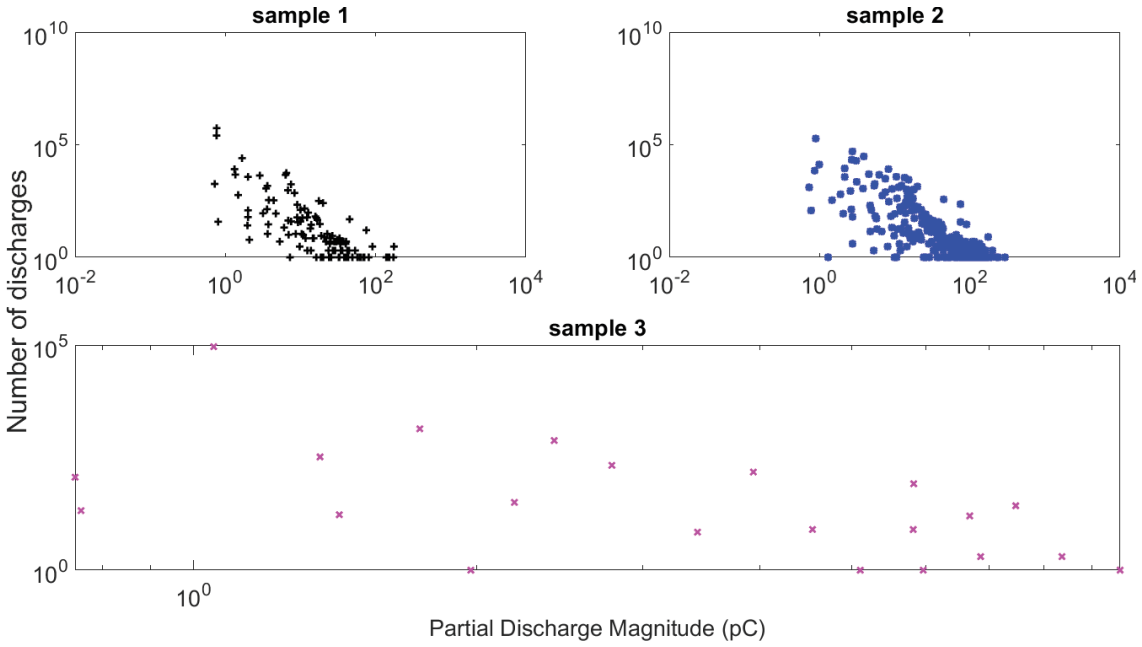

Figure 6-9: Log-log graph showing the distribution of PD in 0.33 vol% C/Epoxy.

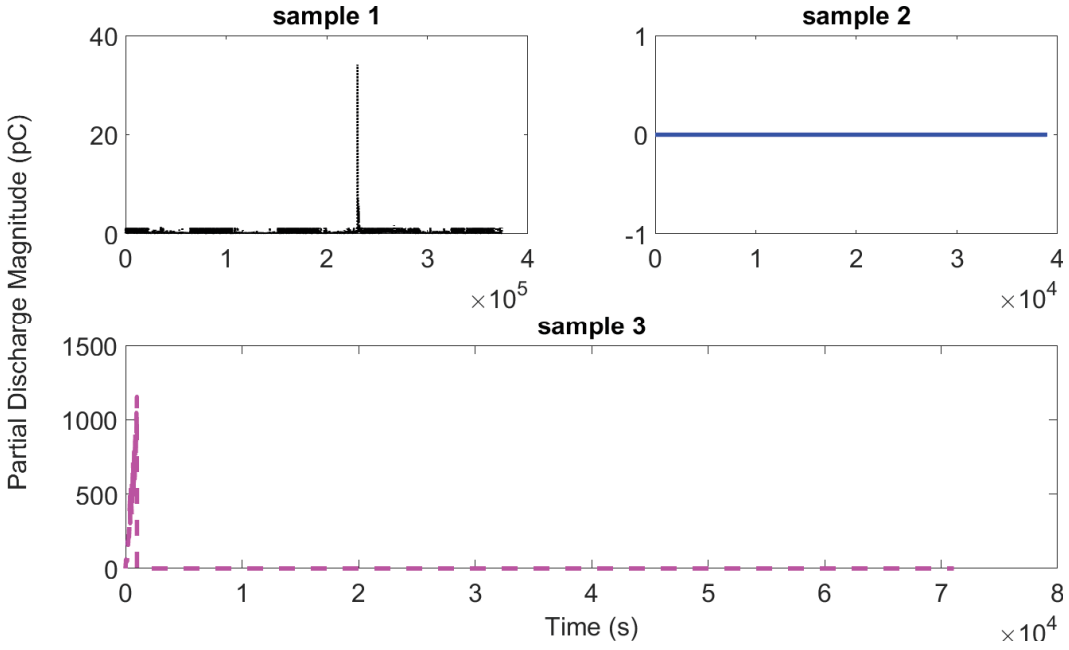

Figure 6-10: Complete partial discharge magnitude time evolution of 0.33 vol% C/Epoxy showing significantly suppressed discharges and repeatability of samples.

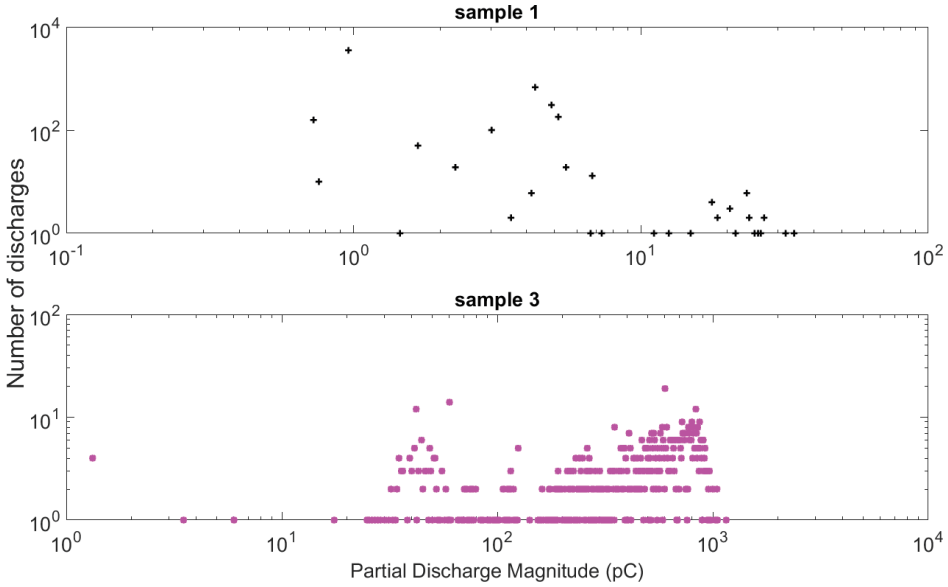

Figure 6-11: Log-log graph showing the distribution of PD in 0.33 vol% C/Epoxy and repeatability of samples.

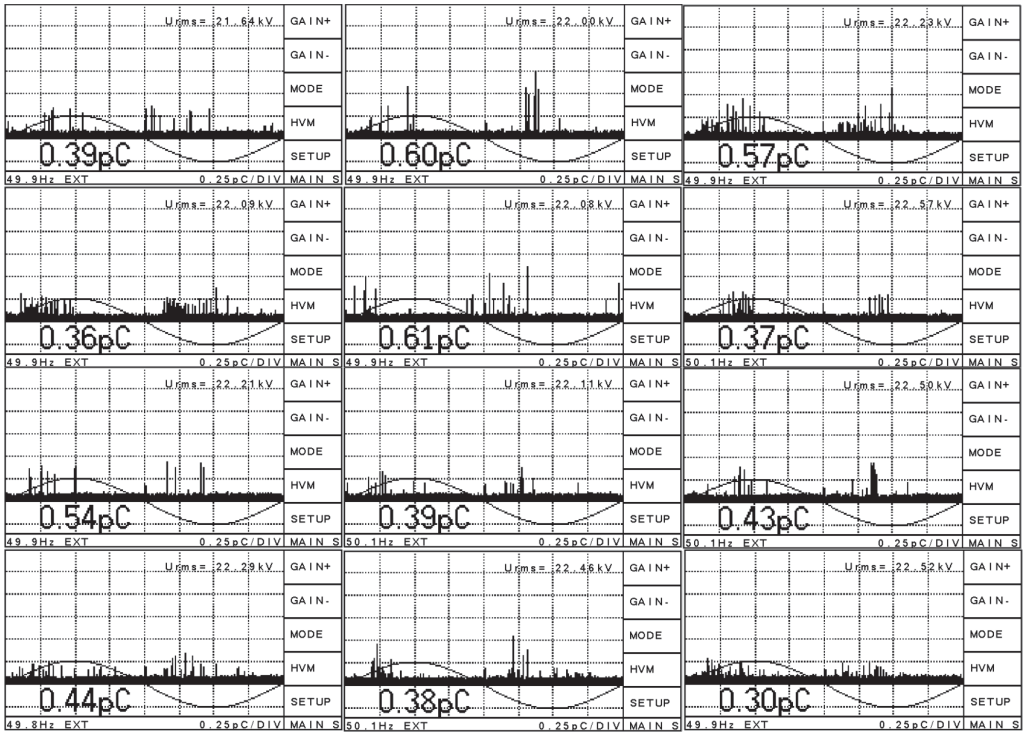

Figure 6-12: PDPRPs recorded every 20 minutes for the first four hours of the 0.33 vol% C/Epoxy.

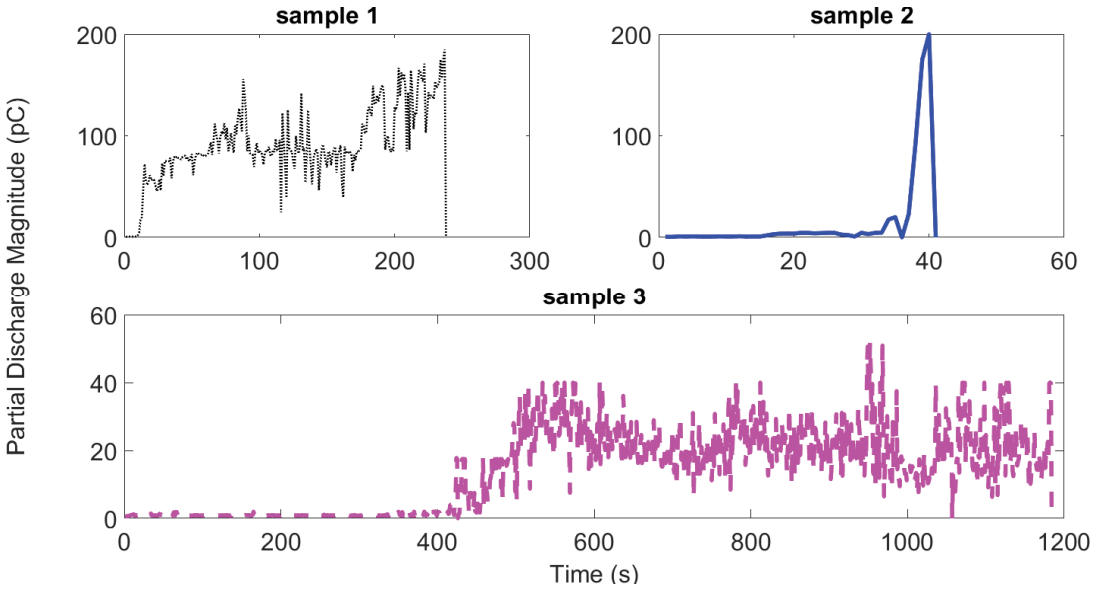

Figure 6-13: Partial discharge magnitude time evolution of 0.89 vol% C/Epoxy showing semiconductor characteristics.

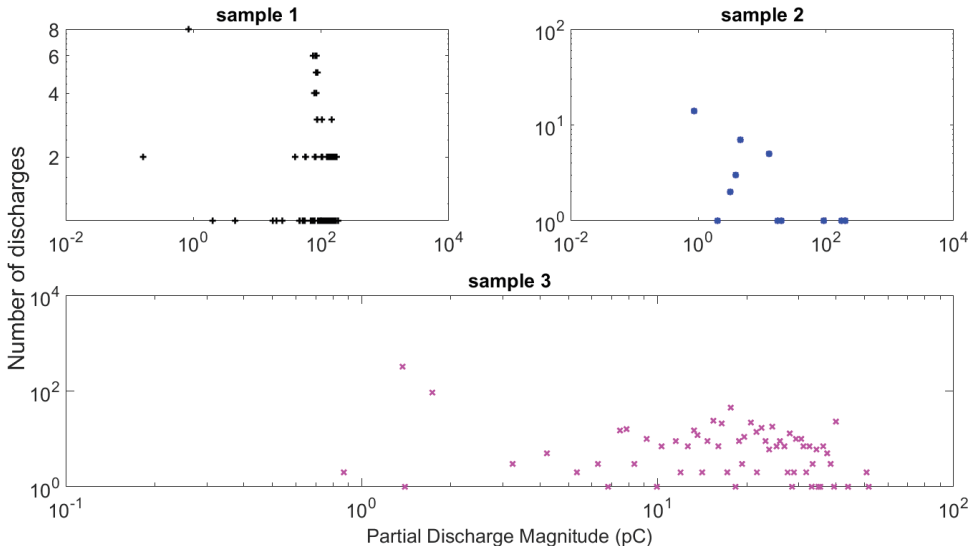

Figure 6-14: Log-log graph showing the magnitude distribution of PD in 0.89 vol% C/Epoxy.

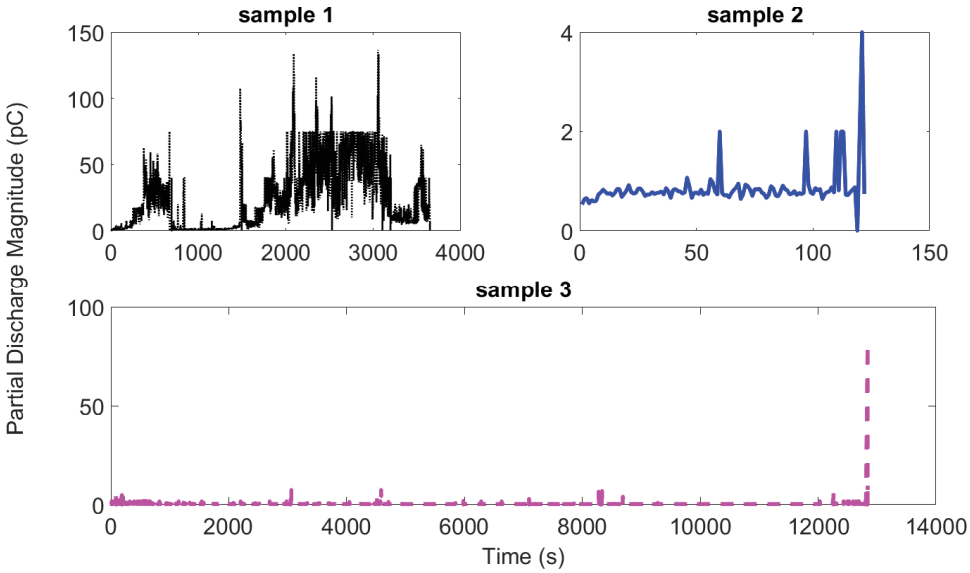

Figure 6-15: Complete partial discharge magnitude time evolution of 0.26 vol% BN/Epoxy.

Time evolution of electrical tree partial discharge magnitude plots in BN/Epoxy for various filler loadings ranging from 0.26 vol% to 2.77 vol% are presented in Figure 6-15 to Figure 6-32. From Figure 6-15 and Figure 6-16, the first set of results is for the 0.26 vol% samples. The first observations are the short material lifetimes of ~1.6 hours compared to 2 hours of pure epoxy. Once PDs start they grow until failure as in epoxy. The distributions indicate ramp like characteristics which indicate predominantly bush tree growth.

Figure 6-17 and Figure 6-18 give the observations for the 0.55 vol% samples. The average lifetime has increased to 14 hours indicating promising results. The PD's from start to failure have no impeded process in the BN/Epoxy sample. The PD magnitudes are no longer suppressed and have increased. The distributions have regions of high concentrations indicating branch characteristics.

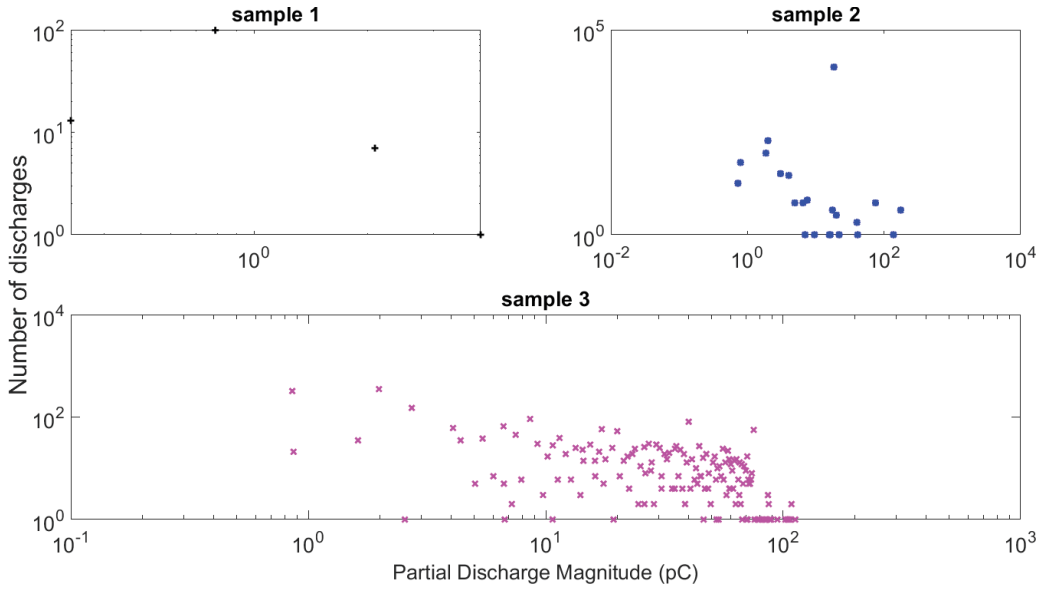

Figure 6-16: Log-log graph showing the magnitude distribution of PD in 0.26 vol% BN/Epoxy.

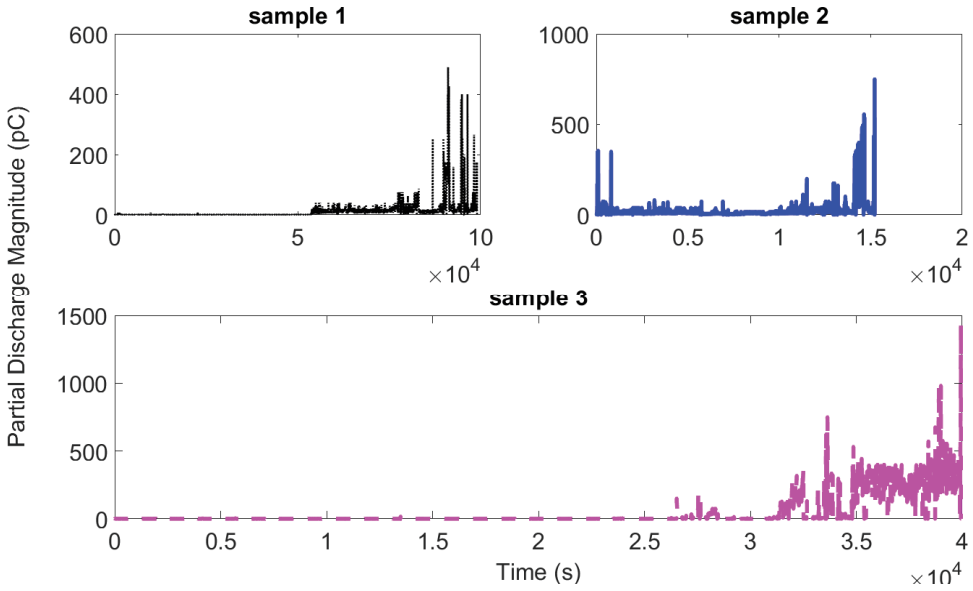

Figure 6-17: Partial discharge magnitude time evolution of 0.55 vol % BN/Epoxy.

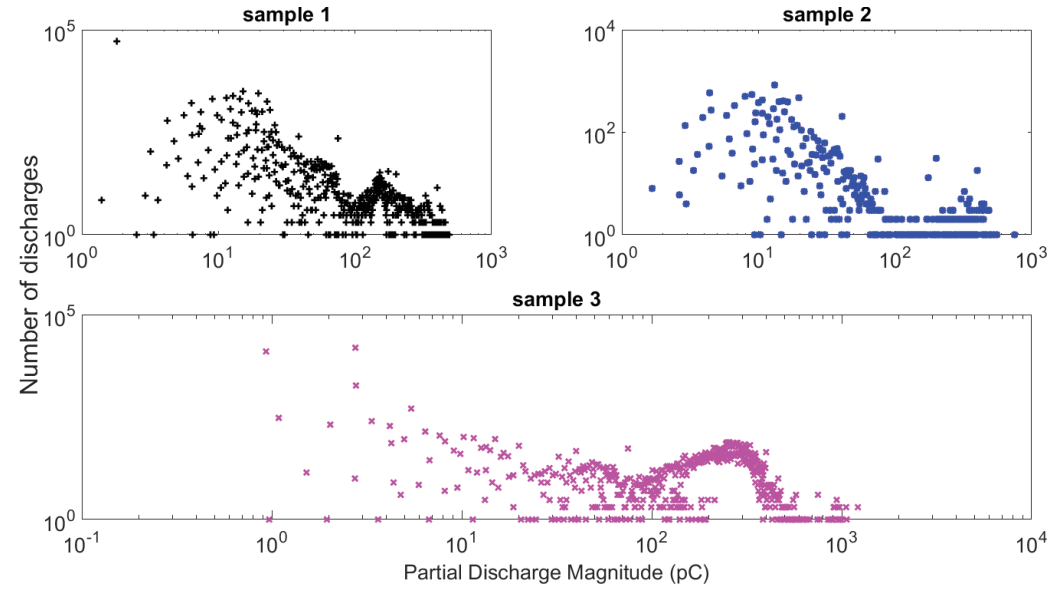

Figure 6-18: Log-log graph showing the magnitude distribution of PD in 0.55 vol % BN/Epoxy.

Figure 6-19 and Figure 6-20 give the observations for the 0.89 vol% samples. The average lifetime has decreased to ~2.9 hours. The PD's from start to failure have no impeded process in the BN/Epoxy sample. The PD magnitudes are beginning to be suppressed until failure. The Distributions are ramp like indicating bush characteristics.

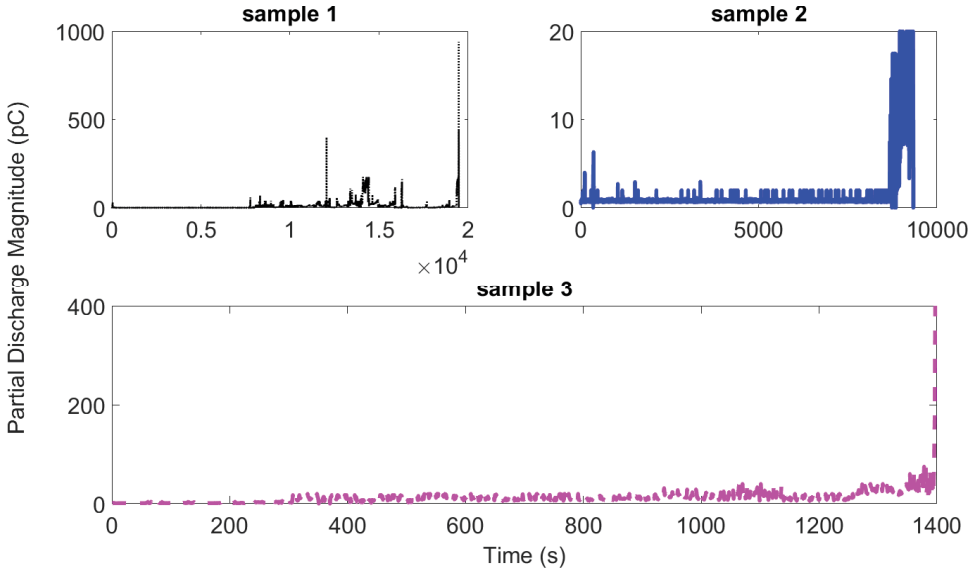

Figure 6-19: Partial discharge magnitude time evolution of 0.89 vol % BN/Epoxy.

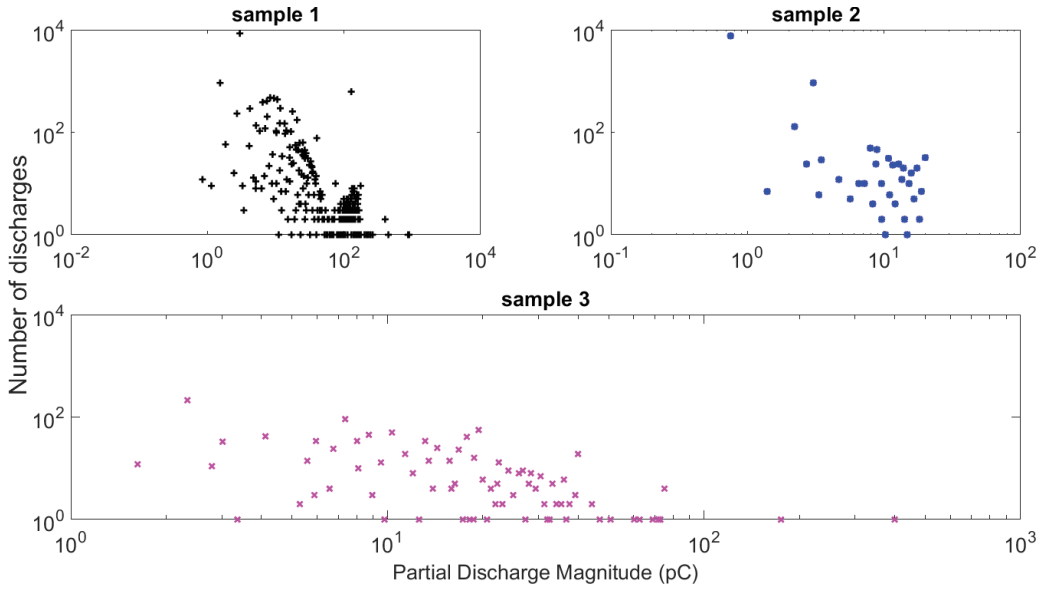

Figure 6-20: Log-log graph showing the magnitude distribution of PD in 0.89 vol % BN/Epoxy.

Figure 6-21 and Figure 6-22 give the electrical tree PD measurements for the 1.09 vol% samples. These were the first sets of samples predicted as optimal. The average lifetime has increased to ~11 hours. There are now periods of no PD activity and resistance to large PD magnitudes. The distributions indicate both bush-branch characteristics as with pure epoxy.

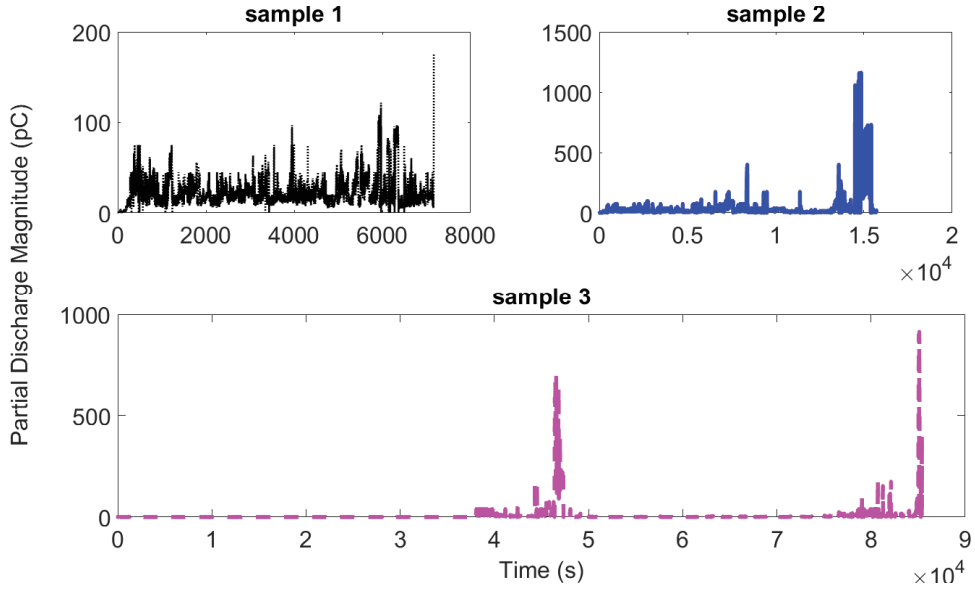

Figure 6-21: Partial discharge magnitude time evolution of 1.09 vol % BN/Epoxy.

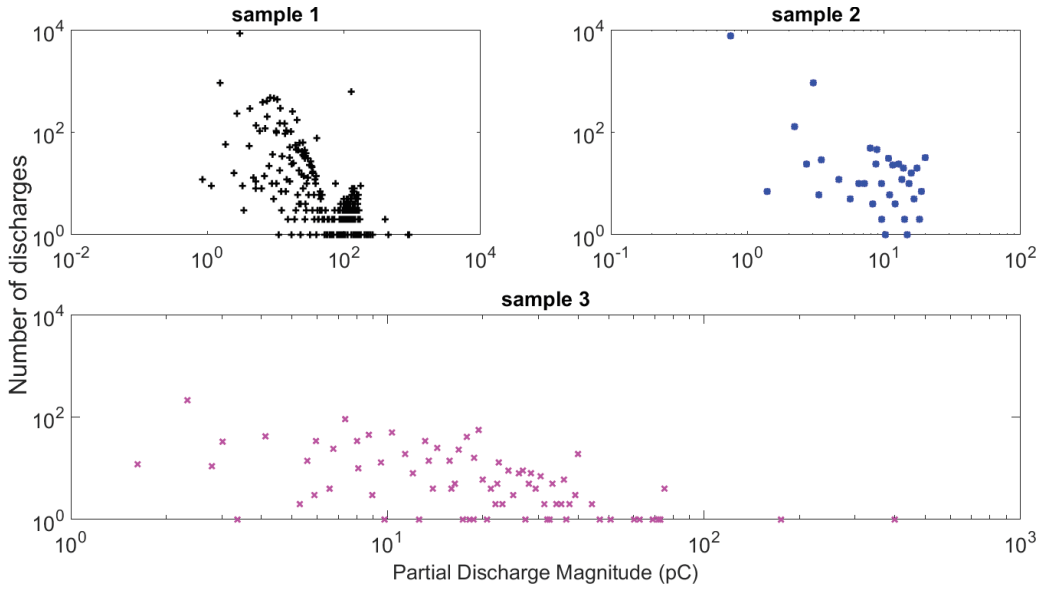

Figure 6-22: Log-log graph showing the magnitude distribution of PD in 1.09 vol % BN/Epoxy.

Figure 6-23 and Figure 6-24 give time-evolution PD magnitude plots of 1.25 vol% BN/Epoxy. These were samples predicted as optimal using rheology. In the beginning, there is a lot of activity which then stops for long durations. Resistant to relatively large discharges and the average time has increased to ~24 hours. The distributions indicate bush-branch characteristics.

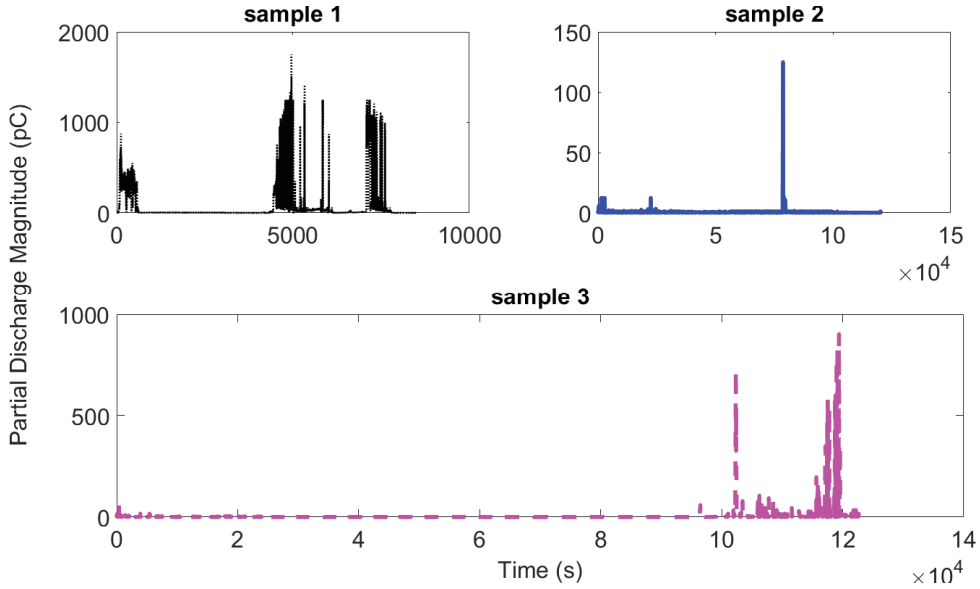

Figure 6-23: Partial discharge magnitude time evolution of 1.25 vol % BN/Epoxy verification sample.

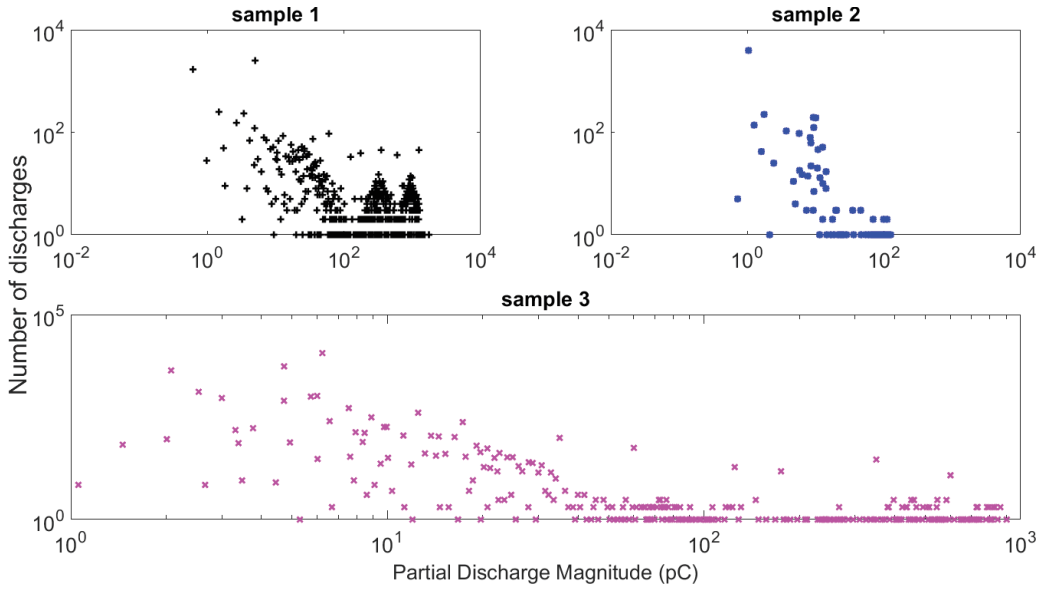

Figure 6-24: Log-log graph showing the magnitude distribution of PD in 1.25 vol % BN/Epoxy verification sample.

Figure 6-25 and Figure 6-26 give the results of the 1.35 vol % BN/Epoxy. At the end of the optimal region. The lifetime of these samples has decreased to 12 h but the distributions still show bush-branch characteristics. There is still suppression characteristics and resistance to relatively large discharges.

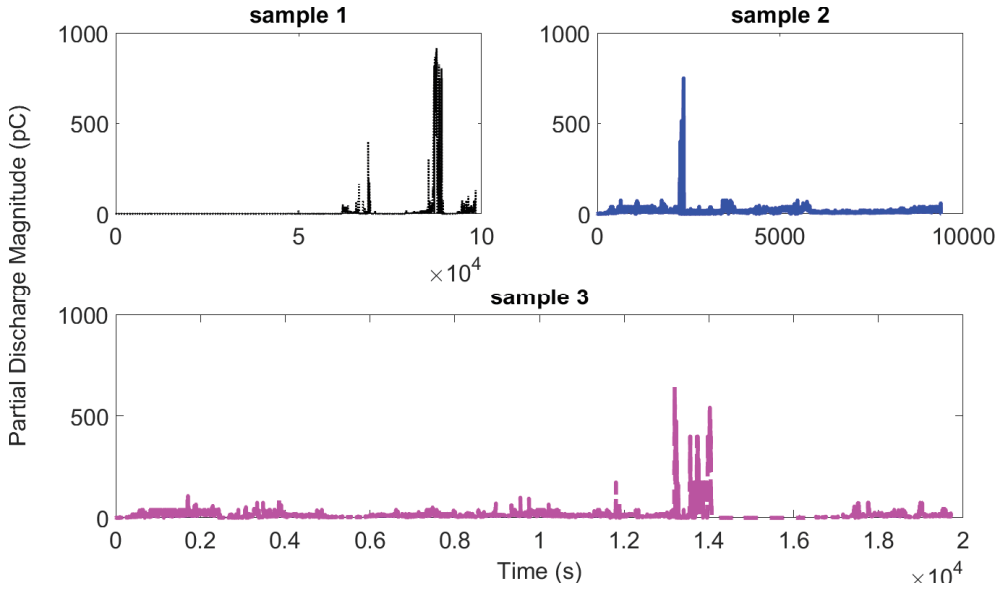

Figure 6-25: Partial discharge magnitude time evolution of 1.35 vol % BN/Epoxy.

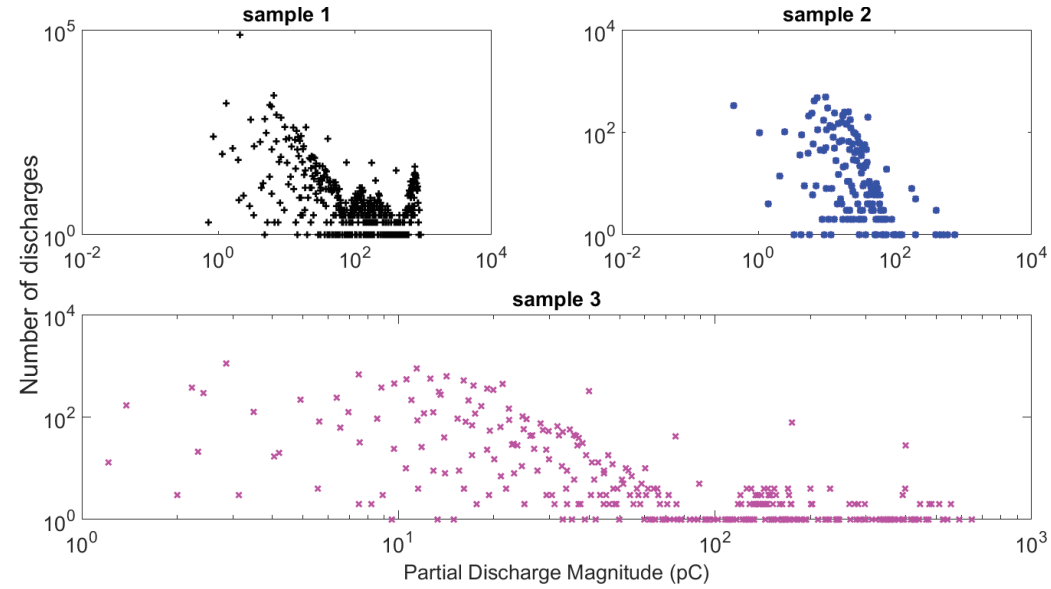

Figure 6-26: Log-log graph showing the magnitude distribution of PD in 1.35 vol % BN/Epoxy.

Figure 6-27 and Figure 6-28 give the results of the 1.65 % BN/Epoxy where the time has decreased further to 3.65 hours. The ability to suppress discharges is lost and continuous discharges ensue from start to failure. There are relatively large PD magnitudes and the discharge distribution indicates bush characteristics.

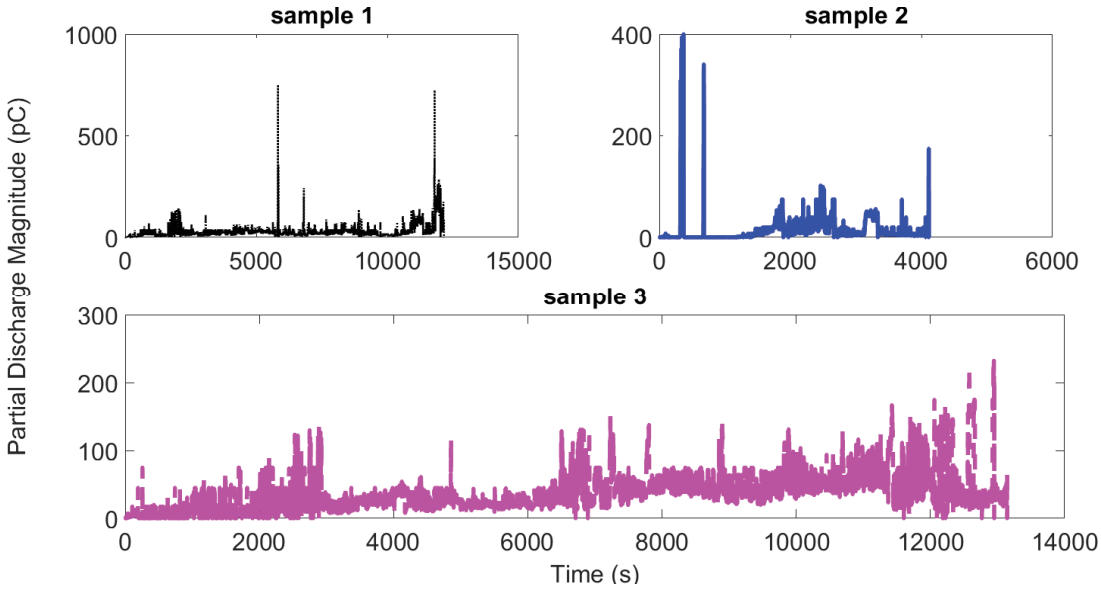

Figure 6-27: Complete partial discharge magnitude time evolution of 1.65 vol % BN/Epoxy.

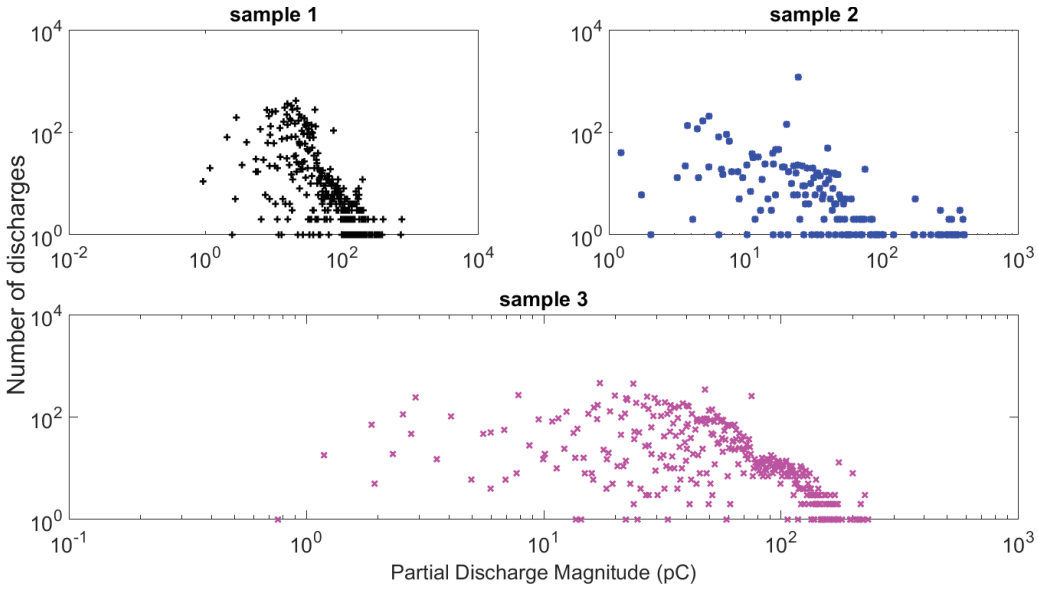

Figure 6-28: Log-log graph showing the magnitude distribution of PD in 1.65 vol % BN/Epoxy.

Figure 6-29 and Figure 6-30 give the results of the 1.96 vol% BN/Epoxy where the time to failure has continued to decrease to 1.09 hours compared to the pure epoxy of ~2 hours. The PD's are present continuously even in small magnitudes. The discharge distribution still indicates bush characteristics.

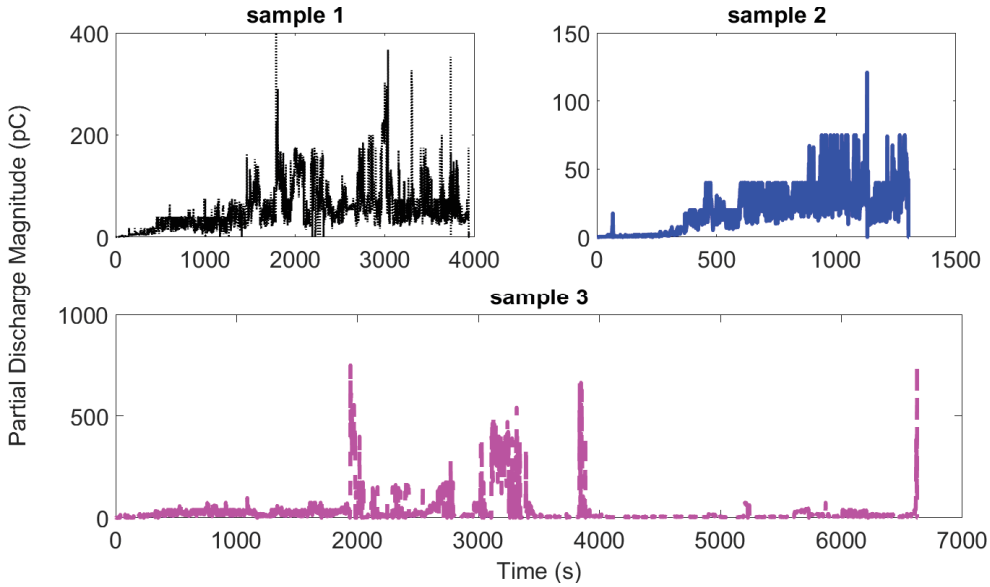

Figure 6-29: Complete partial discharge magnitude time evolution of 1.96 vol % BN/Epoxy.

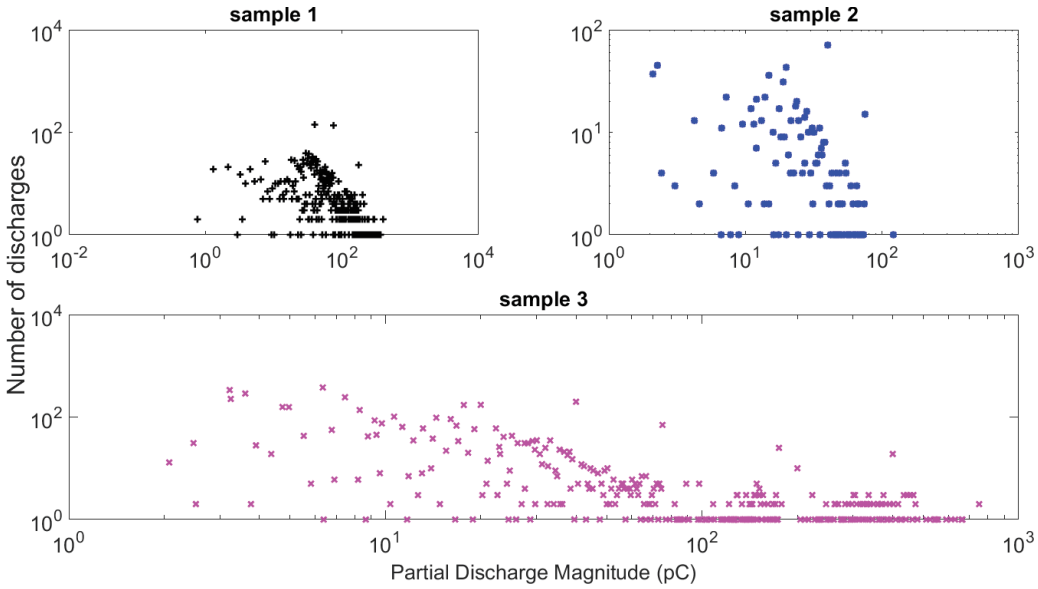

Figure 6-30: Log-log graph showing the magnitude distribution of PD in 1.96 vol % BN/Epoxy.

Figure 6-31 and Figure 6-32 give the results of the 2.77% BN/Epoxy. The average time has decreased further to 30 minutes which has ultimately compromised the material properties of epoxy. There are bush distributions with large PD magnitudes.

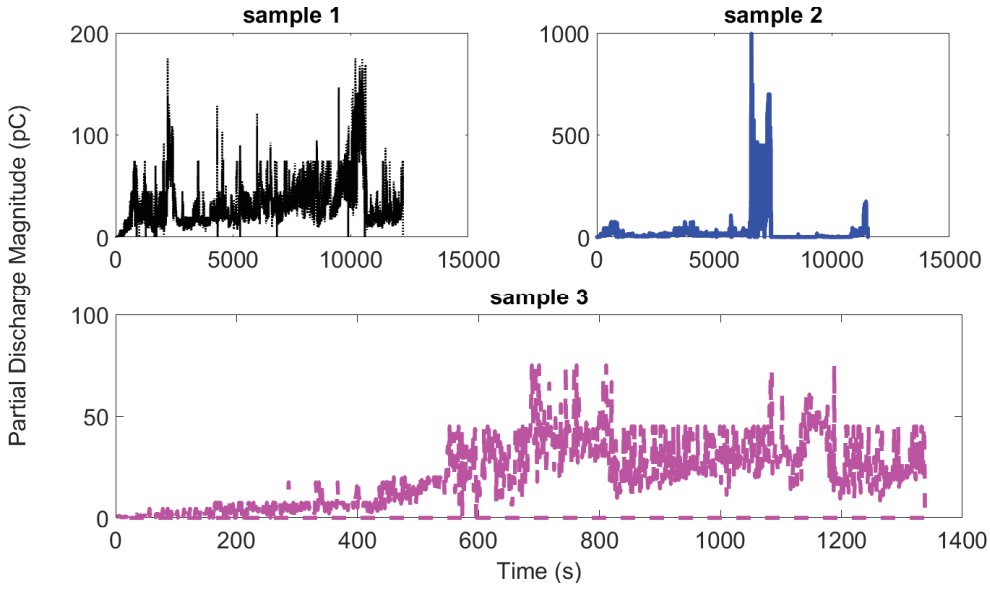

Figure 6-31: Complete partial discharge magnitude time evolution of 2.77 vol % BN/Epoxy.

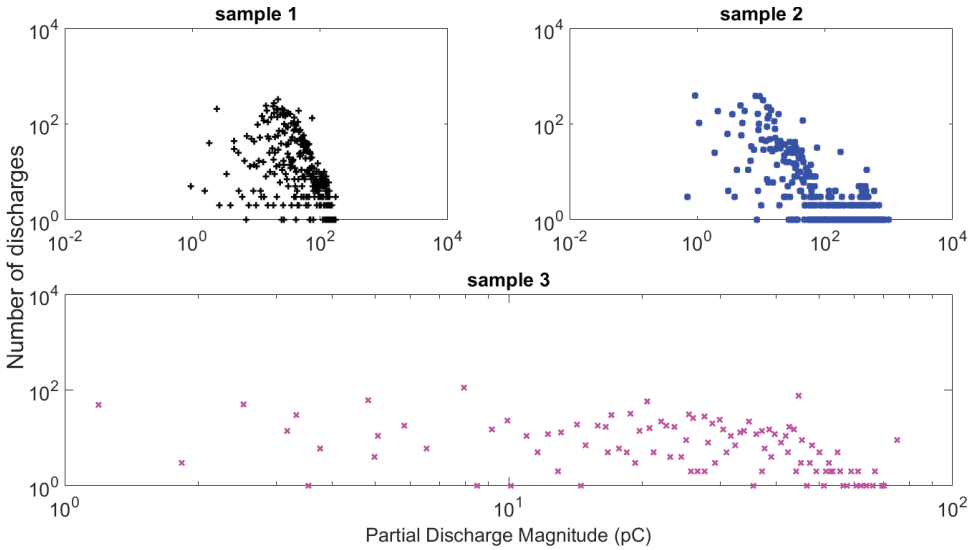

Figure 6-32: Log-log graph showing the magnitude distribution of PD in 2.77 vol % BN/Epoxy.

Up to and including 1.09 vol%, the PD events are generally characterised by alternating short periods of significant PD activity followed by relatively long periods of no or very little PD events. Generally, if periods of PD evanescence are long, the sample tends to take relatively long to fail. In most cases, breakdown occurs during a period of high PD activity. Beyond the loading of 1.35 vol% however, the PD magnitude evolution plots no longer show the distinctive alternating periods of PD activity and periods of no PD. Instead, the nanoparticles go back to being unable to retard the electrical treeing process.

Correlating the PD magnitude time-evolution plots with the corresponding PD magnitude-frequency distributions, regions of concentrations corresponds to constant magnitude PD bursts events. It can be argued that the extent of effectiveness of nanoparticles in suppressing the rate of electrical tree induced degradation is in how the PD activities are restricted to PD bursts periods. In that regard, for BN/Epoxy, 1.09 vol% to 1.35 vol% represent the optimal loading level region where PD activity is restricted to relatively short bursts that are interspaced by relatively long periods of no PD activity.

Similarly, for carbon, the periodical PD burst events occur only in 0.33 vol% samples that also survived for relatively much longer periods compared to the

higher loadings. It is remarkable that the optimal performance of 1.09 vol% to 1.35 vol% for BN/Epoxy and 0.33 vol% for C/Epoxy in electrical tree tests confirm the efficacy of the rheology tests and dielectric spectroscopy which give the loading levels of 1.09 vol % to 1.35 vol% for BN/Epoxy and 0.33 vol% for C/Epoxy as optimal volume fractions for the respective dielectrics. These results as determined through electrical tree PD analysis are consistent with the rheology analysis results as presented in Chapter 4.

The key findings of the tree evolutions are summarised as follows:

1. Although a comprehensive time to failure analysis was not done, there is a correlation between nanoparticle filler loading level and time to failure.

2. There is a correlation between the nature of trees grown and nanoparticle filler loading level. The trees begin as branch trees and slowly transition into bush concentration increases.

3. Optimally loaded samples restrict PD activity to relatively short bursts with long periods of no activity. These regions of no activity may be really small discharges which may not have been detected by the data logger, nevertheless, the magnitude suppression is remarkable.

The following section presents the partial discharge phase -resolved-patterns (PDPRPs) and quantitative statistical analyses of the electrical tree PD data in the C/Epoxy and BN/Epoxy nanodielectrics.

6.4 PD phase-resolved-patterns and quantitative statistical analysis

PD phase-resolved-patterns (PDPRPs) have traditionally been used to characterise PD sources [97]. An illustration of how PDPRPs were generated was shown in Figure 6-1. In some industrial applications, PDPRPs are used to evaluate the quality of the insulation, an example is the resonant test system used by CBI African Cables [98]. PDPRPs can similarly be used to identify the characteristics of new insulation properties like the effect of nanoparticles on the nature of electrical trees.

Gulski, Guastavino, Cerutti and Contin *et. al.* laid the foundation for applying statistical techniques to PD data [97], [99], [100]. The common methods of statistical techniques on PD are an evaluation of statistical parameters; the mean, variance, standard deviation, skewness and kurtosis [97], [99], [100]. In addition to the common methods of analysis, one new method will be discussed, a grouping algorithm according to identified common tree types.

As explained earlier, during the electrical tree analysis, the mean, maximum and minimum PD were recorded every second for the duration of the test. These were presented graphically in the previous section. The corresponding PDPRPs for the entire life of the samples was taken as a video format using Flashback Express recorder by Blueberry software [101]. From the video files, the PDPRPs are recorded with a frame rate of 20 ms. The PDPRPs were sampled every 20 minutes from start to end. The first 300 minutes of PDPRPs for each sample batch will be presented. This will be followed by the statistical analysis of all the data.

6.4.1 PDPRP experimental results and discussion

Each set of the PDPRPs presented in this section comprises of screen shots each taken every 20 minutes during the initial 300-minute period from first 20 kV application. The images are arranged in a chronological order row by row from left to right as labelled in Figure 6-33. From Figure 6-33 for pure epoxy, the PDPRPs show a predominance of relatively small and erratic pulses which are characteristic of mainly bush-branch electrical tree types. For 0.33 vol% C/Epoxy, Figure 6-34, the PRPRPs show that there is mainly branch type PDPRPs.

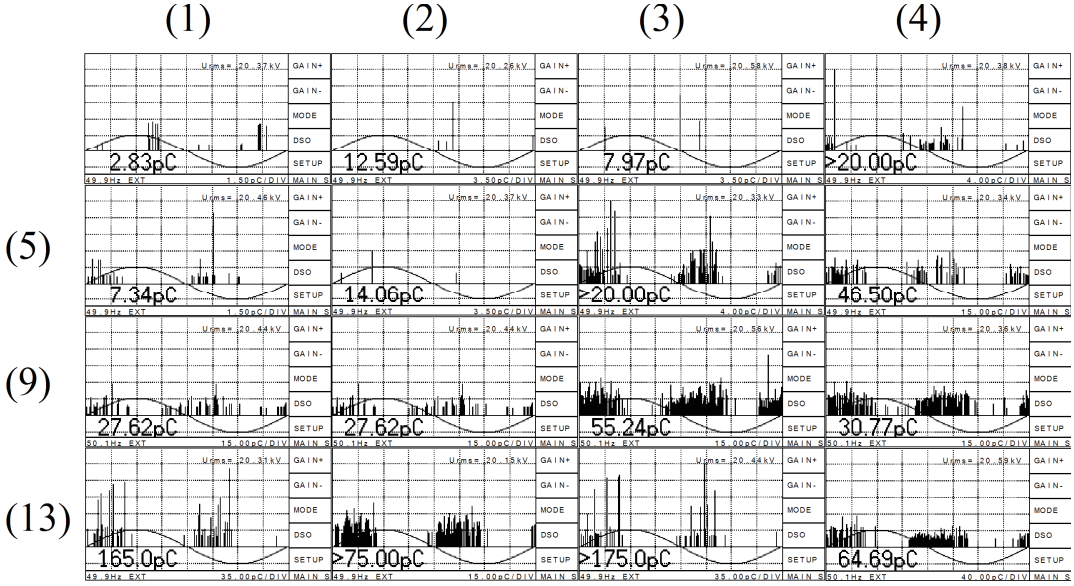

Figure 6-33: Clean epoxy PDPRP evolution showing single erratic pulses with increasing partial discharge magnitudes for the first four hours. The numbering convention is also shown.

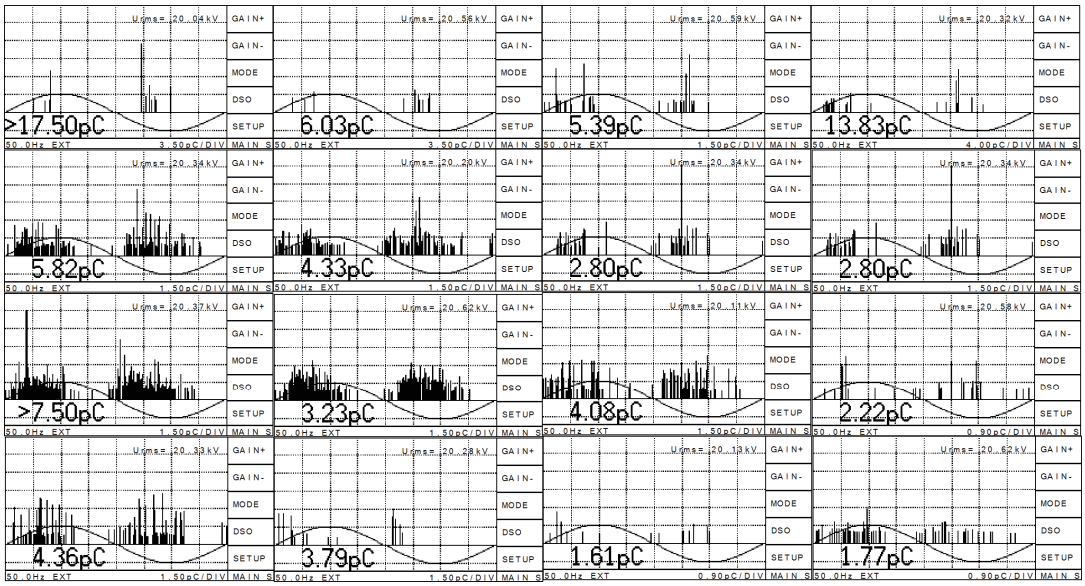

Figure 6-34: C/Epoxy 0.33 vol% showing predominantly small and quasi-uniform PD pulses a characteristic of bush tree types.

For the 0.89 vol% C/Epoxy the samples only lasted ~8minutes, so the PDPRPs taken were on a 30 s time intervals. The 0.89 vol% C/Epoxy results are shown in

Figure 6-35. Similarly, for the 0.26 vol% BN/Epoxy, the samples were at best 1 hour long, hence images were taken every 5 minutes.

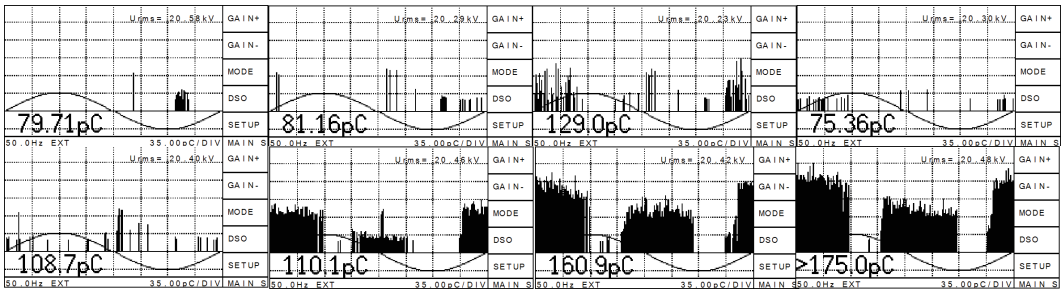

Figure 6-35: 0.89 % C/Epoxy sample 3 showing large tree channel magnitudes. These are characteristic of branch type trees. Images were taken every 30 seconds.

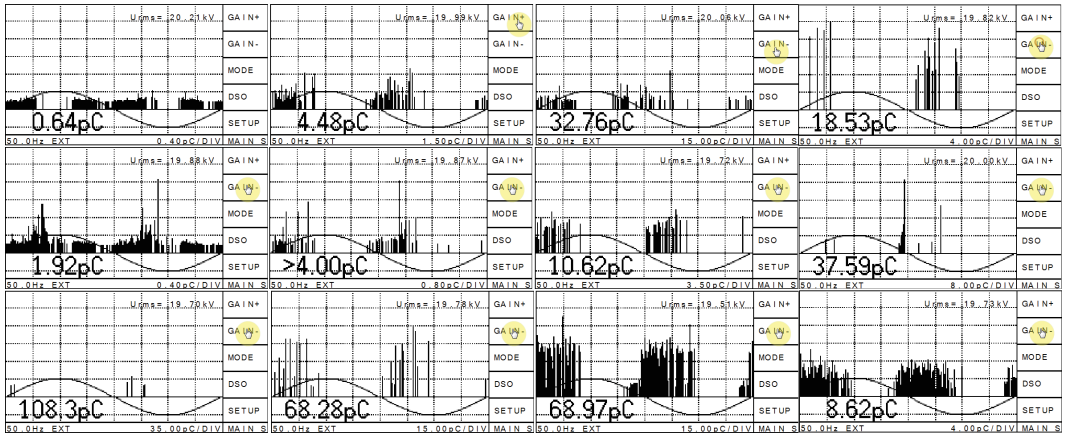

Figure 6-36: PDPRPs 0.25 vol% BN/Epoxy showing branch characteristics taken every 5 minutes.

Figure 6-37 shows the PDPRPs for the 0.55 vol% BN/Epoxy which has both bush and branch type characteristics. Figure 6-38 shows the 0.89 vol% BN/Epoxy sample PDPRPs. There is evidently branch-bush but mainly bush characteristics. Figure 6-39 shows the 1.09 vol % BN/Epoxy sample 2 results. In the beginning there appear to be branch characteristics, but for the remainder, the tree types are mainly bush trees.

Figure 6-40 and Figure 6-41 give the 1.25 vol% and 1.35 vol% BN/Epoxy sample PDPRP results respectively. For both samples the magnitudes are significantly suppressed, not exceeding ~20 pC. The characteristics would typically be referred

to as characteristic of bush type trees, but they could also be branch type trees with very small magnitudes.

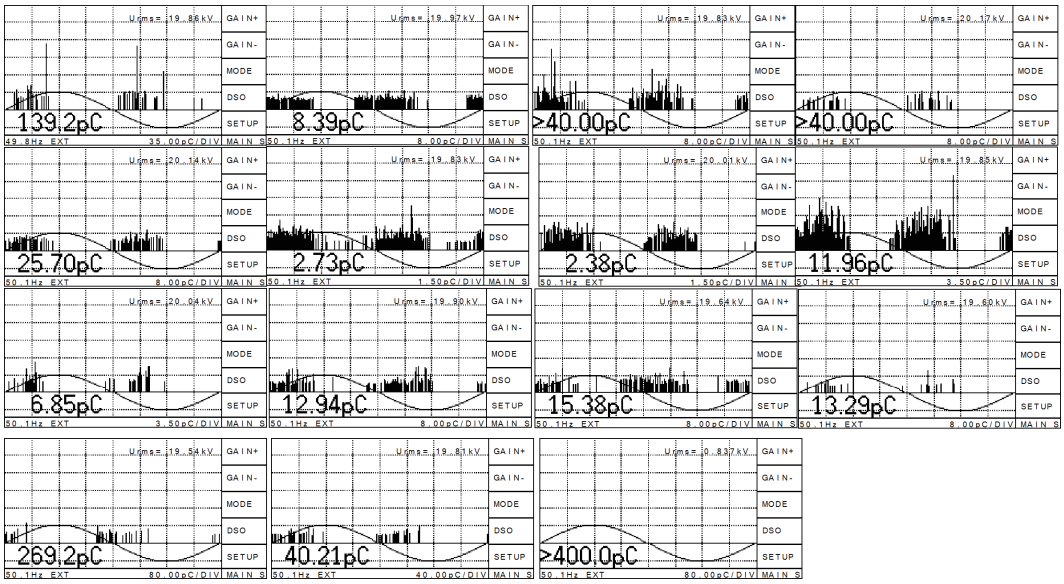

Figure 6-37: PDPRPs for 0.55 vol% BN/Epoxy sample showing both branch and bush characteristics.

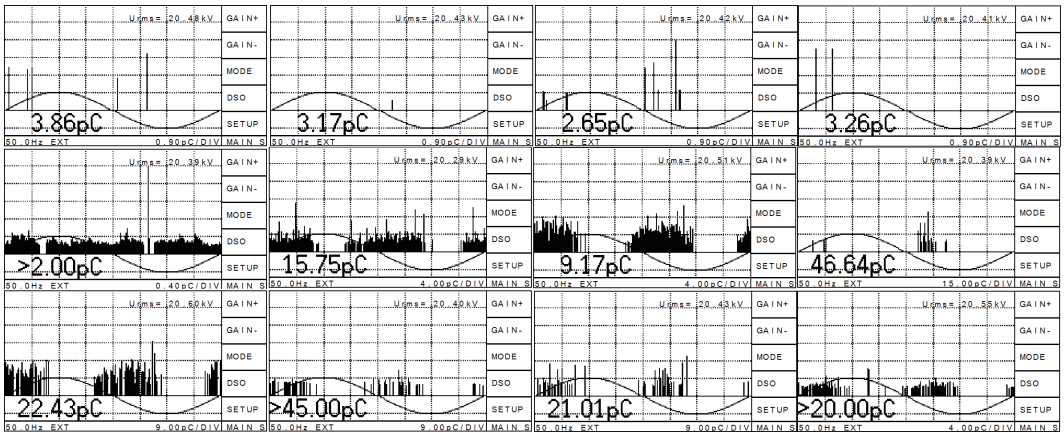

Figure 6-38: PDPRPs for 0.89 vol% BN/Epoxy showing region between bush and branch characteristics.

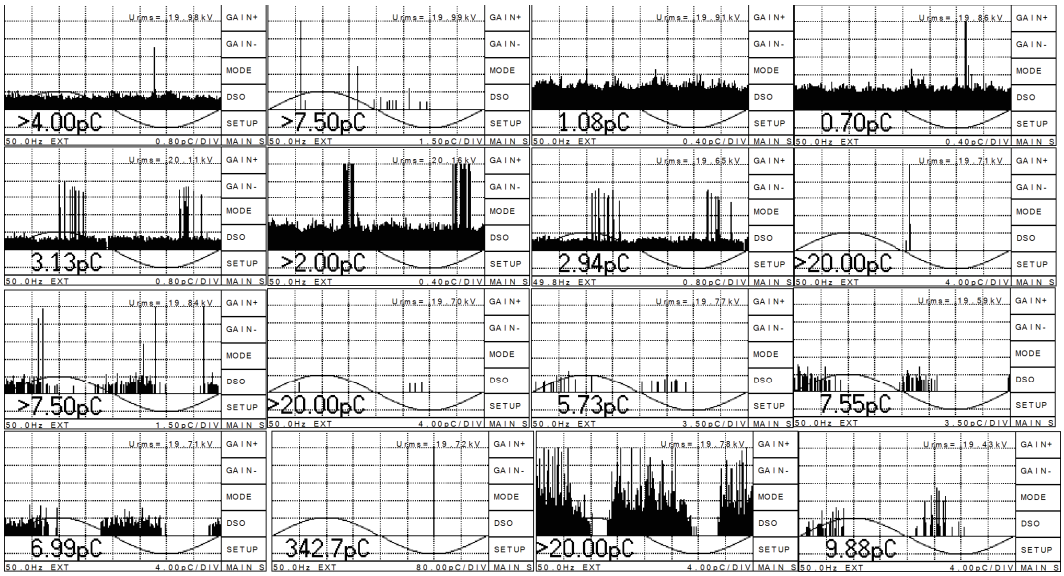

Figure 6-39: PDPRPs of 1.09 vol% BN/Epoxy showing bush-branch, mainly branch type characteristics and suppressed PD magnitudes.

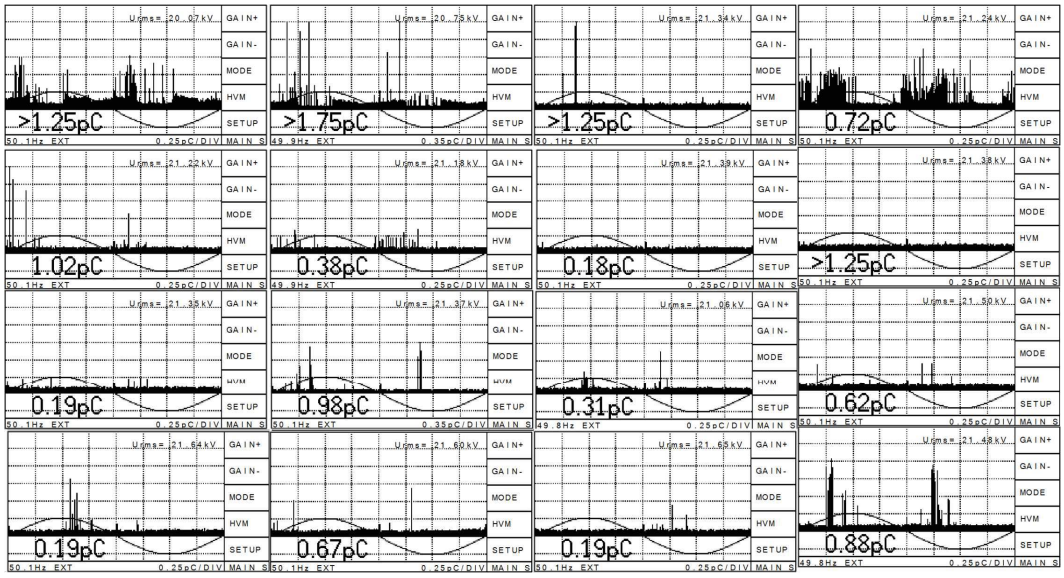

Figure 6-40: PDPRPs for BN/Epoxy 1.25 vol% for first four hours showing suppressed PD magnitudes with branch like characteristics.

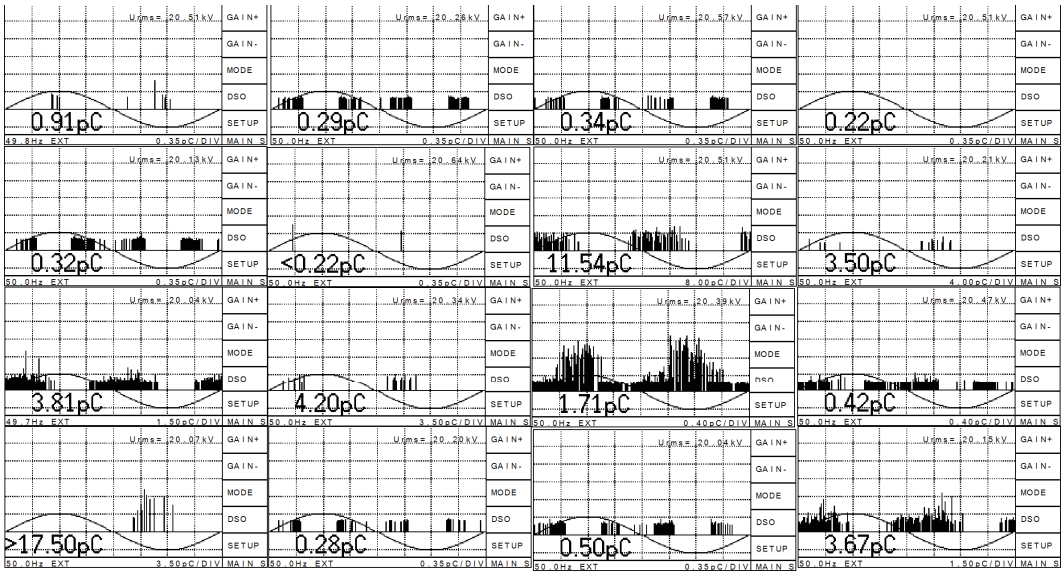

Figure 6-41: PDPRPs for BN/Epoxy 1.35 vol% for first four hours showing decreased PD magnitudes with bush characteristics.

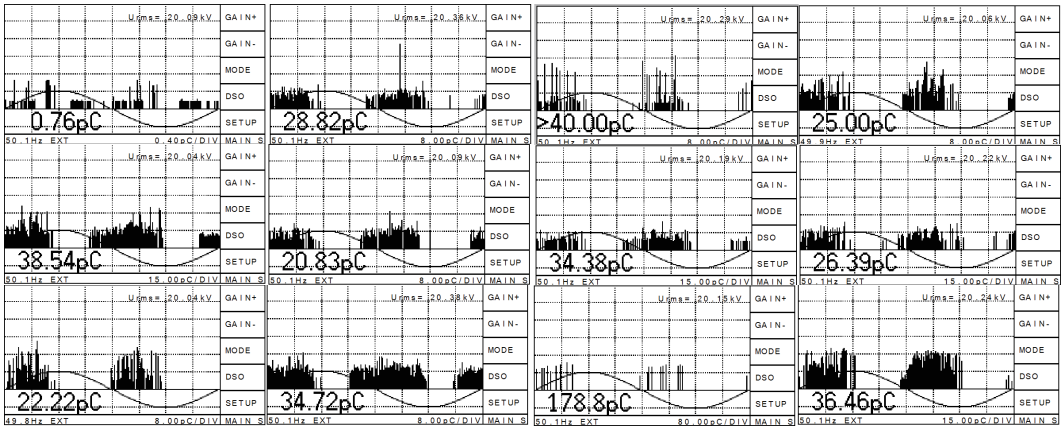

Figure 6-42: PDPRPs of 1.65 vol% BN/Epoxy showing bush characteristics irrespective of magnitude.

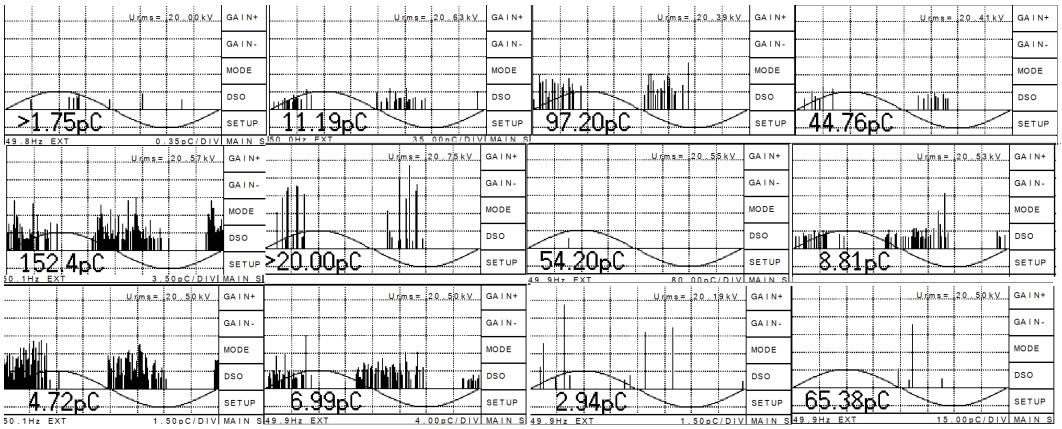

Figure 6-43: PDPRPs of 1.96 vol% BN/Epoxy showing mainly branch type characteristics.

Figure 6-42 and Figure 6-43 give the PDPRPs for 1.65 vol% and 1.96 vol%. The PD magnitudes have dramatically increased in magnitude, but are fairly uniform in distribution which would be characteristic of bush trees. Figure 6-44 give the PDPRPs for 2.77 vol% sample 1. The magnitudes have increased compared to the other samples and quickly goes to failure. From the PD data (Figure 6-6 to Figure 6-32) and the PDPRPs (Figure 6-33 to Figure 6-45), a close scrutiny of the PDPRP and how they correlate to the tree types enables one to group the patterns into categories of type A to D as shown in Figure 6-45. Each PDPRP category represents specific tree types or combinations thereof.

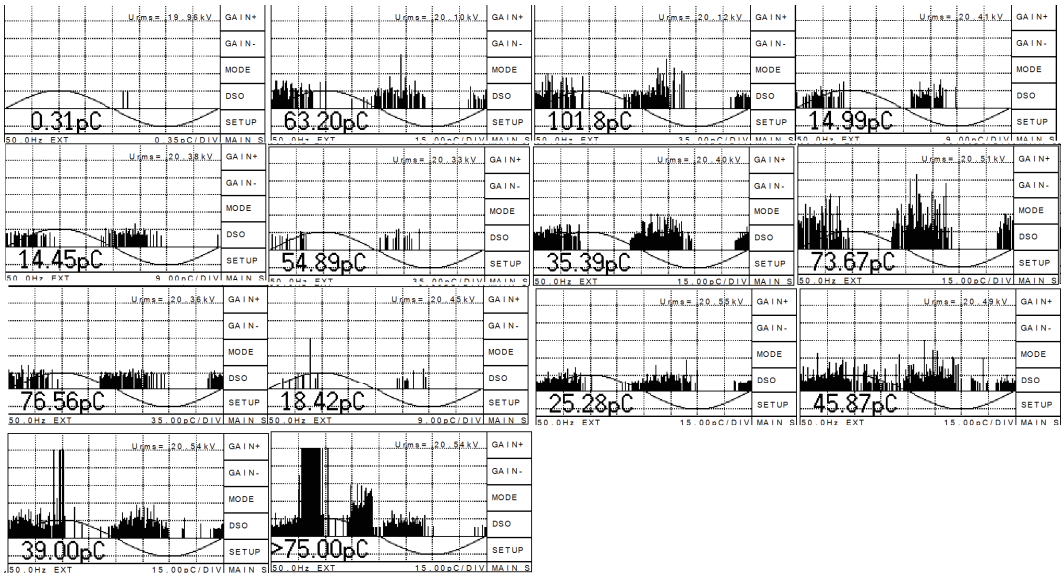

Figure 6-44: PDPRPs of 2.77 vol% BN/Epoxy showing continuously large PD magnitudes with mainly bush characteristics.

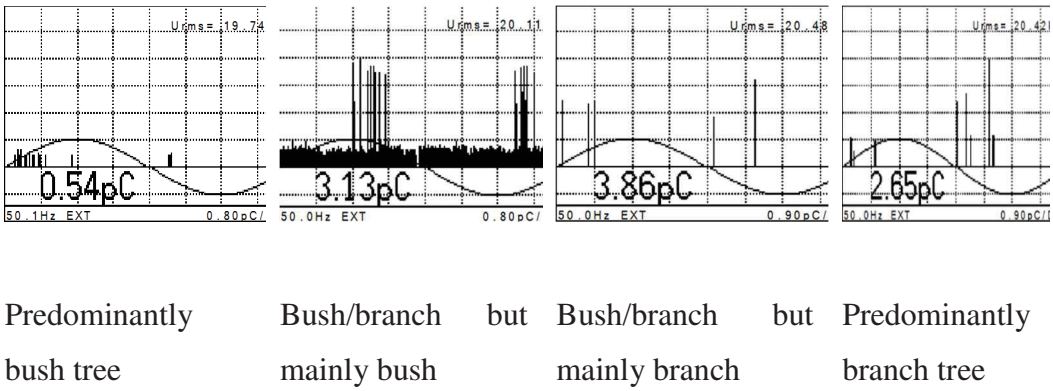

Figure 6-45: Different types of PDPRP corresponding to different types of electrical trees in pure epoxy.

Figure 6-45 shows different PDPRP stages for clean epoxy with predominantly bush (Type A), bush-branch but mainly bush (Type B), bush-branch but mainly branch (Type C), and mainly branch characteristics (Type D).

Bush electrical trees support smaller and quasi-uniformly sized PD pulses while branches support bigger PDs of wide-ranging magnitudes. The resultant PDPRP comprise a mixture of different pulse types presented in Figure 6-45. When continuously observed, electrical tree PDs occur as bursts and the composition of

PD pulses in each half cycle of the excitation voltage change depending on how the electrical tree evolves in shape as it propagates in the insulation gap. Examples of other possible intermediate types are shown in Figure 6-45.

The PD data recorded every second from the electrical tree inception to sample complete failure for all samples were processed using a purpose designed classification algorithm illustrated in Figure 6-47. The full implementation of the algorithm in C++ is given in Appendix C. The algorithm was designed to establish which type of electrical trees occur most often in the samples. Plots of the frequency of occurrence of each PDPRP type at each loading level are presented in Figure 6-47 and Figure 6-48 for BN/Epoxy and C/Epoxy respectively.

In clean epoxy (zero loading) the order of predominance type of PDPRP is Type A, Type D, Type B and then Type C. The differences in predominance across the various PDPRP types, however, is small (~50 individual pulses) and this is characteristic of bush/branch electrical trees. For BN/Epoxy, as the filler loading increases, the order of predominance changes and at 1.09 vol%-1.35 vol%, Type A becomes prevalent by orders of magnitude over other types (40% greater). Beyond 1.25 vol%, the order of predominance changes again such that at 2.77 vol% it almost resembles that of clean epoxy. The predominance of Type A at filler loadings 1.09 vol%-1.35 vol% means that at optimal loading, nanoparticles restrict electrical trees too short quasi-pulse characteristic growth.

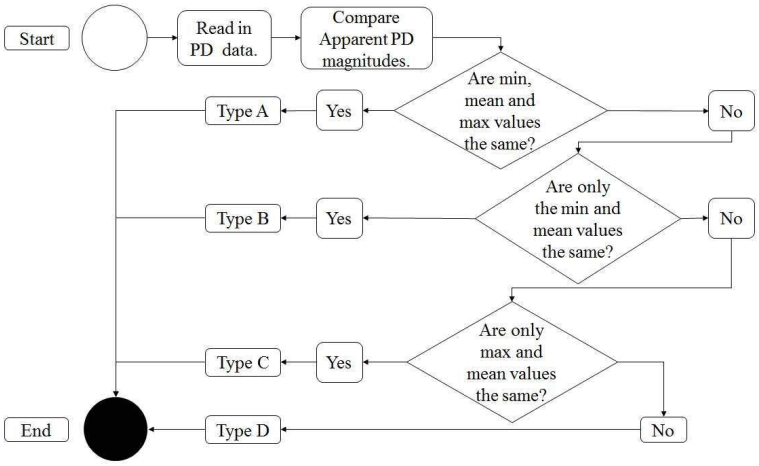

Figure 6-46: Flow diagram showing a possible way of grouping the PD activity. Note, the data was filtered assuming according to the assumed average noise level of 0.5 pC.

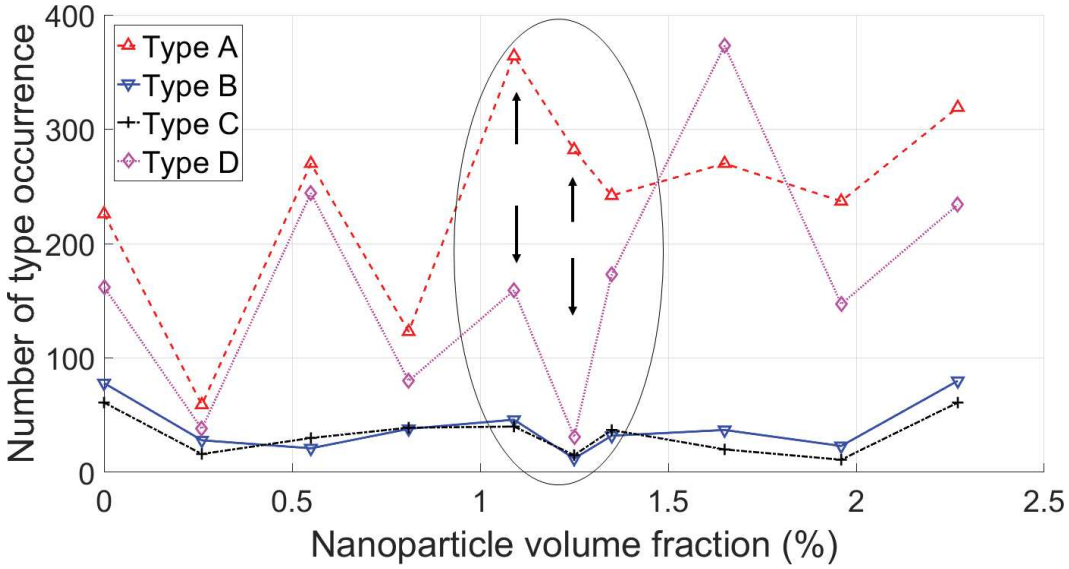

Figure 6-47: PDPRP type variation predominance in BN/Epoxy as a function of particle filler loading level indicating an emphasis on the particular type of tree growth.

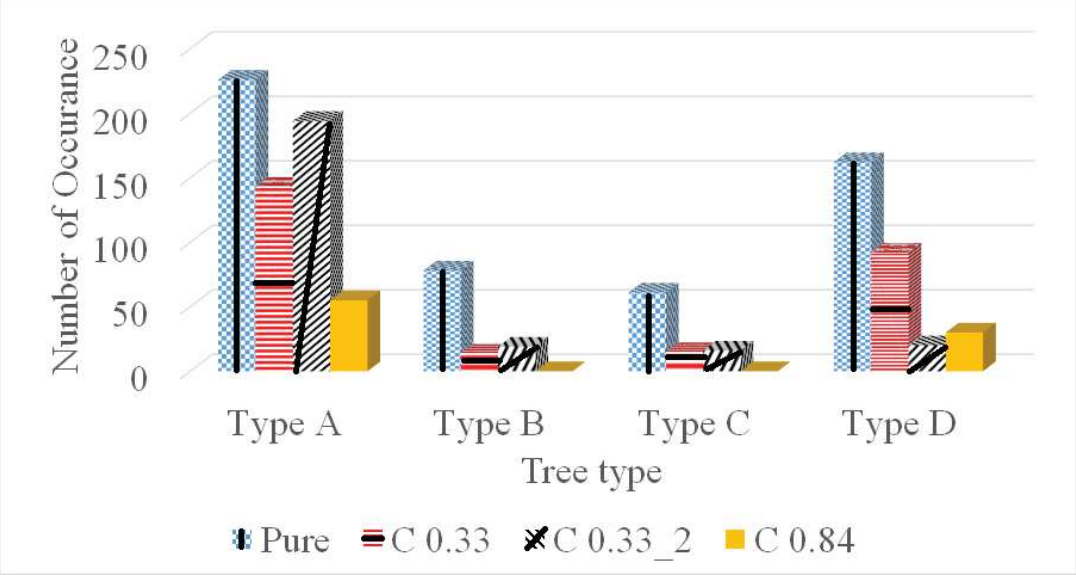

Figure 6-48: PDPRP type variation in C/Epoxy as a function of 0.33 vol% and 0.89 vol% against pure epoxy.

With C/Epoxy, only meaningful PD data was recorded for the 0.33 vol% and 0.89 vol% loaded. Figure 6-48 shows that the shape does not change for C/Epoxy but the categories become increasingly suppressed. As the particle concentration increases, the material changes from more insulating to more conductive as established in the previous chapter with dielectric spectroscopy.

Based on the comprehensive analysis using the PDPRPs and some of the data, it can be concluded that 1.09 vol% -1.35 vol% for BN/Epoxy and 0.33 vol% C/Epoxy have the best characteristics with regard to suppressing electrical tree growth. These are achieved by limiting the PD magnitudes and causing tree paths to have a uniform tree channel size due to the uniform PD magnitudes. The following sub-section discusses the statistical analysis of the PD data.

6.4.2 PD magnitude distribution statistical parameters (mean, variance, skew, and kurtosis) of the electrical tree PD in the nanodielectrics

The information contained in the mean, variance, skewness and kurtosis of a Gaussian distribution is indicated in Figure 6-49 [97], [99], [100]. Electrical trees are dependent on various parameters like material quality, electric fields, and seed electron availability. It is debatable as to the deterministic nature of electrical trees burst they have been established as stochastic [97], [99], [100]. It is therefore

assumed that the partial discharges which occur in electrical trees have some degree of Gaussian distribution [97], [99], [100]. Mean and variance indicates the location and width of the Gaussian distribution, while the skewness and kurtosis indicate the symmetry and concentration of data. The data was filtered (implementation in Appendix C and D) and each sample batch was analysed and the results are summarised in Table 6-1. All summaries and comments made in Table 6-1 are with reference to pure epoxy.

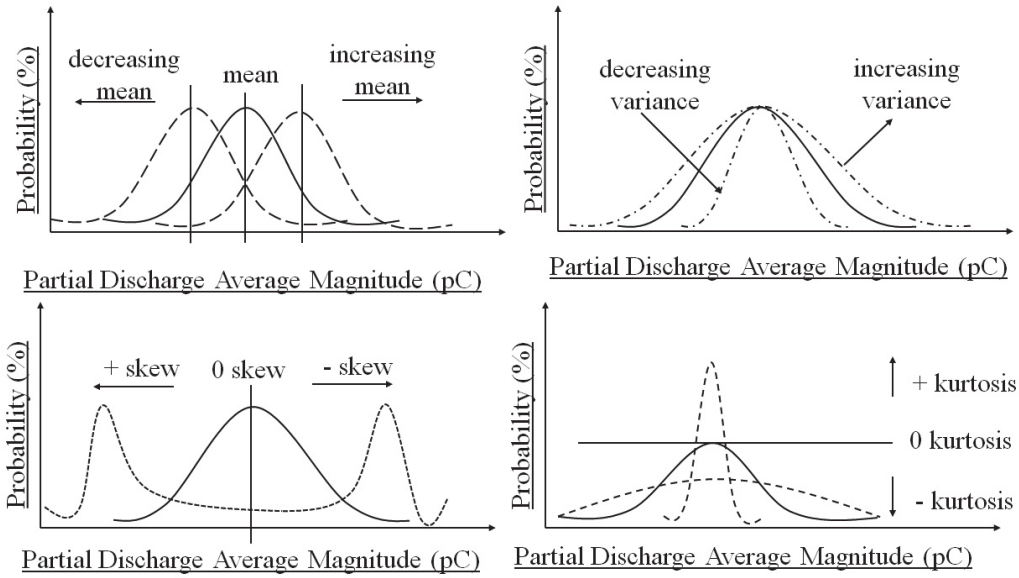

Figure 6-49: How mean, variance, skewness, and kurtosis inform changes to a Gaussian distribution.

The key findings of the PD analysis can be summarised as follows:

1. There is a correlating increase in time to failure and tree discharge distribution with increasing nanoparticle concentration for BN/Epoxy. The optimal samples show an increase in time to failure.
2. For BN/Epoxy, the optimal filler loadings appear to be 1.09 vol% - 1.35 vol%. The PD magnitudes were slightly higher, more concentrated, skewed to the left, but lasted longer, indicating there is a separate reason apart from magnitude suppression which contributes to increased performance. This must be the increased mechanical stiffness which was seen in the previous chapter.

3. By evaluating all the PD data, it is clear there is a transition from a branch like characteristic to bush type characteristics as nanoparticle concentration increases.
4. For C/Epoxy, the electrical tree results confirm that the percolation threshold for C/Epoxy is 0.89 vol%.
5. For C/Epoxy, 0.33 vol% gave dramatically improved electrical tree retardation properties by suppressing the partial discharges for significant periods of time.
6. The CNS particles do not provide as much mechanical stiffness as the BN particles and are at a lower concentration, therefore the partial discharge suppression must be a function of electron scavenging.
7. The mean, variance, skewness and kurtosis parameters of the electrical tree PD magnitude distributions confirm the trends and correlations between the PD types, the filler type and loading levels as established through other PD analysis techniques that were presented earlier.
8. The statistical analysis shows that there is no common trend in the nanodielectric samples and hence the treeing process within the nanodielectrics is still stochastic.

The following section presents the methods used to image the trees to complete the electrical tree analysis.

Table 6-1: Statistical summary of the Partial Discharge results for the different electrical tree samples when compared to pure epoxy.

Sample	Mean	Variance	Skewness	Kurtosis
Pure epoxy	**28**	**1793**	**4**	**23**
Bush-branch		**-Wide variance**	**-Almost Gaussian**	**-Concentrated**
C 0.33 vol %	**2**	**790**	**17**	**792**
More bush	**-significant suppression**	**-lower variance**	**-Skewed to the left**	**-highly concentrated**
C 0.89 vol %	53	1572	2	7
Bush-branch	Higher magnitudes	-Relatively close to epoxy	-Mostly Gaussian	-Mostly Gaussian
BN 0.26 vol %	9	194	28	2608
More bush	-discharges suppressed	-lower variance	-Skewed heavily to the left	- Impulse
BN 0.55 vol%	26	1341	3459	38
Bush-branch	-Same mean	-Relatively close to epoxy	-Skewed significantly to the left	-Concentrated
BN 0.89 vol%	8	7980	9	195
More bush	-discharges suppressed	significantly wide variance	-Almost Gaussian	-More concentrated
BN 1.09 vol %	**29**	**7300**	**6**	**79**
More bush	**-Same mean**	**significantly wide variance**	**-Mostly Gaussian**	**-Concentrated**
BN 1.25 vol %	**34**	**21470**	**22**	**897**
More bush	**-higher mean**	**slightly wider variance**	**-Skewed slightly to the left**	**-highly concentrated**
BN 1.35 vol %	**16**	**3113**	**10**	**164**
More bush	**-discharges suppressed**	**significantly wide variance**	**-Almost Gaussian**	**-More concentrated**
BN 1.65 vol%	27.00	1110.00	5.00	43.00
More branch	-Same mean	-significantly wide variance	-Mostly Gaussian	-concentrated
BN 1.96 vol %	36	2514	3	10
More Branch	Higher mean	-significantly wide variance	-Mostly Gaussian	-Mostly Gaussian
BN 2.77 vol %	28	2716	2	10
More branch	-Same mean	-significantly wide variance	-Mostly Gaussian	-Mostly Gaussian

6.5 Characterising electrical tree micro-tunnels in the nanodielectrics using XCT and AFM

In order to complete the analysis of electrical trees, this section discusses imaging the electrical trees using X-ray Computer Tomography (XCT) and Atomic Force Microscopy (AFM). The purpose of this section is to understand what effect the nanoparticles have on the polymer. It is well established that the growth of a tree and PDs produced have a relation to the tunnels and tubules formed in the tree. Additionally, imaging electrical trees in solid insulation conventionally rely on the insulation being transparent. Given the PD results, it was assumed that there would be electrical tree characteristics observed in nanodielectrics. However, the ability to image an electrical tree using conventional techniques is difficult if a sample is opaque.

Current literature suggests that the use of different microscopy techniques such as Transmission Electron Microscopy (TEM), Scanning Electron Microscopy (SEM), and Atomic Force Microscopy (AFM) may allow for tree structures to be observed [12]. Additionally, microscopy techniques are essentially destructive tests which can be a limitation [12].

A less invasive method of investigating electrical trees in opaque nanodielectrics is the use of X-ray computer tomography (XCT) illustrated in Figure 6-50 which may allow for trees to be observed [12]. XCT can be explained as follows: 2-D slices are taken sequentially using X-rays and detectors to establish differences in density in a sample. All the 2-D slices are then consolidated to create a 3-D image. As was conventional understanding of light microscopes, it is still reliant on the wavelength of the X-ray determining a change in density and hence has potential resolution limitations.

Additionally, XCT is a relatively costly procedure compared to conventional microscopy techniques. It was opted to use XCT to investigate one of the 0.33 vol% C/Epoxy and one of the pure epoxy samples for tree validation. The remaining optimally loaded samples would then be analysed using AFM.

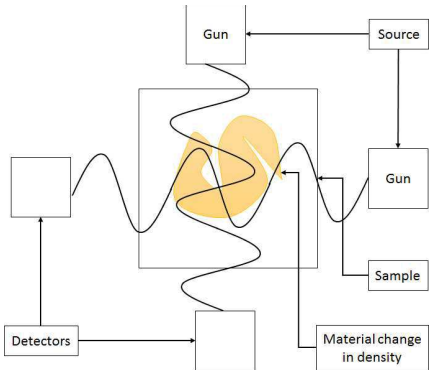

Figure 6-50: Principle operation of X-ray computer tomography.

6.5.1 X-ray Computer Tomography image analysis of the electrical trees.

A Xradia 510 Versa X-ray microscopy computer topographer was used for the XCT analysis made available by Carl Zeiss in Germany.[4] Figure 6-51 and Figure 6-52 show 3D rendered XCT images of pure epoxy confirming that the trees were indeed of the bush-branch type as deduced earlier through PD analysis [42].

In the clean epoxy sample, electrical trees with fine branches down to the sub-nanometre scale are shown with rich contrast. In addition, relatively large channels and flat crack planes were formed. In contrast, Figure 6-53 to Figure 6-56 are the XCT images of the 0.33 vol% C/Epoxy test specimen taken out before failure after 120 hours of continuous 20 kV voltage endurance.

At first glance, there appears to be no electrical tree degradation of the insulation! However, a region enveloping part of the needle tip is clearly discernible as comprising a material with a density different from that of the nanodielectric and the needle (Tungsten). This region is not symmetrical around the needle tip as evident in Figure 6-54 to Figure 6-56 nor does it extend along the entire bevelled part of the needle tip. Such dimensional features rule out the possibility of this region being a result of a mechanical retraction of the needle within the C/Epoxy.

Remarkably, the degraded region follows very closely the profile of the intensified electric field region around the needle tip as depicted in Figure 6-57 and Figure

[4] Acknowledgements are given to Zeiss in Germany for conducting the XCT analysis and providing the results.

6-58. The simulations created using FEMM assume absolutely pristine epoxy completely devoid of any kind of defect.

It is also interesting to note the presence of micro-sized pieces of metal present in the degraded region around the needle tip as shown in Figure 6-53. It is speculated that due to the intensified electric field (>1 MV/mm) along the interface of the needle tip and the C/Epoxy material, energy is imparted to the material resulting in physiochemical processes that may possibly include electrical trees at some stage. In order to establish a full understanding of the void region, the remaining samples were cut and analysed using AFM. The following sub-section explains the AFM analysis methodology.

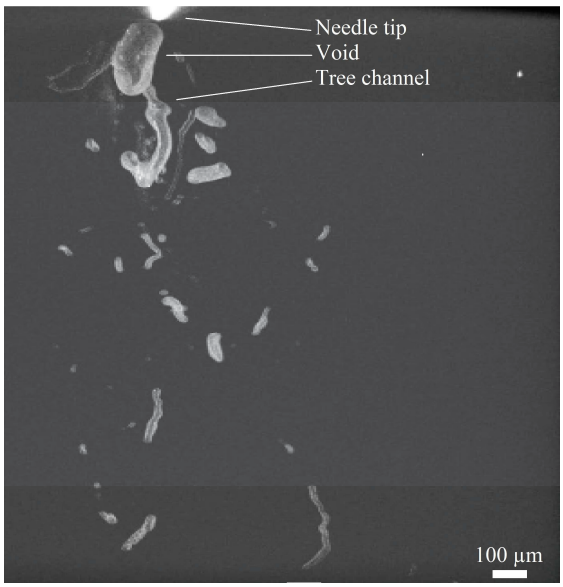

Figure 6-51: 3D rendered XCT image showing the gap between needle and plane of un-failed clean epoxy samples stressed for four hours.

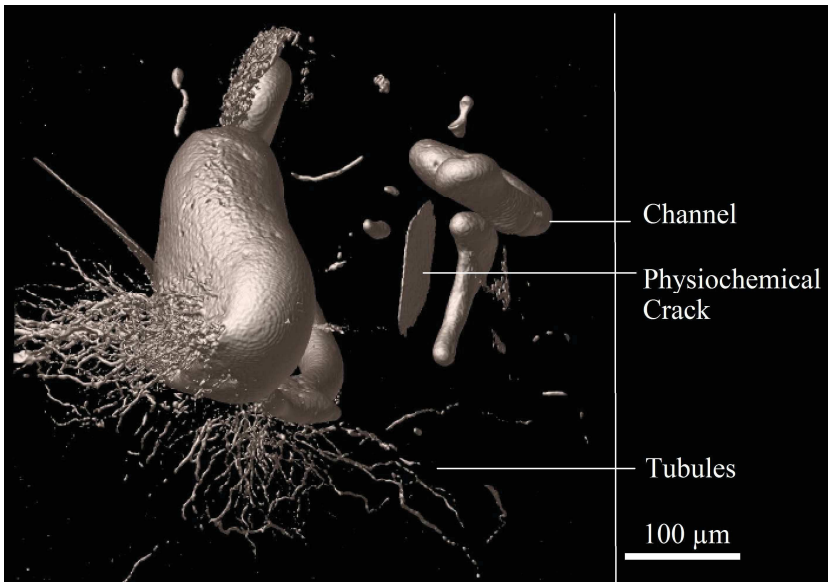

Figure 6-52: 3D rendered image close to the needle tip showing small tubules vs large channels as characteristic of bush-branch trees.

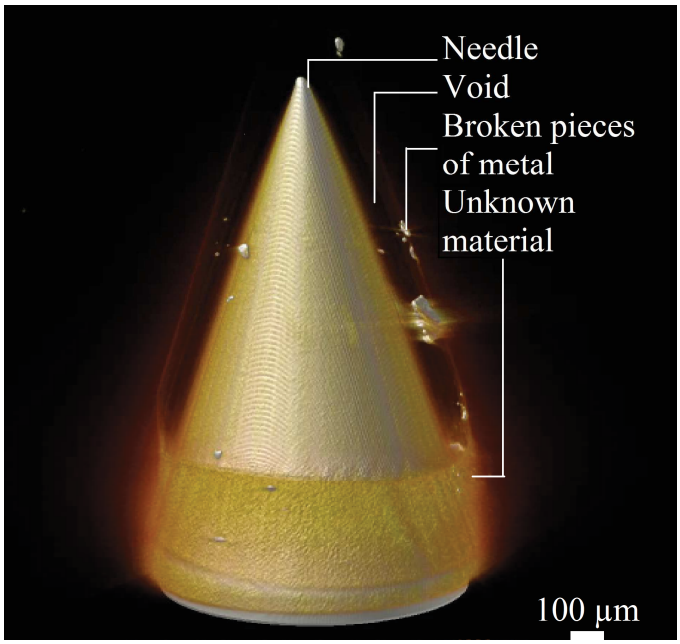

Figure 6-53: 0.33 vol% C/Epoxy after 194 hours showing a void which is different to what has been expected from PD analysis.

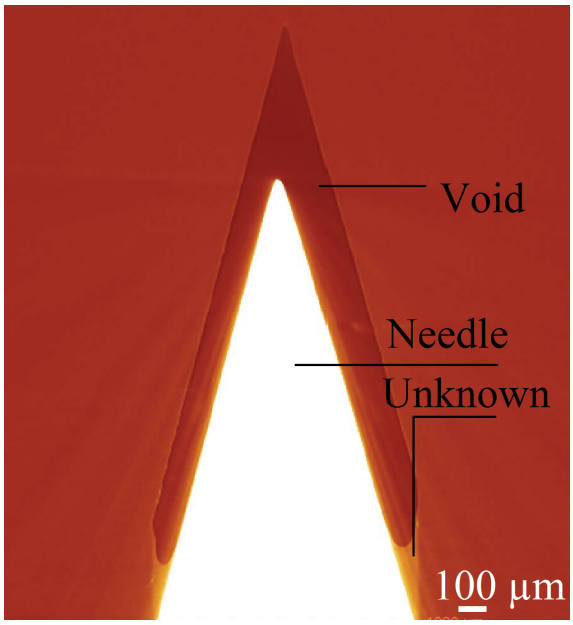

Figure 6-54: 2D side view of void around needle tip in 0.33 vol% C/Epoxy.

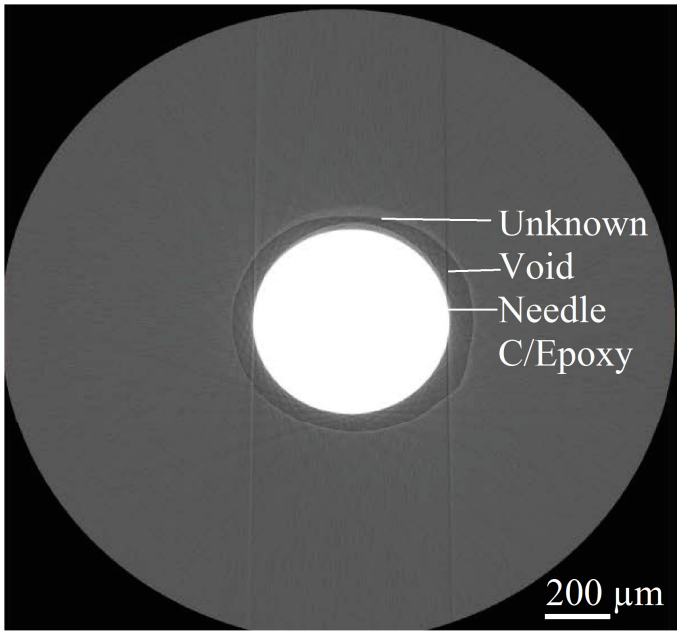

Figure 6-55: Top down view of void around needle tip in 0.33 vol% C/Epoxy.

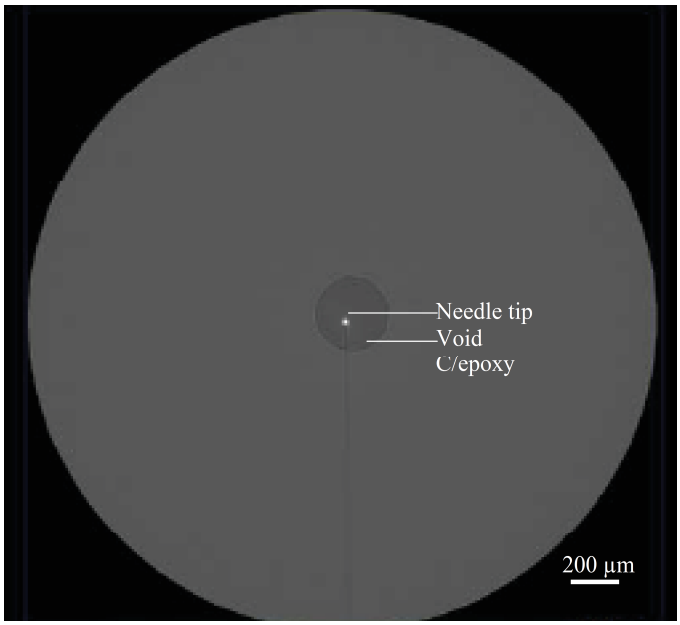

Figure 6-56: Top down view of the void at needle tip in 0.33 vol% in C/Epoxy.

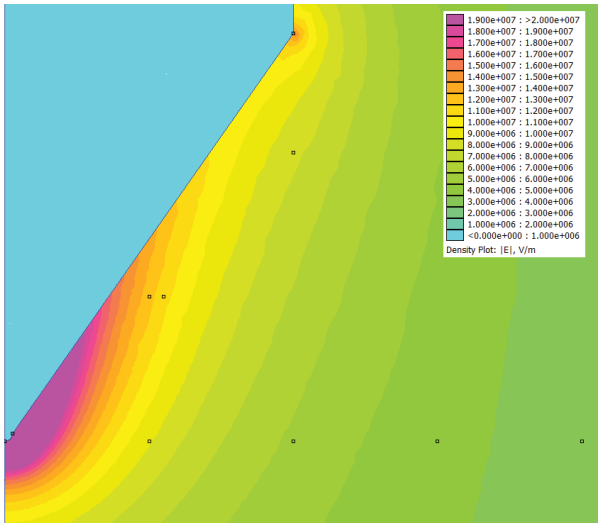

Figure 6-57: FEMM simulation of axis-symmetric results of the needle in pure epoxy.

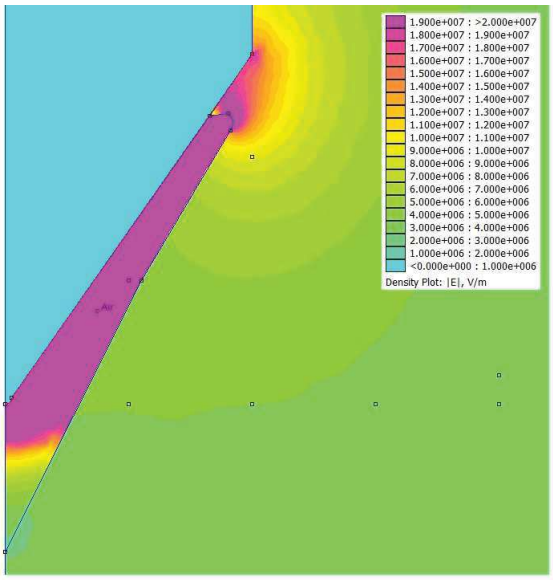

Figure 6-58: FEMM axis-symmetric simulation of reconstructed void showing electric field distribution.

6.5.2 Atomic Force Microscopy profiling of the electrical tree tunnels

The samples were cut in a manner as illustrated in Figure 6-59. Although in a failed sample there would be a full discharge path through the sample material, it was assumed that by cutting the samples by 2 mm from the bottom there would be evidence of electrical tree growth undisturbed by the discharge path.

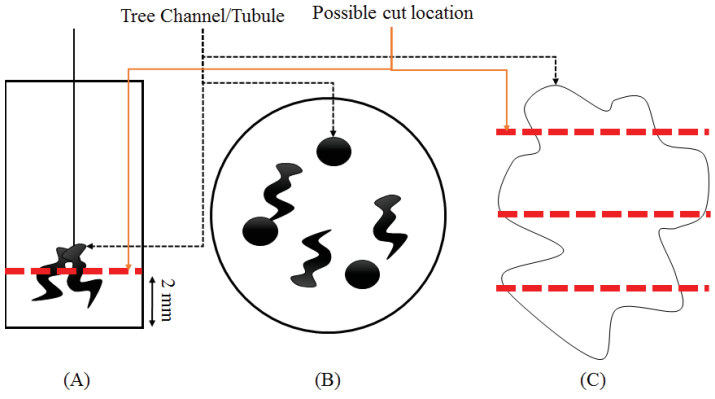

Figure 6-59: Sample preparation methodology to prepare samples after ageing, red/dashed line 2 mm from the base (a) expected sample surface from a bottom-up view (b), and side view of tree channel with possible slicing locations (c).

The hypothesis was that if electrical trees did indeed grow, the tree channels would be possibly vertical or horizontal with reference to the left image in Figure 6-59.

By looking at a bottom-up/top-down view of the sample surface, one would expect to see tree channels as possible circles (vertical trees coming out of the page) or valleys (horizontal trees) illustrated in the middle image of Figure 6-59. Furthermore, when viewing a tree using AFM, depending on the shape of a tree channel, the shaving of the sample surface may result in a tree channel being cut at different locations shown in Figure 6-59 (C). Note, the possibility of slicing a tree channel in many possible locations is a resolution constraint and a challenge when evaluating a tree channel.

After slicing, the samples were surface conditioned as done previously using five stages of sandpaper polishing, sequentially starting at 220 mm, 1200 µm, 9 µm, 3 µm, and ending with 1 µm. The last two stages also required 1 µm grinding paste. The samples were then washed with ethanol and distilled water. Figure 6-60 and Figure 6-61 shows images of the examples of the test specimens after polishing. The sections in the squares in Figure 6-61 show the samples areas which would be further analysed using AFM and shown in Figure 6-62. Figure 6-61 and Figure 6-62 also confirms what was to be expected by the middle image in Figure 6-59. After surface polishing, it is safe to assume that there should be tree tubules or channels visible, however, there is no way of knowing at what orientation a tree path may be in the epoxy, the direction, or the size. The samples were analysed using a Zeiss Veeco dimension 3000 AFM in tapping and Scanning Voltage (SVM) modes.

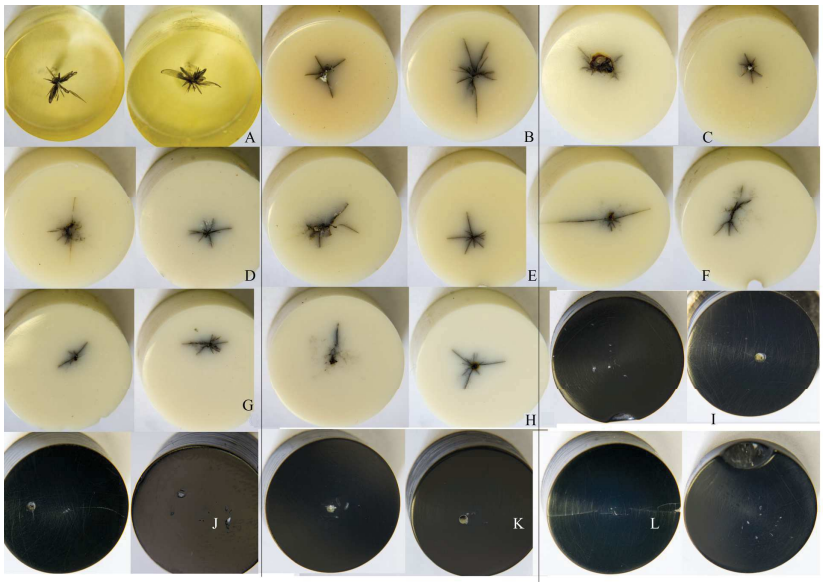

Figure 6-60: Micro-photography images of samples prepared for AFM analysis after electrical tree experiments showing discharge paths 0 % (A), BN/Epoxy samples (B) to (H) sequentially as 0.26 %, 0.55 %, 0.81 %, 1.09 %, 1.35 %, 1.65 %, 1.96 %, and 2.27%. The C/Epoxy samples (I) to (L) as 0.33 %, 0.84 %, 1.57 % and 2.78 %.[5]

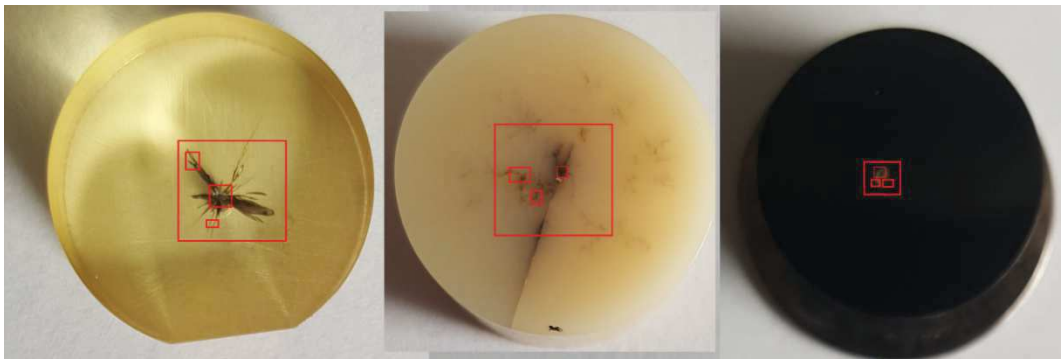

Figure 6-61: Polished sample surface of samples after polishing for AFM with Epoxy (left), 1.09 % BN/Epoxy (middle) and 0.33 % C/Epoxy (right).

[5] Acknowledgements are given to Dr Nyandoro for providing his micro-Nikon camera for taking the micro photography images.

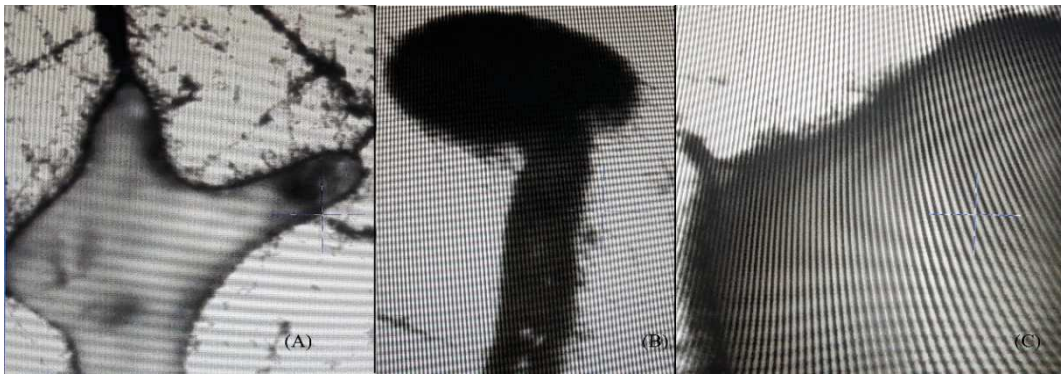

Figure 6-62: Light microscope details of one of the sites investigated on the sample surface of Clean Epoxy (A), BN/Epoxy (B) and C/Epoxy (C) with a 100 µm length scale showing possible areas just before the needle tip.

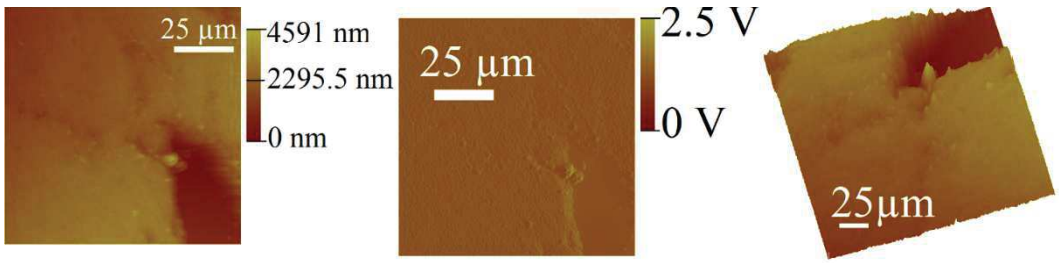

Figure 6-63: AFM results showing tapping mode results (left), SVM results (middle) and 3D rendered image of an electrical tree channel and tubules in pure epoxy (right).

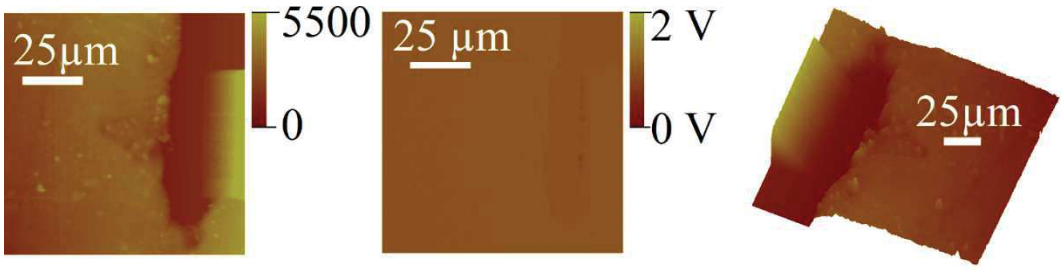

Figure 6-64: AFM results showing tapping mode results (left), SVM results (middle) and 3D rendered image of an electrical tree channel and tubules in BN/ epoxy (right).

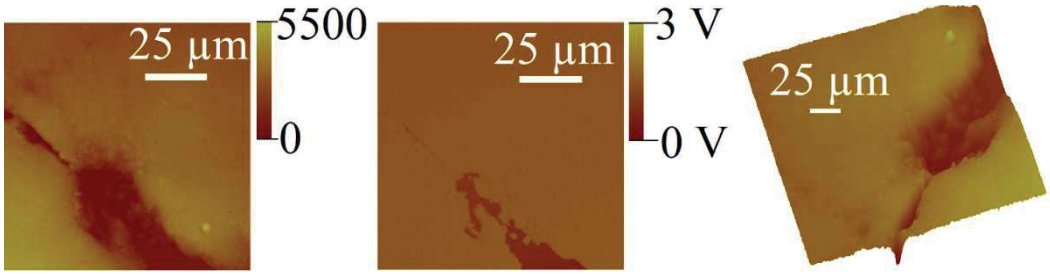

Figure 6-65: AFM results showing tapping mode results (left), SVM results (middle) and 3D rendered image of an electrical tree channel and tubules in C/Epoxy (right).

Figure 6-63, Figure 6-64, and Figure 6-65 give interesting details about the electrical tree channels grown in the different samples. A total of three sites were investigated around each sample surface giving a total of 9 investigated areas for epoxy, BN/Epoxy, and C/Epoxy.

The left image firstly gives the tapping mode results, the middle image gives the SVM results, and the right images gives a 3D rendered image of the height taking into account the tapping mode and SVM results. Once a tree channel was identified, it was tracked until the end and analysed.

From the SVM results, the first observation is that it is possible to partially indicate the presence of particles within the tree channels. Additionally, it is remarkable to note that electrically, the areas devoid of electric potential (i.e. tree channel) are slightly smaller than that of the tapping mode tree results, especially exaggerated in Figure 6-65.

While in tapping mode, the cantilever does not touch the sample surface, but it does when in SVM mode. From Figure 6-64, it is clear from left to right, the generated 3D image clearly shows the tree going around a fairly large interface, assumed to be a particle agglomerate. In Figure 6-65, the SVM results indicate that the particles have retained charge from the tree process. This is indicated by the heightened measured electric potential compared to the other samples. This is significant because it confirms the electron scavenging properties of the CNS particles.

From Figure 6-63Figure 6-64, and Figure 6-65 the tree channels go around the particles. These are exaggerated by the rugged channels shown in the nanodielectric channels from the 3D images compared to the smooth image of pure epoxy in Figure 6-63.

Given all the sites investigated, the dimensions of the tree channels were determined using pixel comparison on the images, and the results are summarised in Figure 6-66. The electrical tree channels appear to be wider in nanodielectrics ~20 µm when compared to pure epoxy ~6 µm. It is also interesting to note the tubule size in BN/Epoxy on average was smaller ~1.2 µm compared to 3 µm in both pure epoxy and C/Epoxy.

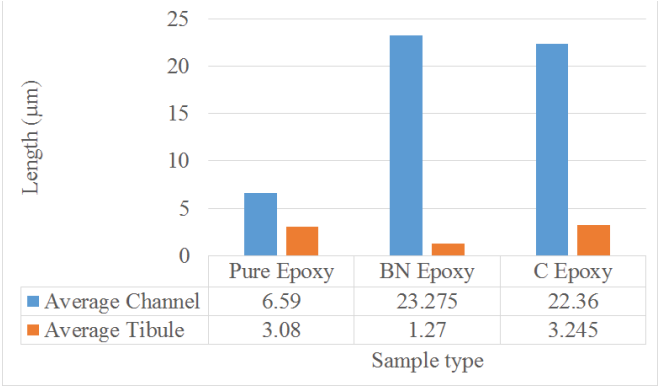

Figure 6-66: Channel and tubule average measurement results of epoxy samples after electrical tree ageing.

This indicates that the electrical trees must have gone over/around the particles present in the BN/Epoxy and C/Epoxy. The electrical tree channels are shown in Figure 6-63 and Figure 6-64 appear to be relatively smooth, while in Figure 6-65, the tree channel is relatively rugged.

However, from Figure 6-62 (b), it can be seen that there are some bumps present in the tree channel. Additionally, the 3D rendered images show that the electrical tree channels in the nanodielectrics are relatively rugged compared to the pure epoxy. From the AFM results, one can conclude that the electrical trees go around/over certain sites/particles. A paper on the AFM analysis of the electrical trees was published in the proceedings of SAUPEC 2017 and is given in Appendix E.

The key findings of the XCT and AFM results are summarised as follows:

1. In optimally loaded C/Epoxy, nano tunnels grow under the influence of the enhanced electric field potential around the needle tip. The summation of these channels appears as a void, and AFM results confirm that trees did indeed grow.
2. XCT confirms that the tree types grown in the epoxy samples were indeed bush-branch type trees as designed by the experiments.
3. The tree channels in optimally loaded nanodielectrics appear to be wider on average implying more energy is needed for a tree to grow through the nanodielectric than in pure epoxy.
4. Electrical trees go around/over certain sites/particles, which implies the electrical tree is a function of the mean free path which changes based on particle loading level.

The following section presents a discussion evaluating the results of the electrical trees in the nanodielectrics.

6.6 Further Discussions

The choice of CNS and BN was to achieve improved mechanical and thermal performance in the Epoxy nanodielectrics. Of the four electrical tree growth phenomena of heat, electrical, chemical and mechanical degradation mechanisms, the nanoparticles possibly remove the heat degradation mechanism. Each nanoparticle then has different methods of retarding the electrical trees which will be discussed independently.

6.6.1 Carbon nanosphere retardation mechanisms.

As mentioned, carbon nanoparticles have been referred to as electron scavengers [72]. It is currently speculated that at low concentrations of CNS, two mechanisms retard the electrical tree growth. The first mechanism is the **CNS particles remove electrons by absorbing them** from the discharge region causing the discharges to be suppressed in magnitude.

As the particle concentration increases, and either the inter-particle distance

decrease or the particles get into contact as evident from the DS results, the C/Epoxy nanodielectric change from being an insulator to a conductor under high voltage conditions.

The second mechanism of tree retardation may be due to a capacitive effect. Under the electric field conditions, electrons may be forced towards the CNS particles. Upon field reversal, the force of the electric field may not necessarily be able to remove the electrons. This causes a repulsive force to the electrons in the channels which result in the trees going around the particles. This is evident in the residual electric potential still on the surface from the SVM AFM results.

Locally around the needle tip, the material is in the dielectric breakdown region due to the high electric field, and hence the material breaks down. However, there is additional mechanical stiffness offered by the nanoparticles so this retards once the electric field at the surface of the material is below the dielectric breakdown strength.

The tree process still results in gaseous by-products developing in the tree channel, but due to the additional mechanical support offered by the nanoparticles in optimally loaded samples, the energy which would cause cracks may change to heat generation.

If the energy absorption phenomena of the C/Epoxy matrix at low concentrations could lead to reactions as seen in equation (2-3), intense heat and various radical gases may have been produced. This would result in chemical reactions as air/oxygen/ozone and/or nitric/nitrous acid reacting with tungsten above ~400 ^{o}C to form brittle tungsten oxide [102]–[104]. Such phenomena could be the origin of the micro-sized metallic pieces observed in the degraded region of the XCT C/Epoxy void.

The electric field simulation results indicate that if the growth of electrical trees was solely dependent on the electric field, then possibly a void as observed in C/Epoxy may energetically occur during the course of the electric field degradation. However, the AFM results present in Figure 6-62 indicate that although the discharge path in C/Epoxy was somewhat circular, there was some type of electrical

tree growth.

Therefore, it is currently speculated that initially, many small nanotubules form around the needle tip as a function of the electric field. These tree tubules are a function of the MV/mm around the needle tip and are pure electrical degradations. Although the material around the needle tip breaks down as a function of dielectric breakdown strength, electrons are being removed from the tubule channels as the region increases in size. Once a certain length is reached, at the surface of the region the electric field is no longer higher than the dielectric breakdown strength of the material, and the tubules no longer propagate. The inter-tubule walls collapse due to mechanical weakness and when observed using XCT, the region appears to be empty.

It should be pointed out that these findings are intriguing and call for further studies to fully understand the localised high electric field-induced degradation in C/Epoxy nanodielectrics. In addition, this study now opens the possibility of using other conductive nanoparticles for an investigation into the effects on electrical trees for nanodielectrics. The following sub-section discusses the possible reasons for electrical tree retardation in BN/Epoxy.

6.6.2 Hexagonal Boron Nitride retardation mechanisms.

Given that the BN particles are electrically inert, they do not offer the electron scavenging mechanisms, which indicates an alternative explanation compared to C/Epoxy. The BN/Epoxy has significantly higher mechanical stiffness compared to the C/Epoxy and pure epoxy established in the previous Chapter. Therefore, the path of least resistance for the electrical tree may only be possible through regions of pure epoxy or relatively weak material compared to both the interphase and nanoparticle. This increased strength causes the trees to take a tortuous route to ground, which is still evident by the various paths on the surface shown in Figure 6-61. A possible explanation of the path an electrical tree may take is shown in Figure 6-67.

At low filler concentrations (Figure 6-67 top left), the added electrical tree retardation is not achieved because there is more epoxy than interphase or

nanoparticle. At an optimal level (Figure 6-67 top right and bottom left), there is a long period of charge carrier build up before enough energy can be developed to penetrate the material. When progress is made these are seen as large PD bursts.

At higher concentrations (Figure 6-67 bottom right), the nanoparticles may orient to provide single channel paths to ground. Alternatively, if agglomerates formed the high concentration material performed as a microcomposite. Given equation (3 - 1) and (3-2) which describe nucleation, at higher concentrations, the particle agglomerates may not break apart or the probability of agglomerates forming has increased. Assuming a large number of agglomerations at higher concentrations, the critical radius of the particles would be larger and hence nucleation does not occur. Therefore, at a high particle loading level, the nanodielectric is binary with particle, epoxy and no interphase. The nanodielectric, therefore, breaks down faster because there are concentrated epoxy paths which can be followed as opposed to a strengthened interphase region which prevents tree movement.

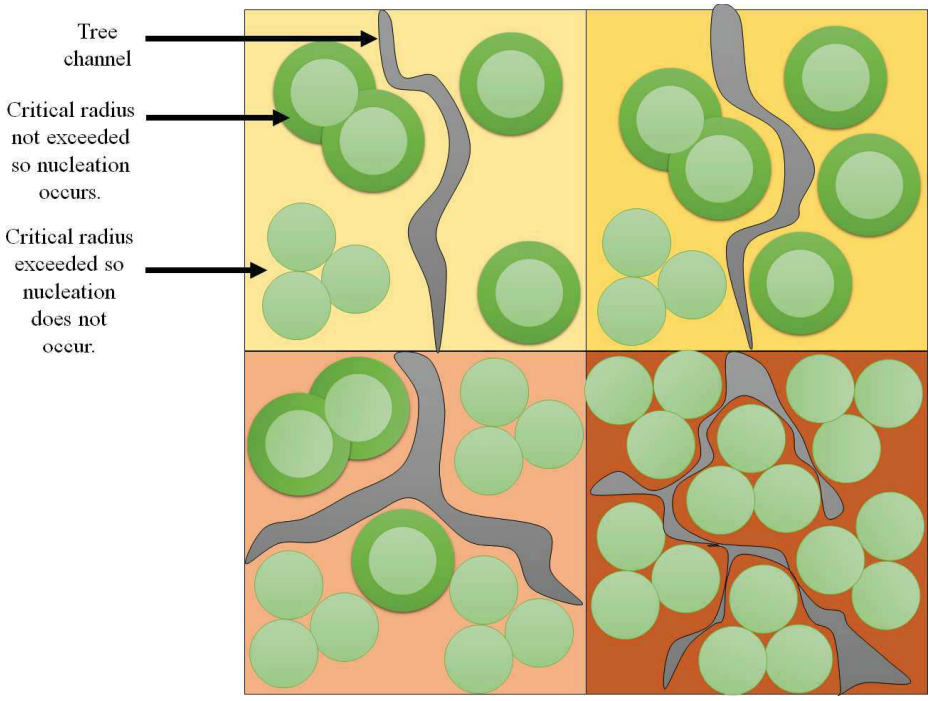

Figure 6-67: Illustration of a possible explanation of electrical tree breakdown within BN/Epoxy for increasing loading levels from left to right, top to bottom.

6.7 Conclusion

This chapter discussed the electrical characterisation of BN/Epoxy and C/Epoxy nanodielectrics using electrical trees. The conclusions of this chapter are summarised as follows:

1. There is a correlating increase in time to failure and tree discharge distribution with increasing nanoparticle concentration and there is an optimal point which confirms the rheology results.
2. For BN/Epoxy, the optimal filler loadings appear to be 1.09 % - 1.35 % where the verified samples of 1.25 % gave the best performance in terms of being able to withhold high PD magnitudes for a sustained period of time.
3. By evaluating all the PD data, it is clear there is a transition from bush/branch like characteristics to bush type characteristics as nanoparticle concentration increases. Additionally, there are favourable more concentrated PD magnitudes in the 1.09 % - 1.35 % for BN/Epoxy.
4. The electrical tree results confirm that the percolation threshold for C/Epoxy is 0.89 %.
5. For C/Epoxy, 0.33 vol% gave dramatically improved electrical tree retardation properties by suppressing the partial discharges for significant periods of time.
6. The statistical analysis of the mean, variance, skewness and kurtosis indicate that the in optimally loaded samples the nanodielectrics are positively skewed with small PD magnitudes being the favourable mechanisms for tree growth.
7. In optimally loaded C/Epoxy, nano tunnels grow in the region that takes the shape of the electric field potential around the needle tip. The summation of these channels appears as a void, but AFM results confirm that trees did indeed grow at some stage.
8. XCT confirms that the tree types grown in the epoxy samples were indeed bush-branch type trees as designed by the experiments.

9. The tree channels in optimally loaded nanodielectrics appear to be wider on average implying more energy is needed for a tree to grow through the nanodielectric than in pure epoxy.
10. There are two mechanisms speculated in optimal C/Epoxy which retard electrical trees apart from removing heat as a degradation mechanism. The electron scavenging and a possible capacitive effect which causes electrical trees to grow around the particles.
11. The mechanism which retards electrical trees in BN/Epoxy is speculated as added mechanical properties. At low concentrations, there is no dramatic added benefit and at high concentrations agglomerations may form causing single favourable paths to ground.

The following chapter discusses an analysis of the heat propagation mechanism in pure epoxy and the nanodielectrics. A background into thermal expansion and thermal conductivity is presented. This is followed by the experimental methodology, results, and discussion.

CHAPTER 7 THERMAL PROPERTIES

"It always seems impossible until it's done." – Nelson Rolihlahla Mandela.

7.1 Introduction

This chapter discusses the thermal characterisation using thermal expansion and thermal conductivity of the nanodielectrics and epoxy samples. The background introduces thermal conductivity and radiation. This is followed by the principle operation of dilatometers and laser flash analysis. The experimental results showing the thermal expansion and thermal conductivity properties of the C/Epoxy and BN/Epoxy nanodielectric are then presented and discussed.

7.2 Background

As stated previously, two of the insulation failure modes in hydro generators are attributed to poor heat transfer and electrical degradation [11], [12]. Inefficient heat transfer in certain areas of the machine results in hot spots which cause deformation of the insulation [11].

One possible result of insulation deformation is the production of gas cavities within the insulation and/or at the interface with metallic surfaces [12], [16]. These deformations coupled with high voltage cause electrical and mechanical stresses resulting in either gas discharges and/or electric field enhancement as explained in Chapter 2.

A good summary on understanding heat transfer properties is provided in [45]. There are two main forms of heat transport within solid materials, namely thermal conduction and thermal radiation. The law of thermal conduction is given by equation (7-1) and Stefan's law which describes thermal radiation is given by equation (7-2). In order to obtain thermal conductivity, the specific heat expressed in (7-3) is required. Specific heat (equation (7-3)) is a measure of how thermally resistive a material is to the addition of thermal energy [45].

$$P = kA\left|\frac{dT}{dx}\right| \tag{7-1}$$

Where:

- P is power (W)
- k is the thermal conductivity $(W/\,(mK))$
- dT is difference in temperature (^oC)
- dx is the difference in length (m).
- A is area in (m^2)

$$P = \alpha AeT^4 \tag{7-2}$$

Where:

- α is a constant equal to $5.6696\times10^{-8}(W/\,(m^2 \cdot K^4))$
- e is the emissivity or ability to absorb energy, and K is absolute temperature.

$$c = \frac{Q}{m\Delta \mathrm{T}} \tag{7-3}$$

Where:

- c is a materials specific heat $(J/(kg \cdot T))$
- Q and m are energy and mass in (J) and (kg) respectively.

Thermal conduction attempts to explain the transport of energy via heat. The two main mechanisms of thermal conduction are the atomic vibrations (non-metals and metals) or free electrons (metals). Thermal radiation or black body radiation describes the rate at which an object radiates energy.

Thermal radiation can also be used to understand how materials absorb energy through the phenomena of how all particles (nano and agglomerates) give off electromagnetic waves due to the individual atomic vibrations. In order to obtain insight into a materials thermal radiation properties, one may observe the thermal expansion, specific heat or thermal diffusivity.

Poor heat transfer may result in insulation deformation due to thermal runaway mechanisms. The poor heat transfer is a function of firstly a materials ability to

absorb the excess energy (insight into thermal radiation), and secondly the materials ability to dissipate or remove the excess energy (thermal conductivity). Materials with improved thermal conductivity and thermal expansion properties may mitigate the insulation problems found in the electrical industry.

As far as electrical properties are concerned, optimally loaded carbon nanosphere (CNS) epoxy (C/Epoxy) and hexagonal Boron Nitride (BN) epoxy (BN/Epoxy) were established based on the rheology and validated through microscopy and partial discharge characteristics provided in previous chapters. These were for BN/Epoxy, 1.09 vol% - 1.35 vol% and 0.33 vol% in C/Epoxy.

The samples were designed for improved electrical tree retardation performance and not improved thermal performance. The thermal properties of the samples also needed to be evaluated to check whether the obtained electrical properties were not at the expense of thermal properties or better still whether the thermal properties were also improved. The objective of using thermally conductive nanoparticles was chosen such that the bulk thermal properties would be increased as a consequence.

7.3 The Thermal Measurement Experimental Methodology

Two thermal experiments were carried out on 0.33 vol% C/Epoxy and 1.25 vol% BN/Epoxy, the first was thermal expansion, followed by thermal conductivity measurements. A complete account of the test specimen's fabrication process is provided in Chapter 4. Samples for thermal conductivity measurements were cut from a bulk material, shown in Figure 4-17. After slicing, as done with the dielectric spectroscopy and microscopy samples, the samples were surface conditioned (smoothed) using five stages of sandpaper polishing, sequentially the grain sizes started at 220 mm, 1200 µm, 9 µm, 3 µm, and ended with 1 µm. The last two stages also required 1 µm diamond grinding paste. The surface conditioning was to ensure no sample surface unevenness was present during the experiments. The final samples had a diameter of 20 mm and thickness of 2 mm.

Cylindrical rods with a diameter of 6 mm and length of 55 mm were prepared for the thermal expansion experiments. The principle operation of a dilatometer is

shown in Figure 7-1 and an Orton Dilatometer LAA/002 shown in Figure 7-2 was used to obtain the thermal expansion results. The sample is placed in a chamber surrounded by a furnace, the temperature of the furnace is increased at a rate of $1\,^{o}C/min$ from $0\,^{o}C$ until melting of the sample is detected. The first sample that was tested was the C/Epoxy samples until a temperature of 310 ^{o}C, at which point the sample began to melt and produce a significant amount of smoke. The pure epoxy and BN/Epoxy samples were then tested until a temperature of 250 ^{o}C to ensure that the samples would not melt during the thermal conductivity experiments.

The principle of operation of laser flash analysis (LFA) in accordance with ASTM E 1461 standard is shown in Figure 7-3 and a Flashline 3000 shown in Figure 7-4 was used to obtain the results. A PyroCeram sample is used as a standard reference to measure the thermal conductivity. The sample under test and the PyroCeram are placed in a chamber. First, a vacuum is pulled and then the chamber is filled with nitrogen gas. The chamber is then set at three predetermined temperatures, for this study the selected temperatures were cable joint operating temperatures of $100\,^{o}C$, $150\,^{o}C$ and $200\,^{o}C$.

A Xenon light source pulses three high intensity light flashes at the samples which is then measured by a detector kept in liquid nitrogen conditions. Within the chamber, below $400\,^{o}C$ the main heat transport mechanism is thermal conductivity or phonon scattering and above it the influence of thermal radiation needs to be considered.

As the selected temperatures were not above $400\,^{o}C$ the main thermal transport was assumed to be thermal conductivity. The thermal expansion and LFA analysis was done at the Council for Scientific and Industrial Research (CSIR) by Cermalab and results made available. The technique measures thermal diffusivity and then determines thermal conductivity and specific heat.

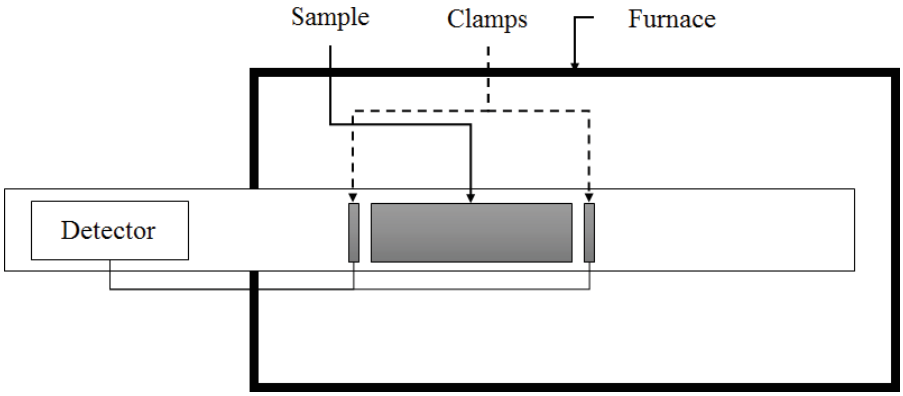

Figure 7-1: Principle operation of dilatometer, a sample is placed between two clamps in a furnace and as the sample expands, the displacements on the clamps are measured.

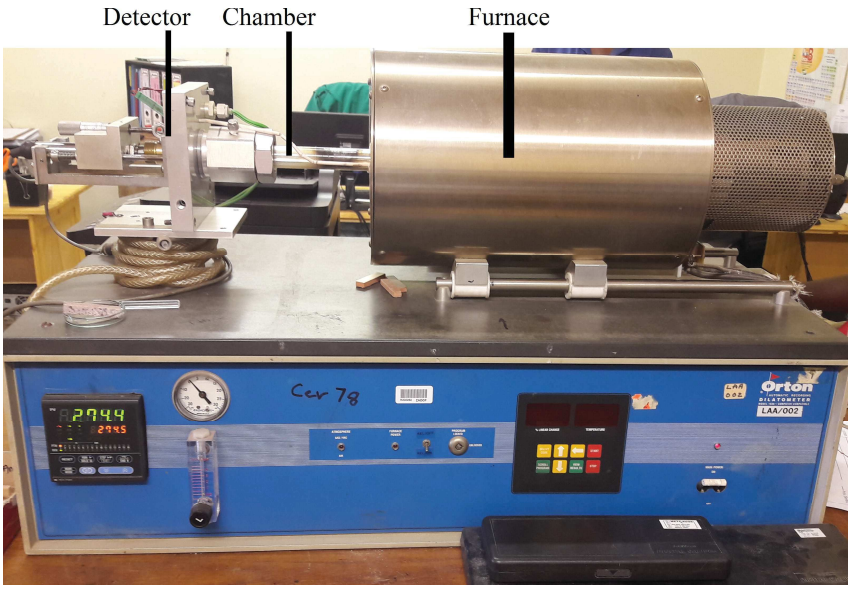

Figure 7-2: Image of Orton dilatometer used to obtain thermal expansion measurements.

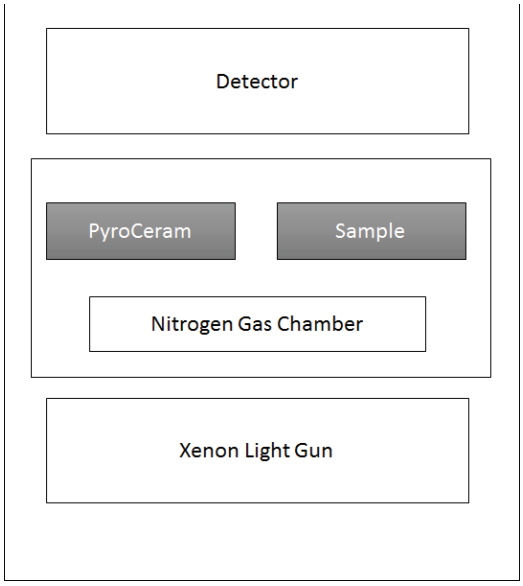

Figure 7-3: Laser flash analysis principle operation according to ASTM E 1461

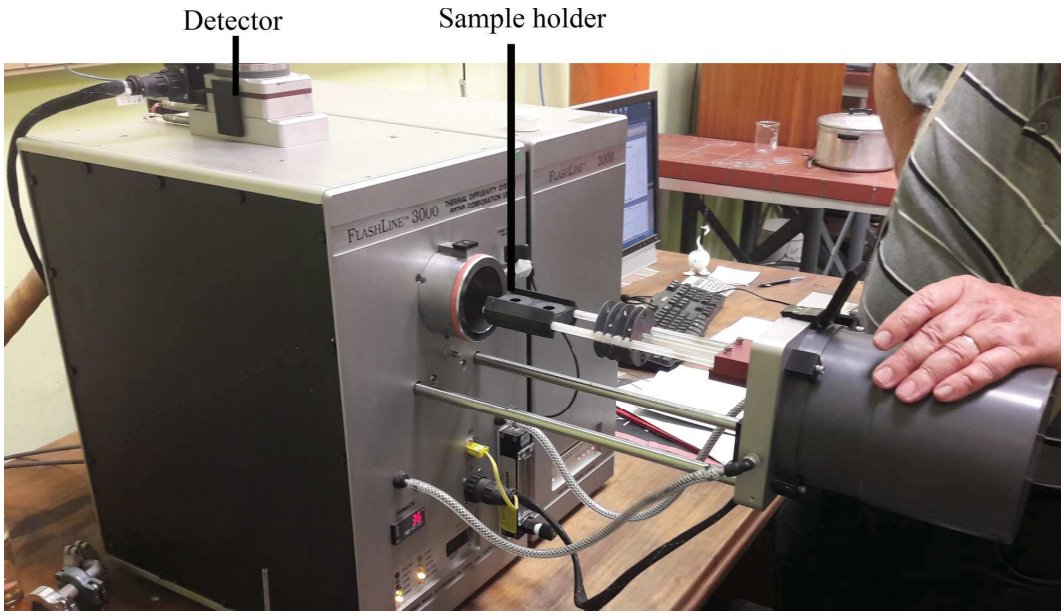

Figure 7-4: Image of Flashline 3000 used to obtain thermal conductivity measurements.

7.4 Thermal expansion and conductivity results and discussion

Figure 7-5 and Table 7-1 give the thermal expansion results for pure epoxy, BN/Epoxy, and C/Epoxy respectively. From Figure 7-5 and Table 7-1 the first observation is that all samples experience a thermal saturation point between $110\,^{o}C$ and $150\,^{o}C$. This saturation point is seen as a dip indicated in Figure 7-5.

This dip indicates a phase transition related to the glass transition temperature of the epoxy as stated in the material data sheet to be around $130\,^{o}C$ to $140\,^{o}C$ [39], [45]. The epoxy moves from a crystalline structure (hard glassy material) to an amorphous (rubbery) structure by transitioning the glass transition temperature. When the epoxy moves from crystalline to amorphous, the polymer chains (Figure 2-2) and grain boundaries (Figure 5-4) are broken and become disorderly [45]. Eventually the, epoxy begins burning and destruction of the sample is then observed at around $310\,^{o}C$.

The results (Figure 7-5 and Table 7-1) show that the rate of expansion for the optimally loaded C/Epoxy is higher than BN/Epoxy and pure epoxy for the entire temperature range. For C/Epoxy, the rate of thermal expansion is 146 %, 30 %, 8.2 %, 2.9 %, and 2.5 % higher than pure epoxy at 50 ^{o}C, 100 ^{o}C, 150 ^{o}C, 200 ^{o}C, and 250 ^{o}C respectively. For the BN/Epoxy, the rate of thermal expansion is 146 % and 13.3 % higher than pure epoxy at 50 ^{o}C and 100 ^{o}C respectively. The BN/Epoxy rate of thermal expansion is then 1.1 %, 0.7 %, and 0.9 % lower than pure epoxy for the remaining temperatures.

Beyond the glass transition temperature, the pure epoxy has a rate of thermal expansion faster than the BN/Epoxy. However, the nanodielectrics maintain similar slopes before and after the glass transition as the pure epoxy. But when comparing the rate of thermal expansion (dilation) properties for both of the nanodielectrics, they have increased when compared to pure epoxy up until $80\,^{o}C$.

Li *et. al.*[63] found that no evidence indicates a relationship between particle loading level and glass transition temperature but that nanocomposites, in general, have a glass transition lower than the pure polymer. They concluded that variations

in glass transition temperature were influenced by the interphase as they altered the mobility of the polymer chains. This would agree with the results shown with the dielectric spectroscopy results presented in Chapter 5.

Within the glass transition temperature range, the dip observed with the pure epoxy is not as pronounced in the nanodielectrics. This is possibly due to the nanoparticles which act as good thermal conductors. The heat transfer through the samples is relatively well maintained while the epoxy becomes amorphous.

The melting point for C/Epoxy is lower (310 ^{o}C) than the material data sheet of the pure epoxy (340 ^{o}C) [39]. This reduced melting point may be due to not using silica particles as conventionally used in the epoxy manufacturing process [39]. The thermal conductivity of the optimally loaded nanodielectrics and pure epoxy was therefore analysed from 25 ^{o}C to 250 ^{o}C.

The thermal expansion results indicate that both of these new materials are better at absorbing excess energy in certain temperature regions than the pure epoxy due to the addition of the nanoparticles, however, the C/Epoxy sample outperforms both samples. Figure 7-6, Figure 7-7 and Table 7-2 give the thermal conductivity and specific heat measurement results of the epoxy, BN/Epoxy, and C/Epoxy samples.

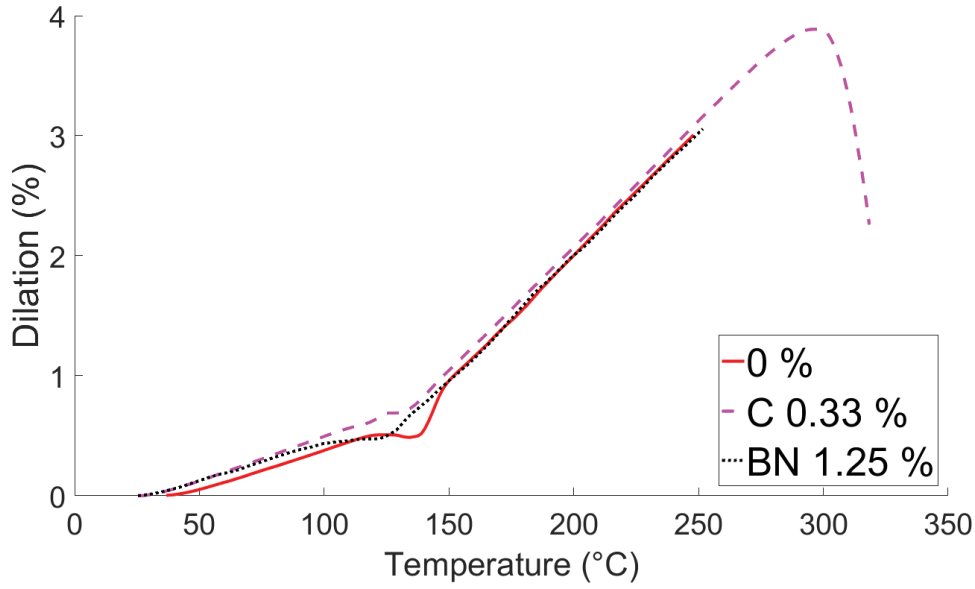

Figure 7-5: Thermal expansion results for epoxy, 0.33 vol% C/Epoxy and 1.09 vol% BN/Epoxy.

Table 7-1: Thermal expansion dilation results at select temperatures.

Temperature (°C)	Epoxy Dilation (%)	Expansion Coefficient ($x10^{-6}$)	BN/Epoxy Dilation (%)	Expansion Coefficient ($x10^{-6}$)	C/Epoxy Dilation (%)	Expansion Coefficient
50	0.05	48.3	0.124	53.1	0.123	57.7
100	0.384	59	0.435	57.9	0.499	67.0
150	0.970	-	0.959	-	1.05	-
200	2.033	209.6	2.018	206.6	2.092	202.4
250	3.00		2.973		3.077	

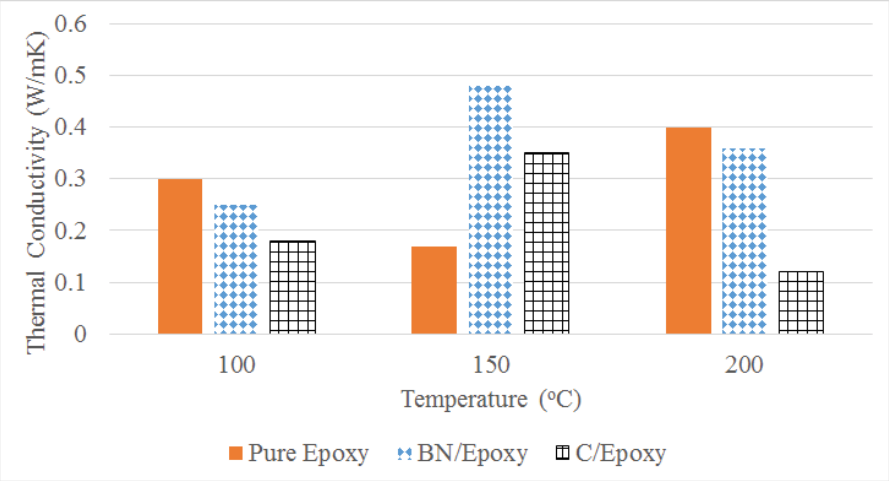

Figure 7-6: Thermal conductivity results of epoxy and the nanodielectrics.

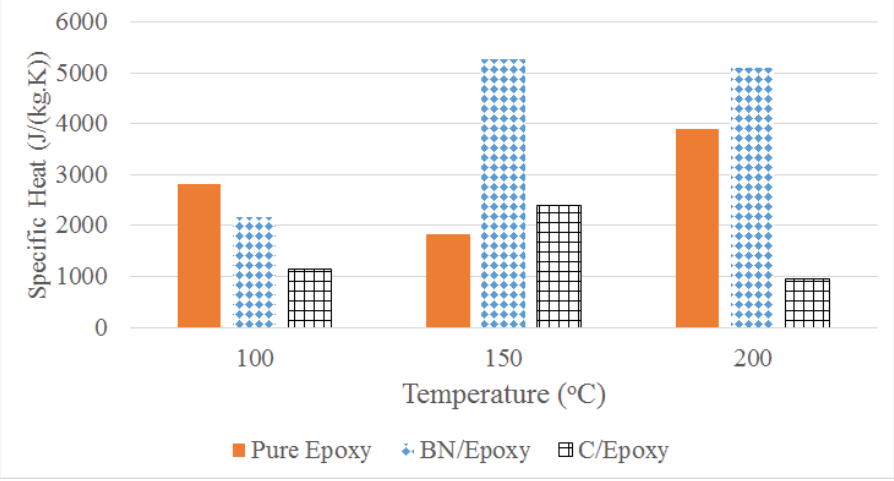

Figure 7-7: Specific heat results of epoxy and the nanodielectrics.

Table 7-2: Laser Flash Analysis measurement results for the epoxy and nanodielectric samples.

Thermal Conductivity (W/(m K))					
Temperature	Pure Epoxy	BN/Epoxy	BN Change relative to pure epoxy (%)	C/Epoxy	CNS Change relative to pure epoxy (%)
100	0.3	0.25	-16.7	0.18	-40
150	0.2	0.48	182	0.35	106
200	0.4	0.36	-10	0.12	-70
Specific Heat (J/(kg K))					
Temperature	Pure Epoxy	BN/ Epoxy	BN Change relative to pure epoxy (%)	C/Epoxy	CNS Change relative to pure epoxy (%)
100	2811	2164	-23	1141	-59
150	1823	5274	189	2389	31
200	3906	5101	31	949	-76
Thermal Diffusivity (cm^2/sec)					
Temperature	Pure Epoxy	BN/ Epoxy	BN Change relative to pure epoxy (%)	C/Epoxy	CNS Change relative to pure epoxy (%)
100	0.0009	0.0009		0.0013	
150	0.0008	0.0007		0.0012	
200	0.0009	0.0006		0.0011	

The temperature dependent thermal conductivities of the investigated materials are presented in Figure 7-6, Figure 7-7 and Table 7-2. At 100 ^{o}C, and 200 ^{o}C the thermal conductivities are lower than the pure epoxy.

For BN/Epoxy and C/Epoxy at 100 ^{o}C the thermal conductivity is lower than epoxy by 16.67 % and 40 % respectively. Similarly, the specific heat has decreased by 23 % and ~60 % for BN/Epoxy and C/Epoxy respectively. The decrease in specific heat indicates that the material should be able to transfer heat energy more easily as the thermal resistance has decreased.

At 150 ºC there is a glass transition from the crystalline epoxy to amorphous epoxy as seen in Figure 7-5. There is an increase in specific heat of ~190 % and ~30 % for BN/Epoxy and C/Epoxy respectively indicating that the thermal resistance has increased and thermal transfer should be more difficult. However, the thermal conductivity increases by ~180 % and ~105 % for BN/Epoxy and C/Epoxy respectively.

At 200 ºC the specific heat has increased for BN/Epoxy and decreased for C/Epoxy by 31 % and 76 % respectively. While the thermal conductivity has decreased by 10 % and 70 % for BN/Epoxy and decreased for C/Epoxy respectively.

These results indicate that the nanodielectrics are complex systems with conduction mechanism which are variable but most probably based on phonon scattering conduction mechanisms [45]. In developing the unified model, Tsekmas e*t. al.* [68] showed that by increasing the particle concentration the thermal conductivity increased from 0.11 W/mK to 0.26 W/mK and 0.36 W/mK for surface conditioned hexagonal and cubic BN (5 vol%) respectively in the same type of epoxy at 20 ºC. They showed that there was a correlation between increased particle concentrations and thermal conductivity.

In the current study, the thermal conductivity of the pure epoxy has a thermal conductivity of 0.3 W/(mK), 0.2 W/(mK) and 0.4 W/(mK) at 100 ºC, 150 ºC and 200 ºC respectively. In the crystalline region, the thermal conductivity is relatively constant. At the glass transition there is a decrease in thermal conductivity and in the amorphous region, the thermal conductivity is higher than the crystalline region. The amorphous region is higher than the crystalline region because there is more kinetic energy in the disordered polymer chains assisting in the thermal transport with increased molecular vibrations.

For the nanodielectrics, the thermal conductivities increase and peak at 150 ºC within the glass transition temperature region before dropping down again. For the C/Epoxy, the thermal conductivity drops below the level of the crystalline region. But for the BN/Epoxy, the both the specific heat and thermal conductivity in the amorphous region is higher than that of the crystalline region.

These effects may be attributed to the interphase which increases the mechanical stiffness of the epoxy observed in Chapter 5. For the nanodielectrics, when the temperature increases, the interphase may prevent large concentrations of amorphous regions forming. And around the glass transition, the material stays crystalline due to the increased stiffness. Possibly the polymer chains orientate such that good interfaces are formed between polymer and particles. As the temperature increases, eventually the material becomes amorphous and the increased thermal conductivities for the nanodielectrics are lost. This would possibly suggest an optimal operating temperature for increased thermal conductivity.

In the present study, 0.48 W/mK and 0.35 W/mK were achieved for non-surface conditioned particles in epoxy. These results also indicate that for example, operating a cable with cable joints or switch gear at 150 ºC as opposed to 100 ºC would yield better performance and good heat dissipation.

Essentially thermal conductivities of optimally filled C/Epoxy and BN/Epoxy investigated in this work varies with temperature. In some temperature ranges, both C/Epoxy and BN/Epoxy perform better than pure epoxy while the opposite applies to other temperature regions. The increase in thermal expansion and thermal conductivity properties still have significant implications for possible applications. If the rate of expansion of the insulation is close to that of metal, it may assist in preventing air gap formation when electrical equipment is in operation and not in operation.

While previously the use of nanoparticles has been restricted to metal oxides and boron nitride particles, now the addition of CNS nanoparticles which is electrically conductive allows for new insights into the effects of nanoparticles on the host insulation system. The possibility of using metallic particles which are significantly greater thermal conductors may provide new possibilities for improved thermal and electrical performance as far as electrical insulation is concerned.

7.5 Conclusion

This chapter discussed the thermal characterisation using thermal expansion and thermal conductivity on the nanodielectrics and epoxy samples. The background

introduced thermal conductivity and thermal radiation. This was followed by the principle operation of dilatometers and laser flash analysis.

The thermal expansion of the optimally loaded nanodielectrics and pure epoxy was analysed from 25 ^{o}C to 250 ^{o}C. The results showed that the rate of expansion for the optimally loaded C/Epoxy is higher than BN/Epoxy and pure epoxy for the entire temperature range. For C/Epoxy, the rate of thermal expansion is 146 %, 30 %, 8.2 %, 2.9 %, and 2.5 % higher than pure epoxy at 50 ^{o}C, 100 ^{o}C, 150 ^{o}C, 200 ^{o}C, and 250 ^{o}C respectively. For the BN/Epoxy, the rate of thermal expansion is 146 % and 13.3 % higher than pure epoxy at 50 ^{o}C and 100 ^{o}C respectively. The BN/Epoxy rate of thermal expansion is then lower with 1.13 %, 0.73 % and 0.9 % lower than pure epoxy for the remaining temperatures.

The Laser flash analysis of the samples indicated that at optimal performance is achieved at 150 ^{o}C as opposed to 100 ^{o}C and 200 ^{o}C. At this temperature, the thermal conductivity was increased by from 0.17 to 0.48 for BN/Epoxy and 0.35 for C/Epoxy indicating an increase of ~180 % and ~105 % respectively.

These results imply that while the electrical performance deemed optimal based on partial discharge characteristics was made possible, considering the types of nanoparticles used, as a consequence the thermal properties were also improved. Chapter 8 consolidates all the results presented and generates a model to explain the nanodielectric material given the new insights.

CHAPTER 8 : CONSOLIDATION OF RESULTS AND FUTURE WORK.

"So much has happened! And I'm sure it's only the beginning. Through the smiles, tears...through the anger, and the laughter that follows. I know that I will keep changing. This is my story. It will be a good one. It all began when I saw this sphere of you" – Yuna

8.1 Introduction

The use of nanoparticles whether for civil or mechanical properties has allowed for good advances in practical use for nanotechnology. Nanoparticles exist in a realm of science where atomic properties and bulk material properties converge and yet these are not well understood. Therefore, there is a requirement for a fundamental understanding of the nanoparticle effects on bulk materials. It is beyond the scope of this work to dwell on the fundamental mechanisms, however, some ideas will be postulated given the current knowledge.

This chapter consolidates the theory and experimental results presented in the previous chapters. Firstly, a discussion on the validity of the existing models is presented with particular emphasis on the body of work dedicated to surface conditioning. A model is then presented which attempts to describe the effects of nanoparticles on the electrical treeing mechanisms and observations from rheology.

8.2 Interphase models discussions and possible enlightenments based on the findings of the present research work

Several models were presented in Chapter 3 which are current attempts to explain the effects taking place in nanodielectrics. As there are six models, there is a challenge in understanding the interphase. The question of the validity of these models is then required based on the experimental results obtained. Apart from the intensity model and the interphase volume model, all other models assume the addition of surface conditioner.

The use of surface conditioner serves two purposes. The first purpose is to create a stronger electrical affinity at the particle surface between each individual particle when particles are in Brownian motion. This is achieved by using surface conditioners which reduce or increase the particle zeta potential. Each individual particle sees a like charge on the particle surface and provided particles do not collide will be repelled based on DLVO theory.

The second function of surface conditioner is to create better bonding between the particle and the host polymer. This assumes that the surface conditioner successfully bonded with the individual particles. If bonding was achieved, then the particles once placed in the chosen host polymer will successfully bond with the host polymer. There is no evidence to support that a particle with surface conditioner successfully bonds with the host polymer.

The first problem with using surface conditioner is a lack of understanding on the long term effects especially with nanodielectric manufacturing considered for high voltage insulation. On the one hand, if each individual particle is electrically higher (positive or negative) this would consequently have an influence on the particles influence on space charge retention for HVDC applications. On the other hand, this may not necessarily be a problem for HVAC applications.

The second problem is the assumption that nanoparticles are always in Brownian motion during the manufacturing process. As presented in Chapter 4, there are other states that are possible for nanoparticles in a medium other than Brownian motion. The consequence of other suspension states is other mechanisms need to be considered during the manufacturing of nanodielectrics. The only model which closely describes the effects observed using rheology is the interphase volume model, however, it is missing a few steps which will be discussed later.

By not using surface conditioner, the results presented in Chapter 5 show that the interphase, a region which has properties which are different to both the particle and host matrix, exists without the addition of surface conditioner. Therefore, the multi-core model, the polymer chain model, new barrier model and unified permittivity and thermal conductivity models, which have been developed in

different regions around the nanoparticle as representative of the interphase cannot be valid for situations that do not have surface conditioner. The interphase may change in the property by the use of surface conditioning, however, the interphase is present with or without surface conditioning and therefore the models will require reinvestigation for their robustness.

A possible answer is based on nucleation (introduced in Chapter 3) observed in the development of alloys and ceramics. Locally, each individual nanoparticle causes an increase in the concentration of atoms within polymer chains around the particles based on DLVO. The influence of the particle may cause agglomerations, but in the situations when agglomerations are not formed, nucleation may occur.

Nucleation around each individual particle would result in polymer nanocrystals forming which are mechanically stronger than virgin polymer. Figure 8-1 and Figure 8-2 describe the development of this model. The interphase measured around the BN particle when compared to the CNS particle resulting in a stronger interphase is possibly due to the heterogeneous nucleation vs homogeneous nucleation of the plate particle vs spherical particle. This would possibly explain the increased Young's modulus around each individual particle seen in Chapter 5.

From Chapter 6 it was discussed for electrical tree retardation, at low concentrations, there may not be enough areas of nucleation which impede the electrical tree process. Conversely, at high concentrations, the probability that agglomerates are present is higher. With the particle sizes greater than the critical radius at higher concentrations it is possible that nucleation does not occur. And hence the interphase does not form. The nanodielectric at higher particle loading levels is, therefore, binary and the only paths to ground are concentrated regions which cause a faster breakdown.

Some of the models attempt to compare experimental results with simulations. Simulation tools are beneficial when fundamental laws are in place and iterative solutions which converge on an answer are possible. The fault with using simulation systems is that the information is dependent on the individual constructing the simulation and initial assumptions. Additionally, when simulations do not agree

with experimental results, curve fitting attempts are used to justify the model which was done by Praeger *et. al.* [62]. They do, however, provide some new insights but their results should be critically evaluated.

Most work on nanodielectrics up until now has been based on mix and test iterations with very little justification to the manufacturing process required to reproduce nanodielectric materials or upscale to industrial applications. Some particle types have been based on conventional knowledge of bulk material properties but the results presented on Carbon nanospheres show that even conductive particles can be considered for nanodielectric manufacturing. Therefore, conventional knowledge based on particle types can be disregarded when pursuing further research. Additionally, this opens a range of opportunities for different particle investigations in polymers which will be discussed later.

Figure 8-1 gives a proposed insight into the placement of particles during nanodielectric manufacturing aka force model, four grids showing possible scenarios, the first grid (top left) showing homogeneous distribution of particles, the second grid (top left), showing a large agglomerate which may influence individual particles, the third grid (bottom left) showing large amounts of particles which may have individual influence on their neighbours and finally the last grid (bottom right) showing larger particles distributed.

Figure 8-2 gives the force model illustrated in greater detail indicating the possible stages different concentrations of nanoparticles may have in the matrix during nanodielectric synthesis. Figure 8-2 (A) indicates randomly distributed and disperse particles which are subject to several forces including stokes law (F_s), DLVO forces (F_{DLVO}), and a movement force of particles (F_m). Figure 8-2 (B) shows a slight increase in concentration highlighting how additional particles can influence the particles. Figure 8-2 (C) shows a free body diagram of some of the forces an individual particle may be subject to. Figure 8-2 (D) and (E) indicates how possibly optimally distributed particles may influence other particles. Figure 8-2(F) shows how an increase in concentration leads to a forced collapse where discrete

agglomerates may form. Figure 8-2 (G) and (H) give further stages of concentration increases to emphasise the last stages of nanoparticle concentrations.

For modelling concerns, Figure 8-1 and Figure 8-2 presents a proposed add-on with regards to a missing step in the interphase volume model. It is a suggested working solution based on the results investigated and will require further work for solidification. The information missing is based on Stokes law well established in colloidal chemistry. For a good understanding of Stokes, law readers are referred to [45], [76], [77]. Stokes law describes the force on a particle shown by equation (8-1) during Brownian motion, the settling velocity of a particle in dilute suspensions (8-2) and concentrated suspensions (not in Brownian motion) (8-3).

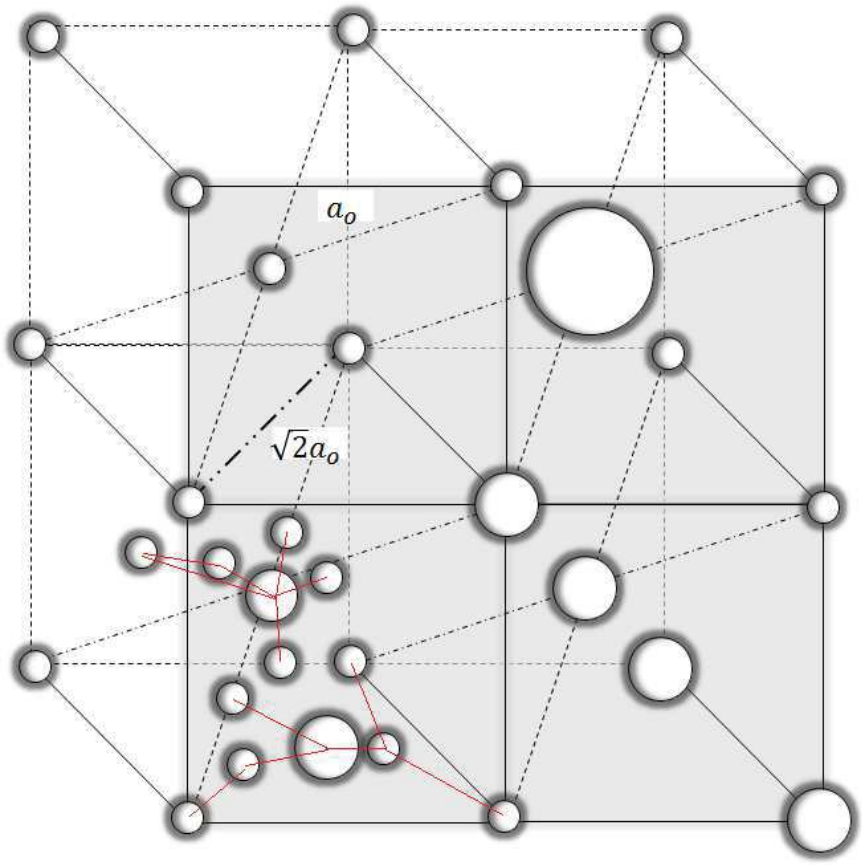

Figure 8-1: An adaption to the interphase volume model, agglomerates form before particles are in continuous contact.

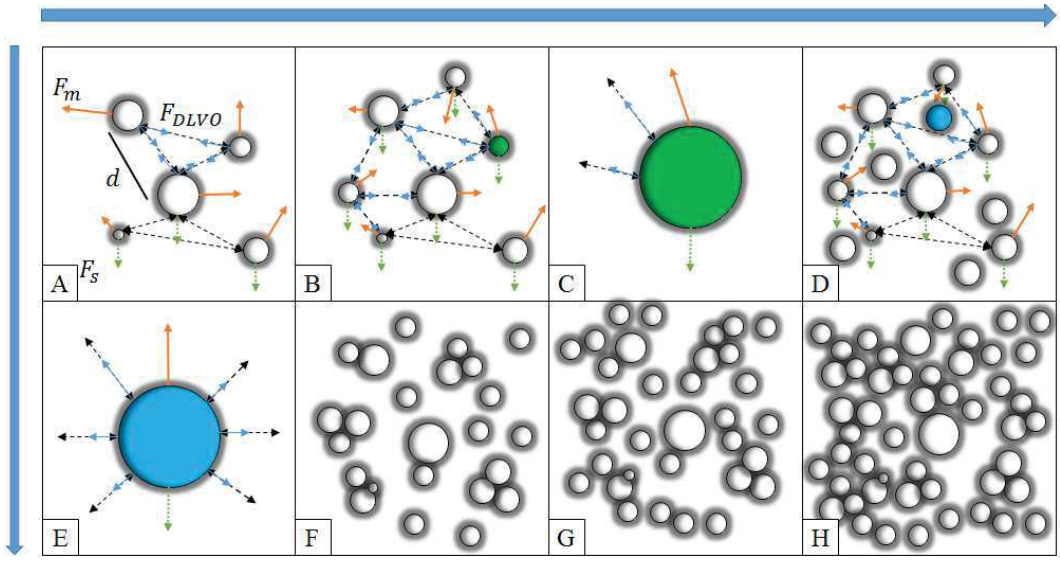

Figure 8-2: An illustration of the different forces on an individual particle as particles concentration increases. Note the forces are labelled as F_m, F_{DLVO}, F_s for movement, DLVO and stokes respectively.

$$F = \frac{r^4 \Delta \rho g}{k_B T} \tag{8-1}$$

Where:

- F is the force on a particle (N), ρ is the particle density (g/cm^3).
- g is the gravitational constant and k_B is the Boltzmann constant.

$$V = \frac{2\Delta \rho g a^2}{9\eta} \tag{8-2}$$

$$V = \frac{2\Delta \rho g r^2}{9\eta}(1-\phi)^{5\pm 0.25} \tag{8-3}$$

Where:

- V is the particle settling velocity (m/s).
- η is the medium/fluid viscosity (Pa.s).
- ϕ is the particle volume fraction (vol%).

The interphase volume model for its assumptions was valid in describing the mathematics of a system which has uniform particle sizes and homogeneously

dispersed and distributed particles. However, it may practically be impossible to achieve absolutely perfect constant particle sizes. Additionally, given the violent mechanism used in most nanodielectric manufacturing processes, the particles will most probably be randomly distributed and not homogenously distributed as described by Fothergill [33], [40].

During the manufacturing, specifically, the particles and polymers investigated in this work, the particles initially start as clumped up in the order of ~1 µm and break up into smaller particles during the high shear mixing. The high shear mixing causes particles to collide in vicious fashion and introduces nano and micro air bubbles. During the vacuum procedure, an attempt to remove air bubbles is made. The final particle placement is based on the host medium, particle shape, the particle interaction with individual particles, particle concentration, and bubbles.

After most of the bubbles have been removed, the remaining particle placement may be both dependent on Stokes law and the interphase volume model mathematics. However, the interphase volume model does not take into account particles being in proximity and particles collapsing to form an agglomerate without influencing other particles as illustrated in the first and second sections of Figure 8-1.

The rheology results presented in Chapter 4 indicate that before particles reach a stage of contact, the particles collapse into agglomerates and become well distributed before being in complete contact. This was further established and validated by the conductivity measurements of the C/Epoxy in Chapter 5 and illustrated in Figure 8-1. The new insight into the interphase being at least two times the size of the particle may shed light on the influence of the distance required for a particle to be attracted to another particle. These may possibly allude to the final modelling required for understanding the nanodielectric mechanism.

8.3 The effect of nanoparticles on electrical treeing

Electrical treeing in virgin polymers is a function of heat, electrical, chemical and mechanical degradation mechanisms. This work did not attempt to stop the event,

but understand the effect and retard the process with the addition of nanoparticles into an epoxy matrix. Two types of particles which were thermally conductive were tested. The BN particles were plate-shaped and electrically insulating. The CNS particles were electrically conductive and spherically shaped. Depending on the particle concentration, the electrical treeing process could be retarded.

The BN particles, which could be oriented in any random assortment and distributed randomly, at optimal concentrations provided larger mechanical support to the epoxy matrix compared to the pure epoxy, however, this could not prevent failure of the insulation below 100 hours under 1 MV/mm electrical degradation. Additionally, the thermal expansion results indicate that beyond certain temperatures, the BN/Epoxy performed equally to pure epoxy which would indicate that the heat degradation mechanism was not changed.

The CNS particles, which could only be distributed randomly, at optimal concentrations did not improve the mechanical properties as significantly as the BN particles but resulted in significantly longer electrical tree degradation than both the BN and pure epoxy samples. Therefore, given the nature of the particle type being an electron scavenger, the driving mechanism for continued electrical tree growth was inhibited by use of conductive particles as electrons were removed from the electrical tree channels.

Additionally, the Atomic Force Microscopy (AFM) analysis showed that the electrical tree would have a tendency to go around the nanoparticle, therefore a model of the proposed electrical tree channel paths based on particle concentration is given in Figure 8-3. At extremely low concentrations of nanoparticles, the particles would be in Brownian motion and may orient randomly, they do not have a significant influence on the host matrix. Therefore, electrical tree channels do not have a real impediment to their growth.

As the particle concentration increases, an optimal region is reached, in this optimal region, the apparent tree channel path to ground is longest. This is possibly due to increasing possible paths of equal lengths to ground, or electrons being removed from the system. As the particle concentration increases, a possible saturation point

of nanoparticles is reached, this may result in an easy simple concentrated path for the tree channel, or the particles provide an easier electrical tree channel path to ground.

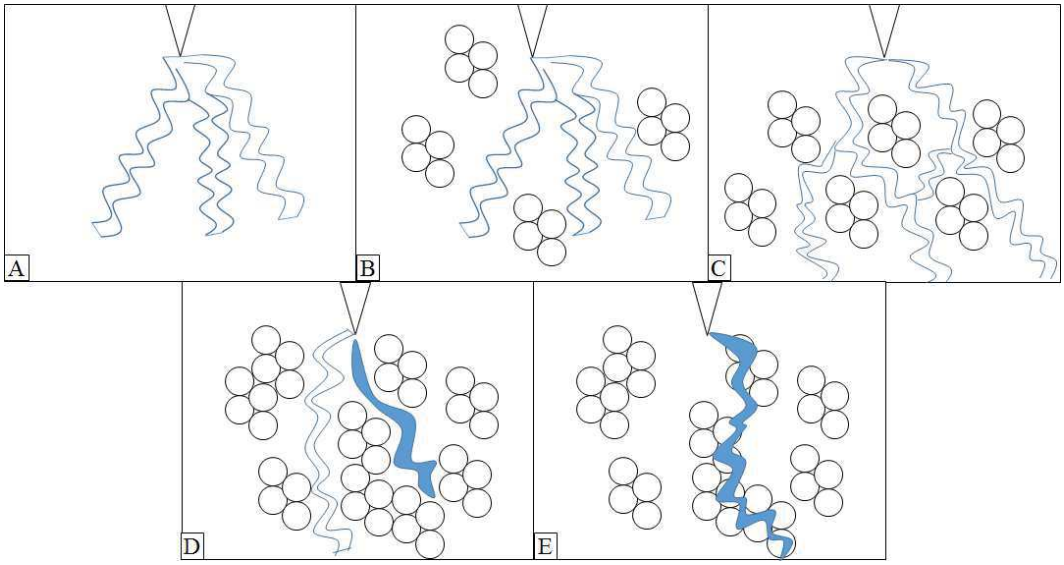

Figure 8-3: Proposed tree channel path model with pure polymer showing various channels paths for varying particle concentrations.

8.4 Impact of this research

The impact of this research is that the nanodielectric manufacturing can be incredibly complicated, or could be as easy as making a cup of coffee. Similar to adding sugar to coffee to improve the "sweetness," of the coffee, too little sugar has no impact on the taste. Too much sugar results in too much "sweetness," and the right amount of sugar allows for it to be just right. This has been well illustrated in the story of Goldilocks [105]. The key contributions can be summarised as follows:

1. Establishing that optimal filler loading level can be determined and reproduced by modifying the nanodielectric fabrication process to include rheological analysis.

2. Discovering that carbon nanospheres can be used to significantly improve electrical and thermal properties of epoxy but only if optimally filled.

3. Successfully characterising electrical tree partial discharges in the

nanodielectrics using PD analysis.

4. Showing a correlation between rheology, microscopy, dielectric spectroscopy and partial discharge analysis in electrical trees.
5. Successfully characterising electrical tree micro tunnel profiles in nanodielectrics using AFM and showing trees grow around nanoparticles.
6. Characterising the mechanical, dimensions and electrical properties of interphase regions in nanodielectrics using AFM techniques.
7. Establishing that you don't necessarily need to achieve both good particle uniform distribution and dispersion to obtain a good nanodielectric (Figure 1-3 D).
8. Establishing that an optimally loaded nanodielectric has an optimal thermal conductivity at a specific temperature which would allow for good performance in the electrical power industry.

Once an optimal amount or "Goldilocks," amount of nanoparticle is added, there is a significantly better performance with regard to electrical tree resistance and thermal conductivity. This is not necessarily the optimal performance with regard to other electrical properties such as dielectric breakdown or space charge. However, due to the analysis of two particle types, it does provide a key to look and find the optimal point within a polymer for a particular type of nanoparticle concentration using rheology. It is now possible to develop a recipe which will allow for the nanodielectric to move from the lab to manufacturing which is discussed in the next sub-section.

8.4.1 The nanodielectric recipe using direct dispersion

The following recipe is proposed by the author in order to push nanodielectrics from the lab to full-scale manufacturing. The steps are presented as follows and are illustrated in Figure 8-4:

1. Select insulation material.
2. Select particles for intended improvement.

3. Determine critical mixing time, and critical mixing speed which may be established with rheology (minimum viscosity), the polymer and a high concentration of particles.
4. Determine optimal loading level by identifying different regions of particle filler loading level and find minimum viscosity within hydrodynamic/colloidal interaction region.
5. Proceed with manufacturing material.
6. Perform necessary tests to characterise and refine nanodielectric material.

Given the results presented in this work, the use of CNS nanoparticles as a conductor is counter-intuitive to conventional wisdom. It is, therefore, possible to investigate any nanoparticle type for their use in nanodielectric performance. Possibly new forms of carbon, metallic particles, other forms of boron nitride. The following section discusses the recommendations for future work.

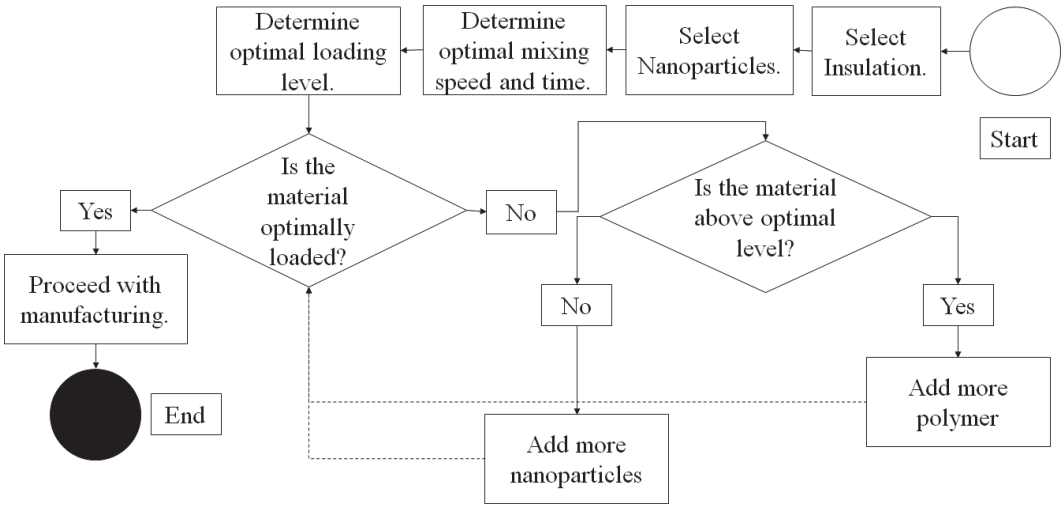

Figure 8-4: Flow diagram showing the nanodielectric recipe using direct dispersion.

8.5 Recommendations for future work

There are a number of possibilities with regard to validation of this work and sights on future applications for nanodielectrics from particle type to nanodielectric synthesis. The following subsections will discuss some challenges not addressed in this work and possible solutions.

8.5.1 Dispersion, Distribution and agglomeration necessities

Even though optimal distribution has allowed for improved electrical performance with regard to BN and CNS particles in epoxy, one may still wish to obtain optimal distribution and distribution Figure 1-4 (D). One way to achieve this is through the use of gold nanoparticles which may be purchased through MINTEK in South Africa.

There are two reasons for gold nanoparticles. The first reason is they will be easily discernible in SEM with a polymer, for example, the epoxy used in this work. Secondly, they provide an opportunity for investigating metallic nanoparticles for nanodielectric applications. Thirdly they are spherical which would allow for easy use within simulations.

The gold nanoparticles from MINTEK will be supplied as particles suspended in distilled water. Two, maybe more objectives can be achieved with the particles. The water can be dried causing the particles to agglomerate which will effectively test distribution properties. Secondly, the particles can be left in the water to investigate dispersion properties.

The first challenge with the dispersion property method will be mixing the water, particles and host polymer and successfully removing the water from the polymer. There will be a need to find the optimal amount for both situations, but it would certainly allow for the ability to determine if indeed perfect dispersion and distribution are necessary for nanodielectric applications.

Alternatively, although surface modification is not a good idea for long term applications because the zeta potential on each individual particle has an electrical charge, it may be possible to control the movement of a particle in a medium using high-frequency electric fields.

With regard to agglomerate formation within nanodielectrics, if agglomerations are indeed a problem and an irreversible process, a possible solution to get around agglomerates would be the use of a centrifuge. By utilising a centrifuge, effectively the agglomerates would go to the bottom of a test beaker, which may be an

additional expense when considering manufacturing applications. This, however, would remove any agglomerates early such that they are not present in the final nanodielectric.

8.5.2 New particle types

Given that CNS particles can be used, it may be interesting to use various CNS constituents such as hollow CNS particles, CNS particles doped with individual atoms such as gold, boron, nitrogen, etc. Specifically, with regard to the hollow carbon spheres, one may choose to grow the spheres which may contain a gas, such as (SF_6). The objective being that should an electrical tree channel encounter a particle, the gas would be released into the channel and electrons would be removed from the tree process. This does how ever run the risk of allowing for different acid formations but would be interesting. One way to achieve this is by doing the entire manufacturing process within an SF_6 environment.

Another application would be the use of quantum dots (various material types but specifically carbon) or hollow carbon nanospheres in Ester oils for use in transformers. Ester oils as established in Chapter 2 do not have a good voltage threshold between partial discharge and streamer breakdown. It may be desired to increase this voltage threshold with the use of quantum dots or hollow carbon nanospheres. The quantum dot particles would need to have a density very similar to the Ester oil. Alternatively, using bubble physics (the primary Bjerknes force) and hollow carbon nanospheres, given the transformer has high electric fields with a typical power frequency, it may be possible to establish each particle in a node or anti-node of the frequencies. This may be a challenge when dealing with transients. But the particles at the very least may offer increased partial discharge and breakdown resistance. The following section provides suggestions for continued work.

8.5.3 Continued work

As it has been established that optimal amounts exist for different particle types, further work can be done on establishing optimal amounts for surface conditioner on particles, and optimal amounts of surface conditioned particles in epoxy. Other properties like dielectric breakdown, space charge, and accelerated ageing may be

used obtain a complete analysis on a final characterisation on the CNS nanodielectric and BN nanodielectric. Additionally, combining the two particle types may allude to better results than what has been achieved in this work.

As South Africa is a water scarce country, once offshore renewable energy solutions are established; It may be of interest to develop cables with high thermal conductivity and ability to withstand sea conditions.

8.6 Conclusion

This chapter provided a discussion on some of the considerations with regard to the nanodielectric manufacturing. Stokes law was introduced and additional considerations to the interphase volume model were presented. A discussion on the effects of the different particles on the ability to retard electrical tree growth was presented and a model was proposed on the electrical tree path followed during nanodielectric manufacturing. The impact of the research was presented and possible recommendations for future work. The following chapter provides conclusions of all the chapters.

CHAPTER 9 CONCLUSION

"Nothing is Predestined. The Obstacles of your past can become the Gateways that lead to new beginnings." - Ralph Blum.

In Chapter 1 it was established that two of the main contributors to high voltage insulation failure were attributed to thermal and electrical stress. This failure could possibly be avoided by improving the insulation through the addition of nanoparticles during the manufacturing process. However, due to strong intermolecular forces on the nanometre scale, the particles clump together or agglomerate and become defects. Non-intrusive methods of observing dispersion/distribution of particles were required to evaluate the quality of the nanodielectrics during manufacturing. Although rheology had been used extensively for polymer research and nanocomposites, there was little research in the development of nanodielectrics. Secondly, in search of thermally conductive insulation, the focus has been based on the use of ceramic/electrically inert particles other than electrically conductive particles such as carbon variants.

A key objective of this work was developing and understanding a manufacturing process which would establish the considerations needed for reproducible results. It was established that rheology could be used to analyse a nanodielectric during the manufacturing process and be validated using conventional microscopy techniques seen by the results in Chapter 4. However, the only insight rheology provides is an insight into particle distribution and not particle dispersion of un-conditioned Boron Nitride (BN) and Carbon Nanosphere (CNS) particles in an epoxy matrix.

In addition to particle distribution, this work has shown that rheology could also be used to identify the seven stages of suspension (particles in a liquid) systems and compared for the different particle types. A reproducible nanodielectric manufacturing process was established using rheology and direct dispersion of nanoparticles in an epoxy matrix. More importantly, rheology could be used to establish an optimal filler loading point. This optimal point is a minimum in the viscosity which is sensitive to particle concentration. This optimal point is

dependent on particle type and is a minimum that exists in the colloidal/hydrodynamic region.

The limitations of Scanning Electron Microscopy (SEM) based on Energy dispersive spectroscopy (EDS) were encountered. The results showed that particle types considered with atomic numbers close to the host matrix cannot be used to validate particle dispersion/distribution. Atomic force microscopy (AFM) could be used to see CNS particles in the C/Epoxy.

In addition to establishing particle distribution, the interphase was measured and new insights into the interphase could be established for two different particle types. The bulk material of the final nanodielectric was shown to approach that of the interphase for optimally filled nanodielectrics.

Dielectric spectroscopy and electrical tree analysis showed that the addition of thermally conductive nanoparticles, irrespective of particle type, or electrical conductivity of the bulk material of the nanoparticle, could retard electrical tree growth. Apart from increasing the electrical resistance and permittivity at optimal loading levels, it is suggested that the particles interrupt the mean free path of an electrical tree by changing the mechanical properties and tree progression mechanisms.

The thermal expansion results show that the nanodielectrics developed have a faster rate of expansion than pure epoxy until 100 ^{o}C. After100 ^{o}C, the BN/Epoxy has a rate of expansion slower than the pure epoxy. By using laser flash analysis, the optimal temperature to operate the nanodielectrics was established as 150°C. At this temperature, the thermal conductivity was increased from 0.17 W/(mK) to 0.48 W/(mK) for BN/Epoxy and 0.35 W/(mK) for C/Epoxy indicating an increase of ~180 % and ~105 % respectively.

Different concentrations of CNS and BN were investigated based on the electrical treeing process thereby alluding to the quality of nanoparticle distribution. Using Rheology, SEM, AFM and Partial Discharges (PD), optimal amounts of nanoparticles in epoxy were established. For these optimal amounts of nanoparticles, the electrical properties according to PD were improved and

subsequently, the thermal expansion properties were improved as a consequence.

The following research questions were developed as the backbone of this research and the corresponding answers are provided:

How can rheology be used as an alternative to microscopy techniques in evaluating the distribution and/or dispersion of particles in a matrix?

Rheology can be used to evaluate the particle distribution not dispersion in a polymer matrix. There are several regions based on particle concentration, and by finding a minimum in the colloidal interaction region may provide an optimal performing nanodielectric. This optimal level is based on a correlation between the minima established using rheology, the inter-particle distance seen using SEM, and the electrical tree performance showed using PD.

How do different concentrations of two different types of thermally conductive nanoparticles [Carbon (C) and Boron Nitride (BN)] affect the electrical and thermal properties of the resultant nanodielectric? Therefore, what are the optimal loading levels of particles for C/Epoxy and BN/Epoxy that give optimal electrical and thermal performance if they can be determined?

At low concentrations of BN particles, there is a compromise to the electrical tree performance, by increasing the concentration, an optimal loading region of 1.09 vol% to 1.35 vol% is reached. Beyond this region, the electrical tree performance is compromised. In the optimal region, the BN particles provide dramatically increased mechanical support making it difficult for trees to propagate. In 0.33 vol% C/Epoxy, low concentrations are required to avoid the percolation threshold. The particles perform as electron scavengers and provide slightly increased mechanical support thereby retarding the tree process.

With respect to the thermal performance, below and above ~120-150 ^{o}C the thermal conductivity in the nanodielectric is favoured by the epoxy. The

particles are too far apart to improve the thermal conductivity and the nanoparticles compromise the thermal performance. In the region of ~120-150 ^{o}C the thermal conductivity and specific heat have increased, indicating that the particles have moved closer together. But because the particles are good thermal conductors the thermal conductivity of the bulk material has increased.

The major contributions of this research work are summarised as follows:

1. The optimal filler loading level can be determined and reproduced by modifying the nanodielectric fabrication process to include rheological analysis. This contribution was published in the international symposium for high voltage engineering and provided in Appendix A [38].

2. Discovering that carbon nanospheres can be used to significantly improve electrical and thermal properties of epoxy but only if optimally filled.

3. Characterising the mechanical, dimensions and electrical properties of interphase regions in nanodielectrics using AFM techniques. This work is under review by the IEEE and is provided in Appendix F.

4. Successfully characterising electrical tree micro tunnel profiles in nanodielectrics using AFM and showing trees grow around nanoparticles. This contribution was published in SAUPEC 2017 and provided in Appendix D.

5. Successfully characterising electrical tree partial discharges in the nanodielectrics using PD analysis. Showing a correlation between rheology, microscopy, dielectric spectroscopy and partial discharge analysis in electrical trees. This work is under review by the IEEE and is provided in Appendix F.

6. Establishing good performance can be achieved without both good particle uniform distribution and dispersion to obtain a good nanodielectric (Figure 1-3 D). Therefore, it is not necessary to utilise surface conditioner for nanodielectric manufacturing.

7. Establishing that an optimally loaded nanodielectric has an optimal thermal conductivity at a specific temperature which would allow for good performance in the electrical power industry. Essentially electrical equipment can be operated at higher temperatures with better performance.

REFERENCES

[1] E. Kuffel, W. S. Zaengl, and J. Kuffel, *High-voltage engineering: fundamentals*, 2nd ed. Oxford [Oxfordshire]; New York: Pergamon Press, 1984.

[2] Haddad M. and Warne D., *Advances in High Voltage Engineering*. Stevenage, Herfordshire, GBR: The Institution of Engineering and Technology, 2004.

[3] M. S. Naidu and V. Kamaraju, *High Voltage Engineering*, 2nd ed. McGraw-Hill, 1995.

[4] M. A. Salam, *Fundamentals of Power Systems*. Oxford United Kingdom: Alpha Science International Ltd., 2009.

[5] J. D. Glover and M. Sarma, *Power System Analysis and Design*, 2nd ed. Boston United States of America: PWS Publishing Company.

[6] P. Kundur *et al.*, 'Definition and Classification of Power System Stability'.

[7] L. Gyugyi, 'Power Electronics in Electric Utilities: Static Var Compensators'.

[8] Merriam-Webster, 'Definition of COMPOSITE'. [Online]. Available: http://www.merriam-webster.com/dictionary/composite. [Accessed: 02-Mar-2016].

[9] T. Pradeep, *A Textbook of Nanoscience and Nanotechnology*. McGraw Hill Education (India) Private Limited: New York, Chicago, San Francisco, Athens, London, Madrid, Mexico City, Milan, New Delhi, Singapore, Sydney, Toronto, 2012.

[10] J. L. Garcia Araco, 'Working Group A1.02 Survey of Hydrogenerator Failures'. Cigre Working Group A1.02, 14-Aug-2003.

[11] M. Reading, A. S. Vaughan, and P. L. Lewin, 'An investigation into improving the breakdown strength and thermal conduction of an epoxy system using boron nitride', in *2011 Annual Report Conference on Electrical Insulation and Dielectric Phenomena (CEIDP)*, 2011, pp. 636–639.

[12] R. Schurch, S. M. Rowland, R. S. Bradley, and P. J. Withers, 'Imaging and analysis techniques for electrical trees using X-ray computed tomography', *IEEE Trans. Dielectr. Electr. Insul.*, vol. 21, no. 1, pp. 53–63, Feb. 2014.

[13] R. Bruetsch, 'High Voltage Insulation Failure Mechanisms', in *Conference Record of the 2008 IEEE International Symposium on Electrical Insulation, 2008. ISEI 2008*, 2008, pp. 162–165.

[14] R. Brutsch, M. Tari, K. Frohlich, T. Weiers, and R. Vogelsang, 'Insulation Failure Mechanisms of Power Generators [Feature Article]', *IEEE Electr. Insul. Mag.*, vol. 24, no. 4, pp. 17–25, Jul. 2008.

[15] S. Li, S. Yu, and Y. Feng, 'Progress in and prospects for electrical insulating materials', *High Volt.*, vol. 1, no. 3, pp. 122–129, 2016.

[16] P. Morshuis, 'Interfaces: To be avoided or to be treasured? What do we think we know?', in *2013 IEEE International Conference on Solid Dielectrics (ICSD)*, 2013, pp. 1–9.
[17] T. J. Lewis, 'Nanometric dielectrics', *IEEE Trans. Dielectr. Electr. Insul.*, vol. 1, no. 5, pp. 812–825, Oct. 1994.
[18] I. A. Tsekmes, R. Kochetov, P. H. F. Morshuis, and J. J. Smit, 'Measuring and modeling the thermal conductivity of epoxy - Boron nitride nanocomposites', in *Proceedings of 2014 International Symposium on Electrical Insulating Materials (ISEIM)*, 2014, pp. 26–29.
[19] C. Green and A. Vaughan, 'Nanodielectrics - How Much Do We Really Understand? [Feature Article]', *IEEE Electr. Insul. Mag.*, vol. 24, no. 4, pp. 6–16, Jul. 2008.
[20] J. Seiler and J. Kindersberger, 'Evidence of the interphase in epoxy nanocomposites', in *2014 International Conference on High Voltage Engineering and Application (ICHVE)*, 2014, pp. 1–4.
[21] C. E. Stephan, G. Liptak, and R. Schuler, 'An improved insulation system for the newest generation of stator windings of rotating machines', *Int. Conf. LARGE HIGH Volt. Electr. Syst.*, vol. 1, pp. 11–101, 1994.
[22] E. T. Thostenson, C. Li, and T.-W. Chou, 'Nanocomposites in context', *Compos. Sci. Technol.*, vol. 65, no. 3–4, pp. 491–516, Mar. 2005.
[23] G. S. M. Monika Šupová, 'Effect of Nanofillers Dispersion in Polymer Matrices: A Review', *Sci. Adv. Mater.*, vol. 3, no. 1, pp. 1–25, 2010.
[24] Y. Y. Huang, S. V. Ahir, and E. M. Terentjev, 'Dispersion rheology of carbon nanotubes in a polymer matrix', *Phys. Rev. B*, vol. 73, no. 12, p. 125422, Mar. 2006.
[25] T. Kashiwagi *et al.*, 'Relationship between dispersion metric and properties of PMMA/SWNT nanocomposites', *Polymer*, vol. 48, no. 16, pp. 4855–4866, Jul. 2007.
[26] I. A. Tsekmes, R. Kochetov, P. H. F. Morshuis, and J. J. Smit, 'Evaluating the effect of particle distribution and dispersion on the dielectric response of boron nitride - epoxy nanocomposites', in *Electrical Insulation Conference (EIC), 2014*, 2014, pp. 329–332.
[27] J. Vermant, S. Ceccia, M. K. Dolgovskij, P. L. Maffettone, and C. W. Macosko, 'Quantifying dispersion of layered nanocomposites via melt rheology', *J. Rheol. 1978-Present*, vol. 51, no. 3, pp. 429–450, May 2007.
[28] I. A. Tsekmes, P. H. F. Morshuis, J. J. Smit, and R. Kochetov, 'Enhancing the thermal and electrical performance of epoxy microcomposites with the addition of nanofillers', *IEEE Electr. Insul. Mag.*, vol. 31, no. 3, pp. 32–42, May 2015.
[29] D. Fabiani, E. A. Cherney, I. R. Vazquez, and T. Andritsch, 'IEEE CEIDP 2012 Workshop on Nanodielectrics', 2012.
[30] G. Iyer, R. S. Gorur, R. Richert, A. Krivda, and L. E. Schmidt, 'Dielectric properties of epoxy based nanocomposites for high voltage insulation', *IEEE Trans. Dielectr. Electr. Insul.*, vol. 18, no. 3, pp. 659–666, Jun. 2011.
[31] M. F. Fréchette, 'What Are Nanodielectrics?', *IEEE Electr. Insul. Mag.*, vol. 29, no. 6, pp. 8–11, Nov. 2013.

[32] V. M. I. Neitzel, ‘Mechanical properties of epoxy composites with high contents of nanodiamond’, *Compos. Sci. Technol. - Compos. SCI TECHNOL*, vol. 71, no. 5, pp. 710–716, 2011.
[33] J. C. Fothergill, ‘Electrical Properties’, in *Dielectric Polymer Nanocomposites*, J. K. Nelson, Ed. Springer US, 2010, pp. 197–228.
[34] T. Heid, M. F. Fréchette, and E. David, ‘Epoxy/BN micro- and submicro-composites: dielectric and thermal properties of enhanced materials for high voltage insulation systems’, *IEEE Trans. Dielectr. Electr. Insul.*, vol. 22, no. 2, pp. 1176–1185, Apr. 2015.
[35] Y. Xu and D. D. L. Chung, ‘Increasing the thermal conductivity of boron nitride and aluminum nitride particle epoxy-matrix composites by particle surface treatments’, *Instrum. Sci. Technol.*, vol. 7, no. 4, pp. 243–256, Jan. 2000.
[36] T. Tanaka, ‘Dielectric nanocomposites with insulating properties’, *IEEE Trans. Dielectr. Electr. Insul.*, vol. 12, no. 5, pp. 914–928, Oct. 2005.
[37] M. Reading and A. Vaughan, ‘Rheological, Thermal and Electrical Properties of Poly(Ethylene Oxide)/Silicon Dioxide Microcomposites’, in *16th International Symposium on High Voltage Engineering (ISH)*, Cape Town, South Africa, 2009.
[38] A. M. Hank, D. R. Cornish, C. Nyamupangadengu, and I. Sigalas, ‘Quantifying Nanoparticle Dispersion Using Rheological Techniques in Epoxy Resin’, in *ISH 2015*, Pilsen, Czech Republic, 2016.
[39] Huntsman, ‘Technical Datasheet Araldite Casting Resin System (Cy 231-1 CH/Aradur Hy 925)’. Huntsman Advanced Materials Electrical Insulation Materials, Jul-2011.
[40] J. C. Fothergill, ‘Ageing, Space Charge and Nanodielectrics: Ten Things We Don’t Know About Dielectrics’, in *IEEE International Conference on Solid Dielectrics, 2007. ICSD ’07*, 2007, pp. 1–10.
[41] S. S. Bamji, ‘Luminescence and Space Charge Phenomena in Polymeric Dielectrics’, in *2008 Annual Report Conference on Electrical Insulation and Dielectric Phenomena*, 2008, pp. 1–12.
[42] J. V. Champion, S. J. Dodd, and J. M. Alison, ‘The correlation between the partial discharge behaviour and the spatial and temporal development of electrical trees grown in an epoxy resin’, *J. Phys. Appl. Phys.*, vol. 29, no. 10, p. 2689, 1996.
[43] L. A. Dissado, ‘Understanding electrical trees in solids: from experiment to theory’, *IEEE Trans. Dielectr. Electr. Insul.*, vol. 9, no. 4, pp. 483–497, Aug. 2002.
[44] S. Urabe, S. Yoshihara, T. Shirakashi, and Y. Hotoda, ‘Study on aging property of hydrophobic epoxy system for outdoor insulation’, in *IEEE/PES Transmission and Distribution Conference and Exhibition*, 2002, vol. 3, pp. 2181–2184 vol.3.
[45] R. A. Serway and J. W. Jewett, *Physics for Scientists and Engineers with Modern Physics, Chapters 1-46*, 7 edition. Brooks Cole, 2007.
[46] ‘Superhydrophobic Coating | Hydrophobic Surface Coating | Water Repellent Coating’. [Online]. Available: http://www.aculon.com/hydrophobic-coatings.php. [Accessed: 04-Mar-2016].

[47] I. Freestone, N. Meeks, M. Sax, and C. Higgitt, 'The Lycurgus Cup — A Roman nanotechnology', *Gold Bull.*, vol. 40, no. 4, pp. 270–277, Dec. 2007.
[48] J. D. Verhoeven, A. H. Pendray, and W. E. Dauksch, 'The key role of impurities in ancient damascus steel blades', *JOM*, vol. 50, no. 9, pp. 58–64, Sep. 1998.
[49] D. V. Kerssenbrock-Kosigk, *Glass of the Alchemists: Lead Crystal- Gold Ruby, 1650-1750*. Corning, N.Y: The Corning Museum of Glass, 2008.
[50] J. C. Mauro, A. J. Ellison, and L. D. Pye, 'Glass: The Nanotechnology Connection', *Int. J. Appl. Glass Sci.*, vol. 4, no. 2, pp. 64–75, Jun. 2013.
[51] 'Image gallery: The Lycurgus Cup', *British Museum*. [Online]. Available: http://www.britishmuseum.org/research/collection_online/collection_object_details/collection_image_gallery.aspx?partid=1&assetid=63060001&objectid=61219. [Accessed: 02-Mar-2016].
[52] 'Image gallery: The Lycurgus Cup', *British Museum*. [Online]. Available: http://www.britishmuseum.org/research/collection_online/collection_object_details/collection_image_gallery.aspx?partid=1&assetid=63061001&objectid=61219. [Accessed: 02-Mar-2016].
[53] 'Creative Commons — Attribution-NonCommercial-ShareAlike 4.0 International — CC BY-NC-SA 4.0'. [Online]. Available: http://creativecommons.org/licenses/by-nc-sa/4.0/. [Accessed: 02-Mar-2016].
[54] 'What is Horizon 2020? - Horizon 2020 - European Commission', *Horizon 2020*. [Online]. Available: /programmes/horizon2020/en/what-horizon-2020. [Accessed: 03-Feb-2017].
[55] C. Wöll, 'The Chemistry and Physics of Zinc Oxide Surfaces', *Prog. Surf. Sci.*, vol. 82, pp. 55–120, 2007.
[56] M. Reibold, P. Paufler, A. A. Levin, W. Kochmann, N. Pätzke, and D. C. Meyer, 'Materials: Carbon nanotubes in an ancient Damascus sabre', *Nature*, vol. 444, no. 7117, pp. 286–286, Nov. 2006.
[57] D. A. Porter, K. E. Easterling, and M. Sherif, *Phase Transformations in Metals and Alloys, Third Edition*, 3 edition. Boca Raton, FL: CRC Press, 2009.
[58] D. R. Askeland, P. P. Fulay, and W. J. Wright, *The Science and Engineering of Materials*, 6 edition. Stamford, CT: CL Engineering, 2010.
[59] T. J. Lewis, 'Interfaces are the dominant feature of dielectrics at the nanometric level', *IEEE Trans. Dielectr. Electr. Insul.*, vol. 11, no. 5, pp. 739–753, Oct. 2004.
[60] T. Tanaka, M. Kozako, N. Fuse, and Y. Ohki, 'Proposal of a multi-core model for polymer nanocomposite dielectrics', *IEEE Trans. Dielectr. Electr. Insul.*, vol. 12, no. 4, pp. 669–681, Aug. 2005.
[61] S. Raetzke and J. Kindersberger, 'Role of interphase on the resistance to high-voltage arcing, on tracking and erosion of silicone/SiO_2 nanocomposites', *IEEE Trans. Dielectr. Electr. Insul.*, vol. 17, no. 2, pp. 607–614, Apr. 2010.
[62] M. Praeger, T. Andritsch, S. G. Swingler, and A. S. Vaughan, 'A simple theoretical model for the bulk properties of nanocomposite materials', in *2014 IEEE Conference on Electrical Insulation and Dielectric Phenomena (CEIDP)*, 2014, pp. 699–702.
[63] S. Li, G. Yin, S. Bai, and J. Li, 'A new potential barrier model in epoxy resin nanodielectrics', *IEEE Trans. Dielectr. Electr. Insul.*, vol. 18, no. 5, pp. 1535–1543, Oct. 2011.

[64] T. Andritsch, R. Kochetov, P. H. F. Morshuis, and J. J. Smit, 'Proposal of the polymer chain alignment model', in *2011 Annual Report Conference on Electrical Insulation and Dielectric Phenomena*, 2011, pp. 624–627.
[65] T. Tanaka, G. C. Montanari, and R. Mulhaupt, 'Polymer nanocomposites as dielectrics and electrical insulation-perspectives for processing technologies, material characterization and future applications', *IEEE Trans. Dielectr. Electr. Insul.*, vol. 11, no. 5, pp. 763–784, Oct. 2004.
[66] J. Zhao, A. B. Morgan, and J. D. Harris, 'Rheological characterization of polystyrene–clay nanocomposites to compare the degree of exfoliation and dispersion', *Polymer*, vol. 46, no. 20, pp. 8641–8660, Sep. 2005.
[67] T. F. Tadros, *Interfacial phenomena and colloid stability. basic principles Volume 1 Volume 1*. 2015.
[68] I. A. Tsekmes, R. Kochetov, P. H. F. Morshuis, and J. J. Smit, 'A unified model for the permittivity and thermal conductivity of epoxy based composites', *J. Phys. Appl. Phys.*, vol. 47, no. 41, p. 415502, 2014.
[69] Nobelprize, 'The Nobel Prize in Chemistry 2014 - Press Release'. [Online]. Available: https://www.nobelprize.org/nobel_prizes/chemistry/laureates/2014/press.html. [Accessed: 06-Dec-2016].
[70] P. Bujard, 'Thermal conductivity of boron nitride filled epoxy resins: temperature dependence and influence of sample preparation', in *InterSociety Conference on Thermal Phenomena in the Fabrication and Operation of Electronic Components: I-THERM '88*, 1988, pp. 41–49.
[71] X. Huang, P. Jiang, and T. Tanaka, 'A review of dielectric polymer composites with high thermal conductivity', *IEEE Electr. Insul. Mag.*, vol. 27, no. 4, pp. 8–16, Jul. 2011.
[72] M. Jarvid *et al.*, 'A New Application Area for Fullerenes: Voltage Stabilizers for Power Cable Insulation', *Adv. Mater.*, vol. 27, no. 5, pp. 897–902, Feb. 2015.
[73] A. A. Deshmukh, S. D. Mhlanga, and N. J. Coville, 'Carbon spheres', *Mater. Sci. Eng. R Rep.*, vol. 70, no. 1–2, pp. 1–28, Sep. 2010.
[74] S. C. Ray, Z. N. Tetana, R. Erasmus, A. Mathur, and N. J. Coville, 'Carbon spheres for energy applications: Raman and X-ray photoemission spectroscopy studies: Bonding configuration of carbon sphere', *Int. J. Energy Res.*, vol. 38, no. 4, pp. 444–451, Mar. 2014.
[75] L. L. Schramm, *Emulsions, Foams, and Suspensions: Fundamentals and Applications*, 1 edition. Weinheim: Wiley-VCH, 2005.
[76] F. A. Morrison, *Understanding Rheology*. OUP USA Topics in Chemical Engineering, 2001.
[77] C. Ancey, 'Plasticity and geophysical flows: A review', *J. Non-Newton. Fluid Mech.*, vol. 142, no. 1–3, pp. 4–35, Mar. 2007.
[78] R. K. I. A. Tsekmes, 'Evaluating the effect of particle distribution and dispersion on the dielectric response of boron nitride - epoxy nanocomposites', pp. 329–332, 2014.
[79] R. Kochetov, *Thermal and Electrical Properties of Nanocomposites, Including Material Processing*. 2012.
[80] R. Kochetov, T. Andritsch, U. Lafont, P. H. F. Morshuis, and J. J. Smit, 'Thermal conductivity of nano-filled epoxy systems', in *IEEE Conference on*

Electrical Insulation and Dielectric Phenomena, 2009. CEIDP '09, 2009, pp. 658–661.
[81] M. Roy, J. K. Nelson, R. K. MacCrone, L. S. Schadler, C. W. Reed, and R. Keefe, 'Polymer nanocomposite dielectrics-the role of the interface', *IEEE Trans. Dielectr. Electr. Insul.*, vol. 12, no. 4, pp. 629–643, Aug. 2005.
[82] N. A. Geisse, 'AFM and combined optical techniques', *Mater. Today*, vol. 12, no. 7–8, pp. 40–45, Jul. 2009.
[83] Y. Cai, H. Li, M. Karlsson, K. Leifer, H. Engqvist, and W. Xia, 'Biomineralization on single crystalline rutile: the modulated growth of hydroxyapatite by fibronectin in a simulated body fluid', *RSC Adv.*, vol. 6, no. 42, pp. 35507–35516, Apr. 2016.
[84] E. T. Herruzo, A. P. Perrino, and R. Garcia, 'Fast nanomechanical spectroscopy of soft matter', *Nat. Commun.*, vol. 5, Jan. 2014.
[85] R. Kochetov, T. Andritsch, P. H. F. Morshuis, and J. J. Smit, 'Anomalous behaviour of the dielectric spectroscopy response of nanocomposites', *IEEE Trans. Dielectr. Electr. Insul.*, vol. 19, no. 1, pp. 107–117, Feb. 2012.
[86] I. Pleşa, P. V. Noţingher, S. Schlögl, C. Sumereder, and M. Muhr, 'Properties of Polymer Composites Used in High-Voltage Applications', *Polymers*, vol. 8, no. 5, p. 173, Apr. 2016.
[87] S. Singha and M. J. Thomas, 'Dielectric properties of epoxy nanocomposites', *IEEE Trans. Dielectr. Electr. Insul.*, vol. 15, no. 1, pp. 12–23, Feb. 2008.
[88] Agilent Technologies, *Agilent Impedance Measurement Handbook: A guide to measurement technology and techniques*, Fourth. .
[89] 'Dielectric properties of epoxy nanocomposites - IEEE Xplore Document'. [Online]. Available: http://ieeexplore.ieee.org/document/4446732/. [Accessed: 20-Nov-2016].
[90] 'Anomalous behaviour of the dielectric spectroscopy response of nanocomposites - IEEE Xplore Document'. [Online]. Available: http://ieeexplore.ieee.org/abstract/document/6148508/. [Accessed: 20-Nov-2016].
[91] S. Singha and M. J. Thomas, 'Reduction of Permittivity in Epoxy Nanocomposites at Low Nano-filler Loadings', in *2008 Annual Report Conference on Electrical Insulation and Dielectric Phenomena*, 2008, pp. 726–729.
[92] J.-P. Peng, H. Zhang, L.-C. Tang, Y. Jia, and Z. Zhang, 'Dielectric properties of carbon nanotubes/epoxy composites', *J. Nanosci. Nanotechnol.*, vol. 13, no. 2, pp. 964–969, Feb. 2013.
[93] Agilent Technologies, 'Agilent Basics of Measuring the Dielectric Properties of Materials'. Agilent Technologies.
[94] S. Singha and M. J. Thomas, 'Permittivity and tan delta characteristics of epoxy nanocomposites in the frequency range of 1 MHz-1 GHz', *IEEE Trans. Dielectr. Electr. Insul.*, vol. 15, no. 1, pp. 2–11, Feb. 2008.
[95] K. T. Chung, A. Sabo, and A. P. Pica, 'Electrical permittivity and conductivity of carbon black-polyvinyl chloride composites', *J. Appl. Phys.*, vol. 53, no. 10, pp. 6867–6879, Oct. 1982.
[96] IEC, 'High voltage test techniques - Partial discharge measurements.' IEC, 2000.

[97] A. Contin, A. Cavallini, G. C. Montanari, G. Pasini, and F. Puletti, 'Digital detection and fuzzy classification of partial discharge signals', *IEEE Trans. Dielectr. Electr. Insul.*, vol. 9, no. 3, pp. 335–348, Jun. 2002.
[98] K. Leeburn, 'Personal Communication'.
[99] F. Guastavino and B. Cerutti, 'Tree growth monitoring by means of digital partial discharge measurements', *IEEE Trans. Dielectr. Electr. Insul.*, vol. 10, no. 1, pp. 65–72, Feb. 2003.
[100] E. Gulski, 'Digital analysis of partial discharges', *IEEE Trans. Dielectr. Electr. Insul.*, vol. 2, no. 5, pp. 822–837, Oct. 1995.
[101] B. S. Limited, 'FlashBack Express - the best free screen recorder'. [Online]. Available: http://www.flashbackrecorder.com/express. [Accessed: 05-Jan-2017].
[102] E. Lassner and W.-D. Schubert, *Tungsten: Properties, Chemistry, Technology of the Element, Alloys, and Chemical Compounds*. Springer Science & Business Media, 2012.
[103] J. L. Sabourin and R. A. Yetter, 'High-Temperature Heterogeneous Reaction Kinetics of Tungsten Oxidation by CO2, CO, and O2', *J. Propuls. Power*, vol. 25, no. 2, pp. 490–498, 2009.
[104] H. Shindo, C. Egawa, T. Onishi, and K. Tamaru, 'Reaction mechanism of ammonia decomposition on tungsten', *J. Chem. Soc. Faraday Trans. 1 Phys. Chem. Condens. Phases*, vol. 76, no. 0, pp. 280–290, Jan. 1980.
[105] J. Marshall and J. Marshall, *Goldilocks and the three bears*. 1988.

Appendix A: Quantifying Nanoparticle Dispersion Using Rheological Techniques in Epoxy.

Executive Summary

This Appendix gives the paper which was received and published in the 19th International Symposium of High Voltage Engineering in Pilsen Czech Republic in August 2016. The paper had a poster presentation which was presented by Mr Darryn Cornish.

The role of Mr Hank, the first author, was in developing the manufacturing process which would be used for the remainder of developing the Nanodielectric materials. This conference paper attempts to introduce the Rheology process used widely in material science to an electrical engineering audience.

Mr Hank manufactured the material, analysed the material using rheology and scanning electron microscopy and wrote the first drafts of this paper. Mr Cornish, Prof Nyamupangadengu and Prof Sigalas provided a significant amount of editorial comments and insights into how to analyse the results presented.

QUANTIFYING NANOPARTICLE DISPERSION USING RHEOLOGICAL TECHNIQUES IN EPOXY RESIN

A. M. Hank[1*], D. R. Cornish[1*], C. Nyamupangedengu[1*] and I. Sigalas[2*]
[1]School of Electrical and Information Engineering, University of the Witwatersrand, Johannesburg, South Africa
[2] School of Chemical and Metallurgical Engineering, University of the Witwatersrand, Johannesburg, South Africa

*Email:Andrew.hank@students.wits.ac.za

Abstract: In nanodielectric technology the ability to uniformly disperse nanoparticles in the host matrix is critical to the quality of the nanodielectric. Due to the nanometre size of the filler particles, their tendency to agglomerate or flocculate is high. Currently many flaws in nanodielectrics have been attributed to the presence of agglomerations. The current state of the art techniques used in determining the uniformity of nanoparticle dispersion is largely based on the use of electron microscopy, such as Transmission Electron Microscopy and Scanning Electron Microscopy. A limitation with these imaging techniques is that the assessment is largely qualitative rather than quantitative. Additionally these techniques rely on the ability to manufacture a nanodielectric before the degree of dispersion can be evaluated. The present paper investigates the use of rheological techniques to assess the uniformity of dispersion within the host matrix. Rheology is based on the principle of correlating viscosity with varying rotational speed of the fluid. Agglomerations significantly alter the output plot of the rheometer in comparison with that of uniformly dispersed nanoparticles. The rheological methodology was tested for 2 wt%, 4 wt% and 8 wt% of Boron Nitride in Epoxy (Araldite CY 231-1). The viscosity characteristics of Araldite showed that 4 wt% was better dispersed than 2 wt% and 8 wt% and was validated through Scanning Electron Microscopy. Future improvements discuss that assessments of rheology for different mixing and dispersing techniques and at different stages of the manufacturing procedure are needed.

1 INTRODUCTION

There is a sustained drive to improve the reliability of electrical equipment in response to the contemporary technological advancements. In that regard, research on the application of nanotechnology in the development of new generation electrical insulation and dielectrics has been found to give promising results [1]. It is anticipated that the application of nanotechnology should enable one to tailor the properties of electrical insulation to meet specific performance requirements. An example is the much desired insulation that has both thermal and electrical characteristics such as thermally conductive epoxy for use in rotating electrical machines [2–5].

To date, however, major shortfalls in the performance of nanocomposites in both laboratory and industrial applications has been limited due to the inability in obtaining uniform dispersion of the nanofillers in the host matrix [6, 7]. On the nanometre scale; intermolecular forces cause the nanoparticles to clump together thus forming agglomerates [6]. Agglomerations have two consequences; either the insulation performs at best like a system with micro-fillers which have not been shown to provide significant benefits [5, 6], or the agglomerations acts as defects by being a site for crack initiation and/or electric stress enhancement resulting in the compromise of the bulk insulation properties [3, 6].

In the research work on the development of nanodielectrics, it is therefore prudent to use a manufacturing process that ensures homogenous nanoparticle distribution and dispersion. As a quality assurance/control measure, the process should include techniques to evaluate the degree of particle dispersion uniformity in the produced nanocomposite. In the literature, assessment of dispersion uniformity is often done using electron microscopy imaging techniques such as Transmission Electron Microscopy (TEM) and Scanning Electron Microscopy (SEM) [4, 8–10]. The fact that these techniques are largely qualitative is a major shortfall. Additionally these techniques require a sample to be manufactured before the quality of dispersion can be assessed.

Various methods have been developed to improve the dispersion [11–13]. These methods include direct particle mixing, surface conditioning of particles, and dispersing particles in other media such as ethanol before adding to the desired material [11–13]. A quantitative measure for the dispersion of nanoparticles is critically required as

an important parameter in the characterisation of nanocomposites [4].

In order to improve on the effectiveness of the current techniques of assessing particle dispersion, it has been suggested in the literature to characterise the dispersion by analysing the properties of samples while still in the liquid phase [5]. As an example the concept of transparency or viscosity retention can be used as a measure of degree of dispersion homogeneity [2, 7]. With low volume fractions (1-10 %), if uniform dispersion has been achieved, the transparency or viscosity of the material should remain unaltered [2, 7]. However, if there is an excess of nanoparticles this may compromise the material characteristics [14].

The present paper investigates a technique of analysing particle dispersion while the material is still in its liquid phase. The focus is on the direct dispersion of hexagonal boron nitride (h-BN) in Epoxy. The technique used is high shear mixing combined with rheology; using the relationship between viscosity variations as an indication of degree of relative uniformity of particle dispersion.

2 THE PRINCIPLE OF RHEOLOGY

Rheology characterises the flow of matter in a system of liquids and has been reviewed in depth by Morrison and Schramm and a simplified process is shown in Figure 1 [15, 16]. Most polymer systems are either Newtonian or non-Newtonian [15, 16]. Figure 2 shows typical rheology parameters and how they are characterised [16]. Some relevant rheological definitions are given as the following [15, 16]:

- The rheological circuit modelling equivalent of ohm's law is viscosity which describes the resistance to the flow of a liquid. Viscosity is defined as the ratio of shear stress (applied force) to shear rate (rate of deformation). The viscosity of a material is the most sought after result of rheology. The shear rate is the ratio of gap dimension to velocity. The shear stress is the ratio of force to area.

- Liquid systems are either Newtonian or Non-Newtonian. Examples of the possible standard systems are shown in Figure 2. Some Non-Newtonian systems are described as thixotropic or rheopexy.

- Thixotropic (shear thinning/pseudoplastic) systems in general have decreasing viscosity with increasing shear rate. A structure decomposition and regeneration test is used to test thixotropic systems. This test emulates industrial processes where fluid materials are used such as pumping, spraying and extrusion. Rheopexy (shear thickening /dilatant) systems are the inverse of thixotropic systems where they increase in viscosity with increasing shear rate. These systems are tested using temperature dependant flow behaviour.

- Suspensions are liquid systems which have particles. For suspensions it is desirable to have systems with high viscosity for dispersing particles to prevent flocculation, sedimentation and agglomeration.

Typically nanocomposites are manufactured using materials which are liquids and follow non - Newtonian characteristics [2, 4].

An example of a measurement instrument is shown in Figure 3 with torque, gap distance, and area. The fluid under test is added to the cup, the bob is rotated at varying speeds. Using the dimensions of the apparatus, the torque and speed are measured. These results are then used to determine the shear rate and shear stress. Using the shear stress and shear rate the viscosity is then determined. A thixotropic material with high viscosity will allow for nanoparticles to be mixed and when left to settle will prevent particle movement [15, 16].

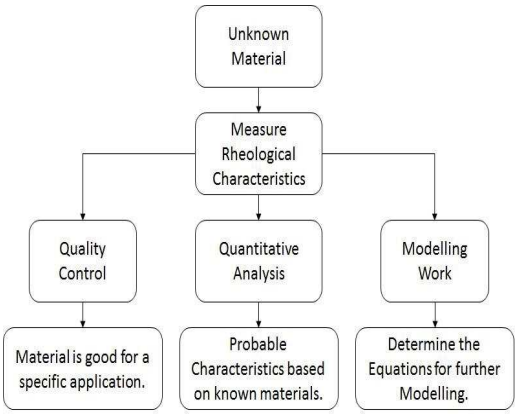

Figure 1: Block diagram describing rheological analysis applications [16].

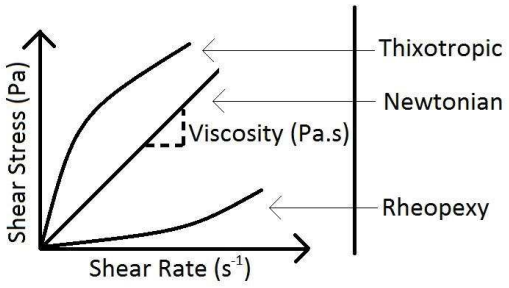

Figure 2: Typical flow characteristics of a material determined using rheology.

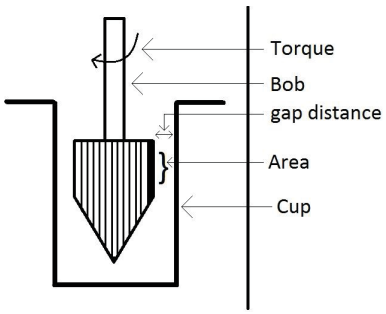

Figure 3: A schematic diagram of a Din Coaxial Cylinder measurement device with grooves used to measure rheological characteristics.

3 THE EXPERIMENTAL PROCEDURE

Araldite CY 231-1 and Aradur HY 925 (Huntsman) were the epoxy material used in this work as they are commonly favoured for good viscosity characteristics, as well as favourable insulation characteristics in medium and high voltage applications [11]. The nanoparticles were h-BN with an average particle size of 80 - 90 nm (Xuzhou Jiechuang New Material Technology Co. Ltd.). In the literature, BN has shown to improve the thermal properties of Epoxy with the benefit of low cost and increased dielectric strength [17, 18].

The samples were prepared following a similar manufacturing process as highlighted in [11, 12]. A Dispermat AE and RheolabQC (Figure 3 Bob CC27/p4478 and cup C-CC27) were used for the high shear mixing and rheology analysis respectively. SEM was used to validate the dispersion because it is a technique that gives a good qualitative surface analysis. A Sigma HD SEM by Carl Zeiss was used for the SEM analysis.

Theoretically the nanoparticles can be mixed in either the resin or the hardener. In the present work Araldite (the resin) was used as the mixing medium because of its higher viscosity compared to the Aradur (the hardener) as is recommended for suspensions. The rheological properties of pure Araldite was compared with 2 wt%, 4 wt% and 8 wt% mixtures of the epoxy and BN respectively, where wt% is percentage of total weight.

All nanoparticles were directly mixed with Araldite through two high rotation stages. These stages were 1000 rpm and 5000 rpm for five minutes respectively. In order to check the effect of prolonged time interval between shearing and rheology measurements; two sets of tests were done: rheology tests immediately after shearing and the same after a 12 hour delay to emulate before shear conditions.

The first rheology test characterised the system and involved three shear stages, the first was a constant 500 s^{-1} for 10 s, followed by a rest state for 30 s and then a linear shear ramp from 0 s^{-1} to 1000 s^{-1} for 10 minutes. The results obtained from the ramp test indicated that the Araldite had both rheopexy and thixotropic behaviour.

A structure decomposition and regeneration test to emulate industrial processes was performed with three stages; 100 s^{-1}, 800 s^{-1} and then back to 100 s^{-1}. After the rheological analysis, the Aradur was added and the same rotation stages to disperse the nanoparticles was applied. The samples were then degassed with a partial vacuum of 400 mb for one hour. These degassed samples were then placed in a stainless steel mould and then cured in an oven at 140° C for three hours. The cured samples had sections shaved off which were then analysed under SEM.

4 THE EXPERIMENTAL RESULTS

The following sub-sections present and discuss in detail the results obtained using rheology and SEM analysis.

4.1 The Rheology Results

The initial rheological results are presented in Figure 4 and Figure 5. It is notable that Araldite depicts dual rheopexy and thixotropic behaviour. Initially the viscosity increases, behaving like a rheopexy fluid, until a shear rate of 100 s^{-1} is reached, at which point it becomes thixotropic in nature. It can be seen in Figure 4 and Figure 5 that despite the complex nature of Araldite's viscosity, the addition of nanoparticles does not significantly change the shape of the curve, but instead offsets the different viscosity characteristic curves depending on the loading level of the fillers. It is possible that the presence of agglomerations results in the offset of the viscosity characteristic curves.

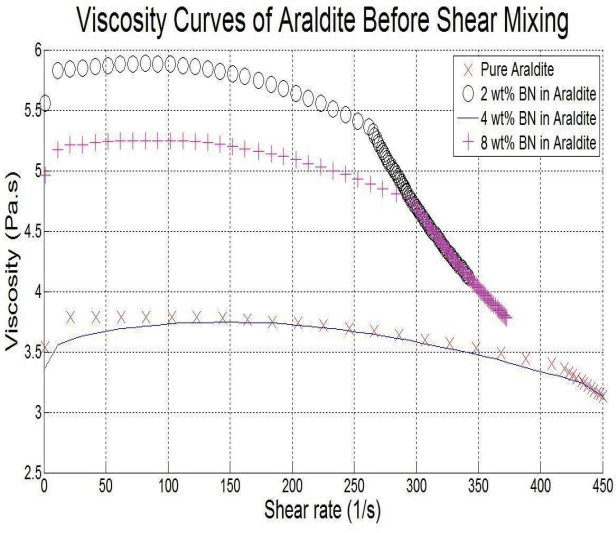

Figure 4: Rheogram of Araldite prior to Rotation Stage showing rheopexy and thixotropic characteristic of Araldite.

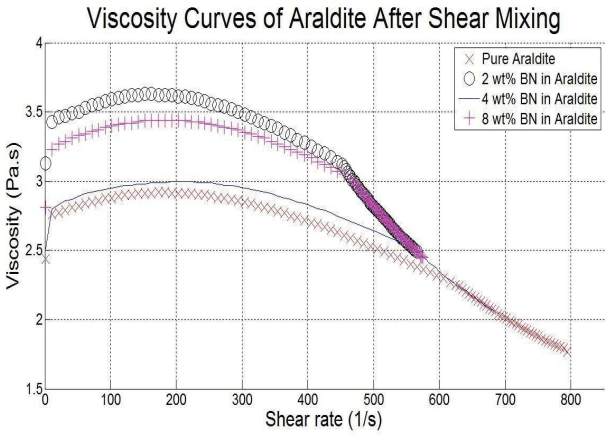

Figure 5: Rheogram of Araldite after Rotation Stage Showing thixotropic characteristic of Araldite.

These results suggest that the 4 wt% Araldite was optimal in dispersion uniformity for the compositions tested as the rheology curve of the mixture practically overlaps that of the pure Araldite. Figure 6 shows the curves that would be expected for an industrial process of a system at rest, followed by high shear conditions and then being left to settle, which implies the system is indeed thixotropic.

Figure 4 through to 6 suggest that while the 4 wt% does not have uniform dispersion, it nevertheless has better dispersion than the 2 wt% and 8 wt% This observation suggests the nanofiller loading level is a parameter that influences the degree of dispersion uniformity but in a non-linear relationship. Furthermore it can be inferred that there is an optimal loading level below and above which the dispersion becomes increasingly non-uniform. This is in agreement with [14] which argues that if the level of loading exceeds a certain amount the integrity of the material is compromised.

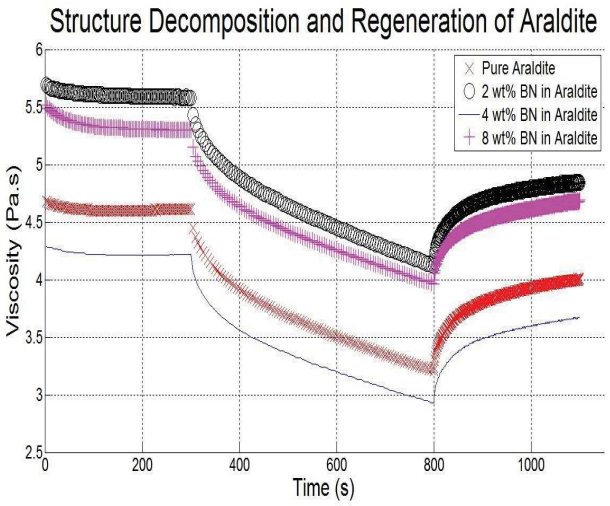

Figure 6: Industrial Process Emulation Results showing the lagging and sagging behaviour.

The structure decomposition and regeneration results in Figure 6 correlate with the viscosities presented in Figure 4 and 5 which are of a different type of test. The downward trends for 2 wt% and 8 wt% in Figure 4 and 5 imply that the rheological process further disperses the particles.

4.2 The SEM Results

A SEM micrograph for unmixed h - BN nanoparticles is shown in Figure 7 which confirms the tendency of nanoparticles to agglomerate. Similar micrographs for the cured Epoxy nanocomposites are shown in Figure 8 through 10.

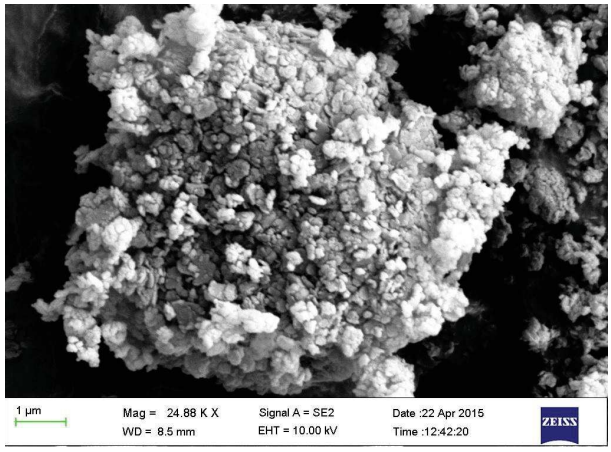

Figure 7: SEM Micrograph showing Pure BN Agglomerate with smaller BN particles.

Comparing the level of dispersion for each sample, it appears that while there are agglomerations, the dispersion of agglomerates in Figure 9 (4 wt%) is better than the dispersion of agglomerates in Figure 8 (2 wt%) and Figure 10 (8 wt%). These SEM results further confirm the rheology analysis results.

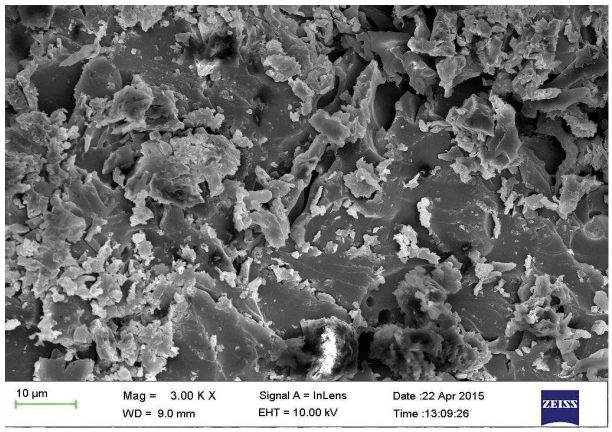

Figure 8: SEM Micrograph of 2 wt% BN in Epoxy at 3 000 Magnification.

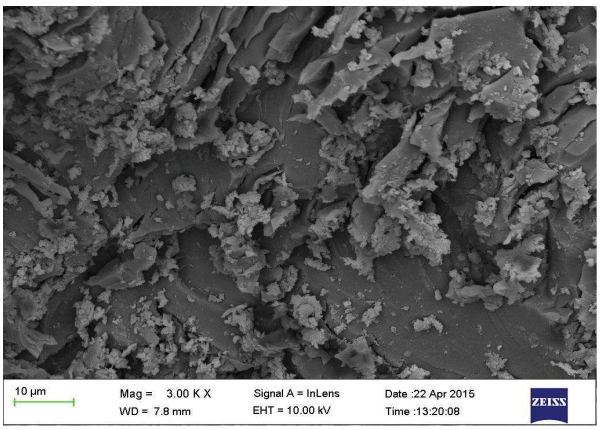

Figure 9: SEM Micrograph of 4 wt% BN in Epoxy at 3 000 Magnification.

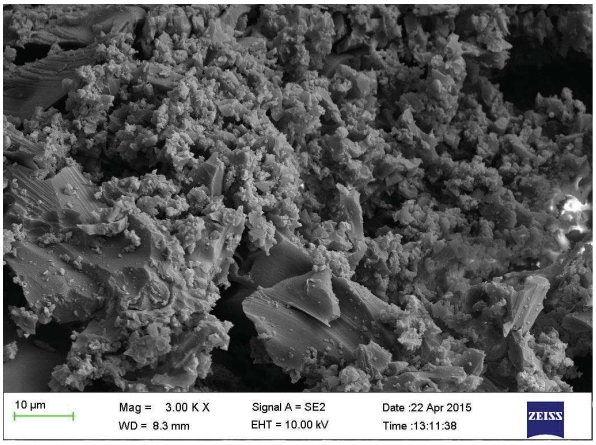

Figure 10: SEM Micrographs of 8 wt% BN in Epoxy at 3 000 Magnification.

In this work the shearing time was chosen to be five minutes. It could be interesting to investigate the effect of different shearing times and speeds. The rheology technique could be extended to assess other manufacturing processes of nanodielectrics such as those which make use of surfactants and ethanol as a medium to break down agglomerates.

5 CONCLUSION

While microscopy techniques have been commonly used in assessing particle dispersion uniformity, rheology technology has proven to give promising results. Furthermore rheology allows evaluation of dispersion at various stages in the manufacturing process. In this paper the rheological results were compared with SEM results and the correlation gives confidence in the ability to use rheological techniques in evaluating the dispersion before the completion of the manufacturing process. Ideally the rheological results would allow for industrial analysis techniques to be developed for large scale production of nanodielectrics.

ACKNOWLEDGMENTS

The authors would like to acknowledge the following funders: ESKOM through the TESP project, the department of trade and industry (DTI) for THRIP funding, the national research foundation (NRF), and the DST-NRF Centre of Excellence in strong materials.

REFERENCES

[1] J. K. Nelson and L. S. Schanddler, “Nanodielectrics 3,” *IEEE Trans. Dielectr. Electr. Insul.*, vol. 21, no. 2, Apr. 2014.

[2] M. Reading and A. Vaughan, “RHEOLOGICAL, THERMAL AND ELECTRICAL PROPERTIES OF POLY(ETHYLENE OXIDE) / SILICON DIOXIDE MICROCOMPOSITES,” in *16th International Symposium on High Voltage Engineering*, 2009.

[3] T. Tanaka, “Dielectric nanocomposites with insulating properties,” *IEEE Trans. Dielectr. Electr. Insul.*, vol. 12, no. 5, pp. 914–928, Oct. 2005.

[4] T. Kashiwagi, J. Fagan, J. F. Douglas, K. Yamamoto, A. N. Heckert, S. D. Leigh, J. Obrzut, F. Du, S. Lin-Gibson, M. Mu, K. I. Winey, and R. Haggenmueller, “Relationship between dispersion metric and properties of PMMA/SWNT nanocomposites,” *Polymer*, vol. 48, no. 16, pp. 4855–4866, Jul. 2007.

[5] G. Iyer, R. S. Gorur, R. Richert, A. Krivda, and L. E. Schmidt, “Dielectric properties of epoxy based nanocomposites for high voltage insulation,” *IEEE Trans. Dielectr. Electr. Insul.*, vol. 18, no. 3, pp. 659–666, Jun. 2011.

[6] G. S. M. Monika Šupová, “Effect of Nanofillers Dispersion in Polymer Matrices: A Review,” *Sci. Adv. Mater.*, vol. 3, no. 1, pp. 1–25, 2010.

[7] C. Green and A. Vaughan, “Nanodielectrics - How Much Do We Really Understand? [Feature Article],” *IEEE Electr. Insul. Mag.*, vol. 24, no. 4, pp. 6–16, Jul. 2008.

[8] B. Lively, W. R. Smoot, S. S. Sangari, and W. Zhong, “A quantitative analysis tool for quality assessment of nanocomposite masterbatches,” *J. Compos. Mater.*, vol. 48, no. 20, pp. 2527–2536, Aug. 2014.

[9] O. Guise and C. Strom, “Quantifying Dispersion in Polymer Systems by Combining Image Analysis and Statistical Analysis,” *Microsc. Microanal.*, vol. 17, no. Supplement S2, pp. 1472–1473, Jul. 2011.

[10] H. S. Khare and D. L. Burris, “A quantitative method for measuring nanocomposite dispersion,” *Polymer*, vol. 51, no. 3, pp. 719–729, Feb. 2010.

[11] R. Kochetov, T. Andritsch, U. Lafont, P. H. F. Morshuis, and J. J. Smit, “Thermal conductivity of nano-filled epoxy systems,” in *IEEE Conference on Electrical Insulation and Dielectric Phenomena, 2009. CEIDP ’09*, 2009, pp. 658–661.

[12] R. Kochetov, T. Andritsch, U. Lafont, P. H. F. Morshuis, S. J. Picken, and J. J. Smit, “Thermal

behaviour of epoxy resin filled with high thermal conductivity nanopowders," in *IEEE Electrical Insulation Conference, 2009. EIC 2009*, 2009, pp. 524–528.

[13] T. Heid, M. Fr??chette, and E. David, "Epoxy/BN micro- and submicro-composites: dielectric and thermal properties of enhanced materials for high voltage insulation systems," *IEEE Trans. Dielectr. Electr. Insul.*, vol. 22, no. 2, pp. 1176–1185, Apr. 2015.

[14] J. C. Fothergill, "Electrical Properties," in *Dielectric Polymer Nanocomposites*, J. K. Nelson, Ed. Springer US, 2010, pp. 197–228.

[15] L. L. Schramm, *Emulsions, Foams, and Suspensions: Fundamentals and Applications*, 1 edition. Weinheim: Wiley-VCH, 2005.

[16] F. A. Morrison, *Understanding Rheology*. OUP USA Topics in Chemical Engineering, 2001.

[17] Y.-X. Fu, Z.-X. He, D.-C. Mo, and S.-S. Lu, "Thermal conductivity enhancement with different fillers for epoxy resin adhesives," *Appl. Therm. Eng.*, vol. 66, no. 1–2, pp. 493–498, May 2014.

[18] X. Huang, P. Jiang, and T. Tanaka, "A review of dielectric polymer composites with high thermal conductivity," *IEEE Electr. Insul. Mag.*, vol. 27, no. 4, pp. 8–16, Jul. 2011.

Appendix B: Investigating the Percolation Threshold of Carbon/Epoxy Nanodielectrics using Dielectric Spectroscopy

Executive Summary

This Appendix presents the paper which was received and published in the 25th South African University Power Electronics Conference (SAUPEC) at the University of Stellenbosch in South Africa in January 2017. The paper had a power point presentation which was presented by Ms N.M. Maphundu and Mr T.I. Rakoma. This paper was a summary of combination of the fourth-year project offered to Ms N.M. Maphundu and Mr T.I. Rakoma.

The role of Mr Hank, was designing and manufacturing the samples used for the investigation, and introducing the students to the nanodielectric theory and technology. Within the paper, providing input into the introduction, discussion and conclusion and image on the models. This conference paper provides introduction to the limitations of carbon nanospheres as a conductive filler particle in investigating the material.

INVESTIGATING THE PERCOLATION THRESHOLD OF CARBON/EPOXY NANODIELECTRICS USING DIELECTRIC SPECTROSCOPY

N.M. Maphundu*, T.I. Rakoma*, A.M. Hank* and C. Nyamupangedengu*

** School of Electrical and Information Engineering, University of Witwatersrand 2050, South Africa.*
Email: noxolo.maphundu@students.wits.ac.za, thabang.rakoma@students.wits.ac.za, andrew.hank@students.wits.ac.za, Cuthbert.nyamupangedengu@wits.ac.za

Abstract: This paper is on developing improved electrical insulation through appropriately mixing carbon nanospheres with epoxy. The dielectric properties of epoxy-based nanodielectrics filled with carbon nanospheres at weight percentage (wt%) loadings of 0.11–3.86 wt% were investigated. The complex permittivity and conductivity of the nanodielectrics at frequency ranges of 40 Hz–10 MHz were derived from measurements. The obtained results show that 0.11 wt% and 0.29 wt% have lower complex permittivity and conductivity compared to pure epoxy. This behaviour is explained by the role of the interphase (interfacial region around the individual nanoparticles). The higher permittivity and conductivity of 0.53–3.86 wt% is explained by the percolation effect. The results show that the permittivity and conductivity are not compromised when appropriate amounts of carbon nanoparticles are added to the epoxy. The presences of carbon nanoparticles, however, significantly improve other insulation properties, such as dielectric strength and thermal conductivity.

Key words: carbon nanospheres, conductivity, dielectric spectroscopy, epoxy, interphase, permittivity, percolation.

1. INTRODUCTION

Research has shown that by mixing appropriate amounts of suitable nanoparticles with conventional electrical insulation, the resultant product (nanodielectrics) can exhibit remarkably improved electrical, thermal and mechanical properties [1, 2]. The improved results are mainly attributed to the unique properties of the nanofiller and the large interfacial area (interphase illustrated in Figure 1) between the nanoparticles and the polymer matrix [3–5]. The interphase allows the nanofiller to alter some properties of the host insulating material.

There are different filler materials such as metal oxides and boron nitride used in the development of nanodielectrics. Carbon nanospheres (CNS) in epoxy is a promising nanodielectric. CNS has attractive properties such as low density, high surface area and stable mechanical and thermal properties [6]. Kosmidou *et. al*. [7] showed that carbon black epoxy nanocomposites have good space charge characteristics. The implications of these findings show promising applications in HVDC technologies.

However, determining the optimal amount of CNS concentration in the polymer matrix is a challenge due to the percolation effect [7, 8]. Additionally, it is key with conductive nano-fillers to obtain a balance between electrical conductivity and desired mechanical and insulating properties [7]. This was evident in [7], where surface modified carbon nanotubes (CNTs) were reported to improve the flexural modulus, strength and storage modulus of the polymer. However, the high electrical conductivity observed becomes the main disadvantage when the nanodielectric is to be considered for electrical insulation. In [9] improved electrical properties as a result of nanodielectrics are presented and these include partial discharges, AC and DC breakdown strength, and improved treeing time.

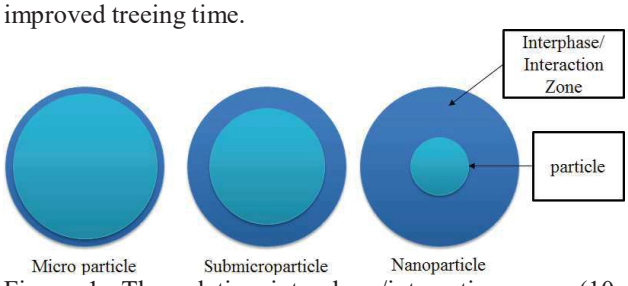

Figure 1: The relative interphase/interaction zone (10-25 nm) to particle relationship shown for micro (1 µm-500 nm), submicro (500 nm-100 nm) and nano (100 nm-1 nm) spherical particles.

The present work investigates the dielectric properties (permittivity, and conductivity) of CNS/epoxy nanodielectrics at different filler loading levels. This was to determine which filler wt% had better functional properties compared to those of pure epoxy. This paper is part of an ongoing larger project by the authors on improving dielectric properties of insulators using different nanoparticles. The unique properties of nanodielectrics are due to the existence of areas around the nanoparticles attributed termed, the interaction zone or interphase.

1.1 The role of the interphase

The interphase is defined as a transitional layer that separates the host polymer and the added filler shown in Figure 1. It has been shown that the interphase has different crystallinity, glass transition temperature, permittivity and thermal conductivity from the host polymer and the nano-filler [1, 8]. In an optimally filled nanodielectrics, the bulk properties are attributed to the interphase [1, 10, 11].

In the literature, lower relative permittivity of epoxy nanodielectrics at lower filler loadings has been reported; which is strongly associated with the presence of the interphase. The interaction of nanoparticles and polymer chains cause the interphase to be more pronounced at lower filler wt% [2, 12]. The nanoparticles cause a hindrance to polymer chains and thus, less polarisation. Another possible reason for low relative permittivity at lower wt% may be due to the hydroxyl groups (OH groups) present on the surface of nanoparticles, which can form a strong interaction with polymer chains [13]. Other work by Singha *et al* [14], claims the epoxide groups may form strong hydrogen bonds with the free OH groups of nanoparticles. They also argue that this may be further enhanced by the amine groups from the hardener that is added during sample synthesis. However, the chemical validation has yet to be explored.

1.2 The percolation effect

Percolation is defined as a transition from an insulator nanodielectric to a conductor nanodielectric as a function of filler concentration [15]. The effect results in pronounced increase of permittivity and conductivity. The critical value at which this transition occurs is known as the percolation threshold [15]. Above the percolation threshold, there is a continuous formation of conductive paths that further enhance the electrical conductivity of the nanodielectric [10]. The present work therefore seeks to identify the percolation threshold of CNS/epoxy nanodielectrics.

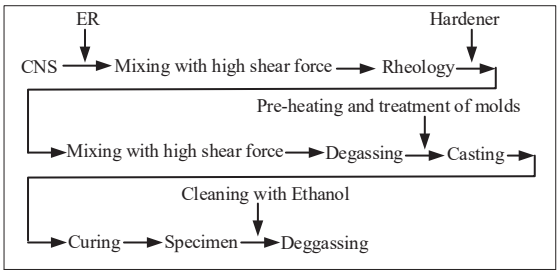

Figure 2: The flow diagram used in the fabrication of epoxy nanodielectrics [16].

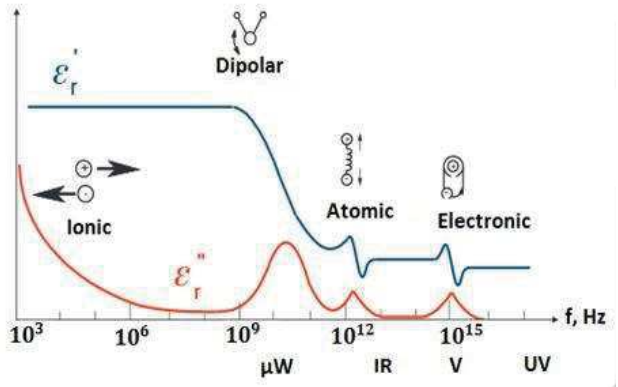

Figure 3: Frequency response of dielectric mechanisms in different regions adapted from [17].

2. EXPERIMENTAL METHODOLOGY

The nanodielectrics were fabricated using a direct dispersion method as shown in Figure 2. The epoxy resin (ER) and hardener used for this study were Araldite CY 231-1 and Aradur HY 925 respectively (Huntsman™). This type of epoxy was preferred for its favourable insulating properties in medium to high voltage applications [16]. The CNS particles used have diameters of 80 – 120 nm. The chemical synthesis of the CNS is detailed in [6].

The manufactured sample sets were: 0.11, 0.29, 0.53, 0.95 and 3.86 wt% loadings of CNS. Three samples per batch were analysed for dielectric spectroscopy (DS) measurements. The filler concentrations of less than 5 wt% were considered in an attempt to avoid agglomeration effects (clumping of particles due to Van der Waals Forces). The conventional rationale was that the agglomerates and pathways may act as defects and compromise the dielectric properties [16]. The final fabricated samples had a diameter of 36 mm and thickness of 1 mm suitable for use with an 4249A Agilent impedance analyser with 16451B test fixture.

2.1 Sample preparation for measurement

The samples were first cleaned with ethanol to remove any trapped residues and were kept under vacuum evacuation 3 h prior to the measurement. It was assumed that 3 h was sufficient to remove trapped air moisture. The samples were coated with silver paint (colloidal silver) to achieve good contact between the electrodes of the test fixture [12]. The silver paint also minimised air gap errors due to sample surface unevenness.

2.2 Dielectric spectroscopy measurement setup

The dielectric spectroscopy (DS) is a measurement technique of complex permittivity as a function of frequency and/or temperature [9]. Through DS, the dynamics of molecular motion of a complex material and characterisation of bulk properties are evaluated [2]. The behaviour of permittivity as a function of frequency is shown in Figure 3. Each frequency region represents a different mechanism which influences the permittivity. Frequency ranges less than 100 MHz are vital for electrical insulation engineering [8]. In the present study, 40Hz – 10 MHz were investigated which lies in the region predominated by dipolar polarisation mechanism [9]. The dipolar polarisation mechanism describes how permanent and induced dipoles orient themselves in response to a changing electric field [12].

A schematic diagram of the DS setup is shown in Figure 4. The measurements were done at ~25 ºC ambient temperature. Each sample set was sandwiched between the electrodes of the test fixture, connected to the impedance analyser. By measuring the complex impedance of the circuit, as a function of frequency,

the real and imaginary parts of the complex permittivity shown in equation (1) arises from equations (2) and (3). The obtained results were then plotted as a frequency response and the results are presented in Section 3. The ratio of energy lost over energy stored known as tan delta is shown by equation 4.

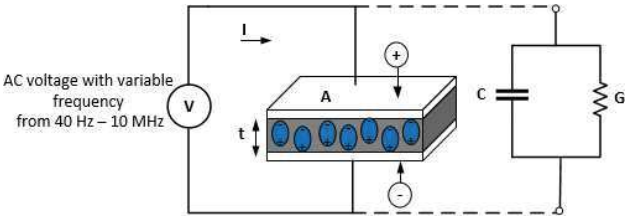

Figure 4: AC powered, parallel plate capacitor model of the dielectric spectroscopy measurement method adapted from [18].

$$\varepsilon^* = \varepsilon' - j\varepsilon'' \quad (1)$$

$$\varepsilon' = \frac{t \cdot \sin\theta}{\varepsilon_0 \cdot A \cdot \omega \cdot |Z|} \quad (2)$$

$$\varepsilon'' = \frac{t \cdot \cos\theta}{\varepsilon_o \cdot A \cdot \omega \cdot |Z|} \quad (3)$$

$$\tan\delta = \frac{\varepsilon''}{\varepsilon'} \quad (4)$$

Where:

- ε' = the real part of the complex permittivity, which represents the relative permittivity that measures the amount of polarisation [9].
- ε'' = the imaginary part of the complex permittivity which represents the dielectric loss of a material that measures the losses that are encountered during polarisation processes [9].
- t = the thickness of the sample [mm]
- A = the area of the samples [mm²]
- ω = the angular frequency [$2\pi f$]

3. EXPERIMENTAL RESULTS AND ANALYSIS

The real and imaginary components of the complex permittivity and the conductivity were investigated in the frequency range of 40 Hz–10 MHz.

Relative permittivity is defined as a measure of the polarizability of a material [19]. Dipoles are created within a dielectric under an externally applied electric field. Figure 5 shows the real part of the permittivity which decreases with increasing frequency for all samples. Figure 6 shows the imaginary part of the corresponding permittivity.

At low frequencies, the dipoles are able to keep up with the frequency and this results in higher polarisation. As the frequency increases, polarisation then lags behind the electric field. This causes the reorientation of the dipoles to be opposed by internal friction, which generates heat and hence energy loss. The increase in loss is manifested as an increase in the imaginary permittivity as shown in Figure 6. A further increase in the frequency of the applied electric field reaches a point where polarization no longer occurs and this is termed the β-relaxation peak [17]. This can be realized at approximately 1 MHz in both the real and imaginary part of complex permittivity (Figure 5 and Figure 6).

The unfilled epoxy sample results as shown in Table 1 and 2 are comparable to Kochetov *et. al.* [20], who used the same epoxy system. The complex permittivity values at low filler loadings highlighted are marginally lower than pure ER. The hindrance of polymer chains due to the presence of CNS results in lower permittivity values as the degree of dipole orientation is reduced [21].

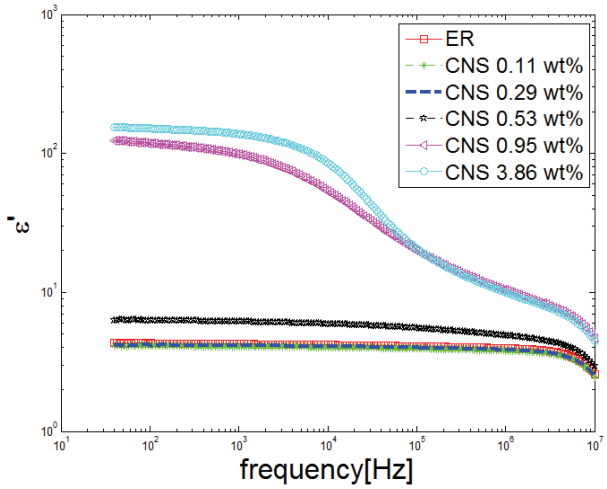

Figure 5: Frequency spectrum of the real part of the complex in carbon/epoxy nanodielectrics.

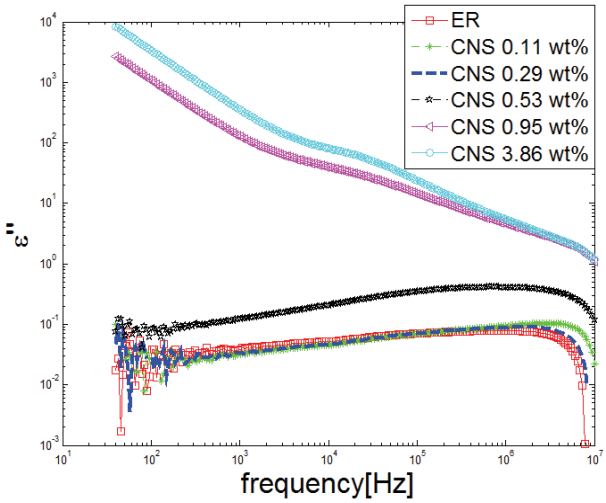

Figure 6: Frequency spectrum of the imaginary part of complex permittivity in carbon/epoxy nanodielectrics.

Table 1: Real part of complex permittivity values at different frequencies.

	40 Hz	1 kHz	0.1 MHz	1 MHz
pure ER	4.36	4.25	4.11	3.97
CNS 0.11 wt%	4.18	4.09	3.96	3.84
CNS 0.29 wt%	4.26	4.14	4.03	3.90
CNS 0.53 wt%	6.31	6.17	5.50	4.90
CNS 0.95 wt%	124.1	98.39	19.89	10.35
CNS 3.86 wt%	155	137.9	20	9.98

Table 2: Imaginary part of complex permittivity values at different frequencies.

	1 kHz	0.1 MHz	1 MHz
pure ER	0.04	0.07	0.07
CNS 0.11 wt%	0.03	0.07	0.09
CNS 0.29 wt%	0.03	0.07	0.09
CNS 0.53 wt%	0.12	0.35	0.41
CNS 0.95 wt%	125.1	14.31	4.56
CNS 3.86 wt%	351.7	23.86	5.45

From Figure 5 and Figure 6, as well as Table 1 and 2; it is noted that permittivity of 0.53 wt% loading is slightly greater than that of pure epoxy. This can be explained by considering the percolation effect. This effect is also noticeable in the 0.95 and 3.86 wt% loadings, where values of ε' and ε'' are higher than that of pure epoxy.

According to Chung *et. al.* [22] the relative permittivity of carbon black (long chains of carbon nanospheres) at 100 kHz is ~100 which is significantly higher than pure ER ~4. The increased number of CNS results in the overlapping of the interphases, according to [9, 10] and hence the carbon permittivity becomes highly prevalent [8, 16]. The inter-particle distance between the nanoparticles decreases with an increase in filler loading. The charge carriers therefore are able to move more freely between nanoparticles. With reference to Figure 7 plotted from equation (5), at low frequencies, the samples with higher filler loadings have conductivity values which are five orders of magnitude greater than pure ER and lower filler loadings. As the frequency increases, the pure ER and lower filler loadings become increasingly conductive, and values of conductivity approach that of heavily loaded samples.

$$\sigma = \varepsilon'' \cdot \omega \cdot \varepsilon_0 \qquad (5)$$

4. DISCUSSION

There are six models used to describe the behaviour of nanodielectrics illustrated in Figure 8 [5, 8, 17–19]. As the models have been developed and further investigations were obtained, these models were further refined to incorporate current understanding. The first model which is the intensity model is based on colloidal chemistry. Essentially, it postulates that the interphase is a function of surface chemistry around the particles. The multi-core model describes how by surface conditioning the particles, the properties of the interphase are three distinct regions. The polymer chain model claims that the interphase is a result of surface conditioning causing the polymer chains around the particles to be more ordered. The new barrier model generalises the first three models by looking at the work energy function of the interphase which causes changes in material properties around the particles. The volume model ignored the properties of the interphase, assumes that it is present, and describes the mathematics of how particles would be ordered in this situation. The simple bulk model uses the volume model to explain what would be observed in the bulk properties of the nanodielectrics.

Currently all work into the modelling have been based on ceramic (metal oxides, boron nitride and clay) nanoparticles and have not investigated conductive particles as candidates. The findings presented in this paper are consistent with all the models except the multi-core and polymer chain model. This is because the CNS particles used were not surface conditioned.

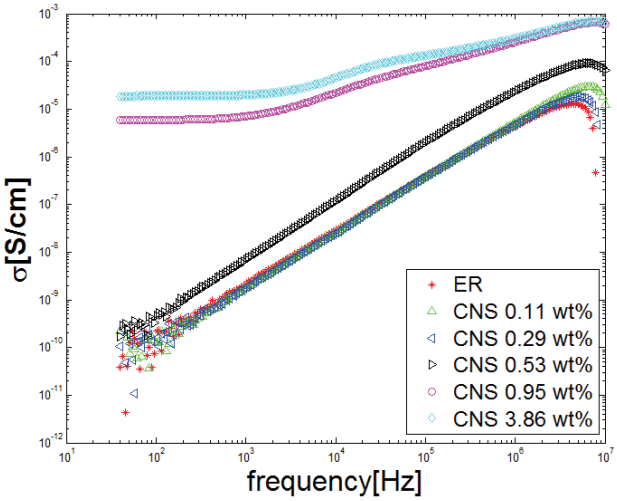

Figure 7: Frequency spectrum of the electrical conductivity in carbon/epoxy nanodielectrics.

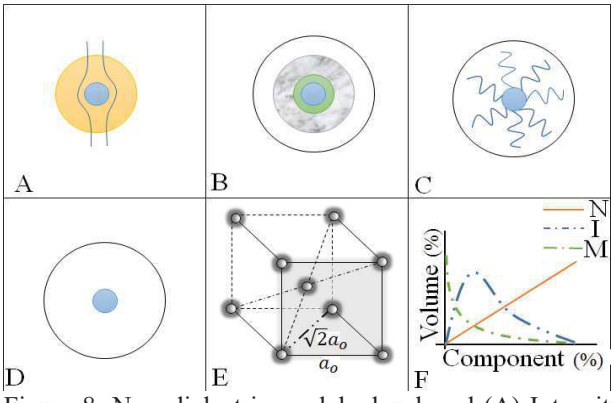

Figure 8: Nanodielectric models developed (A) Intensity model, (B) multi-core model, (C) polymer chain model, (D) New barrier model, (E) Volume model, (F) Simple bulk model where N is nanoparticle, I is interphase and M is matrix [5, 8, 17–19].

Based on the nanodielectrics synthesis, and the results obtained from the dielectric spectroscopy, the effect of humidity, agglomerates and polarisation impedance at low frequencies must be considered. First, other work has shown that nanoparticles have a tendency to absorb water molecules on the surface irrespective of the type of nano-filler. Therefore, the final nanodielectric would possibly have increased values of permittivity. However, the samples were exposed to the same conditions, and therefore any differences in the dielectric properties would be attributed to the different loading levels and not moisture.

One could argue that the presence of agglomerates would be high in the materials analysed due to not using surface conditioning. Although agglomerates may be present in optimally loaded nanodielectrics, the results of this paper show that the agglomerates may not necessarily negatively impact the overall performance of the nanodielectric. However, in high concentration samples, the agglomerates only impact if the percolation threshold has been exceeded.

5. CONCLUSION

The purpose of this study was to investigate the dielectric properties (permittivity and conductivity) of epoxy nanodielectric filled with different wt% of CNS particles. The results can be summarised as follows:

1. The percolation threshold of CNS/Epoxy nanodielectrics is 0.53 wt%.
2. The permittivity and conductivity below the threshold are marginally lower than pure ER.
3. The imaginary part of the complex permittivity and conductivity increases with an increase in frequency for filler loadings below the threshold.
4. Beyond the threshold the permittivity and conductivity are increased by five orders of magnitude compared to low filler loadings and pure ER.
5. The findings are consistent with models available in the literature which explain the interphase phenomena in nanodielectrics.

6. ACKNOWLEDGEMENTS

The authors would like to thank Eskom for their support of the High Voltage Engineering Research Group through the Tertiary Education Support Programme (TESP). They would also like to thank the Department of Trade and Industry (DTI) for THRIP funding and to thank the National Research Foundation (NRF) for direct funding of the research group. Special thanks is given to Prof I. Hofsajer for his exceptional insight and assistance with the dielectric analysis.

REFERENCES

[1] T. J. Lewis, “Nanometric dielectrics,” *IEEE Transactions on Dielectrics and Electrical Insulation*, vol. 1, no. 5, pp. 812–825, Oct. 1994.

[2] R. Kochetov, T. Andritsch, P.H.F. Morshius and J.J. Smit. “Anomalous Behaviour of the Dielectric Spectroscopy Response of Nanocomposites”. *IEEE Transactions on Dielectric and Electrical Insulation*. Vol. 19, No. 1, pp 107 – 117, February 2012.

[3] P. Gonon and A. Boudefel, “Electrical properties of epoxy/silver nanocomposites,” *Journal of Applied Physics*, vol. 99, no. 2, 024308-8. 2006.

[4] M. Roy, J. K. Nelson, R. K. MacCrone, L. S. Schadler, C. W. Reed, and R. Keefe, “Polymer nanocomposite dielectrics-the role of the interface,” *IEEE Transactions on Dielectrics and Electrical Insulation*, vol. 12, no. 4, pp. 629–643, Aug. 2005.

[5] T. J. Lewis, “Interfaces are the dominant feature of dielectrics at the nanometric level,” *IEEE Transactions on Dielectrics and Electrical Insulation*, vol. 11, no. 5, pp. 739–753, Oct. 2004.

[6] A. A. Deshmukh, S. D. Mhlanga, and N. J. Coville, “Carbon spheres,” *Materials Science and Engineering: R: Reports*, vol. 70, no. 1–2, pp. 1–28, Sep. 2010.

[7] T. V. Kosmidou, A. S. Vatalis, C. G. Delides, E. Logakis, P. Pissis, and G. C. Papanicolaou, “Structural, mechanical and electrical characterization of epoxy-amine/carbon black nanonocomposites,” *Express Polymer Letters*, vol. 2, no. 5, pp. 364–372, 2008.

[8] I. Pleşa, P. V. Noţingher, S. Schlögl, C. Sumereder, and M. Muhr, “Properties of Polymer Composites Used in High-Voltage Applications,” *Polymers*, vol. 8, no. 5, p. 173, Apr. 2016.

[9] R. Kochetov, *Thermal and Electrical Properties of Nanocomposites, Including Material Processing*. PhD thesis. Lappeenranta University of Technology. Finland. 2012

[10] S. Raetzke and J. Kindersberger, “Role of interphase on the resistance to high-voltage arcing, on tracking and erosion of silicone/SiO_2 nanocomposites,” *IEEE Transactions on Dielectrics and Electrical Insulation*, vol. 17, no. 2, pp. 607–614, Apr. 2010.

[11] M. Praeger, T. Andritsch, S. G. Swingler, and A. S. Vaughan, “A simple theoretical model for the bulk properties of nanocomposite materials,” in *2014 IEEE Conference on Electrical Insulation and Dielectric Phenomena (CEIDP)*, 2014, pp. 699–702.

[12] “Dielectric properties of epoxy nanocomposites - IEEE Xplore Document.” [Online]. Available: http://ieeexplore.ieee.org/document/4446732/. [Accessed: 20-Nov-2016].

[13] T. Tanaka, M. Kozako, N. Fuse, and Y. Ohki, “Proposal of a multi-core model for polymer nanocomposite dielectrics,” *IEEE Transactions on Dielectrics and Electrical Insulation*, vol. 12, no. 4, pp. 669–681, Aug. 2005.

APPENDIX C. PARTIAL DISCHARGE GROUPING IMPLEMENTATION

C1. Introduction

This Appendix presents the implementation of the partial discharge grouping algorithm implemented in C++. The algorithm is presented in the dissertation on page 132 Figure 6-46. The results were used to generate Figures 6-47 and 6-48 on pages 132 and 133.

C2. Code Implementation

```
/**
Author: Andrew Hank
Description: This code is to analyse partial discharge data and create groups from the data, and place appropriate markers.
*/

#include <iostream>
#include <vector>
#include <fstream>
#include <stdio.h>
#include <math.h>
#include <iomanip>
using namespace std;
///filter data based on predefined states
enum State {Stable,Unstable, Unknown};

///a partial discharge data point is a summary of partial discharge events which happened over one second.
struct PartialDischarge
{
   ///the parameters from the data set will be recorded
```

```
    float minPD = 0;
    float maxPD = 0;
    float avePD = 0;
    int PD_time = 0;
    ///the state of the data will be determined based on the rms voltage and frequency
    State currentState = Unknown;
};


/// a cluster contains the number of points, and a radius.
struct Cluster
{
    int countNumber = 0; ///this is just to track the number of points contained withing the cluster
    float radius = 0.5; ///currently the cluster is defined by a fixed radius.
    ///*** at a later stage adapt the radius to change according to a nearest neighbor. ***
    float location = 0.0; ///the location of the cluster is based on the average pd values.
};
/// as the data deals with floting point numbers, there is a need for a float comparison operator
bool compareFloats(float a, float b, float limit)
{
    if(fabs(a-b) < limit)
        return true;
    else
        return false;
}
/// the main function which will sort the data into appropriate clustes
/** take a discharge and check if it matches any existing clusters.
in the event that it doesn't match any clusters, create an appropriate one*/
void sortData (PartialDischarge &tempDischarge, vector<Cluster>&tempVector)
{
    int containerSize = tempVector.size();
    int flag = 0;
    for(int i = 0; i < containerSize; i++)
```

```
    {
        Cluster &tempCluster = tempVector.at(i);
        float minLim = tempCluster.location-tempCluster.radius;
        float maxLim = tempCluster.location+tempCluster.radius;

        if ( tempDischarge.maxPD > minLim && tempDischarge.maxPD < maxLim)
        ///is the PD within any existing clusters? if so add it to one of them.
        {
            tempCluster.location = (tempCluster.location+tempDischarge.maxPD)/2;///adjust location
            tempCluster.countNumber++;
            flag = 1;
            break;///break the for loop
        }
    }
    if(flag ==0)
    {
        Cluster tempCluster2;
        tempCluster2.location = (tempDischarge.maxPD);
        tempCluster2.countNumber++;
        tempVector.push_back(tempCluster2);
    }
}


int main()
{
    ///define the parameters for the data to be considered stable, if the data is within these values
    ///then the data is deemed to be stable.
    float minV = 18.0;
    float maxV = 22.0;
    float minFreq = 49.0;
    float maxFreq = 51.0;
    float noiseLevel = 0.7;
```

```
int time = 0.0;
float PD_1 = 0.0;
float PD_2 = 0.0;
float PD_3 = 0.0;
float voltage = 0.0;
float freq = 0.0;
float compareResolution = 0.1;

///*** currently the operation only operates on one data file,
/// in the future code will need to be added to fetch multiple data files to process ***
/// for now a hack and slash solution for single file processing will be used.

 ///read in the data file.

///ifstream inputFile("sample_clean_01.txt");
///ifstream inputFile("sample_clean_02.txt");
///ifstream inputFile("sample_clean_03.txt");
///ifstream inputFile("sample_BN_05_1_refined.txt");
///ifstream inputFile("sample_BN_05_2.txt");
///ifstream inputFile("sample_BN_05_3.txt");
///ifstream inputFile("sample_BN_01_1.txt");
///ifstream inputFile("sample_BN_01_2.txt");
///ifstream inputFile("sample_BN_01_3.txt");
///ifstream inputFile("sample_BN_15_1.txt");
///ifstream inputFile("sample_BN_15_2.txt");
///ifstream inputFile("sample_BN_15_3.txt");
///ifstream inputFile("sample_BN_2_1.txt");
///ifstream inputFile("sample_BN_2_2.txt");
///ifstream inputFile("sample_BN_2_3.txt");
///ifstream inputFile("sample_BN_25_1.txt");
///ifstream inputFile("sample_BN_25_2.txt");
///ifstream inputFile("sample_BN_25_3.txt");
```

```
///ifstream inputFile("sample_BN_3_1.txt");
///ifstream inputFile("sample_BN_3_2.txt");
///ifstream inputFile("sample_BN_3_3.txt");
///ifstream inputFile("sample_BN_35_1.txt");
///ifstream inputFile("sample_BN_35_2.txt");
///ifstream inputFile("sample_BN_35_3.txt");
///ifstream inputFile("sample_BN_4_1.txt");
///ifstream inputFile("sample_BN_4_2.txt");
///ifstream inputFile("sample_BN_4_3.txt");
///ifstream inputFile("sample_C_0,1_1.txt");
///ifstream inputFile("sample_C_0,1_2.txt");
///ifstream inputFile("sample_C_0,1_3.txt");
///ifstream inputFile("sample_C_0,25_1.txt");
///ifstream inputFile("sample_C_0,25_2.txt");
///ifstream inputFile("sample_C_0,25_3.txt");
///ifstream inputFile("sample_BN_225_1.txt");
///ifstream inputFile("sample_BN_225_2.txt");
///ifstream inputFile("sample_BN_225_3.txt");

///ifstream inputFile("sample_C_0,09_1.txt");
ifstream inputFile("sample_C_0,09_2.txt");




///create the output files.
ofstream SummariseAnalysis ("C_009_2.csv");

vector <PartialDischarge> PD_data;
///create the clusters
vector <Cluster> typeA;
vector <Cluster> typeB;
vector <Cluster> typeC;
vector <Cluster> typeD;
```

```
vector <PartialDischarge> Transition_Clusters;

/**
read in the time, mean,min and max PD, check if the PD_data is a transition or grouped data.
define if the point is stable or unstable, store the data.
*/


Cluster noiseCluster;
// typeA.push_back(noiseCluster);

while(inputFile >>  time >> PD_1 >> PD_2 >> PD_3 >> voltage >> freq)
{

    PartialDischarge tempDischarge;
    ///create a partial discharge point and define if its stable or not. This does not account for the votlage ramp or breakdown
    tempDischarge.avePD = PD_1;
    tempDischarge.minPD = PD_2;
    tempDischarge.maxPD = PD_3;
    tempDischarge.PD_time = time;


    if(voltage <= maxV && voltage >= minV && freq <= maxFreq && freq >= minFreq)
    {
       tempDischarge.currentState = Stable;
    }
    else
    {
       tempDischarge.currentState = Unstable;
    }

    PD_data.push_back(tempDischarge);
```

```
        if(PD_3 < noiseLevel) ///if the max is less than the noise level, probably noise
        {
           noiseCluster.location = (noiseCluster.location + PD_1+PD_2+PD_3)/3;
           noiseCluster.countNumber++;
        }
        else ///assuming it's not noise
        {
           if(compareFloats(PD_1, PD_3, compareResolution))///if the ave and max are relatively
equal
           {///check if the min is also equal
              if(compareFloats(PD_1,PD_2,compareResolution))///if all the same, electron cluster
              {
                 sortData(tempDischarge,typeA);
              }
              else///probably only ionic clusters
              {
                 sortData(tempDischarge,typeD);
              }

           }
           else if (compareFloats(PD_1,PD_2, compareResolution))
           {/// combination of ion and electron clusters
              sortData(tempDischarge,typeC);
           }
           else
           { /// currently uncharacterised clusters
              sortData(tempDischarge,typeB);
           }
        }

    }
```

```
    typeA.push_back(noiseCluster);


    int tempSize = typeA.size();
    int tempSize2 = typeC.size();
    int tempSize3 = typeD.size();
    int tempSize4 = typeB.size();
    int tempSize5 = PD_data.size();

    SummariseAnalysis << "number of PD discharges: "<< tempSize5 << endl;
    SummariseAnalysis << "number of TypeA clusters: "<< tempSize << endl;


    for(int i = 0; i < tempSize; i++)
    {
       Cluster &outCluster = typeA.at(i);
       SummariseAnalysis << setprecision(3) << fixed <<outCluster.location << "," << outCluster.countNumber << endl;///  << " "<< i << endl;
    }
    SummariseAnalysis << endl << endl << endl;
    SummariseAnalysis << "number of TypeB: "<< tempSize2 << endl;
    for(int i = 0; i < tempSize2; i++)
    {
       Cluster &outCluster = typeC.at(i);
       SummariseAnalysis << setprecision(3) << fixed << " "<<outCluster.location << " " << outCluster.countNumber  << " "<< i << endl;
    }

    SummariseAnalysis << endl << endl << endl;
    SummariseAnalysis << "number of TypeC: "<< tempSize3 << endl;
    for(int i = 0; i < tempSize3; i++)
    {
       Cluster &outCluster = typeD.at(i);
```

```
    SummariseAnalysis << setprecision(3) << fixed << " "<<outCluster.location << " " << outCluster.countNumber  << " "<< i << endl;
  }

  SummariseAnalysis << endl << endl << endl;
  SummariseAnalysis << "number of TypeD: "<< tempSize4 << endl;
  for(int i = 0; i < tempSize4; i++)
  {
    Cluster &outCluster = typeB.at(i);
    SummariseAnalysis << setprecision(3) << fixed << " "<<outCluster.location << " " << outCluster.countNumber  << " "<< i << endl;
  }

  return 0;
}
```

C3. Conclusion

The purpose of this appendix was to present the implementation of the partial discharge grouping algorithm implemented in C++. The code has been provided with appropriate comments. The respective data files could be made available upon request to recreate the relevant analyses.

Appendix D: Statistical table of mean variance, skewness and kurtosis of PD data.

Executive Summary

This Appendix gives the statistical analysis results generated by the C++ code given in Appendix C. Each Partial Discharge (PD) data set was analysed, and coalesced to give a more holistic view and further insight from the PD data. The results are given in Section 6.4.2 of the dissertation.

Sample	PD Number	Mean	Variance	Skewness	Kurtosis	Sample	PD Number	Mean	Variance	Skewness	Kurtosis
Ep-0-1	**2216**	**38.7**	**3096.6**	**4.47**	**30.3**	BN-0.55-1	99020	10.61	706.26	7.58	77.31
Ep-0-2	**17023**	**4.25**	**283.5**	**5.46**	**30**	BN-0.55-2	152160	25.81	3213.62	5.54	33.322
Ep-0-3	**1476**	**42.5**	**1998.55**	**2.68**	**9.44**	BN-0.55-3	39945	42.57	101.8	10363.75	2.79
C-0.33-1	**668086**	**1.15**	**2.19**	**26.92**	**1916.448**	BN-0.89-1	19478	9.95	651.45	10.73	259.52
C-0.33-2	**510609**	**3.72**	**31.18**	**10.61**	**210.81**	BN-0.89-2	9339	1.51	7.85	4.29	18.65
C-0.33-3	**97898**	**0.89**	**0.14**	**8.57**	**104.11**	BN-0.89-3	1397	12.53	23282	13.19	307.03
C-0.33-1*	**374084**	**0.22**	**0.12**	**29.31**	**1594.455**	**BN-1.09-1**	**15710**	**57.23**	**20175.11**	**3.97**	**15.31**
C-0.33-2*	**71080**	**6.26**	**3917.35**	**11.21**	**132.97**	**BN-1.09-2**	**85407**	**6.31**	**1509.73**	**13.21**	**212.98**
C-0.89-1	238	91.06	1394.61	-0.08	0.51	**BN-1.09-3**	**7165**	**22.14**	**216.49**	**2.28**	**8.10**
C-0.89-2	41	14.78	1749.02	3.76	13.69	**BN-1.25-1***	**8482**	**98.87**	**63978.11**	**3.07**	**8.82**
BN-0.26-1	3649	24.83	579.92	0.95	0.23	**BN-1.25-2***	**120290**	**0.36**	**3.38**	**36.47**	**1809.76**
BN-0.26-2	12841	0.38	0.66	79.19	7793.06	**BN-1.25-3***	**122642**	**1.92**	**428.24**	**27.84**	**872.85**
BN-0.26-3	122	0.85	0.16	4.86	31.12	**BN-1.35-1**	**98388**	**14.49**	**7377.12**	**7.66**	**59.81**
BN-1.35-2	**9392**	**16.47**	**472.43**	**15.41**	**362.56**	BN-1.96-2	1304	19.27	277.57	1.12	1.83

Sample	PD Number	Mean	Variance	Skewness	Kurtosis	Sample	PD Number	Mean	Variance	Skewness	Kurtosis
BN-1.35-3	**19713**	**16.84**	**1489**	**7.57**	**70.53**	BN-1.96-3	6629	32.2	5064.42	4.56	23.49
BN-1.65-1	12163	28.96	1142.21	6	70.01	BN-2.77-1	12227	32.79	534.37	1.91	4.94
BN-1.65-2	4114	16.01	1447.78	6.76	52.4	BN-2.77-2	11535	30.97	7360.44	4.85	25.8
BN-1.65-3	13146	36.72	740.22	1.74	5.4	BN-2.77-3	1341	20.91	253.72	0.65	-0.13
BN-1.96-1	3938	56	2201.36	1.98	6.06						

Sample	PD number	Mean	Variance	Skewness	Kurtosis
Pure epoxy	20715	28	1793	4	23
Bush-branch			-Wide variance	-Almost Gaussian -Favours small discharges	-Concentrated
C 0.33 vol %	1721757	2	790	17	792
More bush	-significantly more than epoxy	-discharges suppressed	-Wide variance but Smaller than pure epoxy	-Skewed to the left -Favours small discharges	-Impulse
C 0.89 vol %	279	53	1572	2	7
Bush-branch	-Less than epoxy	-easier to fail than epoxy	Very wide variance	-Mostly Gaussian	-Mostly Gaussian
BN 0.26 vol %	16612	9	194	28	2608
More bush	-Less than epoxy	-discharges suppressed	-Low variance	-Skewed heavily to the left	- Impulse
BN 0.55 vol%	291125	26	1341	3459	38
	-Slightly more than epoxy	-Same mean	-Relatively close to epoxy	-Skewed heavily to the left	-Concentrated
BN 0.89 vol%	30214	8	7980	9	195
	-Slightly more than epoxy	-discharges suppressed	significantly wide variance	-Almost Gaussian	-More concentrated
BN 1.09 vol %	108282	29	7300	6	79
	-significantly more than epoxy	-Same mean	significantly wide variance	-Mostly Gaussian	-Concentrated
BN 1.25 vol %	251414	34	21470	22	897
	-significantly more than epoxy	-Same mean	significantly wide variance	-Skewed slightly to the left	-Impulse
BN 1.35 vol %	127493	16	3113	10	164
	-significantly more than epoxy	-discharges suppressed	significantly wide variance	-Almost Gaussian	-More concentrated
BN 1.65 vol%	29423.00	27.00	1110.00	5.00	43.00
	-Slightly more than epoxy	-Same mean	-significantly wide variance	-Mostly Gaussian	-concentrated
BN 1.96 vol %	11871	36	2514	3	10
	Less than epoxy	Higher mean	-significantly wide variance	-Mostly Gaussian	-Mostly Gaussian
BN 2.77 vol %	25103	28	2716	2	10
	-Slightly more than epoxy	-Same mean	-significantly wide variance	-Mostly Gaussian	-Mostly Gaussian

Appendix E: Electrical tree profiling in Nanodielectrics using Atomic Force Microscopy.

Executive Summary

This Appendix gives the paper which was accepted and published in the 25th South African University Power Electronics Conference (SAUPEC) at the University of Stellenbosch in South Africa in January 2017. The paper had a power point presentation which was presented by Mr A. M. Hank and the paper was awarded the best paper at the conference by Cigré South Africa National Committee.

The role of Mr Hank, was:

1. Designing and manufacturing the samples used for the investigation.
2. Doing the experimental investigations and analyses of the results.
3. Writing editing the paper.

This conference paper shows the feasibility of using Atomic Force microscopy for both electrical tree and nanodielectric research. And provided insight into how electrical trees were influenced by the nanoparticles.

ELECTRICAL TREE PROFILING IN SOLID NANODIELECTRICS USING ATOMIC FORCE MICROSCOPY

***A.M. Hank and *C. Nyamupangadengu**

** School of Electrical and Information Engineering, University of the Witwatersrand 2050, South Africa*
E-mail: andrew.hank@students.wits.ac.za Cuthbert.nyamupangadengu@wits.ac.za

Abstract: Characterisation of electrical tree degradation of solid insulation is an important tool in evaluating the quality of insulation. Imaging electrical trees in nanodielectrics is a challenge. Atomic Force Microscopy was therefore used to investigate the effect of different nanoparticles on the growth of electrical trees in Boron Nitride epoxy and Carbon nanosphere epoxy nanodielectrics. This method allows for characterising nanoparticles which are used in a matrix with low atomic numbers which cannot be done using other microscopy techniques. Electrical degradation was applied to different samples which caused the growth of electrical trees in pure epoxy and the nanodielectrics. The presence of electrical trees was validated with partial discharge measurements. The samples were then also investigated using Scanning Electron Microscopy and Atomic Force Microscopy to evaluate the electrical tree structure and particle nature. The tree channels were measured to be 6 µm in pure epoxy and 20 µm in the nanodielectrics. The electrical trees grown in epoxy appear to be smooth while rugged in the nanodielectrics. The results show that the addition of nanoparticles into an epoxy matrix may cause electrical trees to propagate around the nanoparticles; a process that may possibly impede the electrical tree growth.

Key words: AFM, electrical tree, epoxy, microscopy, nanodielectric, SEM.

1. INTRODUCTION

ELECTRICAL trees are the common ultimate failure mode of solid polymer insulation [1]. Due to enhanced localised electric stress (in the order of MV/mm), energy is transferred from the electric field into the molecular matrix and causes various physiochemical changes. These changes may be scission of molecular bonds, heat, pressure build up and various chemical processes. Degradation of the insulation ensues as tree shaped gas-filled nano or micro-tunnels propagate by means of partial discharge (PD) activity leading to complete insulation failure [1]. Endurance to electrical tree degradation can be regarded as 'the litmus test' of solid polymer insulation quality. In developing new solid polymer insulation, such as nanodielectrics, electrical treeing tests are often used in evaluating the material engineering efforts [2].

Electrical trees have been used to evaluate the time to failure, inception stress, rate of propagation, the types of trees produced, or the PD signatures produced for different trees in solid insulation. It is well established that the growth of a tree, and PDs produced have a relation to the tunnels and tubules formed in the tree. In the literature, conventional wisdom allows for particular types of electrical trees to grow in solid insulation as highlighted by Champion et al. [1]. It is assumed that similar electrical tree characteristics would be observed in nanodielectrics. However, the ability to image an electrical tree using conventional techniques is difficult if a sample is opaque.

Current literature suggests that the use of different microscopy techniques such as transmission electron microscopy (TEM), Scanning electron microscopy (SEM), and atomic force microscopy (AFM) may allow for tree structures to be observed [2]. Additionally, microscopy techniques are essentially distinctive tests which can be a limitation [2].

A less invasive method of investigating electrical trees in opaque nanodielectrics is the use of X-ray computer tomography (XCT) which may allow for trees to be observed [2]. But XCT is a relatively costly procedure compared to conventional microscopy techniques and has resolution limitations. This present paper explores the possibility of using Atomic force microscopy (AFM) as an alternative means of characterising electrical trees especially in nanodielectrics where use of SEM and TEM may not be possible. The nanodielectrics investigated were carbon nanospheres (CNS) and hexagonal boron nitride (hBN) in epoxy. The particles were chosen as good candidates for improved thermal properties [3], [4].

2. EXPERIMENTAL METHODOLOGY

The nanodielectrics were fabricated using a direct dispersion technique [3], [5]. Three types of test specimens were manufactured; pure epoxy and BN/epoxy as controls [5], and C/Epoxy for analysis. As highlighted in [5] see Figure 1, Araldite CY 231-1 and Aradur HY 925 (obtained from Huntsman™) is a type of epoxy that is commonly chosen for favourable insulation characteristics in medium and high voltage applications [5], [6]. The h-BN nanoparticles had an average particle size of 80-90 nm (Xuzhou Jiechuang New Material Technology Co. Ltd.) [5]. A Dispermat AE was used for high mechanical

shear mixing of the Araldite and nanofiller. The CNS nanoparticles had a particle size of 80-120 nm and were synthesized using a procedure detailed in [4]. The material details of the epoxy and nanocomposites are given in Table 1. The densities of the h-BN and CNS was 2.25 g/cm3 and 0.4 g/cm3 respectively. The test samples presented in Table 1 are those deemed to be optimally loaded as determined through other aspects of this work.

Test samples were fabricated casting X-253-1 ogura needles (Ogura Industrial Jewel) which have a 5 µm tip radius with a 30° run off to a maximum needle radius of 1 mm. These needles were held in the moulds using grub screws to ensure a needle plane gap of 3 mm. A final image of a manufactured sample is shown in Figure 2. A silver paint base is applied to ensure the sample makes good contact with electrodes. Three samples were synthesised for each electrical tree test. Saw dust was obtained from the manufactured samples for SEM analysis.

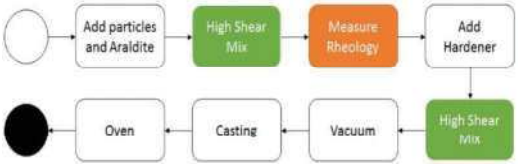

Figure 1: UML Flow diagram showing an adapted form of the generic manufacturing procedure of Epoxy Nanocomposites.

Table 1: Sample Details of Epoxy and optimally filled nanodielectrics.

Sample	Weight percentage of nanofiller (wt%)	Volume fraction of nanofiller (%)
Pure epoxy	0	0
BN epoxy	2.08	1.09
C epoxy	0.7	0.33

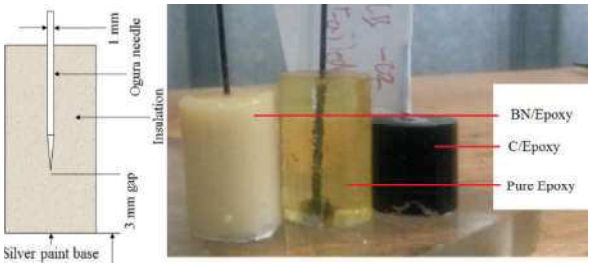

Figure 2: Examples of the test specimen sample configuration and opaque nanodielectrics with transparent pure epoxy.

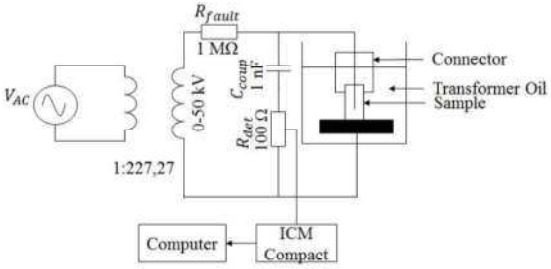

Figure 3: IEC 60270 schematic diagram of test set up used for electrical tree analysis.

SEM images of the samples using a HD Sigma SEM by Zeiss show the pure epoxy in Figure 4, BN/epoxy in Figure 5, and C/epoxy in Figure 6. As can be seen in Figure 4, the epoxy sample does not show any nano particles, the material is fairly solid and the binding of the epoxy chains is solid despite looking at saw dust.

Figure 5 shows that BN particles are well distributed in the epoxy matrix which is one of the requirements of good nanodielectrics. It is unclear to discern currently how the particles have bound to the epoxy matrix. Figure 6 shows that the C/epoxy has multiple levels, there are smaller break offs in the image on top of the surface which was expected of saw dust sample. One challenge, however, is that one cannot discern what is saw dust from the C/epoxy, and what is nanoparticle, given that the epoxy matrix is a carbon base.

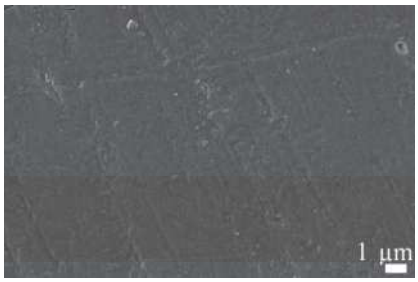

Figure 4: SEM image showing pure epoxy sample surface after surface polishing.

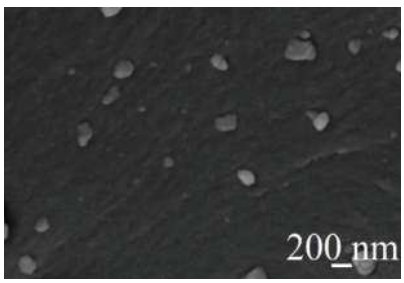

Figure 5: BN/epoxy saw dust sample surface showing inter - particle distance and distribution.

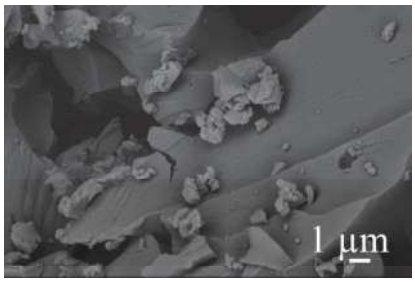

Figure 6: C/epoxy saw dust showing inability to contrast CNS particles in epoxy matrix.

$$E_{max} = \frac{2V}{r \ln(1 + \frac{4d}{r})} \quad (1) \ .$$

Where:

E_{max} is the maximum applied electric field (kV/mm).
V is the applied RMS voltage in kV.
r is the needle tip radius (mm).
d is the gap distance (mm).

Champion et al. [1] showed that depending on the electric field applied, for a needle- plane setup using equation (1), different trees would grow in epoxy samples. The three main categories of electrical trees are branch, bush-branch and branch type trees with corresponding RMS electric fields of ~0.9 MV/mm, ~1.1 MV/mm and 1.3 MV/mm respectively.

Champion et al. [1] further showed that apart from the electric field applied, bush trees are characterised by small micro tunnels and relatively small PD magnitudes ~50-200 pC. Branch trees are characterised by a gradual build-up of PD activity from 10-50 pC to ~750 pC before ultimately failing.

Electrical trees were initiated in the samples by applying 20 kV rms and monitoring the initiation and development of the partial discharges using the PD setup shown in Figure 3. For every second, the maximum, minimum and average apparent PD magnitudes were recorded from tree inception for a time. The electrical treeing was terminated and the tree channels were investigated. A phase resolved pattern was taken every 10 minutes during the process and are shown in Table 2. The clearly distinct PD signals Confirm the presence of electrical trees in the test samples. The samples were then cut and prepared for AFM analysis.

3. ATOMIC FORCE MICROSCOPY ANALYSIS

A detailed explanation of the principle operation of any AFM is provided in [7]. One of the main forms of AFM analysis is tapping mode, with a schematic diagram explaining the operation shown in Figure 7 [7]. A laser is shone on a cantilever and the cantilever is driven using piezo-electric material to oscillate at the cantilever resonant frequency. As the cantilever approaches the sample surface, the cantilever interacts with the Van-der Waals and electrostatic forces of the material. The cantilever experiences resistance to the oscillation, and a control system changes the height to maintain the oscillation. Changes in height are detected by the laser and recorded to obtain a height image [7].

It is important to note that while in tapping mode, the cantilever is not in direct contact with the sample surface. In addition to tapping mode, some AFM microscopes offer scanning voltage microscopy (SVM). While in SVM mode, the cantilever is placed in direct contact with the sample surface. While in contact an electric potential is measured [7]. A Zeiss veeco dimension 3000 Atomic force microscope was used for the AFM analysis in tapping and SVM modes.

Table 2: Results showing phase resolved patterns of one sample at different time stages in electrical tree life.

	10 min	20 min	30 min	40 min
Pure epoxy	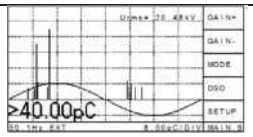	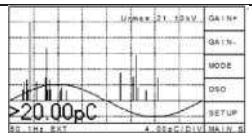	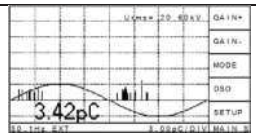	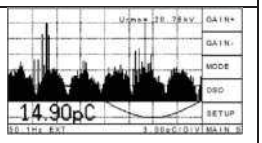
BN Epoxy	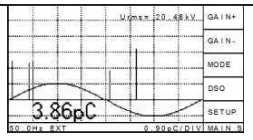	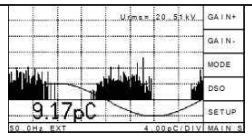	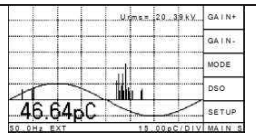	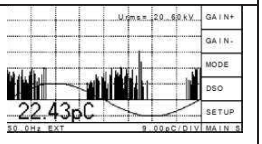
C epoxy	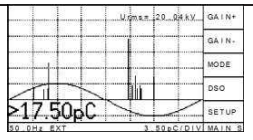	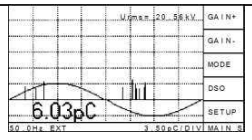	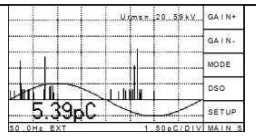	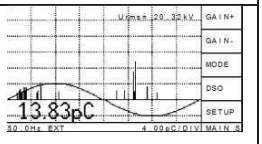

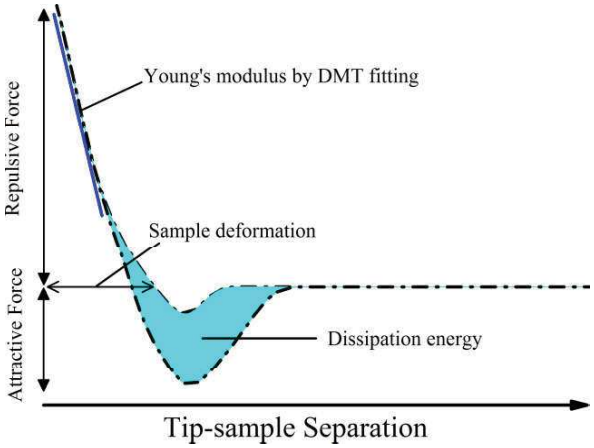

Figure 7: AFM principle of operation while in tapping mode to indicate how a sample deformation and the energy experienced by a cantilever generate a height image [7].

After completing the electrical tree experiments, the samples were cut in a manner as illustrated in Figure 8. It was assumed that by cutting the samples by 2 mm Figure 8 (left which shows a side view of the sample), there would be evidence of electrical tree growth on the surface. The hypothesis was that if electrical trees did indeed grow, the tree channels would be possibly vertical or horizontal with reference to the left image in Figure 8. By looking at a bottom-up/top-down view of the sample surface, one would expect to see tree channels as possible circles (vertical trees coming out of the page) or valleys (horizontal trees) illustrated in the middle image of Figure 8. Furthermore, when viewing a tree using AFM, if the tree channel was indeed circular, the shaving of the sample surface may result in a tree channel being cut at different locations shown in Figure 8 (right). The possibility of slicing a tree channel in many possible locations, may prove to be a challenge when evaluating a tree channel.

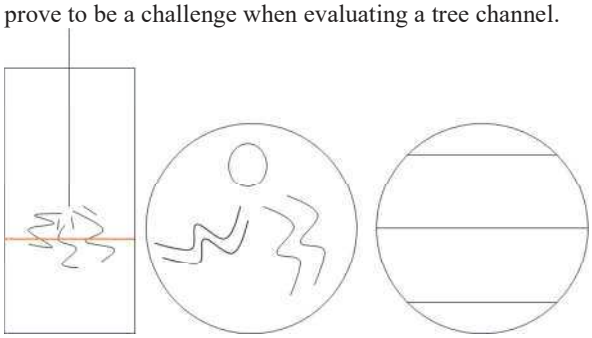

Figure 8: Sample preparation methodology to prepare samples after aging, red line 1 mm from needle tip (left) expected sample surface from a bottom-up view (middle), and side view of tree channel with possible slicing locations (right).

After slicing, the samples were surface conditioned (smoothed) using five stages of sand paper polishing, sequentially starting at 220 mm, 1200 µm, 9 µm, 3 µm, and ending with 1 µm. The last two stages also required 1 µm grinding paste. Figure 9 shows images of the examples of the test specimens after polishing. The sections in the squares in Figure 9 show the samples areas which would be further analysed using AFM and shown in Figure 10. Figure 9 and Figure 10 also confirms what was to be expected by the middle image in Figure 8. After surface polishing, it is safe to assume that there should be tree tubules or channels visible, however, there is no way of knowing at what orientation a tree path may be in the epoxy, the direction, or the size. However, what is required is the ability to analyse the sample surface.

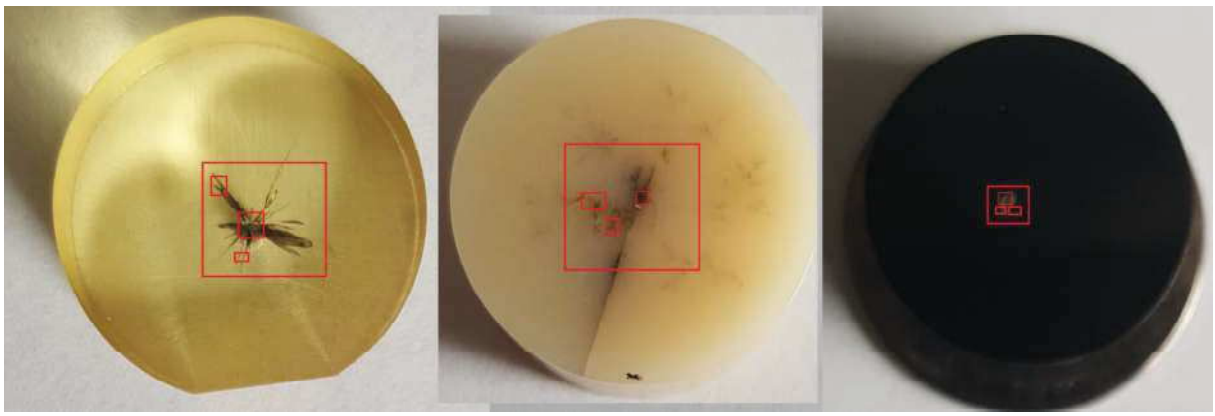

Figure 9: Polished sample surface of samples after shaving with Epoxy (left), BN/Epoxy (middle) and C/epoxy (right).

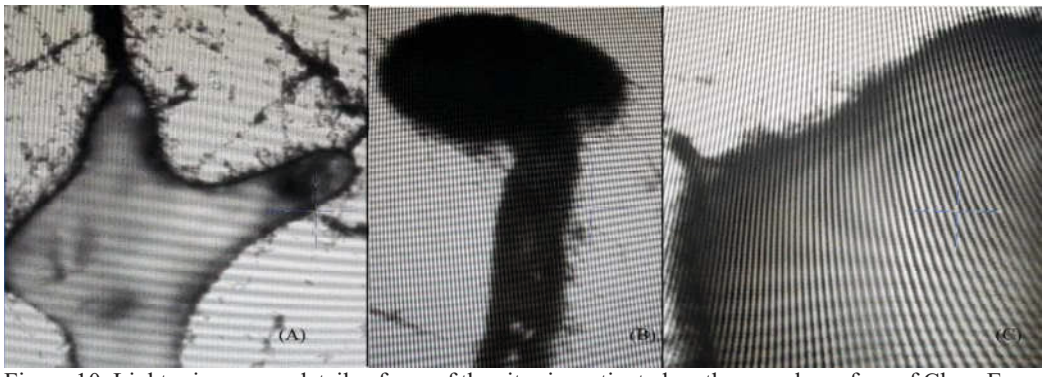

Figure 10: Light microscope details of one of the sites investigated on the sample surface of Clean Epoxy (A), BN/Epoxy (B) and C/Epoxy (C) with a 100 µm length scale showing possible areas just before the needle tip.

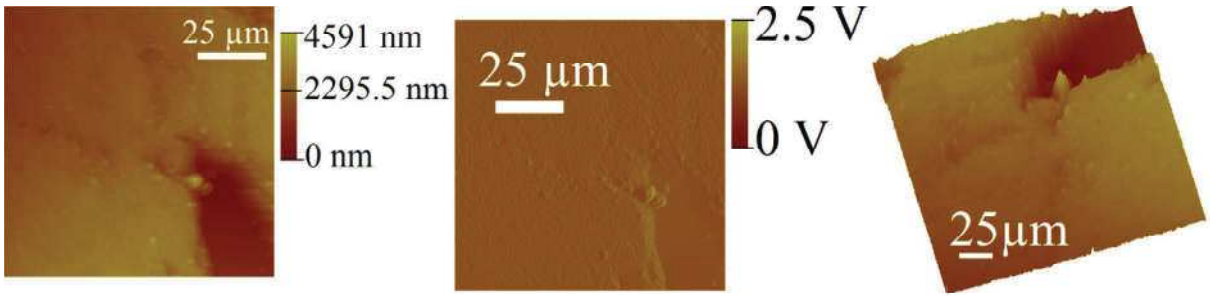

Figure 11: AFM results showing tapping mode results (left), SVM results (middle) and 3D rendered image of an electrical tree channel and tubules in pure epoxy (right).

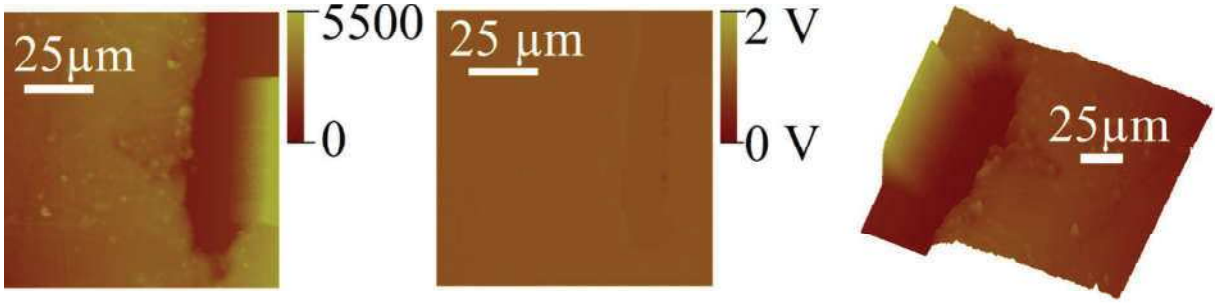

Figure 12: AFM results showing tapping mode results (left), SVM results (middle) and 3D rendered image of an electrical tree channel and tubules in BN/ epoxy (right).

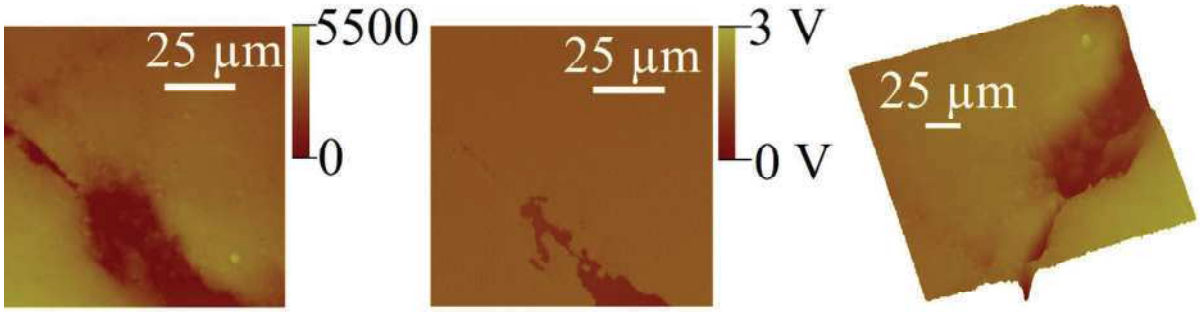

Figure 13: AFM results showing tapping mode results (left), SVM results (middle) and 3D rendered image of an electrical tree channel and tubules in C/epoxy (right).

Figure 11, Figure 12, and Figure 13 give interesting details about the electrical tree channels grown in the different samples. A total of three sites were investigated around each sample surface giving a total of 9 investigated areas for epoxy, BN/epoxy and C/epoxy. The left image firstly gives the tapping mode results, the middle image gives the SVM results, and the right images gives a 3D rendered image of the height taking into account the tapping mode and SVM results. The first observation from the tapping mode results is the shape and width of the tree channels which grew in the samples. Given all the sites investigated, the dimensions of the tree channels are summarised in Figure 14. From Figure 14 the electrical tree channels appear to be wider in nanodielectrics ~20 µm when compared to pure epoxy ~6 µm. It is also interesting to note the tubule size in BN/epoxy on average was smaller ~1.2 µm compared to both pure epoxy and C/epoxy 3 µm.

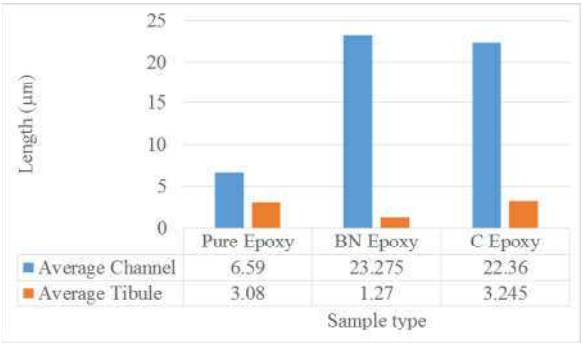

Figure 14: Channel and tubule average measurement results of epoxy samples after electrical tree aging.

From the SVM results, the first observation is that it is possible to partially indicate the presence of particles within the tree channels. Additionally, it is remarkable to note that electrically, the areas devoid of electric potential (i.e. tree channel) are slightly smaller than that of the tapping mode tree results, especially exaggerated in Figure 13. This indicates that the electrical trees must have gone over/around the particles present in the BN/epoxy and C/epoxy. The electrical tree channels shown in Figure 11 and Figure 12 appear to be relatively smooth, while in Figure 13, the tree channel is relatively rugged. However, from Figure 10 (b), it can be seen that there are some bumps present in the tree channel. Additionally, the 3D rendered images show that the electrical tree channels in the nanodielectrics are relatively rugged compared to the pure epoxy. From the AFM results, one can conclude that the electrical trees go around/over certain sites/particles.

4. CONCLUSION

The purpose of this work was to investigate electrical trees grown in epoxy, BN/Epoxy and C/Epoxy. The results indicate firstly that SEM is not a viable candidate to image CNS in epoxy because the particles cannot be discerned in epoxy while SEM can be used to investigate the surface of BN/epoxy and pure epoxy. PD results were used to confirm the presence of electrical trees in the samples. After sample preparation, AFM was used to investigate electrical tree sites. The AFM results show that tree channel diameters are larger in nanodielectrics with ~20 µm channels against ~6 µm in pure epoxy. However, the tree tubules are smaller ~1.2 µm compared to both pure epoxy and C/epoxy ~3 µm. It is however still a challenge to image a tree but AFM and SEM seem as feasible cheaper candidates against XCT.

ACKNOWLEDGEMENTS

The authors would like to thank Eskom for their support of the High Voltage Engineering Research Group through the Tertiary Education Support Programme (TESP). They would also like to thank the Department of Trade and Industry (DTI) for THRIP funding and to thank the National Research Foundation (NRF) for direct funding of the research group.

REFERENCES

[1] J. V. Champion, S. J. Dodd, and J. M. Alison, "The correlation between the partial discharge behaviour and the spatial and temporal development of electrical trees grown in an epoxy resin," *J. Phys. D: Appl. Phys.*, vol. 29, no. 10, p. 2689, 1996.

[2] R. Schurch, S. M. Rowland, R. S. Bradley, and P. J. Withers, "Imaging and analysis techniques for electrical trees using X-ray computed tomography," *IEEE Transactions on Dielectrics and Electrical Insulation*, vol. 21, no. 1, pp. 53–63, Feb. 2014.

[3] I. A. Tsekmes, R. Kochetov, P. H. F. Morshuis, and J. J. Smit, "Measuring and modeling the thermal conductivity of epoxy - Boron nitride nanocomposites," in *Proceedings of 2014 International Symposium on Electrical Insulating Materials (ISEIM)*, 2014, pp. 26–29.

[4] A. A. Deshmukh, S. D. Mhlanga, and N. J. Coville, "Carbon spheres," *Materials Science and Engineering: R: Reports*, vol. 70, no. 1–2, pp. 1–28, Sep. 2010.

[5] A. M. Hank, D. R. Cornish, C. Nyamupangadengu, and I. Sigalas, "Quantifying Nanoparticle Dispersion Using Rheological Techniques in Epoxy Resin," in *ISH 2015*, Pilsen, Czech Republic, 2016.

[6] R. Kochetov, T. Andritsch, U. Lafont, P. H. F. Morshuis, and J. J. Smit, "Thermal conductivity of nano-filled epoxy systems," in *IEEE Conference on Electrical Insulation and Dielectric Phenomena, 2009. CEIDP '09*, 2009, pp. 658–661.

[7] N. A. Geisse, "AFM and combined optical techniques," *Materials Today*, vol. 12, no. 7–8, pp. 40–45, Jul. 2009.



BEST PAPER AWARD

25th Southern African Universities Power Engineering Conference SAUPEC 2017

This certificate is presented to

A.M. Hank

in recognition for the best paper presented at the 25th SAUPEC 2017 held in January 2017

CIGRE SANC

Appendix F: The Criticality of Filler Loading in C/Epoxy and BN/Epoxy Nanodielectrics.

Executive Summary

This Appendix presents the two papers submitted to the Institute of Electrical and Electronic Engineers (IEEE) Transactions on Dielectrics and Electrical Insulation (DEIS) journal which was accepted with major corrections.

The role of Mr Hank, was:

1. Designing and manufacturing the samples used for the investigation.
2. Doing the experimental investigations on the nanodielectrics.
3. Developing the collaboration between colleagues at Uppsala University and in The School of Chemistry.
4. Writing and editing the papers after consolidating all the authors feedback.

The journal papers attempt to emphasise the importance of obtaining the correct number of nanoparticles while presenting the investigations into the dielectric spectroscopy, atomic force microscopy, rheology and electrical trees.

The criticality of filler loading in C/Epoxy and BN/Epoxy nanodielectrics Part 1: AFM, rheology and dielectric spectroscopy

A. M. Hank and C. Nyamupangedengu
School of Electrical & Information Engineering
University of the Witwatersrand, Johannesburg
P. Bag 3, Wits 2050, Johannesburg, South Africa

I. Sigalas
DST-NRF Centre of Excellence in Strong Materials,
School of Chemical and Metallurgical Engineering
University of the Witwatersrand, Johannesburg
P. Bag 3, Wits 2050, Johannesburg, South Africa

B. K. Mutuma and N. J. Coville
DST-NRF Centre of Excellence in Strong Materials and Molecular Sciences Institute,
School of Chemistry, University of the Witwatersrand, Johannesburg
P. Bag 3, Wits 2050, Johannesburg, South Africa

H. Li and K. Leifer
Department of Engineering Sciences
Ångström Laboratory
Uppsala University
Sweden

ABSTRACT

Further to the common practice of using metal oxides like Alumina or other suitable filler material like Boron Nitride for improved thermal performance, this work investigates the use of carbon nanospheres in Bisephenol-A epoxy as a filler material. The present paper focuses on the synthesis aspects of the work and the use of rheology to determine the optimal loading level. It was found that 0.33 vol% for C/epoxy and 1.09 vol% for BN/epoxy were the optimal filler loading levels based on rheology analysis. For C/epoxy, the optimal filler loading level was further confirmed by dielectric spectroscopy. Beyond the percolation threshold, the C/epoxy nanodielectrics exhibit conductive properties. The interphase region around each particle was measured using Atomic Force Microscopy (AFM). It was determined to be 50 nm - 80 nm for a 40 nm accreted Carbon nanosphere particle. The interphase varied in size from ~10 nm to ~90 nm for 80 nm carbon particles based on the presence of other particles. Comparatively, a 70 nm BN particle had an interphase of ~130 nm. The Young's modulus of the interphase region was found to be significantly different from both the host matrix and the nanoparticle, and the bulk properties approach that of the interphase. This is the first of the two papers where the second, electrical tree PD characteristics in the nanodielectric are presented.

Index Terms — **AFM, carbon nanospheres, dielectric spectroscopy, Epoxy, rheology, interphase, filler loading, SEM, TEM.**

1. INTRODUCTION

FILLER loading levels in nanodielectric composites have a large bearing on how well the particles are dispersed and distributed in the host matrix. The differences between particle distribution and dispersion meanings are illustrated in Figure 1. Uniformly dispersed and distributed particles enable optimized establishment of interphase regions around each particle [1]. The interphase region is commonly understood as that responsible for peculiar characteristics of the resultant nanodielectric material [2], [3].

Manuscript received on X Month 2005, in final form XX Month 2005.

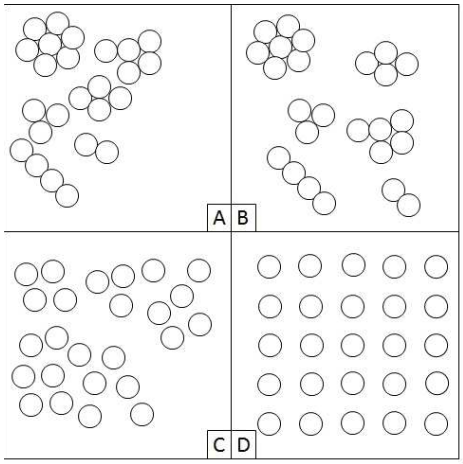

Figure 1: Differences between particle distribution and dispersion. (A) shows poor dispersion and poor distribution, (B) shows good distribution but poor dispersion, (C) shows poor distribution but good dispersion and (D) shows good dispersion and good distribution [4].

How well the particles are dispersed and distributed depends on the material preparation process. Consequently, the efficacy of the material fabrication process has been deemed critical in nanodielectric technology [5].

In nanodielectric research, determination of the filler optimal loading levels has largely been done through the mix and test iterative processes validated by post-manufacturing microscopic analyses. In that regard, Scanning Electron Microscopy (SEM) and Transmission Electron Microscopy (TEM) techniques have been commonly used to determine particle distribution and dispersion.

It is relatively easy to identify particles in SEM/TEM where the filler particles are metal oxides and the host matrix is made of low atomic number elements which make the particles appear different to the host matrix. However, if the particles are of atomic numbers close to the host matrix, it becomes a challenge to evaluate dispersion or distribution of particles using SEM/TEM analyses. SEM and TEM tests are normally conducted on the end product which is destructive and limited in the ability to analyse the final nanodielectric [6].

Work by Tsekmes *et al*. [7] investigated the different effects of dispersion and distribution on the dielectric response of Boron Nitride (BN)-Epoxy nanocomposites. The results showed that samples that had surface modification enabled better dispersion of particles, and had superior thermal performance over unmodified particles.

Ideally, it appears that if good dispersion and distribution (Figure 1 D) can be achieved it may unlock the best performance in nanodielectrics. However, if good performance can be achieved with only good distribution and not necessarily good dispersion (Figure 1 B), this may simplify the manufacturing process, and the quest for ideal characteristics may not be of practical importance.

In principle, the mix and test iterative processes and particle modifications are time-consuming, wasteful and may not be feasible if the bulk manufacturing of nanodielectrics is to be realised.

Recently, however, attempts to predict optimal loading levels through modelling techniques have shown encouraging results [8]. It can be argued therefore that techniques to pre-determine the optimal loading either at the early stages of the manufacturing process or through modelling would be more efficient than the conventional methods. In the present paper an alternative approach, use of rheology, in which the fluid dynamics of the nanodielectric is analysed as part of the nanodielectric synthesis process has been undertaken to possibly investigate the existence of optimal filler loading levels.

Thermal rating is one of the key performance parameters of electrical insulation. Improved thermal performance is, therefore, one of the various possibilities being explored in nanodielectric research worldwide [9]. In that regard, use of a suitable thermal conductive filler such as hexagonal Boron Nitride (hBN) in epoxy has been well explored and produced encouraging results [10]. An alternative filler material for improved thermal conductivity is possibly carbon.

Carbon nanospheres (CNS) particles in epoxy is a promising nanodielectric. CNS has attractive properties such as low density, high surface area and stable mechanical and thermal properties [11]. Kosmidou et. al. [12] showed that carbon black epoxy nanocomposites have good space charge characteristics. The implications of these findings show promising applications in HVDC technologies.

Jarvid *et al.* in [13], reported encouraging findings on nanocarbon dielectrics such as Fullerenes in XLPE. The fact that carbon is also electrically conductive does not make it an obvious candidate nanofiller material for electrical insulation.

Determining the optimal amount of CNS concentration in the matrix is a challenge due to the percolation effect [12], [14]. Additionally, it is key with conductive nanofillers to obtain a balance between electrical conductivity and desired mechanical and insulating properties [12]. This was apparent by findings in [12], where surface-modified carbon nanotubes (CNTs) were reported to improve the flexural modulus, strength and storage modulus of the polymer. But, the high electrical conductivity observed becomes the main disadvantage when the nanodielectric is to be considered for electrical insulation. In [15] improved electrical properties as a result of nanodielectrics are presented and these include partial discharges, AC and DC breakdown strength, and improved treeing time.

The present work explores the use of CNS fillers in epoxy. This paper (the first of two papers on C/epoxy nanodielectrics) focuses on the material preparation aspects and characterisation of the product through Atomic force microscopy (AFM) and dielectric spectroscopy (DS) of the CNS/filler materials. The synthesis of CNS particles and the CNS/filler nanodielectric are described. The fluid dynamic properties of the nanodielectric were then analysed using rheology to determine the optimal loading levels of the nanofiller. The presence of the interphase regions in the nanodielectric was characterised using AFM in more detail than what has been previously presented in [16], [17]. The DS

for the different loading levels were also evaluated. In the second paper, the unique electrical treeing partial discharge (PD) characteristics in the C/Epoxy nanodielectric in comparison to BN/Epoxy and pure epoxy are presented. Electrical tree images obtained using X-ray computer tomography are presented and discussed.

2. THE CARBON NANOSPHERE SYNTHESIS

A comprehensive review of the different types of CNSs that have been made and the synthesis techniques that have been used to make CNSs have been described by Deshmukh *et al*. [11]. The manufacturing of the CNSs used in the present work is a method described in [11].

A vertical chemical vapour deposition (CVD) reactor consisting of a hollow tubular quartz reactor (1.5 mm × 32 mm o.d) loaded in a furnace, a carbon source (acetylene, C_2H_2, Afrox) and a carrier gas argon (Afrox) were used in the CNS synthesis. The furnace was heated to 900 °C at a rate of 10 °C/min under Ar gas (200 mL/min).

At 900°C, the Ar flow valve was closed and a C_2H_2 flow valve opened at a flow rate of 200 mL/min. Acetylene was pyrolyzed in the quartz reactor at 900 °C for 15 min and the CNS product collected in a round bottomed flask connected at the outlet of the reactor. The acetylene flow valve was closed and the quartz reactor cooled under a continuous flow of Ar gas to ambient temperature.

After cooling, the argon flow was stopped and the quartz reactor removed from the furnace. The products were then purified by soxhlet extraction using toluene in an oil bath heated to 150 °C for 16 h. The purified product was then dried for 12 h at 80 °C in a vacuum oven.

The morphology of the synthesised CNSs was ascertained by TEM using an FEI Technai G2 spirit electron microscope operating at 120 kV. A sample specimen was prepared by dispersing a few purified carbon spheres in ethanol (1.0 mL) and the mixture sonicated to form a homogeneous solution.

A few drops of the homogeneous solution were placed onto a carbon-coated copper grid and the grid dried in ambient air for 30 min before inserting it in the microscope. The diameters of the CNS images obtained were measured using Image J 1.48v software.

As can be seen in Figure 2, the CNSs have spherical morphologies and diameter sizes between 80 and 240 nm with an average size of 165±31 nm. The small CNS diameter results from the short residence time of the carbon source in the vertically oriented CVD reactor [18].

As can be seen in Figure 2, the CNSs form independent balls when the radii are above roughly 70 nm. Below 50 nm the CNSs form long chains of spheres. As the synthesis has not been optimised, there is no fixed size distribution. The CNSs were accreted; however, the particles were deemed sufficiently small to be considered for nanodielectric studies. The CNSs were then used in the synthesis of the nanodielectric.

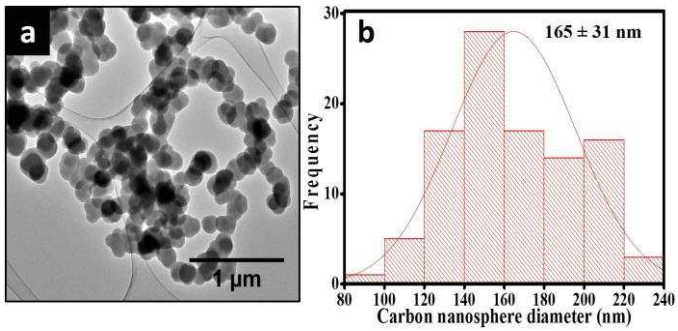

Figure 2: TEM image (A) and particle size distribution (B) of the synthesised CNSs.

3. NANODIELECTRIC SYNTHESIS

The following sub-sections discuss the basic knowledge of rheology, the nanodielectric fabrication, and the results obtained using rheology.

3.1 RHEOLOGICAL TESTS TO DETERMINE THE OPTIMAL FILLER LOADING LEVEL

Rheology characterises the flow of matter in a system of liquids and has been reviewed in depth by Morrison, Schramm and Ancey [19]–[21].

A simplified illustration of possible applications of rheological analyses is shown in Figure 3. Most liquid systems are either Newtonian or non-Newtonian [19], [20]. Ancey [21] provides a useful review of the non-Newtonian fluid characteristics in some media such as soil in water. Although the review by Ancey [21] only covers particle sizes from 1 µm to 1 m (rocks), the concepts and methodology may still be directly transferable to nanometre particles.

Figure 4 shows typical rheology parameters and how they are characterised [20]. Some relevant rheological definitions summarised from [19]–[22] are given as follows:

- The rheological equivalent of ohm's law is viscosity which describes the resistance to the flow of a liquid. Viscosity is defined as the ratio of shear stress (applied force) to shear rate (rate of deformation measured in reciprocal seconds). The viscosity of a material is the most sought after result of rheology. The shear rate is the ratio of gap dimension to velocity. The shear stress is the ratio of force to area.
- Liquid systems are either Newtonian or Non-Newtonian. Examples of the possible standard systems are shown in Figure 4. Some Non-Newtonian systems are described as thixotropic or rheopexy. In particular, when dealing with either epoxy or polyethene, these materials are described as Non-Newtonian [1], [23].
- Thixotropic (shear thinning/pseudoplastic) systems, in general, have decreasing viscosity with increasing shear rate. Rheopexy (shear thickening /dilatant) systems are the inverse of thixotropic systems where they increase in viscosity with increasing shear rate.
- Suspensions are liquid systems which have particles present which may or may not be suspended. Non-Newtonian suspensions have seven states/effects, namely Brownian, hydrodynamic, colloidal, turbulence, friction,

lubrication and collisions. Each state is dependent on the concentration and size of particles which can characterise the bulk material.

Kashiwagi *et al.* [1] analysed the effect of different shear times and shear speeds in PMMA nanocomposites and correlated rheology data with the critical time for obtaining good distribution in PMMA. Additionally, the work showed that utilising high shear rates allowed for a faster critical mixing time. Nevertheless, rheology has been underutilised as an analysis technique in the material characterisation of nanodielectrics [23], [24].

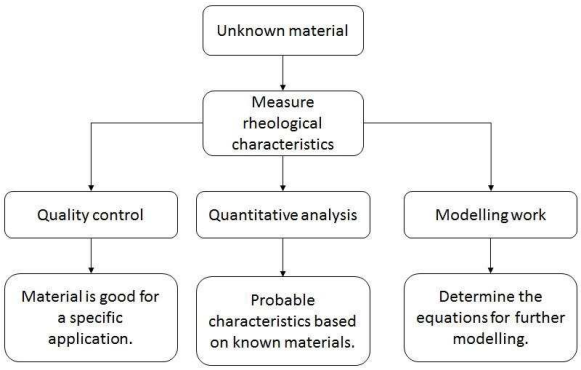

Figure 3: Block diagram describing rheological analysis applications [20].

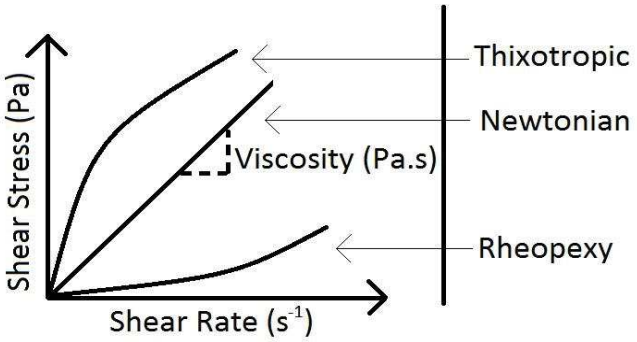

Figure 4: Typical flow characteristics of a material determined using rheology [22].

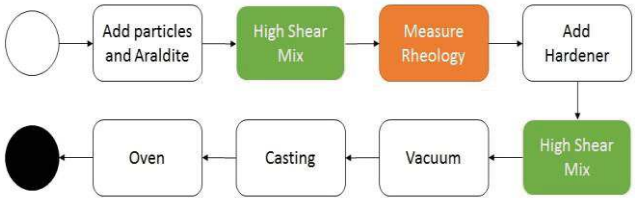

Figure 5: Flow diagram showing an adapted form of the generic manufacturing procedure of Epoxy Nanocomposites. The open circle indicates the start and closed circle indicates the end of the process.

3.2 HIGH SHEAR MIX AND RHEOLOGY MEASUREMENT PROCEDURE

The nanodielectrics were fabricated using a direct dispersion technique [10], [22] as illustrated in Figure 5. Three types of test specimens were manufactured; pure epoxy and BN/epoxy as controls [22], and C/Epoxy for analysis. As highlighted in [22], Araldite CY 231-1 and Aradur HY 925 (obtained from Huntsman™) is a type of epoxy that is commonly chosen for favourable insulation characteristics in medium and high voltage applications [22], [25].

The BN nanoparticles were h-BN with an average particle size of 80-90 nm (Xuzhou Jiechuang New Material Technology Co. Ltd.) see Figure 6 [22]. A Dispermat AE and RheolabQC with a Din Coaxial Cylinder (Bob CC27/p4478 and cup C-CC27) were used for the high shear mixing and rheology analysis respectively.

A schematic of the rheology measurement instrument is shown in Figure 7 with torque, gap distance, and area. The liquid under test is added to the cup and the bob is rotated at varying speeds. Using the dimensions of the apparatus, the torque and speed are measured. These results are then used to determine the shear rate and shear stress. Using the shear stress and shear rate the viscosity is then determined.

Different samples of BN nanoparticles were added to Araldite (8 wt%) to characterise and assess the effect of shear time on the viscosity at 5 000 rpm after different mixing times (5, 10, 15 and 20 min). The results (Table 1) showed that the critical mixing time was achieved at 10 minutes. Beyond 10 minutes the viscosity does not change significantly This confirms the work by Kashiwagi for Epoxy vs PMMA [1] and provided further insight into the fabrication of BN/epoxy done by Tsekmas *et al.* [10], [22]. For a given wt% loading and shear rate, beyond the critical mixing time, the minimum viscosity achieved saturates and there is no indicated benefit from additional mixing apart from generating heat. It was therefore assumed that shearing at 5 000 rpm for 10 min would be sufficient time/shearing rate for use at lower concentrations of both C/Araldite and BN/Araldite.

The material details of the epoxy and nanocomposites are given in Table 2. The densities of the h-BN and CNS was 2.25 g/cm^3 and 0.4 g/cm^3 respectively. Immediately after shearing the Araldite-nanoparticle mixture is analysed using rheology.

Table 1: Viscosity Shear time for 8 Wt % samples normalised to a shear rate of 100 s^{-1}

Shear time (min)	Wt%	Vol%	Viscosity (Pa.s)
5	7.54	4.18	5.1
10	7.54	4.18	4.1
15	7.6	4.22	4.13
20	7.52	4.17	4.09

3.3 RHEOLOGY MEASUREMENT RESULTS AND ANALYSIS

The rheology tests characterised the different Araldite-nanoparticle systems based on the various volume fractions indicated in Table 2 and involved three shear stages. The first shear stage was a constant 500 s^{-1} for 30 s, followed by a rest state for 30 s. These initial stages were to remove any shear history still present from the shear mixing process.

After the rest stage, a linear shear ramp from 0 s^{-1} to 1500 s^{-1} was applied, the results of the shear ramp are shown in Figure 9. This analysis was repeated three times with three independent samples, one immediately after shearing, 1 h after shearing, and 2 h after shearing to observe settling time of agglomerates.

The optimal filler loading that gives optimal particle distribution has been postulated as that which gives a resultant mixture with a viscosity curve that matches that of the host material [23]. Hank *et al.* [22] showed, using rheology and SEM, that 4 wt% loading was better distributed compared to 2 wt% and 8 wt% BN in a BN/Epoxy nanocomposites.

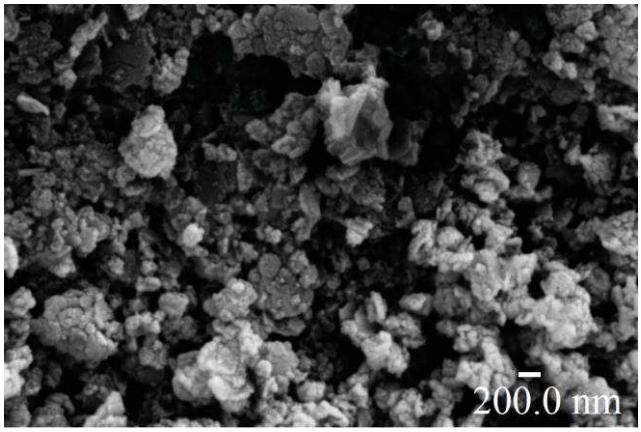

Figure 6: SEM image of the received h-BN particle agglomerates showing a collection of rough h-BN particles with varying particle sizes.

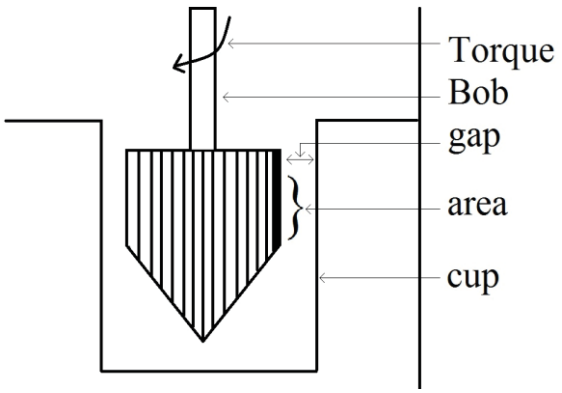

Figure 7: A schematic diagram of a Din Coaxial Cylinder measurement device with grooves used to measure rheological characteristics [22].

Table 2: Sample Details of Epoxy and Nanocomposites. Note 0 % is pure epoxy.

Weight Percentage of nanofiller (wt%)		Volume Fraction of nanofiller (%)		Araldite and nanofiller Viscosity (Pa. s)
Araldite and nanofiller	Araldite, nanofiller and hardener	Araldite and nanofiller	Araldite, nanofiller and hardener	
Hexagonal Boron Nitride				
0	**0**	**0**	**0**	**7.17**
0.98	0.5	0.51	0.26	5.18
2.02	1.03	1.05	0.55	6.15
2.98	1.53	1.56	0.81	6.79
3.96	**2.04**	**2.08**	**1.09**	**7.17**
4.9	**2.53**	**2.59**	**1.35**	**7.17**
5.92	3.08	3.14	1.65	8.3
6.96	3.64	3.72	1.96	8.03
8.02	4.22	4.3	2.27	9.01
Carbon nanospheres				
0.21	**0.11**	**0.7**	**0.33**	**5.9**
0.53	0.29	1.84	0.84	8.32
1	0.53	3.34	1.57	4.33
1.81	0.95	5.71	2.78	6.49

[a] Note 0 % refers to pure epoxy.

This work expands further on BN/Epoxy analysis and extended to C/Epoxy. Note that the numbers in the legend in Figure 8 refer to the volume fraction of nanoparticle in Araldite, and final nanodielectric, obtained from Table 2. From Figure 8, Figure 9 and [22], the first observation to note is that the Araldite is non-Newtonian in nature and the composite shows a slight rise in viscosity until a shear rate of ~100 s^{-1} followed by a slight decrease in viscosity until the yield point is met. After this yield point all materials show a large decrease in viscosity.

Given that the Araldite general "shape" profile of viscosity vs shear rate does not change, but moves up/down in viscosity for different loading levels of BN/Araldite and C/Araldite, the viscosity was normalised to 100 s^{-1} indicated by the line in Figure 8 (A) - (D). The data are summarised in Figure 9 (A) for BN/Araldite and (B) for C/Araldite with the Viscosity measurements given in Table 2. Figure 9 also shows the other normalised rheology results for the different times used for the Araldite-nanoparticle mixtures.

From Figure 9, the different possible suspension situations presented by Ancey [21] are evident. Generally, for both C/Araldite and BN/Araldite, initially, a steep decrease in viscosity is seen which indicates a Brownian motion region, which is then followed by a hydrodynamic/colloidal interaction region. For the h-BN, given that the density of the particles (2.25 g/cm^3) is double that of Araldite (1,18 g/cm^3), any agglomerates present appear to sediment and the viscosity within the hydrodynamic region (1-2%) appears to be faster (lower viscosity) for the rheology for BN/Araldite after one and two hours.

Increasing the concentration of the particles brings the Araldite-nanoparticle mixture into the colloidal interaction

region which causes particles to be attracted to each other and overcome the viscous drag of the Araldite with their van der Waals forces and agglomerate. The viscosity increases until the agglomerates are sufficiently large to begin turbulence effects. In the turbulent effect region, the viscosity decreases until the point where particles are in sufficient contact that a slurry is formed and the bulk viscosity increases again.

The general shape of the rheology results shown in Figure 9 is similar to that of glass transition temperature variation with loading presented by Shengtao Li *et al.* [26] and is in agreement with the theory presented by Ancey [21]. The behaviour is also in agreement with the theoretical model for bulk properties of nanocomposite materials as presented by Praeger *et al.* in [8].

A key conclusion from the rheology analysis is the postulation that the samples with optimal dispersion are points within the hydrodynamic/colloidal interaction regions. In the present case, it would be 2.08/1.09 vol% and 2.59/1.35 vol% in BN/Araldite, and 0.7/0.33 % in C/Araldite (viscosity results bold in Table 2).

Once the rheology analysis is completed the hardener is added in a 100:92 ratio of nanoparticle-Araldite mixture to hardener in accordance with the manufacturer data sheet. This final mixture is sheared again at 5000 rpm for 10 min and then placed in a vacuum chamber to extract air bubbles for 3 h. After degassing, the nanocomposite is poured into preheated (curing temperature) aluminium moulds, and placed in a vacuum oven at 140 ^{o}C to cure for 16 h. The samples are then left to cool to room temperature and left for 5 h before being removed from the oven and moulds. The fabricated samples are then subjected to various tests; in this study the focus was on AFM data and dielectric spectroscopy.

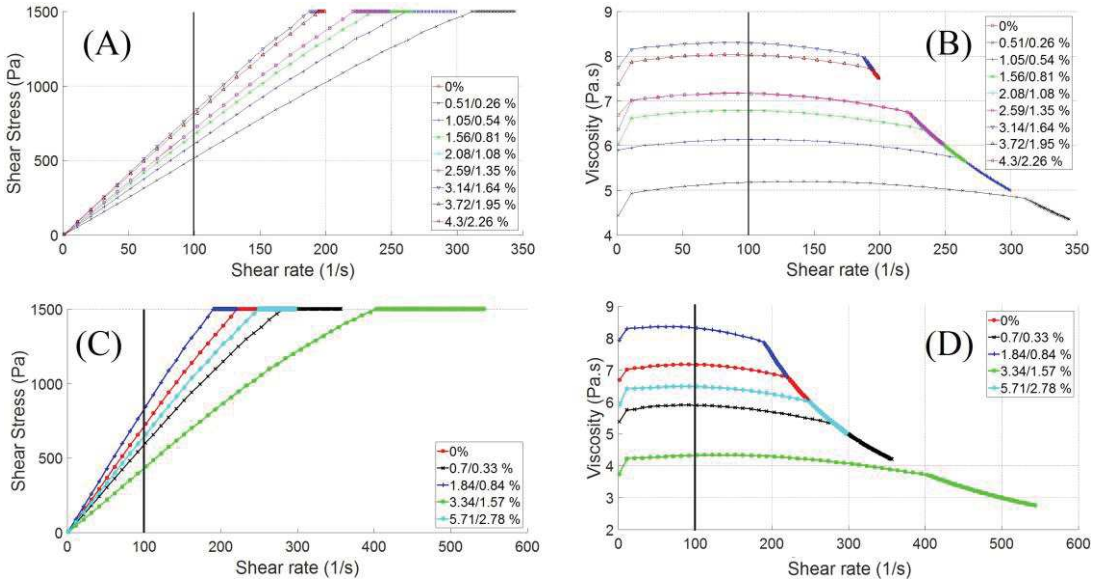

Figure 8: Raw rheology results for the different volume fractions for BN/Araldite in (A) and with Viscosity in (B), the C/Araldite in (C) with the C/Araldite Viscosity in (D).

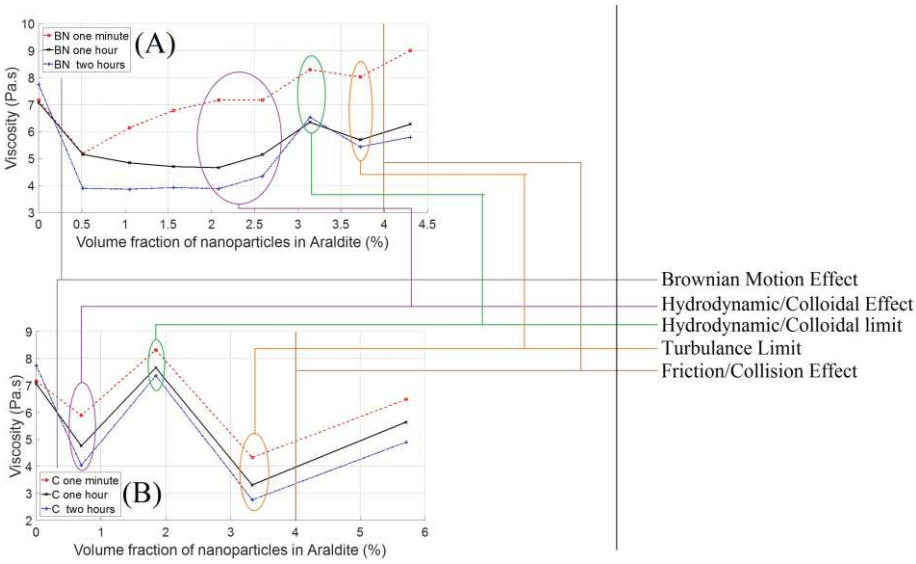

Figure 9: Rheology results showing the normalised rheology results at a shear rate of 100/s and different rheology regions with the BN/Araldite results in (A) and the C/Araldite results in (B).

4. INTERPHASE CHARACTERISATION USING ATOMIC FORCE MICROSCOPY (AFM) TECHNIQUE

AFM is a surface analysis technique like SEM or TEM, but the major benefit is that it does not require a vacuum chamber to perform the analysis. Previous work [2], and [16] on nanocomposites has shown both the presence of the interphase and how AFM can be used to identify agglomerates. The interphase or interaction zone around particles is currently understood as a region around a particle which has properties which are different from both the particle and host matrix [2], and [16]. Peak Force Quantitative Nanomechanical Mapping (PF-QNM) is a relatively innovative technique in AFM analysis. PF-QNM is used to characterise the mechanical properties such as elastic modulus, surface adhesion, and dissipation energy of a material surface in the nanometre scale.

The principle of application is shown in Figure 10 and A Bruker Mode 8 was used to carry out the PF-QNM analysis. The traditional AFM analysis has been explained extensively by [2], and [16].

As illustrated in Figure 10, in the PF-QNM mode, the force as a function of tip-sample separation (force volume curve) is recorded and the Derjaguin, Muller and Toporov model (DMT) Young's modulus, adhesion force and dissipation energy can be extracted in real time [27], [28].

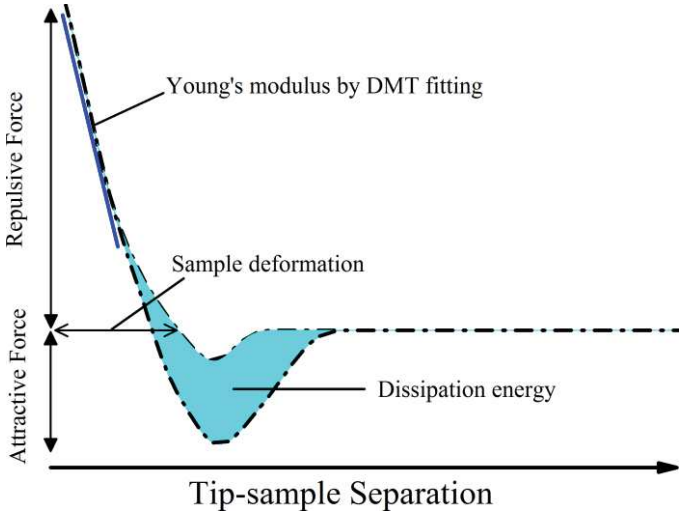

Figure 10: Schematic diagram of the force-separation feedback loop used to determine the PF-QNM

4.1 MEASUREMENT RESULTS AND ANALYSIS

While all the samples were analysed using AFM, the samples of focus were the 1.09 vol% BN/Epoxy and 0.33 % C/Epoxy as they had been deemed optimal through the rheology and electrical treeing tests. The Young's modulus and height results of the base epoxy and the nanocomposites are summarised in Table 3 and the corresponding images presented in Figures 11 – 13. Three tests were performed, the first involved applying a force of 600 nN to characterise the sample surface. The results of the surface characterisation are shown in Figures 11 – 13.

From the surface tests, areas of interest in the nanodielectric are identified such as individual particles and chains in the case of C/epoxy and an individual particle in BN/epoxy. These areas of interest are analysed for Young's modulus of the surface and the results of the different sections are shown in Figure 12 and Figure 13 and summarised in Table 4.

It is difficult to gauge the exact location of the particles since the particles are embedded inside the epoxy, so the force applied is increased in steps of 100 nN from 600 nN to 1000 nN for C/Epoxy and only until 700 nN for BN/Epoxy because beyond 700 nN the AFM cantilever breaks. The results of the force evolution are shown in Figure 14 and Figure 15 and the average Young's moduli from the force evolution is summarised in Table 5.

Table 3: AFM properties of Epoxy and Nanocomposites.

	Average Young's modulus (GPa)	Particle Young's modulus (GPa)	Surface Roughness (nm)
Epoxy	1.7	N/A	3.4
C/Epoxy	4.9	7.5	6.3
BN/Epoxy	34.9	56.8	3.24

Table 4: C/epoxy and BN/epoxy particle and interphase dimensions.

Section	Particle size (nm)	Interphase left (nm)	Interphase right (nm)
C/epoxy AB	40	50	80
C/epoxy CD	80	114	64
C/epoxy EF	80	12.7	99
C/epoxy EF	100	99	31
C/epoxy EF	80	31	92
BN/epoxy AB	70	124	153
BN/epoxy CD	70	135	124

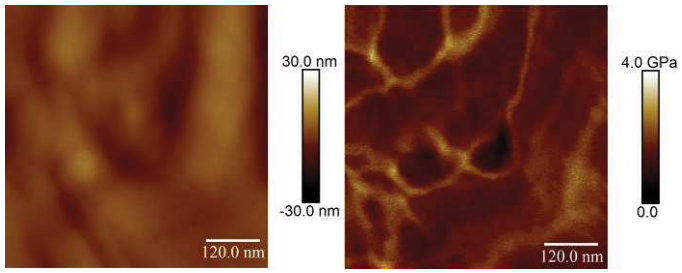

Figure 11: PF-QNM Analysis at 600 nN on pure epoxy, surface height (left) and mechanical properties (right).

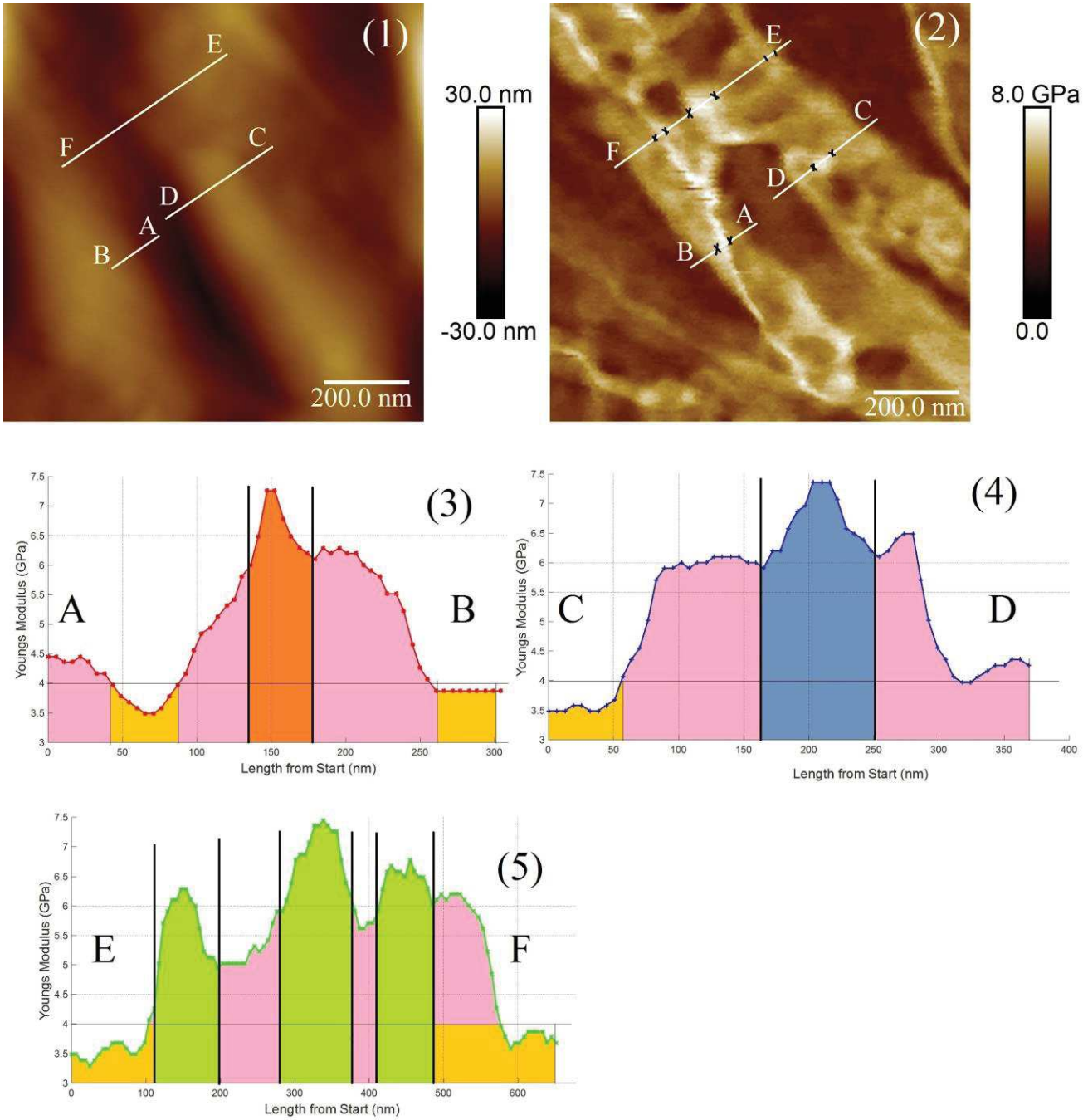

Figure 12: PF-QNM Analysis at 600 nN on C/epoxy, surface height (1) and Young's modulus image (2), the lines of interest for section AB (3) showing mechanical properties, section BC (4) showing mechanical properties and section EF in (5) showing mechanical properties.

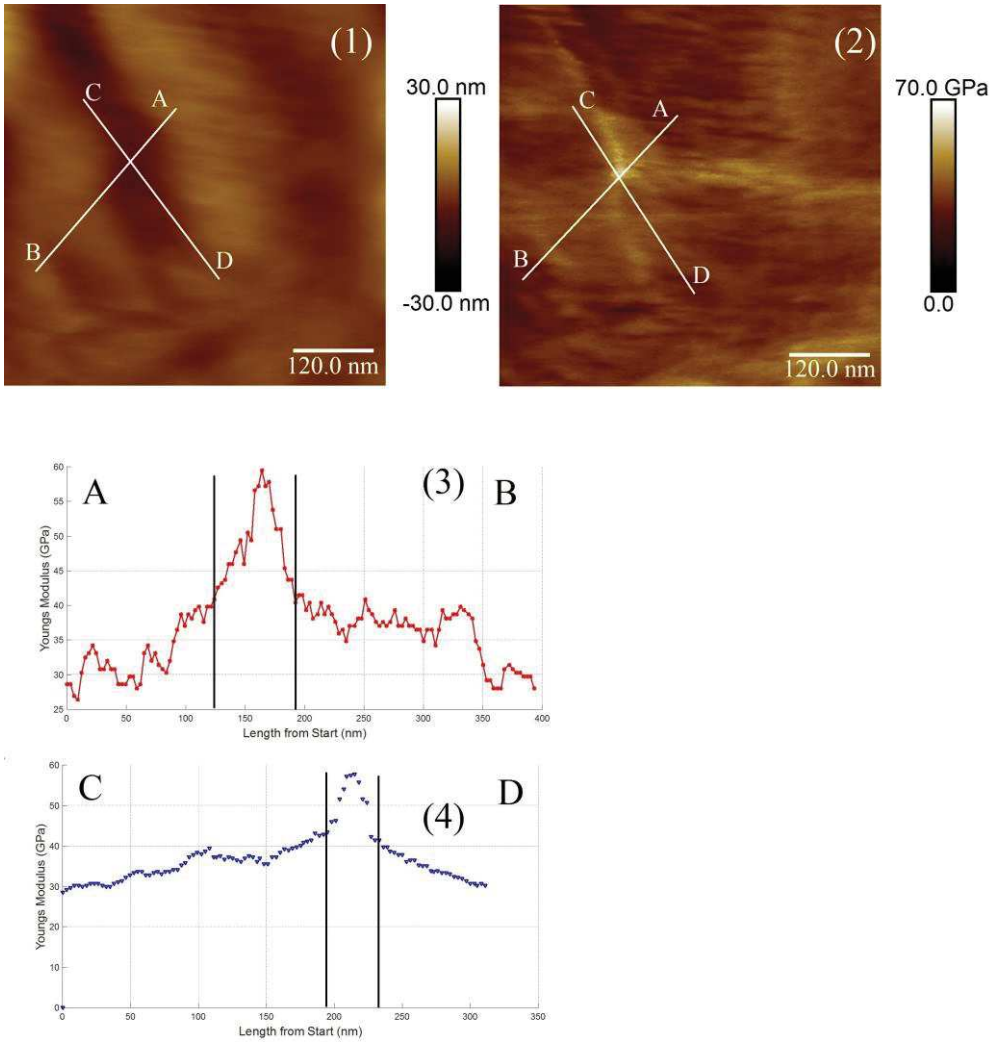

Figure 13: PF-QNM Analysis at 600 nN on BN/epoxy, surface height (1) and Young's modulus image (2), the lines of interest for section AB (3) showing mechanical properties, and section BC (4) showing mechanical properties.

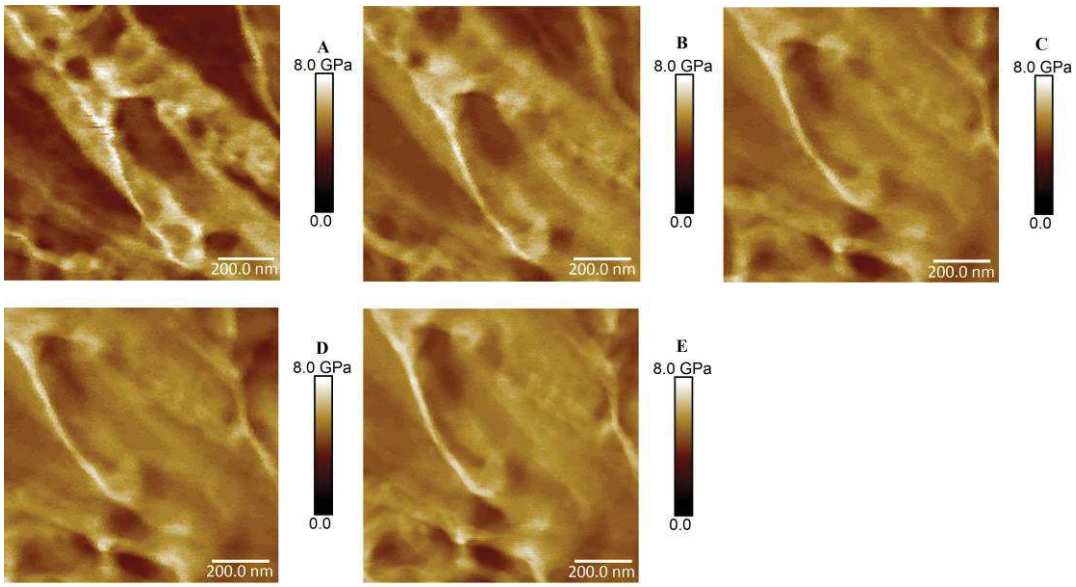

Figure 14: Surface Young's modulus evolution profile of C/Epoxy with the set points at 600 nN (A), 700 nN (B), 800 nN (C), 900 nN (D) and 1 000 nN (E), respectively.

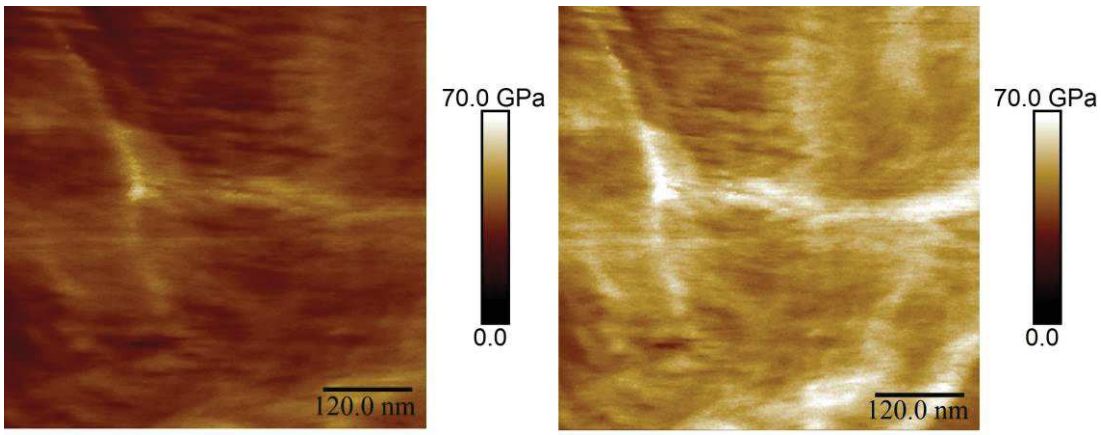

Figure 15: Surface Young's modulus evolution profile of BN/Epoxy with the set points at 600 nN (left) and 700 nN (right).

Table 5: Average Young's modulus results of C/Epoxy and BN/Epoxy for different applied forces.

Force Applied (nN)	Average Surface Young's Modulus (GPa)
C/Epoxy	
600	4.905
700	5.034
800	5.712
900	5.905
1000	5.905
BN/Epoxy	
600	34.951
700	44.589

It is evident that small additions of nanoparticles enhance the average mechanical properties of Epoxy as shown in Table 3. Figure 11 shows that the Young's modulus for epoxy ranges from 1 GPa to 3.5 GPa with an average Young's modulus of 1.7 GPa. This is in agreement with Young's modulus reported in the material data sheet [29]. It is also evident that epoxy has "grain boundaries" that could be oriented from the cross-linking process.

From Figure 12 (1), in the height image, the surface does not show the presence of nanoparticles. The Young's modulus image in Figure 12 (2) shows the Young's modulus of the C/Epoxy composite. The brightest areas show the presence of nanoparticles while the darkest areas are the pure epoxy. From the Young's moduli profiles, the size of nanoparticles, interphase and matrix can be determined for different sections and are shown in Figure 12 (3) - (5) and summarised in Table 4. Smaller carbon nanoballs form nano-chains as evident in Figure 2 and these appear as well in Figure 12 (2).

The BN particle present in Figure 13 (1) shows a Young's modulus significantly higher than that of CNS with 56.8 GPa vs 7.5 GPa. By applying various set point forces, the evolution of the Young's modulus mapping of the surface is shown in Figure 14, Figure 15 and Table 3, it is demonstrated that the bulk Young's modulus approaches that of the interphase regions shown in Figure 12 (3) – (5) and Figure 13 (2) and (3). A summary of the particle and interphase dimensions obtained from Figure 12 (3) – (5) and Figure 13 (2) and (3) is provided in Table 4.

As described by [2], and [16], the interphase is a material which is different to both the particle and host matrix. As mentioned earlier, Table 3 shows that the average epoxy DMT Young's modulus is 1.7 GPa, however, there were regions shown in Figure 11 which reach 3.5 GPa. It was assumed that any material in the nanodielectrics which were above ~4 GPa would be either particle or interphase. It was further assumed that the nano filler would be significantly different than the epoxy. From Figure 12, C/Epoxy an 80 nm carbon nanosphere (indicated by the highest DMT Young's modulus ~7.5 GPa) shows an interphase (higher than 4 GPa and lower than 7 GPa) which can vary from ~10 nm to ~90 nm based on the influence of other particles. A 40 nm particle as part of an accreted nanoline shows an interphase of 50 nm (left) and 80 nm right in Figure 13 (A). In Figure 13 (2) and (3) the BN nanoparticle of ~70 nm has an interphase of ~130 nm. It is evident that the interphase is dependent on particle shape, particle size and particle type. Figure 12 (5) shows that overlapping interphases between two particles and close together would be higher than that of particles further apart.

5. DIELECTRIC SPECTROSCOPY OF C/EPOXY

Relative permittivity is a measure of the polarizability of a material obtained by using frequency and/or temperature [15]. One method of obtaining permittivity is through dielectric spectroscopy (DS) [15]. Through DS, the dynamics of molecular motion of a complex material and the resultant characterisation of bulk properties can be evaluated [30]. The permittivity behaviour of a material as a function of frequency is shown in Figure 16. Each frequency region reveals a different mechanism which influences the permittivity. Frequency ranges less than 100 MHz are important regions for electrical insulation engineering [14]. In the present study, the 40Hz – 10 MHz of the C/epoxy samples were investigated and this region is dominated by dipolar polarisation mechanisms [15].

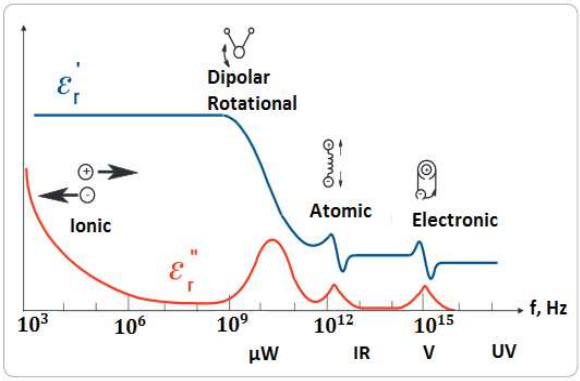

Figure 16: Frequency response of dielectric mechanisms in different regions (adapted from [31]).

$$\varepsilon^* = \varepsilon' - j\varepsilon'' \quad (1)$$.

$$\varepsilon' = \frac{t \cdot \sin\theta}{\varepsilon_0 \cdot A \cdot \omega \cdot |Z|} \quad (2)$$

$$\varepsilon'' = \frac{t \cdot \cos\theta}{\varepsilon_o \cdot A \cdot \omega \cdot |Z|} \quad (3)$$

Where:

- ε' = the real part of the complex permittivity, which represents the relative permittivity that measures the amount of polarisation [15].
- ε'' = the imaginary part of the complex permittivity which represents the dielectric loss of a material, or the losses that are encountered during the polarisation processes [15].
- t = the thickness of the sample [mm]
- A = the area of the samples [mm²]
- ω = the angular frequency [$2\pi f$]

The dipolar polarisation mechanism describes how permanent and induced dipoles orient themselves in response to a changing electric field [32]. The final fabricated samples had a diameter of 36 mm and thickness of 1 mm suitable for use with an Agilent impedance analyser 4249A with the 16451B test fixture and a test voltage of 500 mV. A total of three samples were analysed using DS. A schematic diagram of the DS experimental setup is shown in Figure 17.

The samples were first cleaned with ethanol to remove any trapped residues and were kept under vacuum evacuation 3 h prior to the measurement. It was assumed that 3 h was sufficient to remove any trapped air moisture. The samples were coated with silver paint (colloidal silver) to achieve good contact between the electrodes of the test fixture [32]. The silver paint also minimised air gap errors possibly introduced by sample surface unevenness.

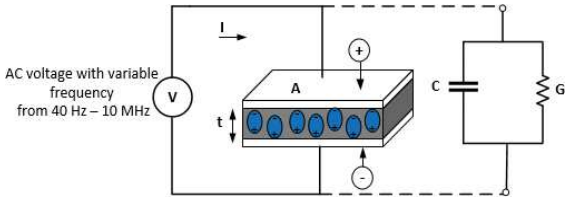

Figure 17: AC powered, parallel plate capacitor model of the dielectric spectroscopy measurement method adapted from [34].

The measurements were done at ~25 ºC ambient temperature. Each sample set was sandwiched between the electrodes of the test fixture, and connected to the impedance analyser. By measuring the complex impedance of the circuit, as a function of frequency, the real and imaginary parts of the complex permittivity were determined. These are shown in equation (1) (derived from equations (2) and (3)). The obtained results were then plotted as a frequency response and the results are presented in Figure 18 to 20 and table 6 and 7.

4.1 MEASUREMENT RESULTS AND ANALYSIS

The real and imaginary components of the complex permittivity and the conductivity were investigated in the frequency range of 40 Hz–10 MHz and dipoles are created in this range within a dielectric under an externally applied electric field. Figure 18 shows the real part of the permittivity which decreases with increasing frequency for all samples. Figure 19 shows the imaginary part of the corresponding permittivity.

At low frequencies, the dipoles are able to keep up with the frequency and this results in higher polarisation. As the frequency increases polarisation then lags behind the electric field. This causes the reorientation of the dipoles to be opposed by internal friction, which generates heat and hence energy loss. The increase in loss is manifested as an increase in imaginary permittivity as a function of frequency as shown in Figure 19. A further increase in the applied electric field reaches a point where polarisation no longer occurs and this is termed the β-relaxation peak [31], this is seen at around 1 MHz in both the real and imaginary parts of the complex permittivity (Figure 18 and Figure 19).

The unfilled epoxy sample results as shown in Table 6 and Table 7 and are comparable to data observed previously by Kochetov et. al. [25] for the same epoxy. The complex permittivity values at low filler loadings highlighted in Table 6 and 7 are marginally lower than pure epoxy. The hindrance of polymer chains due to the presence of CNS results in lower permittivity as the degree of dipole orientation is reduced [35].

From Figure 18, Figure 19, Table 6 and 7; it is noted that permittivity of 0.84 vol% is slightly greater than that of pure epoxy. This can be explained by considering the percolation effects. The effects are noticeable in the 0.84, 1.57 and 2.78 vol% shown in Figure 18 and 19, where values of real and imaginary permittivity and are higher than that of pure epoxy. For higher filler loading samples, both the real and imaginary permittivity decrease with increase with frequency.

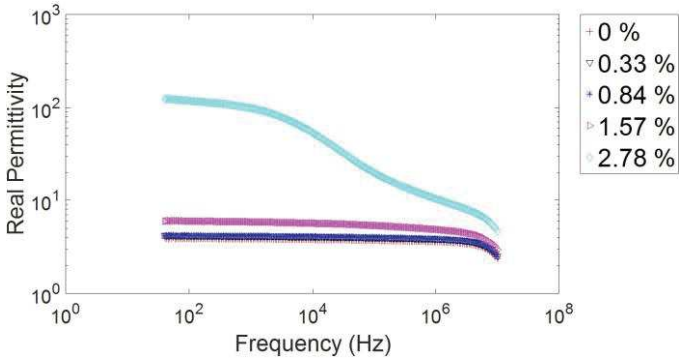

Figure 18: Frequency spectrum of the real part of the complex permittivity in C/epoxy nanodielectrics.

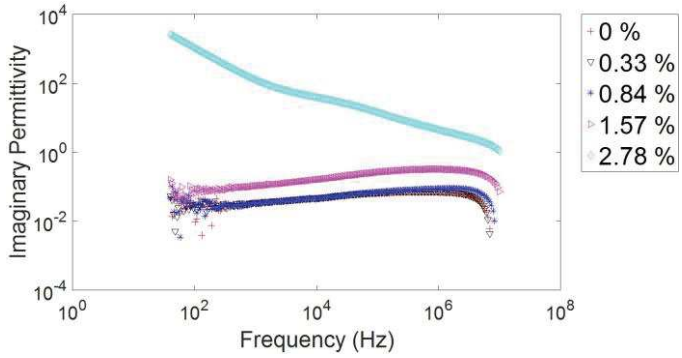

Figure 19: Frequency spectrum of the imaginary part of complex permittivity in C/epoxy nanodielectrics.

Table 6: Real part of complex permittivity values at different frequencies.

Vol%	40 Hz	1 kHz	0.1 MHz	1 MHz
0	**3.95**	**4.25**	**4.11**	**3.97**
0.33	**3.91**	**4.09**	**3.96**	**3.84**
0.84	4.14	4.14	4.03	3.90
1.57	5.98	6.17	5.50	4.90
2.78	88.4	98.39	19.89	10.35

Table 7: Imaginary part of complex permittivity values at different frequencies.

Vol%	40 Hz	1 kHz	0.1 MHz	1 MHz
0	**0.05**	**0.04**	**0.07**	**0.07**
0.33	**0.011**	**0.03**	**0.07**	**0.09**
0.84	0.046	0.03	0.07	0.09
1.57	0.163	0.12	0.35	0.41
2.78	130.1	125.1	14.31	4.56

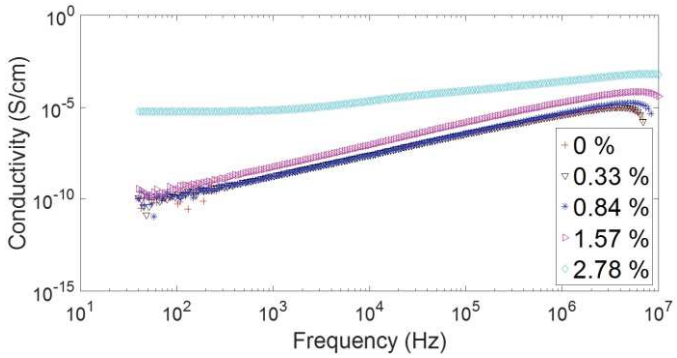

Figure 20: Frequency spectrum of the electrical conductivity in C/epoxy nanodielectrics.

According to Chung et. al. [36] the relative permittivity of carbon black at 100 kHz is ~100 which is significantly higher than pure epoxy ~3. The increased number of CNS particles results in the overlapping of the interphases, according to [15], and [37], and carbon permittivity then becomes prevalent [8, 16]. The inter-particle distance between the nanoparticles decreases with the increase in filler loading. The charge carriers, therefore, are able to move more freely between nanoparticles. With reference to Figure 20 was plotted from equation (4). At low frequencies, the higher loaded samples have conductivities which are five orders of magnitude greater than pure epoxy. As expected, the same increase was found for data collected on samples with lower filler loadings. As the frequency increases, the pure epoxy and lower filler loadings become increasingly conductive and approaches that of heavily loaded samples.

$$\sigma = \varepsilon'' \cdot \omega \cdot \varepsilon_0 \qquad (4) \ .$$

6. DISCUSSION

There are six models used to describe the behaviour of nanodielectrics [5, 8, 17–19]. As the models have been developed and further investigations were obtained, these models were further refined to incorporate current understanding. The first model, the intensity model, is based on colloidal chemistry; essentially it postulates that the interphase is a function of surface chemistry around the particles. The multi-core model describes how by surface conditioning the particles, the properties of the interphase are three distinct regions.

The polymer chain model claims that the interphase is a result of surface conditioning causing the polymer chains around the particles to be more ordered. The new barrier model generalises the first three models by looking at how the work energy function of the interphase changes the material properties around the particles. The volume model ignored the properties of the interphase, assumes that it is present, and describes the mathematics of how particles would be ordered in this situation. The simple bulk model builds on the volume model and simulations to explain what would be observed at bulk properties of the nanodielectrics.

Currently, all work into the modelling have been based on

ceramic (metal oxides, boron nitride and clay) nanoparticles and have not investigated conductive particles as candidates. The findings presented in this paper are consistent with all the models except the multi-core, polymer chain model and new barrier model. This validity is because the CNS nanoparticles used were not surface conditioned.

Based on the nanodielectric synthesis, and the results obtained from the dielectric spectroscopy, the effect of humidity, agglomerates and polarisation impedance at low frequencies must be considered. Firstly, other work has shown that nanoparticles have a tendency to absorb water molecules on the surface, irrespective of the type of nano-filler. Therefore, the final nanodielectric would possibly have increased values of permittivity. However, the samples were exposed to the same conditions, and therefore any differences in the dielectric properties would be attributed to the different loading levels and not moisture.

One could argue that the presence of agglomerates would be high in the materials analysed due to not using surface conditioning. Although agglomerates may be present in optimally loaded nanodielectrics, the results of this paper show that the agglomerates may not necessarily negatively impact the overall performance of the nanodielectric. But, in high concentration samples, the agglomerates only impact if the percolation threshold has been exceeded.

7. CONCLUSION

In this paper, it has been demonstrated that it is possible to use carbon nanospheres in fabricating carbon/epoxy nanodielectric material. Rheology was used to characterise the different Araldite-nanoparticles concentration stages and highlight the hydrodynamic/colloidal interaction regions as possible optimal loading conditions. AFM tests were used to dimension the interphase regions around the particles. The key findings are summarised as follows:

i. The rheology of nanoparticles in epoxy follows rheology characteristics of non-Newtonian liquids. The different regions on the rheology curves based on concentration have been identified.
ii. The optimal loading level of 2.08/1.09 vol% for BN/Epoxy and 0.7/0.33 % for C/Epoxy was found using rheology and analysed using AFM analysis.
iii. Using the Young's modulus as a measurement parameter in the AFM analysis of the nanodielectrics, the interphase region around each particle was determined. Furthermore, The Young's modulus of the interphase region was found to be significantly different from both the host matrix and the nanoparticle.
iv. The interphase appears to be dependent on nanoparticle type, shape and size. And the bulk material Young's modulus approaches that of the interphase.
v. The percolation threshold for C/Epoxy was determined to be 0.89 vol%, and below it, the permittivity is lower than pure epoxy, but the permittivity approaches conductive properties as the frequency increases.
vi. Above the percolation threshold, the permittivity increases by five orders of magnitude compared to pure epoxy and lower filler loadings.
vii. The results are consistent with models previously reported, however, the models proposed which rely on the interphase being results of surface conditioning are questioned.

In the second paper, distinct time-evolution trends of electrical tree partial discharges (PDs) magnitude follow distinct time-evolution trends in the C/epoxy and BN/epoxy.

ACKNOWLEDGMENTS

The authors would like to acknowledge Erasmus Mundus for the INSPIRE scholarship which enabled one of the authors to travel to Uppsala Sweden and form collaborative ties. In South Africa, Eskom and the National Research Foundation (NRF) are gratefully acknowledged for their continued support of the high voltage engineering research work at the University of the Witwatersrand, Johannesburg. The DST-NRF Centre of Excellence in Strong Materials is thanked for funding and equipment.

REFERENCES

[1] T. Kashiwagi *et al.*, "Relationship between dispersion metric and properties of PMMA/SWNT nanocomposites," *Polymer*, vol. 48, no. 16, pp. 4855–4866, Jul. 2007.

[2] M. Roy, J. K. Nelson, R. K. MacCrone, L. S. Schadler, C. W. Reed, and R. Keefe, "Polymer nanocomposite dielectrics-the role of the interface," *IEEE Transactions on Dielectrics and Electrical Insulation*, vol. 12, no. 4, pp. 629–643, Aug. 2005.

[3] C. W. Reed, "Polymer Nanodielectrics - Basic Concepts," *IEEE Electrical Insulation Magazine*, vol. 29, no. 6, pp. 12–15.

[4] D. Fabiani, E. A. Cherney, I. R. Vazquez, and T. Andritsch, "IEEE CEIDP 2012 Workshop on Nanodielectrics," 2012.

[5] C. Calebrese, L. Hui, L. S. Schadler, and J. K. Nelson, "A review on the importance of nanocomposite processing to enhance electrical insulation," *IEEE Transactions on Dielectrics and Electrical Insulation*, vol. 18, no. 4, pp. 938–945, Aug. 2011.

[6] R. Schurch, S. M. Rowland, R. S. Bradley, and P. J. Withers, "Imaging and analysis techniques for electrical trees using X-ray computed tomography," *IEEE Transactions on Dielectrics and Electrical Insulation*, vol. 21, no. 1, pp. 53–63, Feb. 2014.

[7] R. K. I. A. Tsekmes, "Evaluating the effect of particle distribution and dispersion on the dielectric response of boron nitride - epoxy nanocomposites," pp. 329–332, 2014.

[8] M. Praeger, T. Andritsch, S. G. Swingler, and A. S. Vaughan, "A simple theoretical model for the bulk properties of nanocomposite materials," in *2014 IEEE Conference on Electrical Insulation and Dielectric Phenomena (CEIDP)*, 2014, pp. 699–702.

[9] E. A. Cherney, "Nanodielectrics Applications - Today and Tomorrow," *IEEE Electrical Insulation Magazine*, vol. 29, no. 6, pp. 59–65, Nov. 2013.

[10] I. A. Tsekmes, R. Kochetov, P. H. F. Morshuis, and J. J. Smit, "Measuring and modeling the thermal conductivity of epoxy - Boron nitride nanocomposites," in *Proceedings of 2014 International Symposium on Electrical Insulating Materials (ISEIM)*, 2014, pp. 26–29.

[11] A. A. Deshmukh, S. D. Mhlanga, and N. J. Coville, "Carbon spheres," *Materials Science and Engineering: R: Reports*, vol. 70, no. 1–2, pp. 1–28, Sep. 2010.

[12] T. V. Kosmidou, A. S. Vatalis, C. G. Delides, E. Logakis, P. Pissis, and G. C. Papanicolaou, "Structural, mechanical and electrical characterization of epoxy-amine/carbon black nanocomposites," *Express Polymer Letters*, vol. 2, no. 5, pp. 364–372, 2008.

[13] M. Jarvid *et al.*, "A New Application Area for Fullerenes: Voltage Stabilizers for Power Cable Insulation," *Adv. Mater.*, vol. 27, no. 5, pp. 897–902, Feb. 2015.

[14] I. Pleşa, P. V. Noţingher, S. Schlögl, C. Sumereder, and M. Muhr, "Properties of Polymer Composites Used in High-Voltage Applications," *Polymers*, vol. 8, no. 5, p. 173, Apr. 2016.

[15] R. Kochetov, *Thermal and Electrical Properties of Nanocomposites, Including Material Processing*. 2012.

[16] S. Raetzke and J. Kindersberger, "Role of interphase on the resistance to high-voltage arcing, on tracking and erosion of silicone/SiO2 nanocomposites," *IEEE Transactions on Dielectrics and Electrical Insulation*, vol. 17, no. 2, pp. 607–614, Apr. 2010.

[17] M. Fréchette *et al.*, "Polymer composites with a large nanofiller content: a case study involving epoxy," *IEEE Transactions on Dielectrics and Electrical Insulation*, vol. 21, no. 2, pp. 434–443, Apr. 2014.

[18] S. C. Ray, Z. N. Tetana, R. Erasmus, A. Mathur, and N. J. Coville, "Carbon spheres for energy applications: Raman and X-ray photoemission spectroscopy studies: Bonding configuration of carbon sphere," *International Journal of Energy Research*, vol. 38, no. 4, pp. 444–451, Mar. 2014.

[19] L. L. Schramm, *Emulsions, Foams, and Suspensions: Fundamentals and Applications*, 1 edition. Weinheim: Wiley-VCH, 2005.

[20] F. A. Morrison, *Understanding Rheology*. OUP USA Topics in Chemical Engineering, 2001.

[21] C. Ancey, "Plasticity and geophysical flows: A review," *Journal of Non-Newtonian Fluid Mechanics*, vol. 142, no. 1–3, pp. 4–35, Mar. 2007.

[22] A. M. Hank, D. R. Cornish, C. Nyamupangadengu, and I. Sigalas, "Quantifying Nanoparticle Dispersion Using Rheological Techniques in Epoxy Resin," in *ISH 2015*, Pilsen, Czech Republic, 2016.

[23] M. Reading and A. Vaughan, "Rheological, Thermal and Electrical Properties of Poly(Ethylene Oxide)/Silicon Dioxide Microcomposites," in *16th International Symposium on High Voltage Engineering (ISH)*, Cape Town, South Africa, 2009.

[24] C. Green and A. Vaughan, "Nanodielectrics - How Much Do We Really Understand? [Feature Article]," *IEEE Electrical Insulation Magazine*, vol. 24, no. 4, pp. 6–16, Jul. 2008.

[25] R. Kochetov, T. Andritsch, U. Lafont, P. H. F. Morshuis, and J. J. Smit, "Thermal conductivity of nano-filled epoxy systems," in *IEEE Conference on Electrical Insulation and Dielectric Phenomena, 2009. CEIDP '09*, 2009, pp. 658–661.

[26] S. Li, G. Yin, S. Bai, and J. Li, "A new potential barrier model in epoxy resin nanodielectrics," *IEEE Transactions on Dielectrics and Electrical Insulation*, vol. 18, no. 5, pp. 1535–1543, Oct. 2011.

[27] Y. Cai, H. Li, M. Karlsson, K. Leifer, H. Engqvist, and W. Xia, "Biomineralization on single crystalline rutile: the modulated growth of hydroxyapatite by fibronectin in a simulated body fluid," *RSC Adv.*, vol. 6, no. 42, pp. 35507–35516, Apr. 2016.

[28] E. T. Herruzo, A. P. Perrino, and R. Garcia, "Fast nanomechanical spectroscopy of soft matter," *Nature Communications*, vol. 5, Jan. 2014.

[29] Huntsman, "Technical Datasheet Araldite Casting Resin System (Cy 231-1 CH/Aradur Hy 925)." Huntsman Advanced Materials Electrical Insulation Materials, Jul-2011.

[30] R. Kochetov, T. Andritsch, P. H. F. Morshuis, and J. J. Smit, "Anomalous behaviour of the dielectric spectroscopy response of nanocomposites," *IEEE Transactions on Dielectrics and Electrical Insulation*, vol. 19, no. 1, pp. 107–117, Feb. 2012.

[31] Agilent Technologies, *Agilent Impedance Measurement Handbook: A guide to measurement technology and techniques*, Fourth. .

[32] S. Singha and M. J. Thomas, "Dielectric properties of epoxy nanocomposites," *IEEE Transactions on Dielectrics and Electrical Insulation*, vol. 15, no. 1, pp. 12–23, Feb. 2008.

[33] Haddad M. and Warne D., *Advances in High Voltage Engineering*. Stevenage, Herfordshire, GBR: The Institution of Engineering and Technology, 2004.

[34] Agilent Technologies, "Agilent Basics of Measuring the Dielectric Properties of Materials." Agilent Technologies.

[35] S. Singha and M. J. Thomas, "Permittivity and tan delta characteristics of epoxy nanocomposites in the frequency range of 1 MHz-1 GHz," *IEEE Transactions on Dielectrics and Electrical Insulation*, vol. 15, no. 1, pp. 2–11, Feb. 2008.

[36] K. T. Chung, A. Sabo, and A. P. Pica, "Electrical permittivity and conductivity of carbon black-polyvinyl chloride composites," *Journal of Applied Physics*, vol. 53, no. 10, pp. 6867–6879, Oct. 1982.

[37] S. Raetzke and J. Kindersberger, "Role of interphase on the resistance to high-voltage arcing, on tracking and erosion of silicone/SiO_2 nanocomposites," *IEEE Transactions on Dielectrics and Electrical Insulation*, vol. 17, no. 2, pp. 607–614, Apr. 2010.

[38] T. J. Lewis, "Interfaces are the dominant feature of dielectrics at the nanometric level," *IEEE Transactions*

on Dielectrics and Electrical Insulation, vol. 11, no. 5, pp. 739–753, Oct. 2004.

[39] T. Tanaka, M. Kozako, N. Fuse, and Y. Ohki, "Proposal of a multi-core model for polymer nanocomposite dielectrics," *IEEE Transactions on Dielectrics and Electrical Insulation*, vol. 12, no. 4, pp. 669–681, Aug. 2005.



Mr Andrew M. Hank was born in Johannesburg, South Africa. He received his Bachelor in Science honours degree in Electrical Engineering from the University of the Witwatersrand in 2014. In 2015, he began his Masters Studies and was awarded the INSPIRE Scholarship to pursue research and Studies at Uppsala University in Sweden Currently he is completing his master's studies at the University of the Witwatersrand, Johannesburg. His main interests are in High Voltage, insulation systems, Nanosensors, power electronics and Lightning research.



Prof. Cuthbert Nyamupangedengu was born in Zimbabwe. He received the Bachelors honours degree in electrical engineering from the University of Zimbabwe in 1994. At the University of the Witwatersrand, Johannesburg, in 2004, he was awarded the M.Sc. Engineering (with distinction) and in 2011, the PhD. He is a lecturer at the University. Before moving to the University of the Witwatersrand, Cuthbert was an engineer in the Zimbabwe Electricity Supply Authority from 1995 to 2005 in various capacities mainly in power system planning and development. His passion is research on the diagnosis of high voltage insulation.



Prof. Iakovos Sigalas is a professor of Ceramic Science in the School of Chemical and Metallurgical Engineering at the University of the Witwatersrand, Johannesburg, and the Ceramic Materials Focus Area Coordinator of the DST-NRF Centre of Excellence in Strong Materials, South Africa.



Ms Bridget K. Mutuma was born in Kenya. She received her Bachelor's degree with honours in Analytical Chemistry from Kenyatta University in 2009. She was awarded the MSc. in Material Science and Engineering from the Kangwon National University, South Korea through the Korean Government Scholarship Program (KGSP) in 2013. Currently, she is a PhD candidate in the School of Chemistry at the University of Witwatersrand. Her research interests are carbon nanostructures synthesis and characterization, photocatalysis, organic photovoltaic devices, biosensors and chemical sensors.



Prof. Neil J. Coville is currently Emeritus Professor at the University of the Witwatersrand, Johannesburg. South Africa. He obtained his PhD at McGill University, Montreal. His current research interests include Fischer-Tropsch catalysis, synthetic routes to shaped carbon materials and the use of the carbons in catalysis, solar cells and sensors. Current studies involve the synthesis of hollow carbon spheres for use as nanoreactors.



Mr Hu Li was born in China. He received his bachelor and master degrees in Materials Science and Engineering from Shandong University in 2009 and 2012, respectively. Starting from 2012, he began his PhD study at Uppsala University, Sweden and his main research interests are graphene and related 2D materials, nanofabrication's, atomic force microscopy and gas sensing.

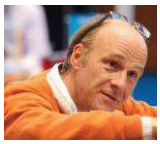

Prof. Klaus Leifer is working as a Professor of Experimental Physics at Uppsala University. His research is dedicated to Nanoanalysis, electron microscopy. His group has elaborated several materials science and device platforms based on nanoparticles, down to single molecules and 2D materials.

The criticality of filler loading in C/Epoxy and BN/Epoxy nanodielectrics Part 2: Electrical Tree PD Characteristics

A. M. Hank and C. Nyamupangedengu
School of Electrical & Information Engineering
University of the Witwatersrand, Johannesburg
P. Bag 3, Wits 2050, Johannesburg, South Africa

I. Sigalas
DST-NRF Centre of Excellence in Strong Materials,
School of Chemical and Metallurgical Engineering
University of the Witwatersrand, Johannesburg
P. Bag 3, Wits 2050, Johannesburg, South Africa

B. K. Mutuma and N. J. Coville
DST-NRF Centre of Excellence in Strong Materials and Molecular Sciences Institute,
School of Chemistry, University of the Witwatersrand, Johannesburg
P. Bag 3, Wits 2050, Johannesburg, South Africa

ABSTRACT

Further to the common practice of using metal oxides like alumina or other suitable filler material such as Boron Nitride for improved thermal performance, this work investigates the use of carbon nanospheres in bisephenol-A epoxy in comparison to BN/Epoxy. The present paper explores various electrical tree PD analysis techniques used in studying the relationship between filler loading levels and electrical treeing phenomena in C/Epoxy and BN/Epoxy nanodielectrics. The results confirm that as deduced through rheology tests (presented in part 1) 0.33 vol% for C/Epoxy and 1.09 vol% for BN/Epoxy are the optimal filler loading levels for the particle types studied in this work. On exceeding the optimal vol%, the loss of the desired behaviour of the C/epoxy and BN/epoxy nanodielectrics is remarkably discrete. X-ray Computer Tomography (XCT) analyses of the electrical trees in severely aged clean epoxy confirm the existing knowledge of electrical treeing phenomena in conventional solid insulation. In optimally filled C/Epoxy however a new explanation of the electrical treeing process is required.

Index Terms — **Carbon nanoparticles, Rheology, Interphase region, filler loading.**

1. INTRODUCTION

ELECTRICAL trees are the common ultimate failure mode of solid polymer insulation [1]. Due to enhanced localised electric stress (in the order of MV/mm), energy is transferred from the electric field into the molecular matrix and causes various physiochemical changes. These changes may be scission of molecular bonds, heat, pressure build up and various chemical processes. Degradation of the insulation ensues as tree shaped gas-filled micro-tunnels propagate by means of partial discharge (PD) activity leading to complete insulation failure [1]. Endurance to electrical tree degradation can be regarded as 'the litmus test' of the quality of solid polymer insulation. In developing advanced solid polymer insulation, such as nanodielectrics, electrical treeing tests are often used in evaluating the material engineering efforts [2].

The electrical treeing phenomena in insulation is studied by analysing various characteristics such as time-to-failure, inception stress, rate of propagation, the types of trees, or the corresponding PD signatures produced by different trees. It is well established that the growth of a tree and PDs produced, have a relationship with the nature of the micro-tunnels formed in the electrical tree.

This is the second of two papers on the development of carbon nanosphere (CNS) C/Epoxy composites in comparison with hexagonal Boron Nitride (BN) BN/Epoxy composites and pure Epoxy. In the first paper rheology techniques were used to determine the optimal filler loading levels for C/Epoxy (0.33 vol%) and for BN/Epoxy (1.09 vol%).

The interphase region around each particle was measured using Atomic Force Microscopy (AFM). The interphase varied in size from ~10 nm to ~90 nm for 80 nm carbon particles depending on the presence of other particles.

Manuscript received on X Month 2005, in final form XX Month 2005.

Comparatively, a 70 nm BN particle had an interphase of ~130 nm.

In this second paper the C/Epoxy and BN/Epoxy nanodielectrics of various loading levels were subjected to electrical tree induced degradation until complete failure. The electrical tree partial discharges were studied to establish the influence of filler loading levels on the treeing partial discharge phenomena.

Jarvid et al [3] reported a 26% increase in electrical tree initiation stress when XLPE was modified by mixing with fullerenes and forming a CBM/XLPE nanodielectric. They did not however report on how the trees evolved up to complete failure and this could be due to the assumption that once initiated, electrical trees quickly progress to failure.

In our previous work evidence was presented that the tree propagation agent (PD activity) could be suppressed for relatively long periods [4]. Additionally, there have been reports of significant delay in time-to-failure under electrical treeing degradation in nanodielectrics [5]. The initiation of electrical trees and propagation to complete bridging of the electrode gap may therefore not necessarily result in imminent failure [6]. Such a phenomenon which tends to occur in nanodielectrics needs further investigation to understand the underlying mechanisms especially with regard to how the nanoparticles influence the growth of electrical trees.

In the present paper the focus of treeing studies is on the evolution behaviour of electrical tree partial discharges in C/Epoxy and BN/Epoxy whose optimal filler loading levels have been postulated through rheology analysis. X-ray computer tomography (XCT) images of the trees, statistical analyses of the PD distribution and existing knowledge of treeing phenomena are used in interpreting the PD measurement results.

2. EXPERIMENTAL SETUP AND TEST PROCEDURES

A complete account of the test specimen's fabrication process is provided in part 1. Test samples were fabricated using X-253-1 Ogura needles (Ogura Industrial Jewel™) which have a 5 µm tip radius with a 30° run off to a maximum needle radius of 1 mm. In the casting mould the needle was held in place by means of grub screws to ensure a needle plane gap of 3 mm. An image of examples of manufactured samples is shown in Figure 1. A silver paint base was applied to ensure the sample makes good contact with electrodes. The needle coupling facility to the high voltage source was specially made so as to be corona free. The entire test sample was immersed in insulating oil to avoid spurious discharges and flashovers. The experiments are conducted in a shielded high voltage laboratory with an average noise level of 0.4 pC.

Three samples were synthesized for each full electrical tree aging test. Sets of three C/Epoxy and BN/Epoxy samples with each set being of different particle loading levels were subjected to the electrical treeing tests. Control tests were made on three identical clean epoxy samples.

The evolution of the electrical tree partial discharges was monitored using a previously reported system according to IEC 60270 with an ICMCompact™ PD measurement system [7]. A schematic diagram of the setup is shown in Figure 2.

Champion *et al.* [8] showed that for a needle-plane setup, different trees would grow in epoxy samples that depended on the electric field applied. The three main categories of electrical trees, corresponding to electric field magnitude determined from equation (1), are branch, bush-branch and branch types trees with corresponding RMS electric fields of ~0.9 MV/mm, ~1.1 MV/mm and 1.3 MV/mm respectively.

$$E_{max} = \frac{2V}{r \ln\left(1 + \frac{4d}{r}\right)} \quad (1)$$

Where:

- E_{max} is the maximum applied electric field.
- V is the applied RMS voltage in kV.
- r is the needle tip radius.
- d is the gap distance.

Champion *et al.* [8] also showed that bush trees are characterised by small micro-tunnels and relatively small PD magnitudes ~50-200 pC. Branch trees are characterised by a gradual build-up of PD activity from 10-50 pC to ~750 pC before ultimately failing.

Each sample was subjected to a 50 Hz sinusoidal linear ramp until 20 kV RMS to establish an electric field of ~1 MV/mm on the needle tip. The maximum, minimum and average apparent PD magnitudes were recorded every second from the moment of tree inception until complete failure. Concurrently the corresponding partial discharge phase-resolved-patterns (PDPRP) were recorded. Various statistical techniques were used to evaluate the PD data collected from the tests.

In electrical tree studies, microscopic imaging techniques are often useful. There is however a challenge with imaging electrical trees in nanodielectrics given that most imaging techniques require transparent samples or destructive techniques. Currently one of the only techniques to circumvent transparency problems is the use of XCT [9]. An Xradia 510 Versa X-ray microscopy computer topographer was used for the XCT analysis. Two of our samples shown in Figure 1 were evaluated by XCT. Figure 1 (a) shows the C/Epoxy sample that was maintained at a voltage for eight days without failing and (b) one of the clean epoxy samples after four hours of electrical tree aging, which was also taken for XCT analysis.

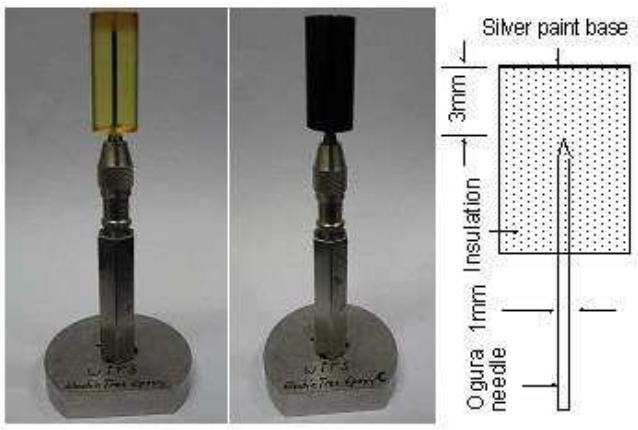

Figure 1: Examples of the clean epoxy and C/epoxy test samples; note the lack of transparency in the C/Epoxy sample.

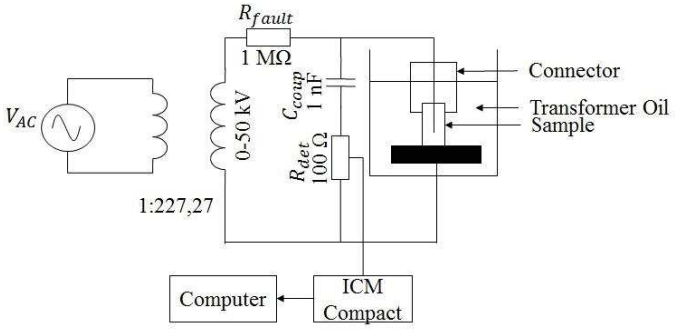

Figure 2: IEC 60270 schematic diagram of test set up used for Partial discharge analysis.

3. ELECTRICAL TREE ANALYSES

Four techniques were applied to the electrical tree PD data analyses: PD-magnitude-time evolution from start to failure, the PD-magnitude-frequency plots, PD phase-resolved pattern (PDPRP) classifications and the XCT imaging correlated with electrical field simulation results produced using FEMM.

3.1 PD TIME EVOLUTION ANALYSIS

The PD time evolution from start to failure and the distribution of PD activity according to number of discharges and magnitude of discharges for each sample set are shown in Figure 3 to Figure 10. Figure 3 shows electrical tree PD magnitudes of clean epoxy samples 1, 2 and 3. Samples 1 and 2 show predominant branch like characteristics while sample 3 shows mainly bush characteristics, and this is in agreement with the results reported by Champion et al. [8]. Figure 4 shows that there is effectively a random magnitude probability of discharges which can be present in the trees and this is characteristic of branch type trees as established by Champion et al. [8].

In clean epoxy, as shown in Figure 3, the presence of PD activity is sustained from inception to the moment of complete failure with no interspaced periods of PD evanescence.

The C/Epoxy samples showed remarkable behaviour. For C/Epoxy, the ability to achieve samples which could hold the 20 kV voltage was limited to a maximum 0.89 vol% filler loading level. All other samples could not hold a voltage of 2 kV and would fail within seconds! The C/Epoxy nanocomposite of volume fractions above 0.89 vol% performed as semiconductors. Results of C/Epoxy samples with loading levels above 0.89 vol% were therefore not analysed further.

In Figure 5 the 0.33 vol% C/Epoxy sample 2 maintained a voltage for eight days without failure, while sample 1 and 3 failed earlier. Compared to pure epoxy the overall magnitude of the PD was suppressed. The maximum in pure epoxy was in the order of ~750 pC near failure, while the discharges in C/epoxy do not exceed ~150 pC. Figure 6 shows that like pure epoxy, the distribution of PD was still branch nature but with smaller magnitudes.

Figure 7 and Figure 8 give the results of 0.89 vol% C/Epoxy which effectively performed as a semiconductor. Sample 3 (Figure 7) failed at 17 kV. For the 0.33 vol% samples (Figure 5) and 0.89 vol% (Figure 7) C/Epoxy the average PD activity is around ~50 pC. This suggests that the type of electrical trees produced in C/Epoxy is of a bush nature compared to the branch nature observed in clean epoxy.

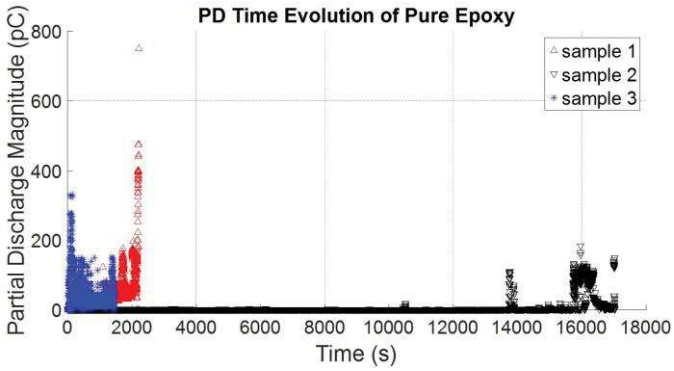

Figure 3: Complete partial discharge magnitude time evolution of pure epoxy showing bush- branch characteristics.

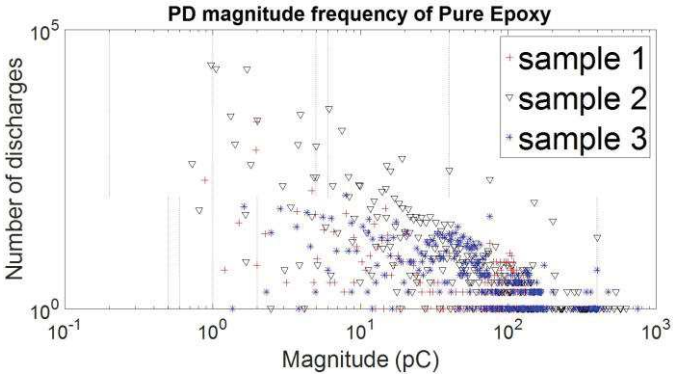

Figure 4: Log-log graph showing distribution of PD in pure epoxy.

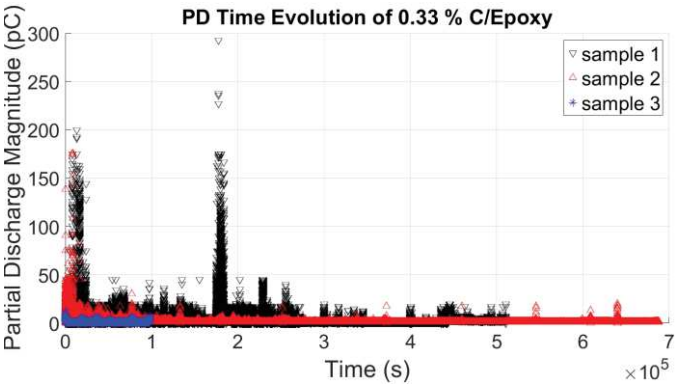

Figure 5: Complete partial discharge magnitude time evolution of C/epoxy showing bush- branch characteristics.

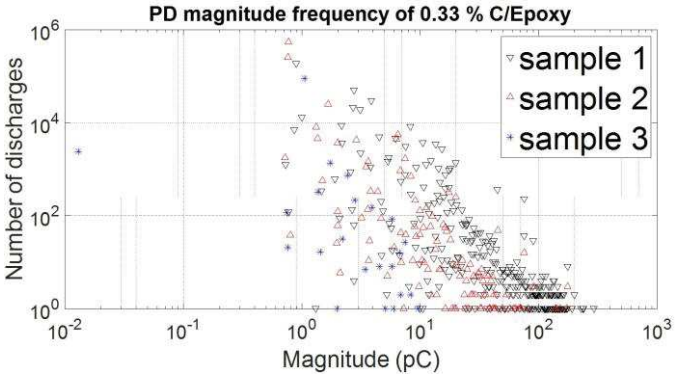

Figure 6: Log-log graph showing distribution of PD in 0.33 % C/epoxy.

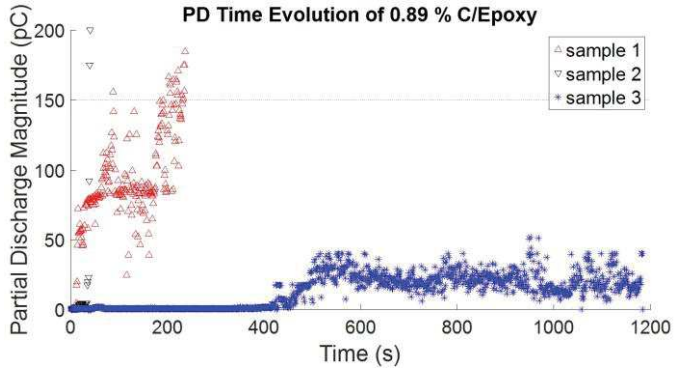

Figure 7: Complete partial discharge magnitude time evolution of C/epoxy showing semiconductor characteristics.

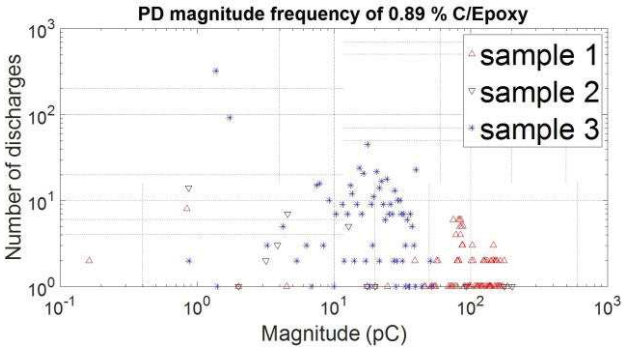

Figure 8: Log-log graph showing distribution of PD in 0.89 % C/epoxy.

Time evolution of electrical tree partial discharge magnitude plots in BN/Epoxy for various filler loadings ranging from 0.2 vol% to 2.77 vol% are presented in Figure 9. Up to and including 1.09 vol%, the PD events are generally characterised by alternative short periods of significant PD activity followed by relatively long periods of no or very little PD events. Generally, if periods of PD evanescence are long, the sample tends to take relatively long to fail. In most cases breakdown occurs during a period of high PD activity. Beyond the loading of 1.09 vol% however, the PD magnitude evolution plots no longer show the distinctive alternating periods of PD activity and periods of no PD. Instead, the PD plots exhibit no specific trends.

An alternative analysis of the PD data using log scale PD magnitude versus frequency scatter distributions is presented in Figure 10. The distributions depict a distinct profile shape; semi-circular with an appended rectangle. As the filler loading level increased, a spike formed in the rectangular area with the spike longest at the filler loading of 1.09 vol%. Beyond this, the spike became smaller. Correlating the PD magnitude time-evolution plots in Figure 9 with the corresponding PD magnitude frequency distributions in Figure 10, revealed that the 'spike growth' shape corresponded to PD burst events. It can be argued that the ability of nanoparticles to suppress the rate of electrical tree induced degradation relates to how the PD activity is restricted to PD burst periods. In that regard, for the 1.09% BN/Epoxy, the optimal loading level corresponds to when the PD activity is restricted to relatively short bursts that are interspaced by relatively long periods of no PD activity. Similarly, for carbon, the periodic PD bursts events occur only in 0.33 vol% samples that also survived for much longer periods when compared to higher loadings. The optimal loading of 1.09 vol% for BN/Epoxy and 0.33 vol% for C/Epoxy as determined through electrical tree PD analysis is consistent with the rheology analysis results presented in part 1 of this study.

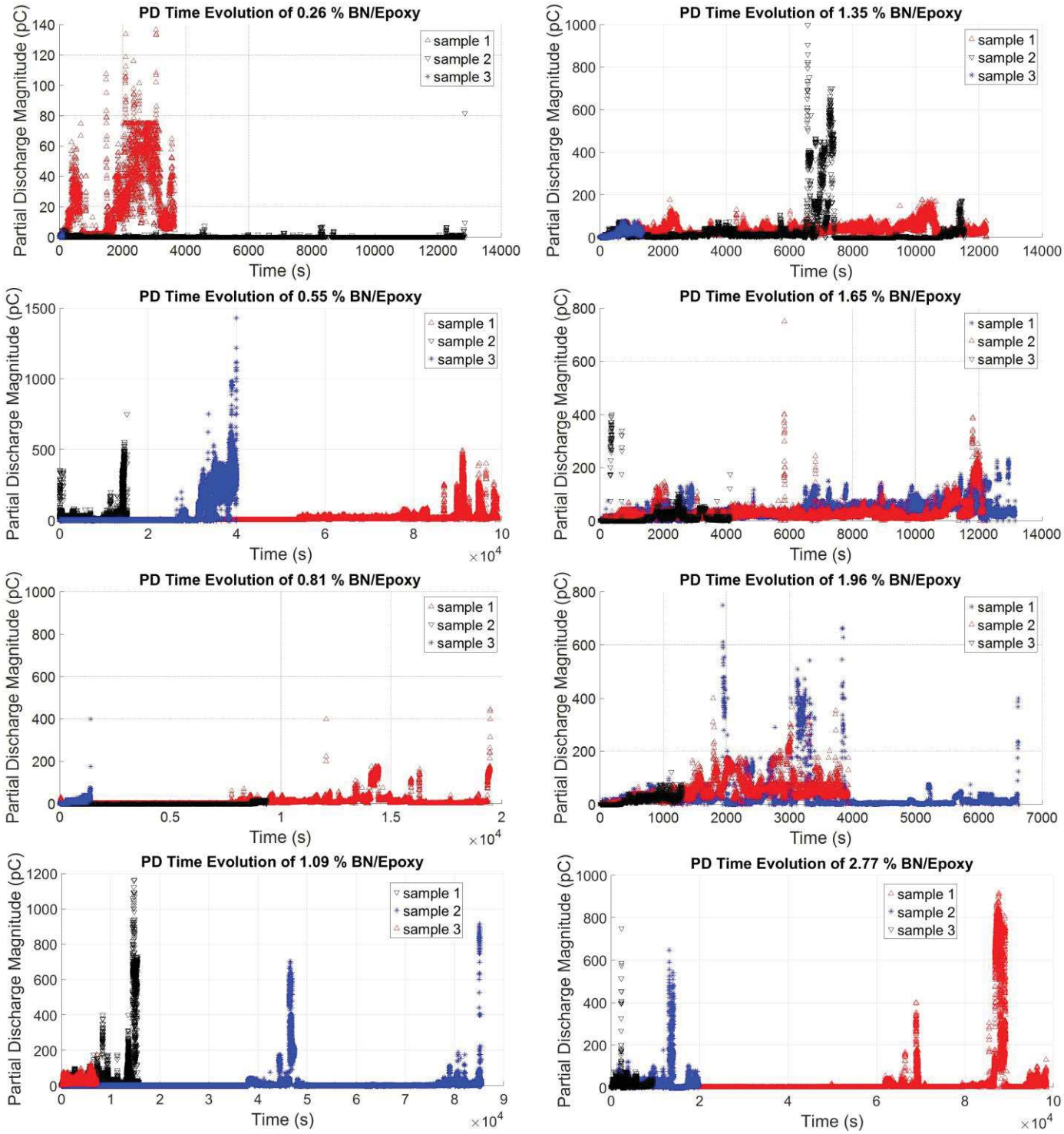

Figure 9: PD time evolution showing the progression of PD for different BN/Epoxy samples with varying nanoparticle volume fractions.

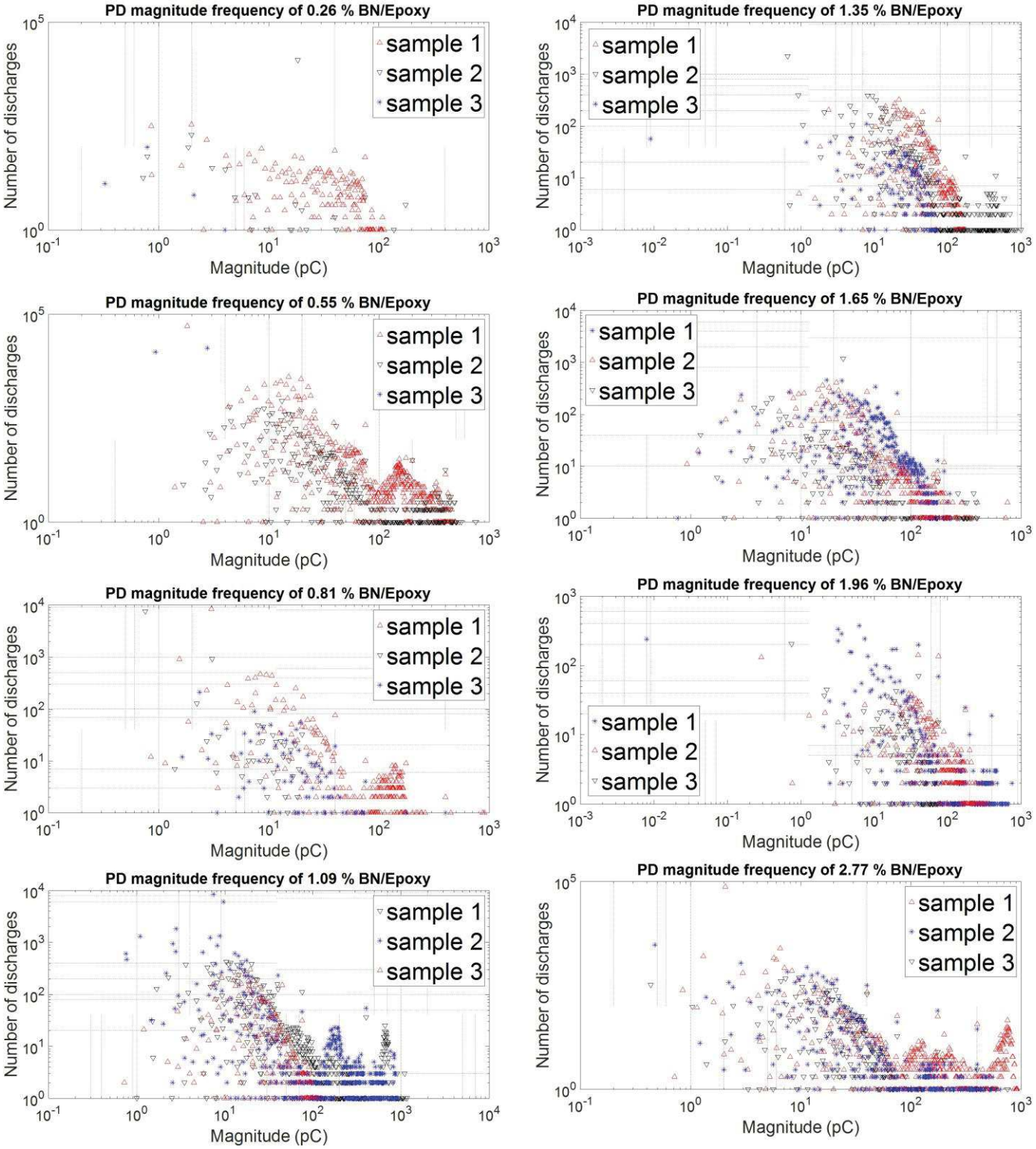

Figure 10: Log-log plots showing the change in distribution of PD in BN/epoxy with varying volume fractions.

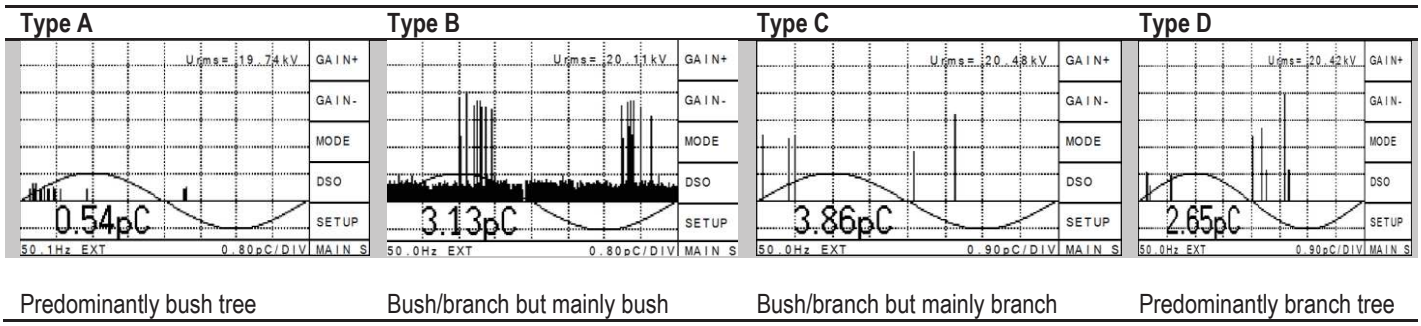

Figure 11: Different types of PDPRP corresponding to different types of electrical trees in pure epoxy.

PD phase-resolved-patterns (PDPRPs) have traditionally been used to characterise PD sources [10]. In that regard, the PDPRPs for each loading level were evaluated to determine the influence of nanoparticles on the latter PDPRP.

As mentioned earlier in Section 2, the electrical trees comprise of both short micro-tunnels (the bush) and the long micro-tunnels (the branches). Figure 11 shows different PDPRP types for clean epoxy with predominantly bush (Type A), bush-branch but mainly bush (Type B), bush-branch but mainly branch(Type C), and mainly branch characteristics (Type D).

Bush electrical trees support smaller and quasi-uniformly sized PD pulses while branches support bigger PDs of wide-ranging magnitudes. The resultant PDPRP comprise of a mixture of different pulse types presented in Figure 11. When continuously observed, electrical tree PDs occur as bursts and the composition of PD pulses in each half cycle of the excitation voltage change depending on how the electrical tree evolves in shape as it propagates in the insulation gap.

Examples of other possible intermediate types are shown in Figure 11. The PDPRP data for all samples, recorded every second, from the electrical tree inception to sample complete failure were processed using a purpose designed classification algorithm illustrated in Figure 12. Plots of the frequency of occurrence of each PDPRP type at each loading level are presented in Figure 13 and Figure 14 for BN/epoxy and C/epoxy respectively.

In the clean epoxy (zero loading) the order of predominance type of PDPRP is Type A, Type D, Type B and then Type C. The differences in predominance across the various PDPRP types however is small and this is characteristic of bush/branch electrical trees. For BN/Epoxy, as the filler loading increased, the order of predominance changed and at 1.09 vol%, Type A became prevalent by orders of magnitude over other types (40% greater). Beyond 1.09 vol%, the order of predominance changed again such that at 2.77 vol% it almost resembles that of clean epoxy. The predominance of Type A at filler loading of 1.09 vol% means that at the optimal loading, nanoparticles restrict electrical trees to bush types.

With C/Epoxy, only meaningful PD data was recorded at 0.33 vol% and 0.89 vol% filler loadings. Figure 14 shows that the PDRDP type combinations of C/epoxy are similar to those of clean epoxy but the number of occurrence become increasingly suppressed. As the particle concentration increased, the material changes from more insulating to more conductive.

All PD analyses outcomes for BN/Epoxy as a function of filler loading point to 1.09 vol% as the filler loading that gives optimal PD performance. A SEM image (Figure 15) of the 1.09 vol% BN/Epoxy shows individual and relatively small agglomerates of BN particles all fairly uniformly distributed. In contrast, a much lower loading of 0.55 vol% (Figure 16) has more and much bigger clumps with fewer individual particles and not as uniformly distributed as at 1.09 vol%. Similar SEM analysis of C/Epoxy is not possible as carbon particles and epoxy cannot be contrasted.

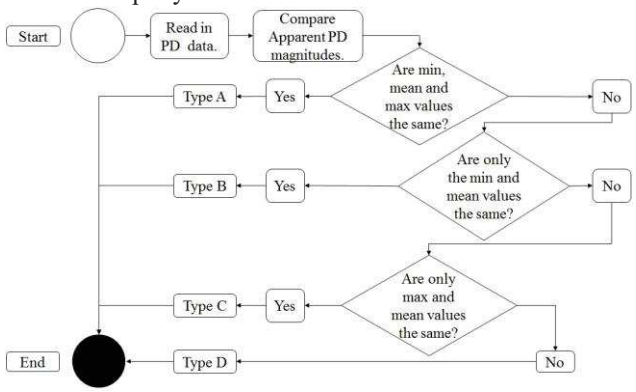

Figure 12: Flow diagram showing a possible way of grouping the PD activity.

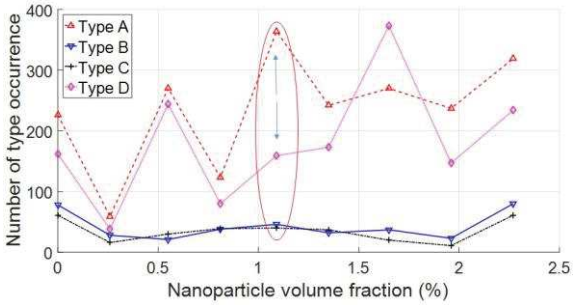

Figure 13: PDPRP type variation predominance in BN/Epoxy as a function of particle filler loading level indicating emphasis on particular type of tree growth.

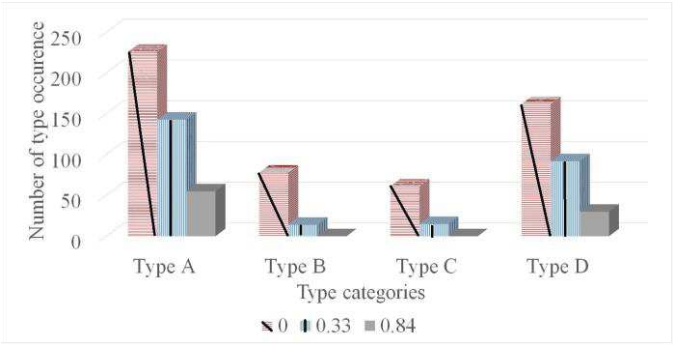

Figure 14: PDPRP type variation in C/Epoxy as a function of 0.33 vol% and 0.89 vol% against pure epoxy.

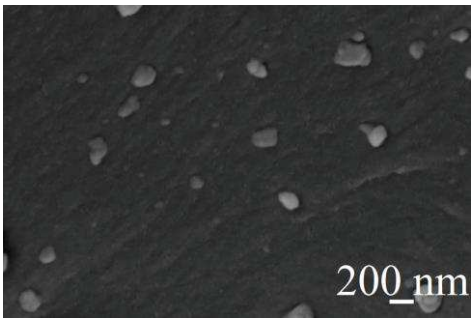

Figure 15: SEM image showing surface of 1.09 vol% BN/Epoxy nanodielectric with individual and large clusters of particles well distributed.

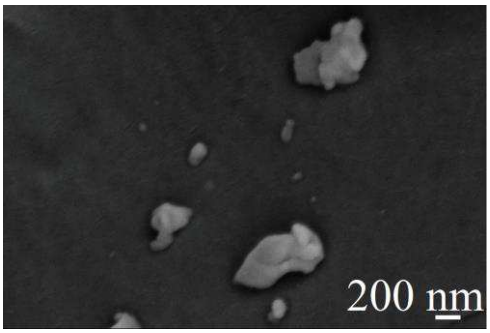

Figure 16: SEM showing surface of image of 0.55 vol% BN/Epoxy nanodielectric with larger clumps of particles poorly distributed.

3.2 X-RAY COMPUTER TOMOGRAPHY IMAGE ANALYSIS

A 0.33 vol% (optimally field) C/Epoxy test sample that had been exposed to 194 hours of voltage application and a clean epoxy sample that had survived 4 hours of continuous voltage application were analysed using a 3-D X-ray microscopy computer topographer (XCT). Figure 17 and Figure 18 show 3D rendered XCT images of pure epoxy confirming that the trees were indeed of bush-branch type as deduced earlier through PD analysis. In the clean epoxy sample, electrical trees with fine branches down to the sub-nanometre scale are shown with rich contrast.

In addition, relatively large channels and flat crack planes were formed. In contrast, Figure 19 to Figure 22 show the XCT images of the 0.33 vol% C/epoxy test specimen taken out before failure after eight days of continuous 20 kV voltage endurance. There appears to be no electric trees! However, a region enveloping part of the needle tip is clearly discernible as comprising a material with a density different from that of the nanodielectric and the needle (tungsten). This region is not symmetrical around the needle tip as evident in Figure 20 to Figure 22 nor does it extend along the entire bevelled part of the needle tip.

Such dimensional features rule out the possibility of the effect arising from mechanical retraction of the needle within the C/epoxy. Remarkably, the degraded region follows very closely the profile of the intensified electric field region around the needle tip as depicted in electric field plots in Figure 23 and Figure 24. The simulations assume absolutely pristine epoxy completely devoid of any kind of defect.

It is also interesting to note the presence of micro-sized pieces of metal present in the degraded region around the needle tip as shown in Figure 19. It is speculated that due to the intensified electric field (1 MV/mm) along the interface of the needle tip and the C/Epoxy material, energy is imparted into the material resulting in physiochemical processes that may possibly include electrical trees at some stage.

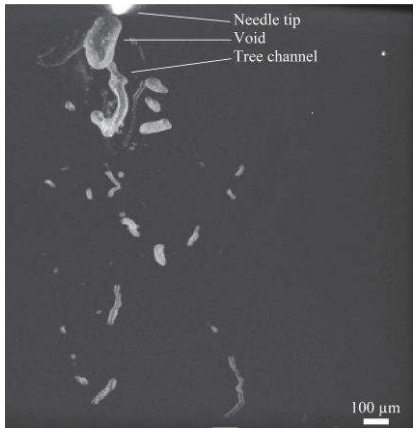

Figure 17: 3D rendered XCT image showing gap between needle and plane of un-failed clean epoxy samples stressed for four hours.

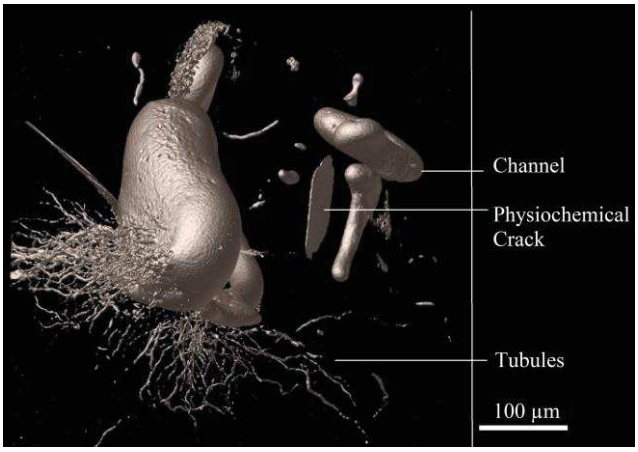

Figure 18: 3D rendered image close to the needle tip showing small tubules vs large channels as characteristic of bush-branch trees.

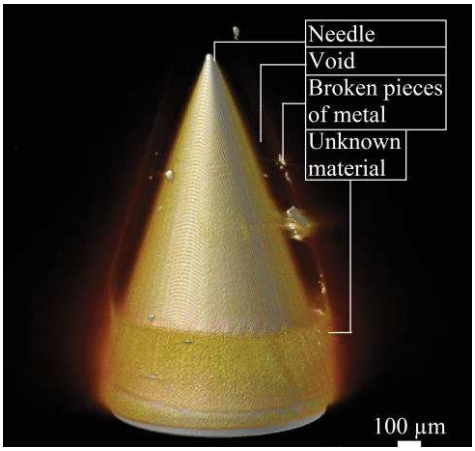

Figure 19: 0.33 vol% C/epoxy after 194 hours showing a void which is different to what has been expected from PD analysis.

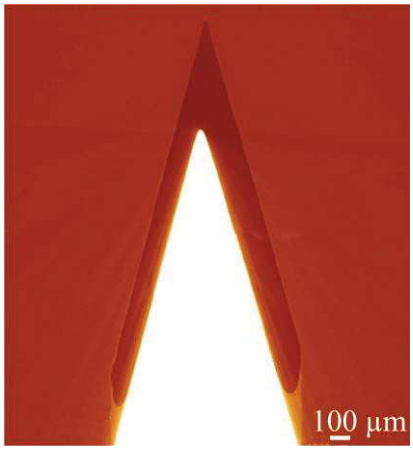

Figure 20: 2D side view of void around needle tip in 0.33 vol% C/epoxy.

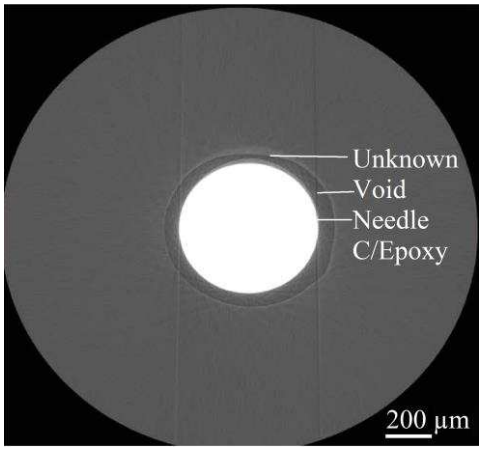

Figure 21: Top down view of void around needle tip in 0.33 vol% C/epoxy closer to the total needle circumference on the bevel of the needle.

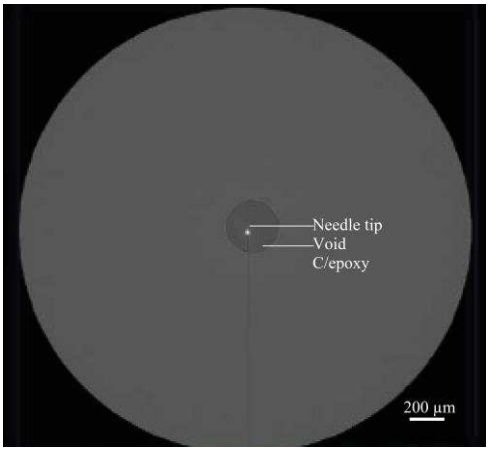

Figure 22: Top down view of void at needle tip in 0.33 vol% in C/epoxy closer to 5 µm tip showing the non-concentric void compared to needle tip location.

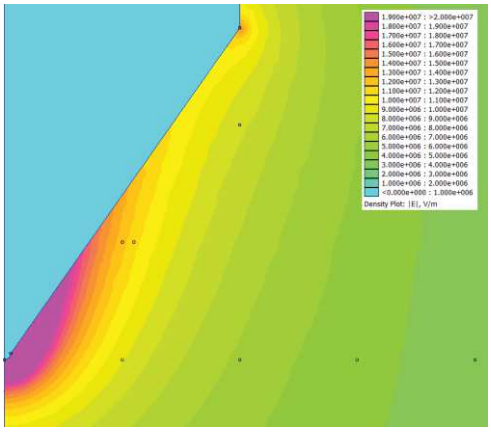

Figure 23: FEMM simulation of axis symmetric results of needle in pure epoxy.

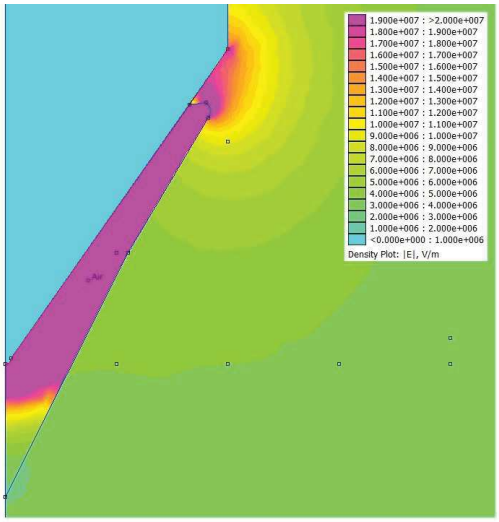

Figure 24: FEMM axis-symmetric simulation of reconstructed void showing electric field distribution.

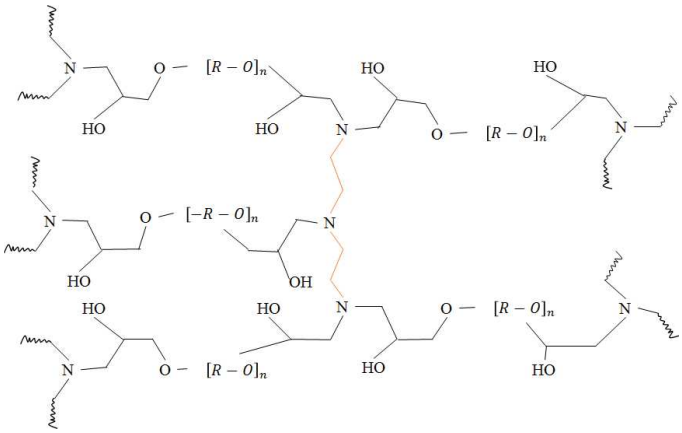

Figure 25: Fabricated epoxy chain showing chemical structure of Araldite cross-linked with hardener [11].

4. DISCUSSION

The chemical structure of fabricated epoxy is shown in Figure 25. The growth of electrical trees in media such as epoxy is a function of the electrical degradation, molecular scission, and gaseous build up within the channels. The nature of the environment within the channels as the tree propagates through the insulation was not investigated in this study. It is currently speculated that the trees contain radicals, photon, and phonon emission, and ion formation and combination as the partial discharges occur [12].

It is evident from Figure 18 that due to gaseous build up that micro-cracks form during the treeing process. If the molecular chains are shown in Figure 25 break into the primary components, it may be possible that reactions that take place during corona with air occur shown in (2) [12].

$$\begin{aligned} 3O_{2(g)} + hv &\Rightarrow 2O_{3(g)} \\ N_{2(g)} + O_{2(g)} + hv &\Rightarrow 2NO_{(g)} \\ NO_{(g)} + 0.5 \times O_{2(g)} &\Rightarrow NO_2 \\ 2NO_{2(g)} + H_2O_{(g)} &\Rightarrow HNO_{3(g)} + HNO_2 \end{aligned} \qquad (2)$$

Within the BN/epoxy nanodielectrics, the nature of the trees formed changes for the concentration of particles within the matrix. These results offer further insight into the volume and bulk models [13], [14]. As the particle concentration increased, the particles reached a point of optimal distribution, beyond which saturation occurred and agglomerates formed. As the agglomerates increased in size, the composite performed more like a submicro or micro-composite than a nanocomposite. The particle type, however, does not significantly prevent trees from forming. This is because the BN/composites mechanically were shown from AFM data to be harder than C/Epoxy or pure epoxy as shown in part 1.

Carbon nanoparticles have been referred to as electron scavengers [3]. It is currently speculated that at low concentrations of CNS, the particles remove electrons from the discharge region causing the discharges to be suppressed in magnitude. As the particle concentration increases, and either the inter-particle distance decreases, or the particles get into contact, the C/epoxy nanodielectric changes from being an insulator to a conductor under high voltage conditions.

If the energy absorption phenomena of the C/Epoxy matrix at low concentrations could lead to reactions as seen in (2), intense heat and various radical gases may have been produced. This would result in chemical reactions as air/oxygen/ozone and/or nitric/nitrous acid reacting with tungsten above ~400 ºC to form brittle tungsten oxide [15] - [17]. Such phenomena could be the origin of the micro-sized metallic pieces observed in the degraded region. The electric field simulation results indicate that if the growth of electrical trees was solely dependent on the electric field, then possibly a void as observed in C/epoxy may energetically occur during the course of the electric field degradation.

It should be pointed out that these findings are intriguing and call for further studies to fully understand the localised high electric field-induced degradation in C/Epoxy nanodielectrics. In addition, this study now opens the possibility of using other conductive nanoparticles for investigation into the effects on electrical trees for nanodielectrics.

5. CONCLUSION

In this paper it has been demonstrated that it is possible to use carbon nanospheres to fabricate carbon/epoxy nanodielectrics which may withstand electrical tree degradations at low concentrations. Electrical tree analyses were used to characterise the different nanoparticle concentration effects on epoxy. SEM and PD results were used to establish that the optimal loadings were 1.09 vol% and 0.33 vol% for BN/epoxy and C/epoxy respectively. The key findings are summarised as follows:

i. Conductive nanoparticles may be candidates for retarding electrical tree growth in nanodielectrics.
ii. Various electrical tree PD analyses techniques were used to confirm the predetermined optimal loading levels.

iii. XCT was used as an additional analysis tool to evaluate the change in electrical tree nature given non-transparent nanodielectrics. Additionally, XCT was used to confirm electrical tree phenomena in a conventional solid insulator.

iv. Conventional knowledge associated with the mechanism of electrical trees and PD in optimally filled C/Epoxy nanodielectrics will need re-evaluation given the XCT and electric field results.

ACKNOWLEDGEMENTS

Erasmus Mundus for the INSPIRE scholarship which enabled the ability of one of the authors to travel to Uppsala Sweden and form collaborative ties. In South Africa, Eskom and the National Research Foundation (NRF) are gratefully acknowledged for their continued support of the high voltage engineering research work at the University of the Witwatersrand, Johannesburg.

REFERENCES

[1] F. Guastavino and B. Cerutti, "Tree growth monitoring by means of digital partial discharge measurements," *IEEE Transactions on Dielectrics and Electrical Insulation*, vol. 10, no. 1, pp. 65–72, Feb. 2003.

[2] M. G. Danikas and T. Tanaka, "Nanocomposites-a review of electrical treeing and breakdown," *IEEE Electrical Insulation Magazine*, vol. 25, no. 4, pp. 19–25, Jul. 2009.

[3] M. Jarvid *et al.*, "A New Application Area for Fullerenes: Voltage Stabilizers for Power Cable Insulation," *Adv. Mater.*, vol. 27, no. 5, pp. 897–902, Feb. 2015.

[4] C. Nyamupangedengu and D. R. Cornish, "Time-evolution phenomena of electrical tree partial discharges in Magnesia, Silica and Alumina epoxy nanocomposites," *IEEE Transactions on Dielectrics and Electrical Insulation*, vol. 23, no. 1, pp. 85–94, Feb. 2016.

[5] T. Andritsch, U. Lafont, P. H. F. Morshuis, and J. J. Smit, "Electrical tree propagation time to breakdown for epoxy resin composites containing alumina and silica nanoparticles," presented at the 18th International Symposium of High Voltage Engineering, Seoul, Korea, pp. 1694–1698.

[6] T. Tanaka, "Mechanisms of crossover phenomenon in tree length vs. applied voltage characeteristics between base epoxy and its nanocomposites," in *18th International Symposium of Highvoltage Engineering*, Seoul, 2013.

[7] IEC, "High voltage test techniques - Partial discharge measurements." IEC, 2000.

[8] J. V. Champion, S. J. Dodd, and J. M. Alison, "The correlation between the partial discharge behaviour and the spatial and temporal development of electrical trees grown in an epoxy resin," *J. Phys. D: Appl. Phys.*, vol. 29, no. 10, p. 2689, 1996.

[9] R. Schurch, S. M. Rowland, R. S. Bradley, and P. J. Withers, "Imaging and analysis techniques for electrical trees using X-ray computed tomography," *IEEE Transactions on Dielectrics and Electrical Insulation*, vol. 21, no. 1, pp. 53–63, Feb. 2014.

[10] A. Contin, A. Cavallini, G. C. Montanari, G. Pasini, and F. Puletti, "Digital detection and fuzzy classification of partial discharge signals," *IEEE Transactions on Dielectrics and Electrical Insulation*, vol. 9, no. 3, pp. 335–348, Jun. 2002.

[11] Huntsman, "Technical Datasheet Araldite Casting Resin System (Cy 231-1 CH/Aradur Hy 925)." Huntsman Advanced Materials Electrical Insulation Materials, Jul-2011.

[12] Haddad M. and Warne D., *Advances in High Voltage Engineering*. Stevenage, Herfordshire, GBR: The Institution of Engineering and Technology, 2004.

[13] S. Raetzke and J. Kindersberger, "Role of interphase on the resistance to high-voltage arcing, on tracking and erosion of silicone/SiO_2 nanocomposites," *IEEE Transactions on Dielectrics and Electrical Insulation*, vol. 17, no. 2, pp. 607–614, Apr. 2010.

[14] M. Praeger, T. Andritsch, S. G. Swingler, and A. S. Vaughan, "A simple theoretical model for the bulk properties of nanocomposite materials," in *2014 IEEE Conference on Electrical Insulation and Dielectric Phenomena (CEIDP)*, 2014, pp. 699–702.

[15] E. Lassner and W.-D. Schubert, *Tungsten: Properties, Chemistry, Technology of the Element, Alloys, and Chemical Compounds*. Springer Science & Business Media, 2012.

[16] J. L. Sabourin and R. A. Yetter, "High-Temperature Heterogeneous Reaction Kinetics of Tungsten Oxidation by CO2, CO, and O2," *Journal of Propulsion and Power*, vol. 25, no. 2, pp. 490–498, 2009.

[17] H. Shindo, C. Egawa, T. Onishi, and K. Tamaru, "Reaction mechanism of ammonia decomposition on tungsten," *J. Chem. Soc., Faraday Trans. 1*, vol. 76, no. 0, pp. 280–290, Jan. 1980.



Mr. Andrew M. Hank was born in Johannesburg, South Africa. He received his Bachelor in Science honours degree in Electrical Engineering from the University of the Witwatersrand in 2014. In 2015, he began his Masters Studies and was awarded the INSPIRE Scholarship to pursue research and Studies at Uppsala University in Sweden Currently he is completing his master's studies at the University of the Witwatersrand, Johannesburg. His main interests are in High Voltage, insulation systems, Nano sensors, power electronics and Lightning research.



Prof Cuthbert Nyamupangedengu was born in Zimbabwe. He received the Bachelors honours degree in electrical engineering from the University of Zimbabwe in 1994. At the University of the Witwatersrand, Johannesburg, in 2004, he was awarded the M.Sc. Engineering (with distinction) and in 2011, the Ph.D. He is a lecturer at the University. Before moving to the University of the Witwatersrand, Cuthbert was an engineer in the Zimbabwe Electricity Supply Authority from 1995 to 2005 in various capacities mainly in power system planning and development. His passion is research on diagnosis of high voltage insulation.



Prof. Iakovos Sigalas is a professor of Ceramic Science in the School of Chemical and Metallurgical Engineering at the University of the Witwatersrand, Johannesburg, and the Ceramic Materials Focus Area Coordinator of the DST-NRF Centre of Excellence in Strong Materials, South Africa.



Ms. Bridget K. Mutuma was born in Kenya. She received her Bachelor's degree with honours in Analytical Chemistry from Kenyatta University in 2009. She was awarded the MSc. in Material Science and Engineering from the Kangwon National University, South Korea through the Korean Government Scholarship Program (KGSP) in 2013. Currently, she is a PhD candidate in the School of Chemistry at the University of Witwatersrand. Her research interests are carbon nanostructures synthesis and characterization, photocatalysis, organic photovoltaic devices, biosensors and chemical sensors.



Prof Neil J. Coville is currently Emeritus Professor at the University of the Witwatersrand, Johannesburg. South Africa. He obtained his PhD at McGill University, Montreal. His current research interests include Fischer-Tropsch catalysis, synthetic routes to shaped carbon materials and the use of the carbons in catalysis, solar cells and sensors. Current studies involve the synthesis of hollow carbon spheres for use as nanoreactors**.**